Comparison of Advanced Control Schemes Implemented on Hydraulic Actuated Robot Manipulator

In Memory of Gitte Mørk

AALBORG UNIVERSITY

SEKTOREN
Fibigerstræde 16
9220 Aalborg Ø

Title:	Comparison of Advanced Control Schemes Implemented on Hydraulic Actuated Robot Manipulator
Semester:	EMSD 10
Semester theme:	Master Thesis
Project period:	4^{th} of February to 3^{th} of June 2008
ECTS:	30
Supervisors:	Torben O. Andersen, Prof., M.Sc., Ph.D. Henrik C. Pedersen, Ass. Prof., M.Sc., Ph.D.
Project group:	Pon101-P16B

Kristian Holm Nielsen

Lasse Schmidt

Copies:	5
Pages, report:	131 (-blanks)
Pages, appendix:	96

SYNOPSIS:

This thesis concerns the establishment, implementation, testing, and finally comparison of an array of controllers on an electro hydraulic robot manipulator. The result of the thesis is the comparison of the established controllers, which has the purpose of evaluating the performance of the chosen controllers, implemented on the electro hydraulic robot manipulator, when used as a position servo. The controllers are tested regarding a set of criteria involving tracking performance, number of transducers needed and robustness towards disturbances. As a base of testing, a series of classical linear controllers have been established, and also a series of non-linear controllers such as adaptive and learning controllers have been implemented and tested against each other and the linear control schemes.

In order to simulate the behavior of the electro hydraulic servo robot with the various controllers implemented, a non-linear model has been developed, and for the development and analysis of the controllers also a linear model has been developed. Selected controllers have then been implemented on the physical electro hydraulic servo robot.

By signing this document, each member of the group confirms that all participated evenly in the project work and thereby that all members are collectively liable for the content of the report.

Preface

This thesis documents a master thesis completed by group P101-P16B at the 10^{th} semester at M.Sc education in mechanical engineering/Electro-Mechanical System Design at the University of Aalborg. The thesis concerns testing of the performance of various controllers, linear and non-linear, on an electro hydraulic position servo. The testing of the controllers is carried out on a non-linear model of the electro hydraulic position servo constituted by a robot manipulator. Selected controllers is then implemented and subsequently tested on the physical robot. After having implemented and tested the various controllers, a comparison is carried out in order to decide which controller types are best suited for an electro hydraulic position servo.

The thesis is divided into four main parts - a part concerning the system modeling and trajectory planning, a part concerning linear control design, a part concerning advanced control design and finally a part regarding comparison of the chosen controllers, together with final conclusions and perspectives.

Material which has relevance for the thesis but does not belong inside this documentation is accompanied either in paper format in the appendix of the report or on the appended CD. The CD contains various MATLAB/SIMULINK models of the robot constituting the electro hydraulic servo system, data sheets, program code and a PDF-version of the thesis etc.

Group P101-P16B, June 2008

Contents

Chapter 1

Thesis Outline, System Overview & Approach

Contents

In this chapter the thesis outline and the system utilized in this thesis are presented. Following this the problem formulation of the thesis is accounted for, followed by a description of the approach for solving the problem formulation.

1.1 Thesis Outline

This thesis is carried out in order to investigate the performance of an array of controllers both linear and non-linear controllers such as adaptive and learning controllers implemented on a hydraulic servo system (hence forward designated HSS). The idea is to test the various controllers regarding tracking performance, robustness to disturbances, and the amount of equipment involved, in utilizing the abilities of the controllers, such as position, velocity, acceleration, and pressure transducers.

The controllers will be tested on a nonlinear model of a hydraulic two bar linkage robot manipulator. All the established controllers are tested in simulation, and chosen controllers are implemented and tested on the physical system. A linear model of the HSS is also developed in order to design the linear controllers, and also in order to develop a simplified linear model of the HSS to facilitate the design of some of the nonlinear controllers.

1.2 Overall System Description

The overall system consists of two subsystems namely a hydraulic system and solid-state mechanical system. These are presented in the following.

1.2.1 Solid-State Mechanical Subsystem

The solid-state mechanical subsystem is, as seen on figure 1.1, constituted by two links and a base. On each link, or arm, is mounted a servo system consisting of a cylinder, safety valve and servo valve. Link I is connected to the base of the robot by a revolute joint, and also connected to link II by a revolute joint. Link I and II, including their belonging servo systems, will in the remaining of this thesis be designated HSS I and HSS II, respectively.

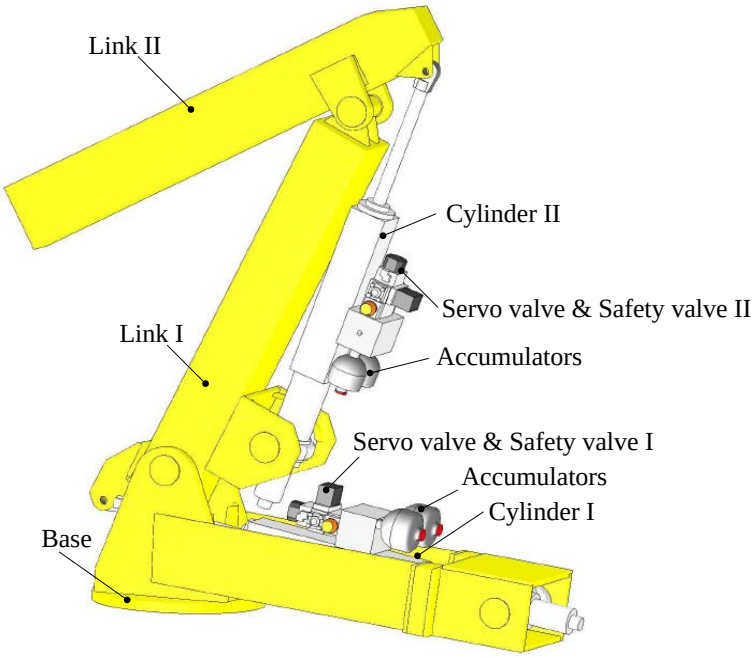

Figure 1.1: Overview of robot manipulator.

1.2.2 Fluid Mechanical Subsystem

The fluid mechanical subsystem is constituted of two identical fluid mechanical subsystems, one for each link on the system. In figure 1.2 is shown a schematic of the fluid mechanical subsystem. On each side of the cylinders is mounted a pressure transducer supplying information on the pressure of both sides of the pistons. Directly on the cylinders is mounted a safety valve which cuts of supply to the cylinders if the power to the safety valves is cut, which facilitates an emergency stop. The servo valves are mounted after the safety valves in the flow line to the cylinders. On each supply- and return line is mounted an accumulator in order to minimize pressure fluctuations in the system. As seen on the figure a drain is connected to each cylinder, indicating that leakage oil is

returned to the reservoir. The cylinders are constructed in a way that minimizes coulomb friction by allowing a clearance between the piston and the cylinder wall. By doing so allows for a larger leakage flow than for cylinders where this is not implemented, however at the same time it removes stiction phenomena.

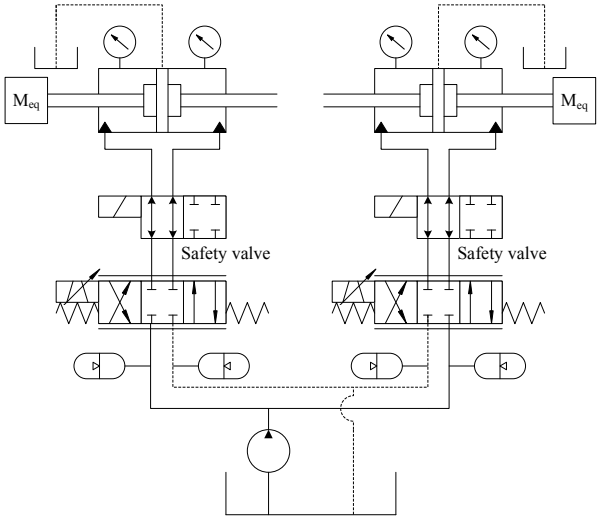

Figure 1.2: Diagram of hydraulic system.

1.3 Problem Formulation

The problem initiating this thesis is the question if, whether or not, there is something to gain by using more advanced, and possibly also more demanding nonlinear control schemes for controlling a hydraulic servo system, instead of more classical linear controllers.

To solve this task the following problems that need to be solved are:

- Which design criteria should be used for designing the various controllers?
- How can the controllers and their performance be compared?
- Which controllers perform the best?

1.4 Thesis Approach

In the following the approach for this thesis is described. The approach is divided into the following elements.

- Development of system models
- Verification of models
- Trajectory planning

- Establishment of linear controllers
- Establishment of nonlinear controllers
- Comparison of controllers
- Conclusions

In the following, the above listed elements will be briefly described.

1.4.1 Development of System Models

In order to develop and test the various controllers in this thesis, a nonlinear and linear model are developed. The nonlinear model for test of controllers, and the linear model which is to be used for linear control design.

1.4.2 Verification of Models

In order to insure the validity of the nonlinear model outputs, this is compared with transducer outputs from the physical system, and the nonlinear model is tuned to fit this. The outputs from the nonlinear and linear models is then compared in order to validate the linear model near an operating point.

1.4.3 Establishment of Linear Controllers

As basis for comparison of controllers, a series of classical linear controllers are establishment. Furthermore some extensions to these controllers are made.

1.4.4 Establishment of Nonlinear Controllers

A series of nonlinear controllers in the form of various adaptive and learning controllers are establishment.

1.4.5 Comparison of Controllers

After having implemented the controllers on the nonlinear model, and in some cases on the physical system, a comparison of the controllers will be made on the basis of performance, equipment needed in the form of transducers, and robustness towards disturbances.

1.5 Evaluation Criteria

In the following a list of evaluation criteria is set up and subsequently elaborated.

- Tracking performance
- Number of sensors needed
- Robustness towards disturbances

1.5.1 Tracking Performance

The tracking performance of each controller will be tested on the nonlinear model and for some controllers implemented on the physical system. In order to evaluate the tracking performance the system is to follow a a certain trajectory, either in actuator space, or for the tool center point (TCP). The difference between the desired trajectory and the actual trajectory followed by the HSS's is then evaluated, by observing the rms tracking error and the peak tracking error. By doing so the controllers ability to handle time varying references is evaluated.

1.5.2 Number of Transducers Needed

Depending on the complexity of the controllers, a varying amount of transducers are needed in order to secure the necessary amount of feedback signals from the HSS making the controller in question more expensive and at the same time also more prone to errors in the form of transducer failure. This hopefully is countered by increased controller performance.

1.5.3 Robustness Towards Disturbances

When the HSS's is in operational mode a number of disturbance input to the system is to be expected, and therefore a crucial parameter in the evaluation of the controllers is their robustness towards such disturbances. In order to test this robustness each controller is, on the nonlinear model in simulink, subjected to mass step at a given point in time of the trajectory, and the ability to reject the disturbance is then evaluated.

1.5.4 Final Conclusions

Based on the comparisons of the various controllers a conclusion is made stating which controllers are the most suited for this type hydraulic servo system.

1.6 Summary

In this chapter the thesis outline and a system description has been given. Further a problem formulation has been setup, and an approach for how to solve the problem formulation has been given. The tasks for solving the problem formulation are various modeling work and verification, trajectory planning, establishment of linear controllers, establishment of nonlinear controllers, and finally a comparison of the established controllers followed by conclusions made from this thesis.

Part I

System Modeling & Trajectory Planning

Chapter 2

Dynamic Model of Robot Manipulator

Contents

In this chapter the non-linear dynamic model of the robot manipulator is accounted for. Here the overall considerations regarding the kinematics and kinetics of the robot manipulator are described, and a more detailed derivation of the model are found in appendix A. Finally, the model verification will be carried out.

2.1 Solid-State Mechanical Subsystem

The solid state part of the model is derived as a two degree of freedom system. The flexible behavior of the system is neglected in the model, and the system is hence considered as consisting of completely rigid bodies. The kinematics of the system is derived based on the joint angles (illustrated in figure 2.1):

$$\underline{q} = [\theta_I \ \theta_{II}]^T \tag{2.1}$$

The solid state part of the model is derived in joint space by use of the Newton-Euler formulation:

$$\underline{\tau} = [\tau_{LI} \ \tau_{LII}]^T = \underline{\underline{D}}(\underline{q})\ddot{\underline{q}} + \underline{H}(\underline{q}, \dot{\underline{q}}) + \underline{G}(\underline{q}) \tag{2.2}$$

Here the joint load torques are related to the forces applied from the hydraulic system (via the cylinder pistons), by the *drive jacobian* $\underline{\underline{J}}_d$, which yields:

$$\underline{\tau_L} = \underline{\underline{J}}_d^T \underline{F_L} \tag{2.3}$$

Hence the non-linear dynamic model of the solid state part of the system compliant with the hydraulic system, is established as:

$$\underline{F_L} = \underline{\underline{J}}_d^{-T} \underline{\tau_L} = \underline{\underline{J}}_d^{-T} \underline{\underline{D}}(\underline{q})\ddot{\underline{q}} + \underline{J}_d^{-T} \underline{H}(\underline{q}, \dot{\underline{q}}) + \underline{\underline{J}}_d^{-T} \underline{G}(\underline{q}) \tag{2.4}$$

As mentioned previously, the complete derivation of the nonlinear model is found in appendix A.

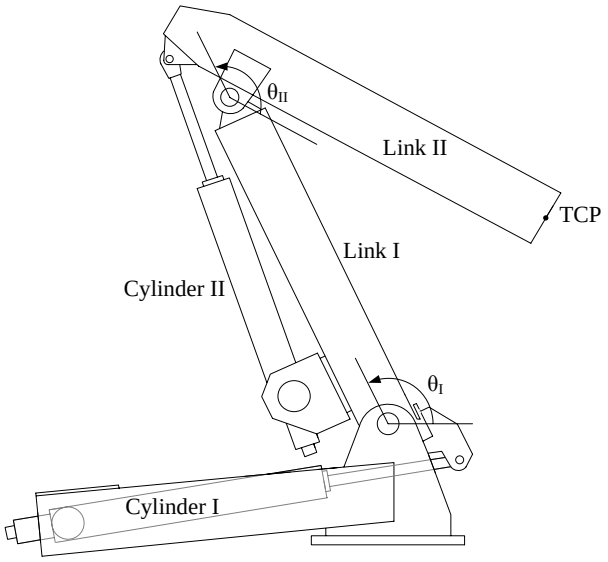

Figure 2.1: Robot manipulator.

2.2 Fluid Mechanical Subsystem

The hydraulic system model is established as two individual actuator models. The models are based on the force equilibriums, and the flow continuities of the two actuators, and the hydraulic servo valves are represented by orifice equations, relating the load pressure and spool position voltage to the flow through the servo valves. Flow forces, pressure loss in hoses etc., has been neglected. The model derivation of the hydraulic system is found in appendix A.

2.3 Model Verification

The nonlinear model is verified with respect to experimental measurements on the physical system. In the following, the model is verified regarding gravitation and dynamics of the system. This is carried out by sampling the valve input signals given to the servo valves of the physical system, and feeding these to the nonlinear model, and hence observing and comparing the variations in load pressure of the two cylinders.

2.3.1 Verification of Gravitation

The model of the system has been derived such that it is possible to apply a load element to the system near the TCP. However, the load element for this use has not been available, and hence the model is verified only for the *no load* situation.

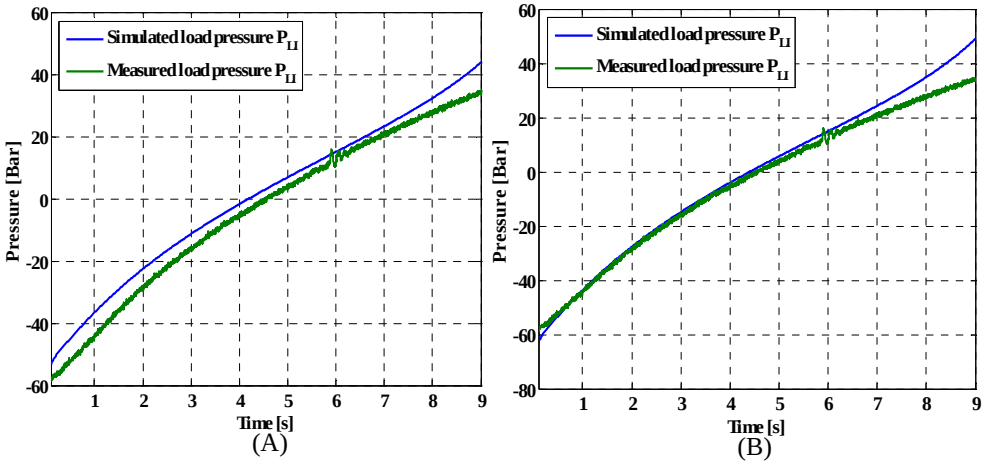

Figure 2.2: (A) Load pressure P_{LI}. Both cylinder pistons are initially in extended position. Cylinder I is retracted, while cylinder II is kept in fixed position. (B) Load pressure P_{LI}. Cylinder I is initially in extended position, and cylinder II in retracted position. Cylinder I is retracted, while cylinder II is kept in fixed position.

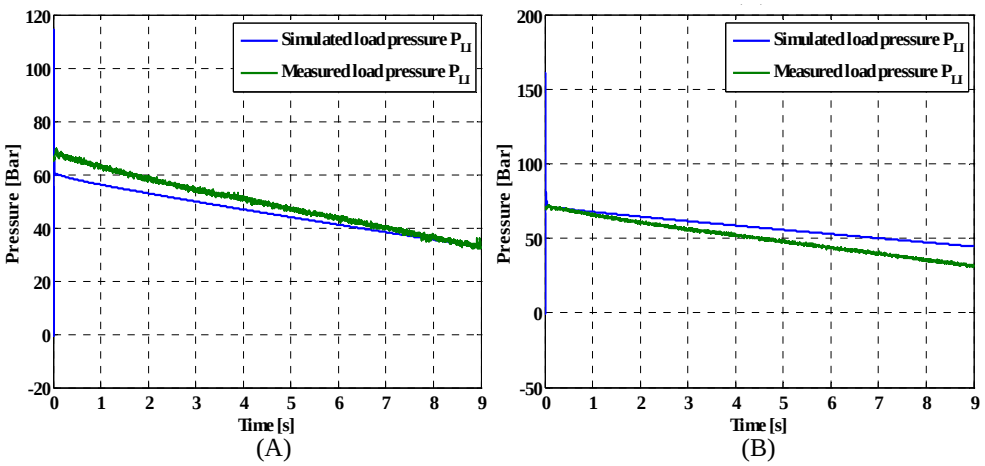

Figure 2.3: (A) Load pressure P_{LI}. Cylinder I is initially in retracted position, and cylinder II in extended position. Cylinder I is extended, while cylinder II is kept in fixed position. (B) Load pressure P_{LI}. Both cylinder pistons are initially in retracted position. Cylinder I is extended, while cylinder II is kept in fixed position.

In order to verify the gravitational terms of the model, the experiments are carried out with constant low velocity on the pistons, thereby not exiting any dynamics of the system. The low velocity will cause the coriolis- and viscous friction terms to be small, and hence having no significant influence on the system. Thereby these can be neglected. Furthermore, as the pistons are moving with constant velocity, not exiting the system

dynamics, the gravitational terms and coulomb friction can be verified by evaluating the load pressures of the cylinders.

From figures 2.2 and 2.3 it is found that the static terms of link I has been modeled sufficiently accurate, compared to the physical system. However, from figures A.16 and A.17 of appendix A (verification plots for link II), it is found that this is less accurate than that of the verification for link I. This is assumed to be due to inaccuracies in the modeling regarding masses lengths and so on. However, it is found that the model is a sufficiently accurate rendering of the physical system regarding gravitation.

2.3.2 Verification of Dynamics

In order to verify the dynamics of the model, the dynamics of the hydraulic system need to be excited. This is carried out by applying a series of step inputs to the servo valve. These steps are applied randomly, and are of different magnitude, and the input signals over time is different for the two actuators. The inputs are applied simultaneously for the two actuators. Hence it is possible to verify the dynamics of the complete system. The results are shown in figure 2.4.

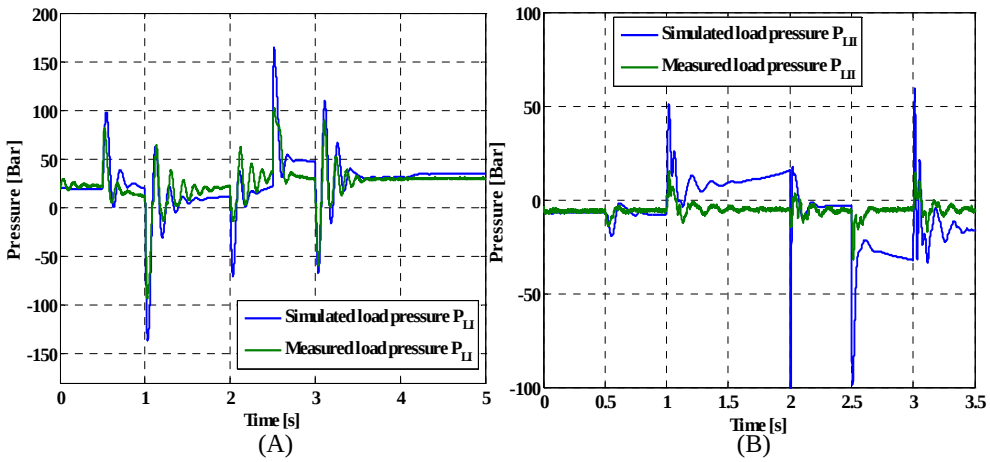

Figure 2.4: Load pressures resulting from the random step inputs. (A) Load pressure for cylinder I P_{LI}. (A) Load pressure for cylinder II P_{LII}.

During the data acquisition shown in figure 2.4, the initial positions for the cylinder pistons is the center position of the cylinders. The position for cylinder I has during simulations displaced itself approximately 80 $[mm]$ to each side from its initial position, thereby making it possible to verify the dynamics in most of its position range. Cylinder II has displaced itself approximately 40 $[mm]$ to each side of its initial position, during the experiment. This is a relatively small part of the position range, but due to the nearly constant inertia load on cylinder II, this is considered acceptable.

From figure 2.4 it is found that the model resembles the physical system, both regarding the pressure level and regarding the frequency of the resulting transients in the pressure. Regarding cylinder II, this is less accurate. However, still the pressure transients seen on the model resembles these of the physical system.

From the dynamic verification, it is found that the model is sufficiently accurate in resemblance to the physical system, implying that the model can be used in the design of various control systems. Hence the model is considered verified.

2.4 Summary

In the above, a dynamic model of the robot manipulator, both solid state and fluid mechanical, has been established. The developed model was subsequent tested, by comparison of pressure data from the physical system, regarding both dynamics and gravitation. It was found that the model proved adequately accurate for the development and testing of controllers.

Chapter 3

Linear Model of Robot Manipulator

Contents

This chapter concerns the development of the linear model of the robot manipulator. This is carried out by simplifying the expressions of the non-linear model, and linearizing non-linear terms. In this chapter an overall description of the linear model development is accounted for, and a complete derivation of this is found in appendix C. Finally, the linear model is compared to the non-linear model, and verified.

The linear model is established for the individual actuators, hence considering these as SISO systems. The index i can either denote I or II.

3.1 Linear Model

The linear model is derived for an operating point, chosen as the center position of the cylinder (accounted for in appendix C). The describing linear equations are given by:

$$M_{eqi}s^2x_{Pi} = p_{Li}A_i - B_{vi}sx_{Pi} - F_{Di} \tag{3.1}$$

$$q_{Li} = K_{qi}u_{vi} + K_{qpi}p_{Li} \tag{3.2}$$

$$p_{Li} = \frac{4\beta_{Fi}}{V_{\Sigma i}s}(q_{Li} - sA_ix_{Pi} - C_{Li}p_{Li}) \tag{3.3}$$

Where:

M_{eqi}:	equivalent mass	$[kg]$
p_{Li}:	load pressure	$[Pa]$
A_i:	ram area	$[m^2]$
B_{vi}:	viscous damping	$[kg/s]$
x_{Pi}:	piston position	$[m]$
F_{Di}:	disturbance	$[N]$

q_{Li}:	load flow	$[m^3/s]$
β_{Fi}:	bulk modulus	$[Pa]$
$V_{\Sigma i}$:	total volume of cylinder chambers and hoses	$[m^3]$
C_{Li}:	internal leakage coefficient	$[m^s/s/Pa]$

Represented by a block diagram, the linear model appears as shown in figure 3.1.

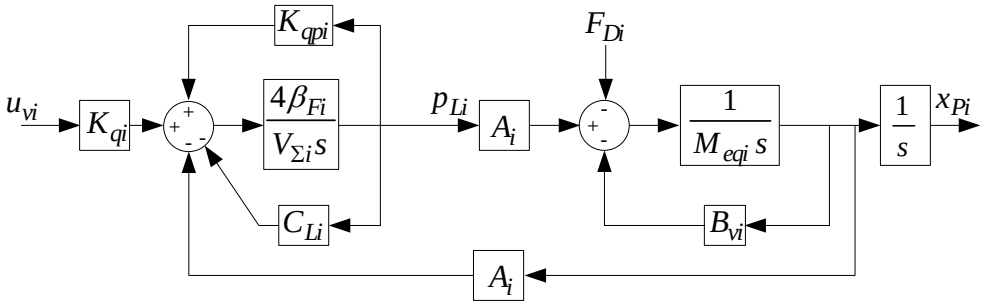

Figure 3.1: Block diagram of system.

Reducing the block diagram of figure 3.1, the transfer function representing the relationship between the servo valve input u_{vi} and the cylinder position x_{Pi} is obtained as:

$$G_i(s) = \frac{X_{Pi}(s)}{U_{vi}(s)} = \frac{K_i}{T_{ni}^2 s^2 + 2\zeta_i T_{ni} s + 1}\frac{1}{s} \tag{3.4}$$

Here the coefficients are give by:

$$K_i = \frac{A_{Pi}K_{qi}}{(C_{Li} - K_{qpi})B_{vi} + A_{Pi}^2} \tag{3.5}$$

$$\omega_{ni} = \frac{1}{T_{ni}} = \sqrt{\frac{4\beta_{Fi}}{V_{\Sigma i}M_{eqi}}((C_{Li} - K_{qpi})B_{vi} + A_{Pi}^2)} \tag{3.6}$$

$$\zeta_i = \frac{4\beta_{Fi}(C_{Li} - K_{qpi})M_{eqi} + V_{\Sigma i}B_{vi}}{2T_{ni}(4\beta_{Fi}((C_{Li} - K_{qpi})B_{vi} + A_{Pi}^2))} \tag{3.7}$$

Note that K_{qpi} is defined negative in appendix C.

3.2 Verification of Linear Model

It is needed to verify that the linear models does in fact represent the nonlinear model in the operating point (OP). This is carried out by applying small inputs to the two servo valves (due to the fact that the situation with a slight opening of the valve, is the most critical for the servo valve)- when the velocity of the piston in the nonlinear model reaches steady state, and is at the center position of the cylinder, a step input of $u_{vi} = 0.1$ $[V]$ is applied to excite the dynamics - at this point values of the actual load pressures and bulk modulus' are obtained, and these values are substituted in the coefficients of the linear model. Then a step input equal to one applied to the non-linear model at the operating point, is applied to the linear model, and as these are established for the operating point

in the center position of the cylinder, it is possible to examine whether the linear models actually represents the nonlinear model at this point. The results are shown in figure 3.2.

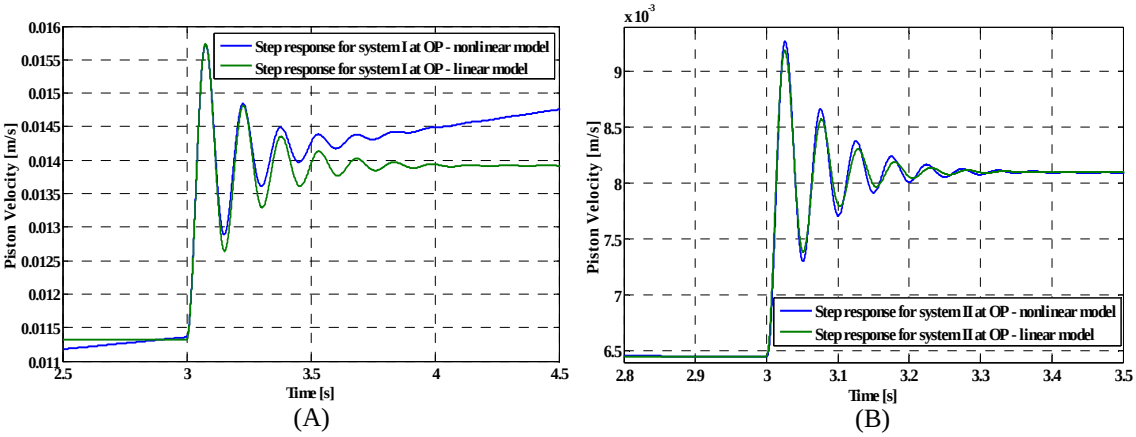

Figure 3.2: Transient responses of non-linear- and linear models. Operating point is reached at time $t = 3\ [s]$. (A) Verification of HSS I. (B) Verification of HSS II.

It is seen from figures 3.2 (A) and (B), that the transient behavior of the linear models are very similar to those of the nonlinear model near the operating point. As it would be expected, it is also seen that the linear models deviates from the nonlinear model the further away from the operating point the cylinder pistons moves.

It is concluded that the linear models are sufficiently accurate in resemblance to the nonlinear model near the operating point, and hence suitable for linear control design.

3.3 Summary

In this chapter a linear model of the robot manipulator has been derived, and subsequently verified by applying small inputs to the servo valves near the operating of the linear model and comparing outputs of the linear model to those of the nonlinear model. From comparison it was found that the resemblance to the nonlinear model was adequate and the linear model is hence considered verified.

Chapter 4

Trajectory Planning

Contents

In this chapter the planning of the trajectory will be carried out. This involves the shape of the trajectory for the tool center point, ensuring that the system is loaded in a proper way to be able to evaluate the performance of the control systems. The shape of the trajectory will be based on the wanted positions, velocities and accelerations/decelerations experienced by the system when the trajectory is executed.

4.1 Introduction

In order to evaluate the performance of the controllers applied in this thesis, the trajectories must be planned in such a way, that the robot manipulator is properly loaded regarding power consumption, thereby meaning regarding necessary flow and load pressure for the individual actuators. It has, by the project group, been decided to apply two trajectories from which the performance of the controllers will be evaluated. Here two scenarios are used - a scenario concerning robot control, where the tool center point (henceforward designated *TCP*) of the robot manipulator is to track a specified trajectory, and a scenario concerning servo control where the actuators are to follow a specified trajectory regardless of the resulting TCP trajectory - the chosen scenarios are for the robot control scenario a rectangular trajectory, and for the servo control scenario a trajectory where actuators are to retract and extend within a specified period of time. Henceforward these trajectories are designated RECT for the rectangular trajectory, and IOT for the in/out trajectory. In this chapter, the boundaries for these trajectories are defined, and within these the position, velocity and acceleration profiles are established (note that TCP-coordinates are denoted x_D, y_D).

4.2 General Trajectory Boundaries

Previous to establishing the trajectories, the boundaries for these must be considered. This involves the physical position boundaries for the system, and the maximum allowable power consumption used by the system to complete the trajectories. The position boundaries defined by the kinematic constraints defines the working area for the TCP, which is shown in figure 4.1.

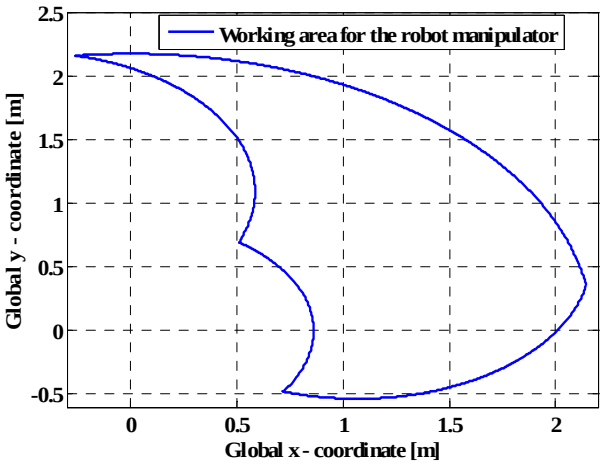

Figure 4.1: Working area for the TCP of the robot manipulator.

In the following subsections, the mentioned boundaries are described.

4.2.1 Physical Position Boundaries

The actuators have a build-in mechanical damping that damps the movement of the cylinder piston at the endpoints of the piston position ranges, and it is desirable to avoid these endpoints when designing the trajectory, as the sudden increased damping at the endpoints of the cylinder ranges will act as undesired disturbances - hence the project group has redefined the working area limits for the actuators to be (note the complete stroke length is 0.350 $[m]$):

$$0.032\ [m] < x_i < 0.318\ [m] \tag{4.1}$$

This damping effect has positive influence regarding damaging if the actuators are encountering actuator saturation. However, as the robot manipulator in this thesis is operating at a relative high pressure $P_S = 167\ [bar]$, this damping effect will possibly not be sufficient to avoid damage - hence an outer control loop is designed to oppose this, ramping down the control input to the servo valves, near the endpoints of the cylinder ranges. The boundary at which the control input is ramped down is chosen as the points at which the mechanical damping is initiated. The outer control loop consists of a first order polynomial that is multiplied to the control input, along with the necessary conditions. This

outer loop is the given as:

$$\frac{35}{16}u_{Pi}u_{vi} \quad , \quad 0\ [m] \leq x_{Pi} \leq 0.032\ [m] \tag{4.2}$$

$$u_{vi} \quad , \quad 0.032\ [m] < x_{Pi} < 0.318\ [m] \tag{4.3}$$

$$\left(-\frac{35}{16}u_{Pi} + \frac{175}{16}\right)u_{vi} \quad , \quad 0.318\ [m] \leq x_{Pi} \leq 0.350\ [m] \tag{4.4}$$

Where:

x_{Pi}:	piston position	$[m]$
u_{Pi}:	voltage signal corresponding to the piston position	$[V]$
u_{vi}:	control input	$[V]$

The function above is illustrated below in figure 4.2.

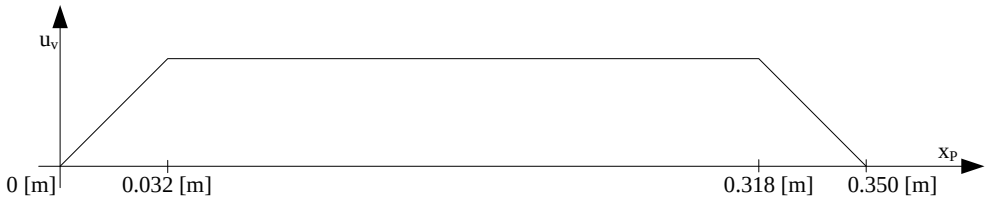

Figure 4.2: Sketch of how the outer loop functions.

4.2.2 Allowable Power Consumption

The trajectories must be planed in such a way, that the boundaries for maximum available power are not exceeded. These boundaries are defined by the pressure-flow (PQ) characteristics for the individual actuators. The PQ-characteristic for servo HSS I (equivalent for servo HSS II) is shown in figure 4.3 (A).

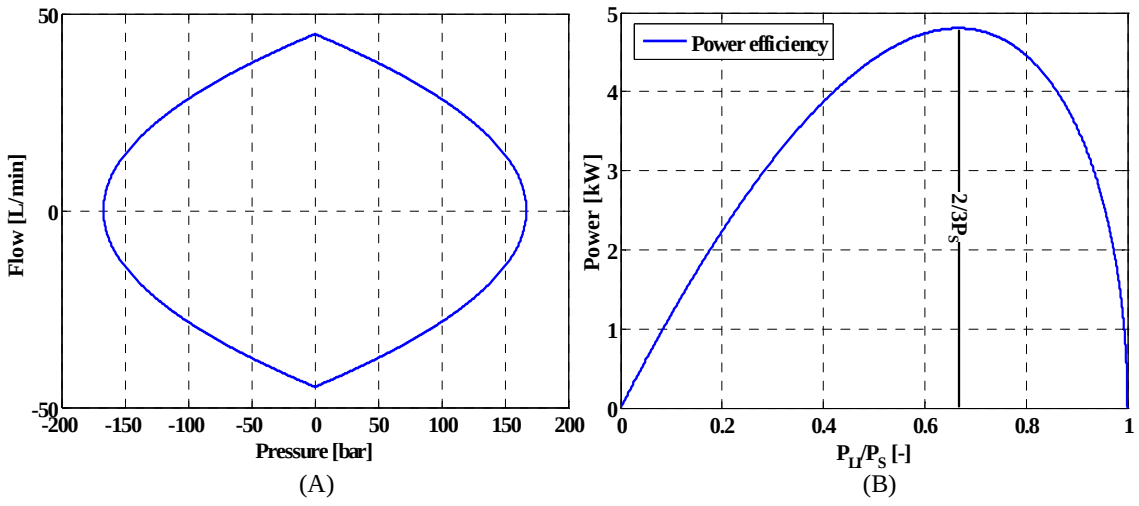

Figure 4.3: (A) PQ-characteristic for HSS I. (B) Power efficiency for HSS I. Both figures are plotted for a load pressure of $P_S = 167\ [bar]$.

It is necessary to plan the trajectories such that the systems are able to correct the tracking error, meaning that it must ensured that the power needed to control the robot manipulator is present. As shown in figure 4.3 (B) the power efficiency is dramatically decreasing when exceeding a load pressure of 2/3 of the supply pressure, and hence the power boundaries for the allowable power consumption for the robot manipulator to complete the trajectories are defined at 2/3 of the supply pressure, in order to have enough power for control.

4.3 Trajectory Generation

In this section the trajectory generation is described. The notation x can be equivalent with any position in the system such as TCP coordinate, piston position etc. In this thesis the trajectories will be described by linear functions with parabolic blends as described by [Craig s 210-212]. The following equations are derived from figure 4.4. For linear

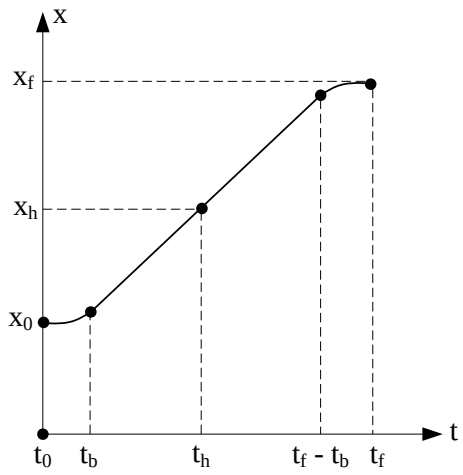

Figure 4.4: Linear segment with parabolic blends

functions with parabolic blends, and blends having the same duration in time there is symmetry at the halfway point in time and position (t_h, x_h). In order to have a smooth curve the velocity at the end of the blend region must be the same as at the beginning of the linear segment, which yields equation 4.5:

$$\ddot{x} \cdot t_b = \frac{x_h - x_b}{t_h - t_b} \tag{4.5}$$

Where:

$\ddot{x}$:	acceleration	$[m/s^2]$
x_h:	halfway position	$[m]$
x_b:	blend end position	$[m]$
t_b:	blend time	$[s]$
t_h:	halfway time	$[s]$

The position of x_b is given by equation 4.6, where x_0 is the initial position:

$$x_b = x_0 + \frac{1}{2} \cdot \ddot{x} \cdot t_b^2 \tag{4.6}$$

Combining expressions 4.5 and 4.6, and isolating t_b, noting that $t = 2 \cdot t_h$, yields (according to [Craig, 2005]):

$$t_b = \frac{t_f}{2} - \frac{\sqrt{\ddot{x}^2 \cdot t^2 - 4 \cdot \ddot{x} \cdot (x_f - x_0)}}{2 \cdot \ddot{x}} \tag{4.7}$$

Where the chosen acceleration is constrained by equation 4.8:

$$\ddot{x} \geq \frac{4 \cdot (x_f - x_0)}{t^2} \tag{4.8}$$

Where:

t:	duration of motion	$[s]$
x_f:	end position of the motion	$[m]$
x_0:	start position of the motion	$[m]$

In the following the above described theory as applied to obtain the trajectories RECT and IOT.

4.4 Trajectory Profiles (RECT)

By use of the equations derived in the previous section, the position-, velocity and acceleration profiles for the TCP-trajectory are defined as functions of time. The trajectories are established by reaching a compromise between physical boundaries, the flow- and pressure boundaries and expression 4.8, to achieve trajectories where the robot manipulator is properly loaded. The obtained trajectories are presented in the following.

4.4.1 Trajectory Profiles for the TCP

The position-, velocity- and acceleration profiles for the x_D-axis of the TCP is shown in appendix D.

The resulting trajectory profiles are shown in figures 4.5 and 4.6.

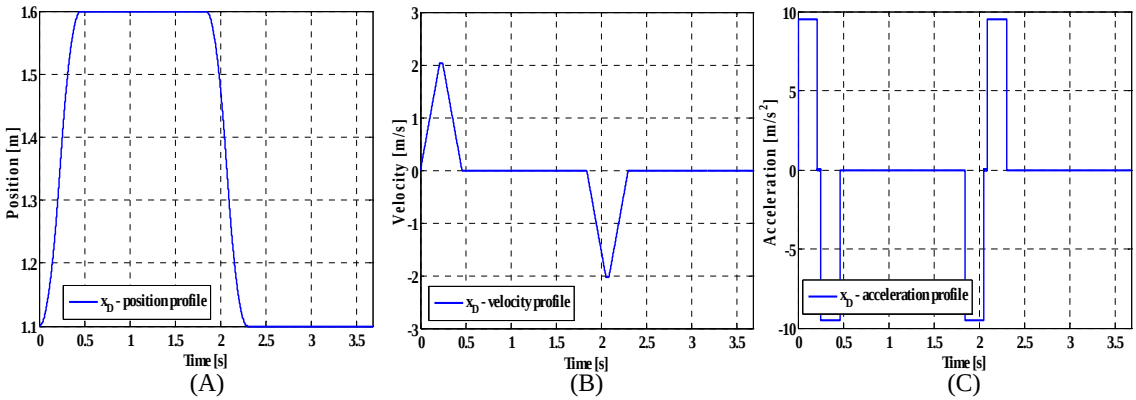

Figure 4.5: TCP trajectory profiles for x_D.

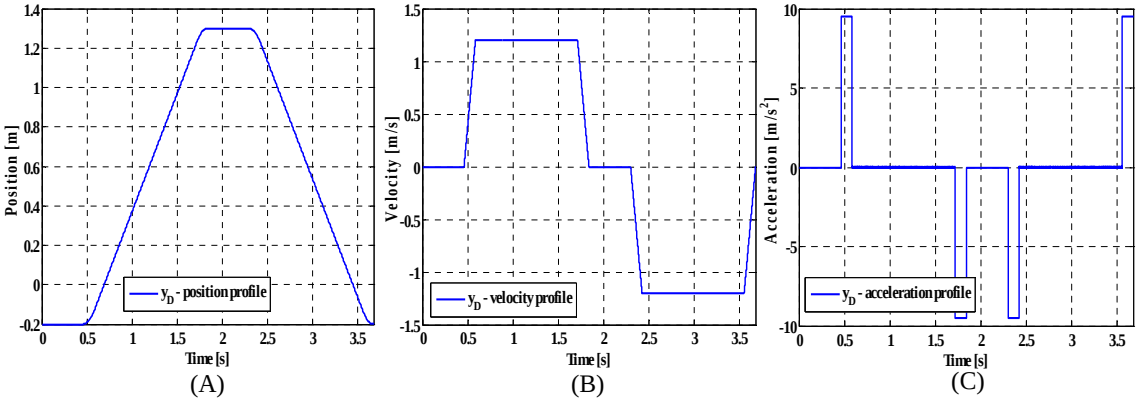

Figure 4.6: TCP trajectory profiles for y_D.

From the above trajectory profiles for the TCP, the trajectory profiles in joint and actuator space are obtained by use of the inverse kinematic constraints. This is carried out in the following.

4.4.2 Inverse Kinematics

As the trajectory of the TCP has now been established, the corresponding trajectories in joint- and cylinder space need to be determined, and for this the inverse kinematic constraints between the TCP and the individual joints, and between the joints and the actuators, are used. This is carried out regarding position, velocity and acceleration.

Inverse Kinematics - Joint Space

Based on figure 4.7 the inverse position kinematics are derived.

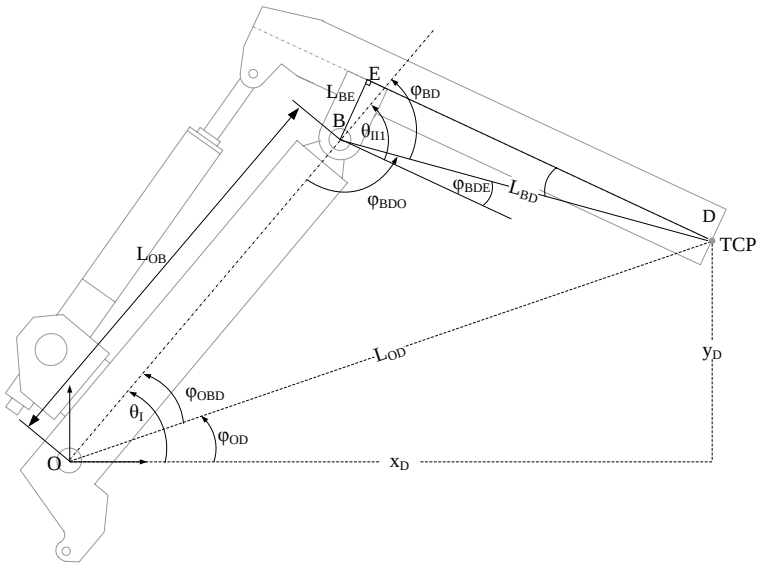

Figure 4.7: Sketch used to to derive the inverse position kinematic.

It is seen from figure 4.7, that:

$$L_{OD} = \sqrt{x_D^2 + y_D^2} \quad \text{and} \quad \varphi_{OD} = arctan\left(\frac{y_D}{x_D}\right) \tag{4.9}$$

Hence the angle θ_I is found as:

$$\theta_I = \varphi_{OBD} + \varphi_{OD} = arccos\left(\frac{L_{OB}^2 + x_D^2 + y_D^2 - L_{BD}^2}{2L_{OB}\sqrt{x_D^2 + y_D^2}}\right) + arctan\left(\frac{y_D}{x_D}\right) \tag{4.10}$$

Regarding angle θ_{II1}, this is found as:

$$\theta_{II1} = \pi + \varphi_{BDE} - \varphi_{BDO} = \pi + \varphi_{BDE} - arccos\left(\frac{L_{OB}^2 + L_{BD}^2 - x_D^2 - y_D^2}{2L_{OB}L_{BD}}\right) \tag{4.11}$$

The inverse velocity kinematics is derived by use of the jacobian. The forward kinematics for the TCP related to the joints are:

$$\underline{r}_D = \begin{bmatrix} x_D \\ y_D \end{bmatrix} = \begin{bmatrix} cos(\theta_I)L_{OB} + cos(\theta_I + \theta_{II1})L_{BD} - sin(\theta_I + \theta_{II1})L_{BE} \\ sin(\theta_I)L_{OB} + sin(\theta_I + \theta_{II1})L_{BD} + cos(\theta_I + \theta_{II1})L_{BE} \end{bmatrix} \tag{4.12}$$

Then the time derivative of the forward kinematic constraints, defines the the forward kinematic velocity constraints:

$$\dot{\underline{r}}_D = \begin{bmatrix} \dot{x}_D \\ \dot{y}_D \end{bmatrix} = \begin{bmatrix} \frac{\partial x_D}{\partial \theta_I} & \frac{\partial x_D}{\partial \theta_{II1}} \\ \frac{\partial y_D}{\partial \theta_I} & \frac{\partial y_D}{\partial \theta_{II1}} \end{bmatrix} \begin{bmatrix} \dot{\theta}_I \\ \dot{\theta}_{II1} \end{bmatrix} \tag{4.13}$$

Hence the velocity of the joint angles are:

$$\begin{bmatrix} \dot{\theta}_I \\ \dot{\theta}_{II1} \end{bmatrix} = \begin{bmatrix} \frac{\partial x_D}{\partial \theta_I} & \frac{\partial x_D}{\partial \theta_{II1}} \\ \frac{\partial y_D}{\partial \theta_I} & \frac{\partial y_D}{\partial \theta_{II1}} \end{bmatrix}^{-1} \begin{bmatrix} \dot{x}_D \\ \dot{y}_D \end{bmatrix} \tag{4.14}$$

The inverse acceleration kinematics is determined as the time derivative of the inverse velocity kinematics, which yields:

$$\begin{bmatrix} \ddot{\theta}_I \\ \ddot{\theta}_{II1} \end{bmatrix} = \begin{bmatrix} \frac{d}{dt}\left(\frac{\partial x_D}{\partial \theta_I}\right) & \frac{d}{dt}\left(\frac{\partial x_D}{\partial \theta_{II1}}\right) \\ \frac{d}{dt}\left(\frac{\partial y_D}{\partial \theta_I}\right) & \frac{d}{dt}\left(\frac{\partial y_D}{\partial \theta_{II1}}\right) \end{bmatrix}^{-1} \begin{bmatrix} \ddot{x}_D \\ \ddot{y}_D \end{bmatrix} \tag{4.15}$$

Inverse Kinematics - Actuator Space

The kinematic constraints relating the joint angles, angular velocities and angular accelerations to the linear positions, velocities and accelerations in actuator space can be found in appendix A.1.1 (note that $\dot{\theta}_{II1} = \dot{\theta}_{II}$ and $\ddot{\theta}_{II1} = \ddot{\theta}_{II}$). Combining these constraints, the inverse kinematic relations between the TCP and the actuators are established.

4.4.3 Trajectory Profiles in Joint- & Actuator Space

In figure 4.8, the trajectory profiles in joint space are presented, and the trajectory profiles in actuator space are shown in figure 4.9.

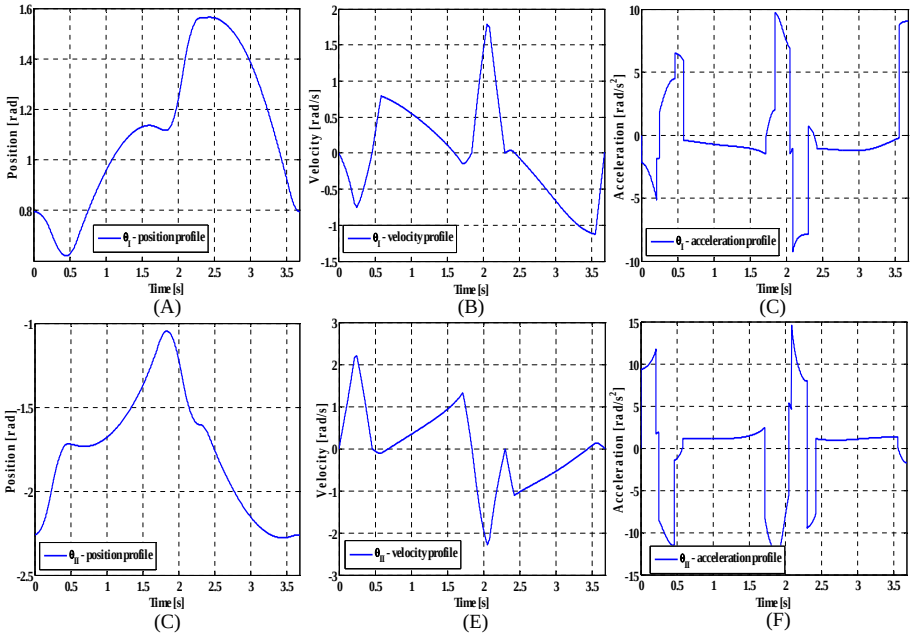

Figure 4.8: Joint space trajectory profiles. Sub-figures (A), (B), (C) are profiles for θ_I. Sub-figures (D), (E), (F) are profiles for θ_{II}.

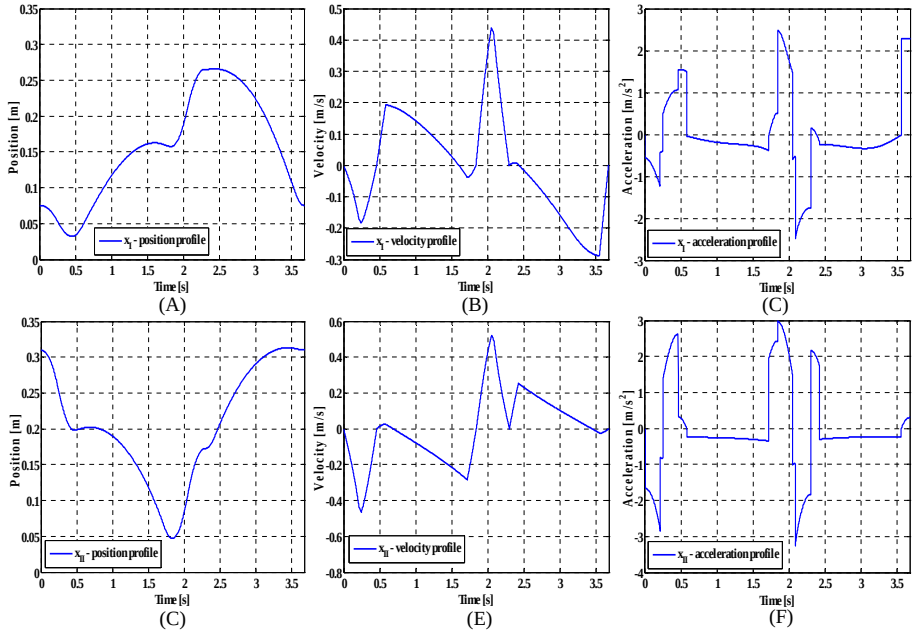

Figure 4.9: Actuator space trajectory profiles. Sub-figures (A), (B), (C) are profiles for x_I. Sub-figures (D), (E), (F) are profiles for x_{II}.

4.5 Trajectory Profiles (IOT)

In a similar way as for the RECT, the position-, velocity and acceleration profiles are established for the IOT - however here the trajectories for the actuator axes are equal to each other, hence $\ddot{x}_I = \ddot{x}_{II} = \ddot{x}_i$. The position-, velocity- and acceleration profiles for the actuator axes are shown in table 4.1.

$Time\ [s]$	$x_i\ [m]$	$\dot{x}_i\ [m/s]$	$\ddot{x}_i\ [m/s^2]$
$0 < t < t_{b11}$	$q_{0xi} + 0.5\ddot{x}_i t^2$	$\ddot{x}_i t$	$\ddot{x}_i$
$t_{b11} < t < (t_{f11} - t_{b11})$	$\ddot{x}_i t_{b11} t - 0.5\ddot{x}_i t_{b11}^2 + q_{0xi}$	$\ddot{x}_i t_{b11}$	0
$(t_{f11} - t_{b11}) < t < t_{f11}$	$-0.5\ddot{x}_i(t - (t_{f11} - t_{b11}))^2 + \ddot{x}_i t_{b11} t - 0.5\ddot{x}_i t_{b11}^2 + q_{0xi}$	$-\ddot{x}_i(t - t_{f11})$	$-\ddot{x}_i$
$t_{f11} < t < t_{f11} + t_{b22}$	$q_{1xi} - 0.5\ddot{x}_i(t - t_{f11})^2$	$-\ddot{x}_i(t - t_{f11})$	$-\ddot{x}_i$
$t_{f11} + t_{b22} < t < t_{f22} - t_{b22}$	$-\ddot{x}_i t_{b22}(t - t_{f11}) + 0.5\ddot{x}_i t_{b22}^2 + q_{1xi}$	$-\ddot{x}_i t_{b22}$	0
$t_{f22} - t_{b22} < t < t_{f22}$	$0.5\ddot{x}_i(t - (t_{f22} - t_{b22}))^2 - \ddot{x}_i t_{b22}(t - t_{f11}) + 0.5\ddot{x}_i t_{b22}^2 + q_{1xi}$	$\ddot{x}_i(t - t_{f22})$	$\ddot{x}_i$

Table 4.1: Position-, velocity- and acceleration profiles for the actuator axes.

4.5.1 Trajectory Profiles in Actuator Space

In figure 4.10, the IOT profiles in joint space are presented.

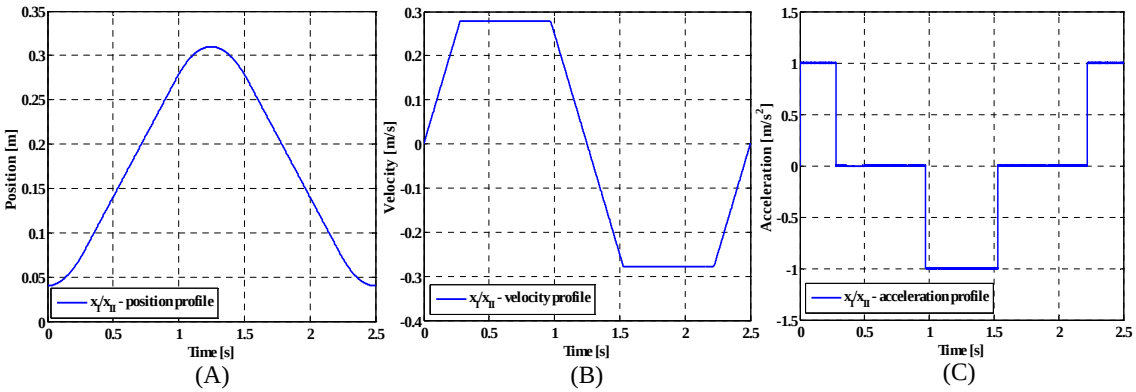

Figure 4.10: Actuator space trajectory profiles. (A) Position profile. (B) Velocity profile. (C) Acceleration profile.

It should be noted that in the acceleration profile for the IOT trajectory, that the jerk is not bounded. As the jerk is not bounded, the demand for the system to track the reference smoothly, is that the acceleration can de- or increase momentarily, which requires that the pressure build-up changes momentarily. This is not possible in reality, and hence it can not be expected that the system will be able to track the trajectories smoothly.

4.6 Necessary Pressure & Flow

In the following the power consumption used to complete the defined trajectories are presented. This is presented as the flow and pressure necessary, for the solid mechanical part of the robot manipulator to complete the trajectories.

4.6.1 Pressure & Flow for the RECT

From figure 4.11 (A) it is seen that actuator I is fairly well loaded when it has to complete the RECT, as it in some situations regarding necessary pressure, reaches the defined boundary of $P_L = 2/3P_S$. As the actuator does not need to use the available maximum flow, it is found that it will be possible, with a suitable control system, to complete the RECT. From figure 4.11 (B), it is found that actuator II is not very well loaded which is due to the relatively low inertia load, and the relatively low flow requirement, when completing the RECT.

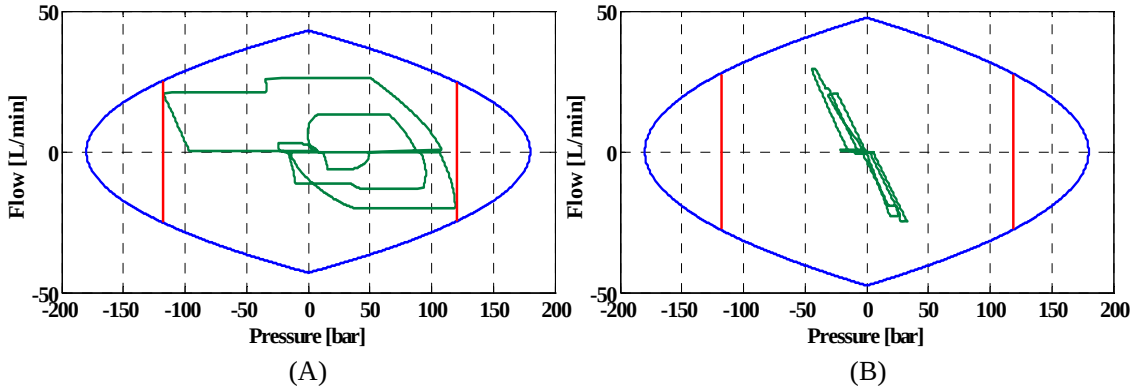

Figure 4.11: Necessary flow and pressure to complete the rectangular trajectory. (A) Actuator I. (B) Actuator II. (The red lines expresses the $2/3$ P_S boundary).

The resulting rectangular trajectory appears as shown in figure 4.12.

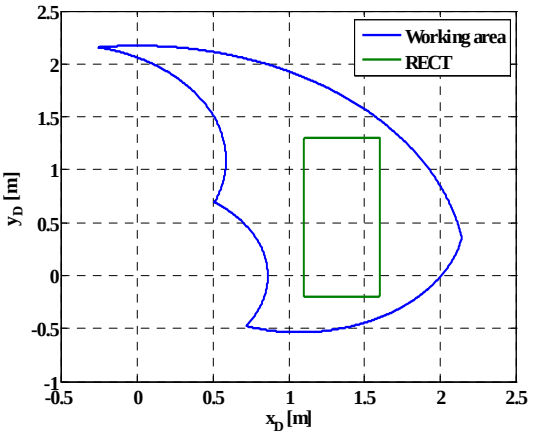

Figure 4.12: Rectangular trajectory for the TCP (RECT).

4.6.2 Pressure & Flow for the IOT

From figures 4.13 (A) and (B), it is clear that neither HSS I or HSS II is very well loaded, when completing the IOT. However, it is found that this trajectory is still suitable to evaluate the servo performance of the individual actuators. If the IOT were completed with a faster time rate, the flow necessity would be increased.

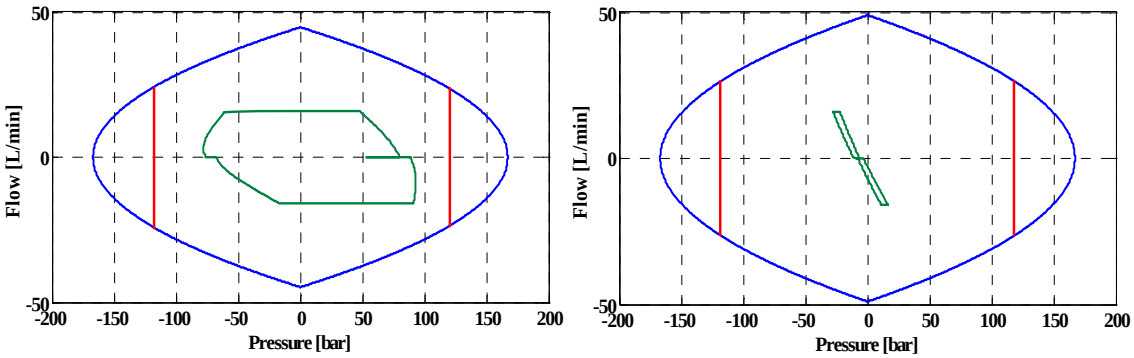

Figure 4.13: Necessary flow and pressure to complete the in/out trajectory. (A) Actuator I. (B) Actuator II. (The red lines expresses the $2/3\ P_S$ boundary).

4.7 Summary

In this chapter the trajectories used to evaluate the controller performance have been established. The limits for the trajectories have been defined as the physical position boundaries, along with the flow- and pressure boundaries. Furthermore the position boundaries have been redefined to avoid the mechanical damping at the endpoints of the actuators.

In order to establish the trajectories two scenarios have been set up - a robot control scenario, and a servo control scenario. In the robot control scenario, the TCP is to follow a specified trajectory, in this case a rectangular trajectory, which requires fairly large variations in the actuator space trajectories. In the servo control scenario, the actuators are to track the same trajectory, which in this case is a retraction and extension of the actuators, over a specified period of time of 2.50 $[s]$. In the RECT, the TCP has to complete the rectangular trajectory within a time period of 3.68 $[s]$.

Part II

Linear Control Schemes

Chapter 5

Classic Linear Control

Contents

In this chapter classic linear controllers/compensators are developed and implemented on the nonlinear model. The control types chosen to be tested in this chapter are a proportional controller, a proportional + integral controller, a Lead compensator, a Lag compensator and a Lag-Lead compensator.

5.1 Introduction

As mentioned in the meta text, this chapter concerns the development of classical linear controllers/compensators using position feedback. The controller development will be performed by use of linear control theory applied on the SISO transfer functions established in chapter 3. The nomenclature of this chapter, not previously defined, is given below.

K_{Pi}:	proportional gain	$[-]$
K_{PIi}:	proportional gain	$[-]$
K_{ci}:	proportional gain	$[-]$
T_{PIi}:	time constant	$[s]$
T_{leadi}:	time constant	$[s]$
T_{lagi}:	time constant	$[s]$
α_i:	scaling factor	$[-]$
β_i:	scaling factor	$[-]$
γ_{leadi}:	scaling factor	$[-]$
γ_{lagi}:	scaling factor	$[-]$

5.1.1 Design Specifications

In order to facilitate the design and comparison of the chosen linear controllers, design specifications are setup in the following. First and foremost the system must remain stable

for all chosen controllers, and accompanying parameters, which is done by ensuring that the phase and gain margins (henceforward designated PM and GM, respectively), as a minimum, are always positive. However to ensure a certain clearance, it is desirable to have $GM > 6 - 8$ $[dB]$ and $PM > 45° - 60°$[Rasmussen, 1996]. Furthermore it is, since the actuators are to follow the specified trajectories, desired to have an error as small as possible.

5.1.2 Design Approach

The control design process will be performed by use of the frequency responses for the individual servo systems, which are considered as position servos. In the design phases, when the different controller types have been found to satisfy the design specifications, the compensated system responses are evaluated when subjected to step-, ramp-, and sinusoidal (parabolic-like) inputs, respectively, in order to evaluate their performance on position, velocity and acceleration inputs primarily regarding oscillatory behavior. The ramp and sinus inputs are chosen because the reference position profiles for the cylinder pistons (in both the RECT and IOT) are primarily made up by ramp- and parabolic like segments. The controllers are discretely implemented on the laboratory setup, and this might cause accelerations and decelerations of such magnitude that it, in some cases, could resemble a step input. Therefore in order to ensure the desired system stability in such situations, a step is also included to test the system with the chosen controllers. Since the trajectories in actuator space as mentioned are composed of linear and parabolic segments, the ramp and sinusoidal inputs will be of main interest, when tuning the controllers, and a response to a step input only secondary.

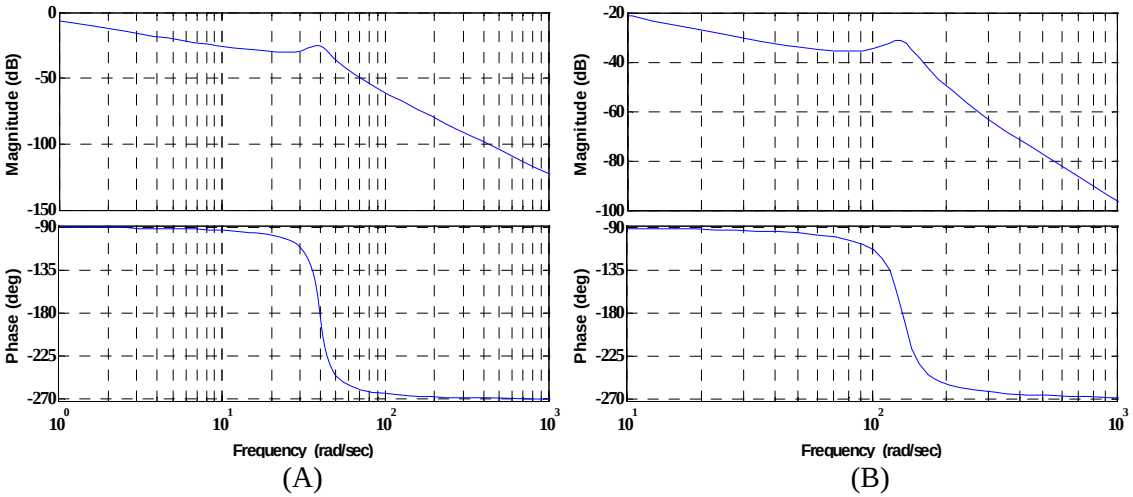

Figure 5.1: Frequency response for the plants. (A) HSS I. (B) HSS II.

The chosen controllers will be tuned within the boundaries of the stability requirements previously mentioned for the open loop frequency response, and by ensuring that the resonance peak does not rise above unity gain to ensure stability. Furthermore, the performance of the compensated systems are evaluated by observing how well the system

tracks the step, ramp and sinusoidal inputs, and possibly subsequently adjusted.

The controllers established in this chapter are especially suited for regulator problems with constant references, but has poor performance regarding position servo problems with trajectory tracking (varying references). Efforts to compensate for this are taken in the following chapter. The frequency responses for the uncompensated systems are shown in figure 5.1.

The natural frequencies and damping ratios for the uncompensated systems are:

$$\omega_{nI} = 39.68\ [rad/s] \quad , \quad \omega_{nII} = 133.01\ [rad/s] \tag{5.1}$$

$$\zeta_{nI} = 0.11\ [-] \quad , \quad \zeta_{nII} = 0.12\ [-] \tag{5.2}$$

5.2 Proportional Control (P)

The first controller to be implemented is a proportional (P) controller which has the purpose of speeding up the transient response of the system. The proportional gain is tuned until a reasonable compromise between step, ramp and sinusoidal response is obtained. Due to the fact that the system is a type 1 system, there will be a steady state error for ramp and sinusoidal inputs, when utilizing a proportional controller. Applying a proportional controller to a system only affects the magnitude of the frequency response, and the phase remains unaltered. When the proportional gain is increased for HSS I and II both the gain margin and phase margin is minimized until the compensated system satisfies the design specifications. The frequency response for the compensated system are shown in appendix E.

The margins obtained for the tuning of the proportional controller for HSS I and II are:

$$GM_I = 7.50\ [dB] \quad \wedge \quad PM_I = 88.90\ [^\circ] \tag{5.3}$$

$$GM_{II} = 7.89\ [dB] \quad \wedge \quad PM_{II} = 88.60\ [^\circ] \tag{5.4}$$

5.3 Proportional Integral Control (PI)

In order to compensate for the steady state error on the ramp input, when using a proportional controller, an integral term is applied to controller. The structure for the PI controller is:

$$G_c(s) = K_{PIi}\frac{T_{PIi}s + 1}{T_{PIi}s} \tag{5.5}$$

It is seen that applying a PI controller to a HSS increases the system type by 1, so the compensated system becomes a type 2 system. It must be taken into account when applying a PI controller to a type 1 system, that the DC-phase becomes $-180\ [^o]$. Hence in order to avoid instability of the system, one must choose the position of the zero of the PI controller at a relatively low frequency assuring that no low frequent dynamics causes instability of the system.

Like for the proportional controller, the PI controller is tuned observing the phase and gain margin of the frequency response. As mentioned above the PI compensated HSS is a type 2 system with an initial phase of -180 [°] - the zero enables the possibility of adjusting the PM - hence it is possible to adjust the compensated system to meet the design specifications regarding GM and PM. The gains and the time constants of the PI controllers of the two compensated systems are tuned to meet the following margins:

$$GM_I = 7.96\ [dB] \quad \wedge \quad PM_I = 62.40\ [^\circ] \tag{5.6}$$
$$GM_{II} = 6.37\ [dB] \quad \wedge \quad PM_{II} = 67.60\ [^\circ] \tag{5.7}$$

It is noted that when applying a PI controller, integrator anti wind up also must be implemented. The anti wind up is briefly accounted for in appendix G.

5.4 Proportional Lead Compensator

The motivation for applying a lead compensator is to increase the bandwidth of the compensated system and hence increase the speed of the response. The basic structure of a lead compensator is given by:

$$G_c(s) = K_{ci}\frac{T_{leadi}s + 1}{\alpha_i T_{leadi}s + 1} \quad ; \quad \alpha_i < 1 \tag{5.8}$$

The lead compensator is implemented in the forward path of the HSS in cascade with the plant, and is essentially a PD controller. The zero and pole of the lead compensator is placed near the resonance peak in order to add phase lead here. Here the zero is placed in the low frequency region and the pole in the high frequency region. The lead compensator speeds up the response due to the added phase lead - however, due to the relatively poor damped system, little effect is obtained by using the lead compensator. Furthermore the zero and pole has been placed, and the gain designed in such a way, that the performance specifications are met regarding GM and PM, and the frequency responses of the compensators and compensated systems are found in appendix E. The achieved margins for the compensated systems are:

$$GM_I = 7.15\ [dB] \quad \wedge \quad PM_I = 91.40\ [deg] \tag{5.9}$$
$$GM_{II} = 7.90\ [dB] \quad \wedge \quad PM_{II} = 91.70\ [deg] \tag{5.10}$$

5.5 Proportional Lag Compensator

In this section a lag compensator is established. The motivation for applying a lag compensator is to decrease the steady state velocity error. The basic structure of a lag compensator is given by:

$$G_c(s) = K_{ci}\frac{T_{lagi}s + 1}{\beta_i T_{lagi}s + 1} \quad ; \quad \beta_i > 1 \tag{5.11}$$

The lag controller is applied with both the pole and zero are placed in the low frequency region, such that the phase contribution of the compensator approximately does not in-

fluence the phase near the resonance peak. By doing so, it is avoided to add additional negative phase to the already poorly damped system. Then by subsequently adjusting the compensator gain, increased gain at lower frequencies is achieved, reducing the steady state error. However, the placement of a pole in the low frequency region reduces the bandwidth and hence the speed of the transient response. On the other hand, this enables the possibility of increasing the gain further than it would be possible, if the lag compensator was not introduced.
As the lag compensator (and the lead compensator) does not introduce any additional free integrators to the compensated system, the system type remains a type 1, which yields a static velocity error - it is not possible in any way to alter the system to a type 2 system by using only a lag compensator, but the steady state velocity error will be reduced due to the possibility of increasing the gain further. The frequency responses of the compensators and compensated systems are found in appendix E.

The achieved margins for the lag compensated systems are:

$$GM_I = 7.74\ [dB] \quad \wedge \quad PM_I = 65.50\ [deg] \tag{5.12}$$
$$GM_{II} = 7.18\ [dB] \quad \wedge \quad PM_{II} = 82.70\ [deg] \tag{5.13}$$

5.6 Proportional Lag-Lead Compensator

In this section a lag-lead compensator is established. Implementing this type of compensator is motivated by the possibility for achieving the advantages of lead- and lag compensators regarding speed of the transient response and the reduction of the steady state error, respectively. Essentially, the lag-lead compensator consists of a lead and a lag compensator placed in cascade with each other and the plant, hence the structure of the lag-lead compensator is:

$$G_c(s) = K_{ci}\frac{T_{lagi}s+1}{\gamma_{lagi}T_{lagi}s+1}\frac{T_{leadi}s+1}{\gamma_{leadi}T_{leadi}s+1} \quad ; \quad \gamma_{leadi} < 1 < \gamma_{lagi} \tag{5.14}$$

The lag part of this compensator is placed in the low frequency region in a way similar to the lag compensator in order to increase the gain at lower frequencies. The lag compensator is placed near the resonance peak in order to add phase in this frequency area. As for the previous mentioned compensators, the frequency responses of the compensators and compensated systems are found in appendix E.

The margins achieved by applying lag-lead compensators to the systems are:

$$GM_I = 7.00\ [dB] \quad \wedge \quad PM_I = 66.90\ [deg] \tag{5.15}$$
$$GM_{II} = 7.04\ [dB] \quad \wedge \quad PM_{II} = 67.60\ [deg] \tag{5.16}$$

In the following the simulation results for the systems implemented with the described controllers are presented. The controller parameters designed for the above controllers are found in appendix F.

5.7 Simulation Results

The trajectory tracking for the RECT of the compensated systems configured with the different controllers are shown in figures 5.2 and 5.3 along with their errors. It is clear that these controllers provide poor position tracking performance, as these are not suitable for tracking continuous changing trajectories.

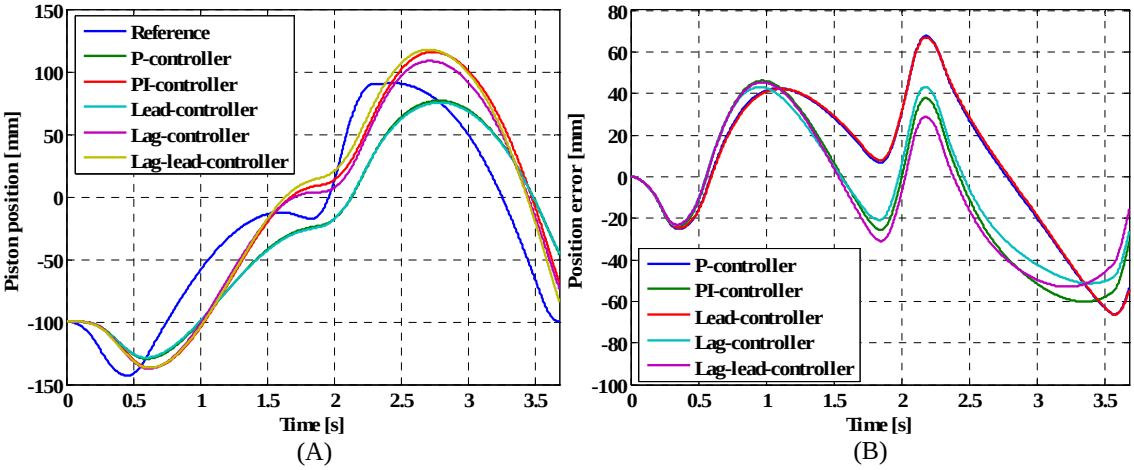

Figure 5.2: Trajectory tracking for HSS I. (A) Trajectory tracking. (B) Tracking errors

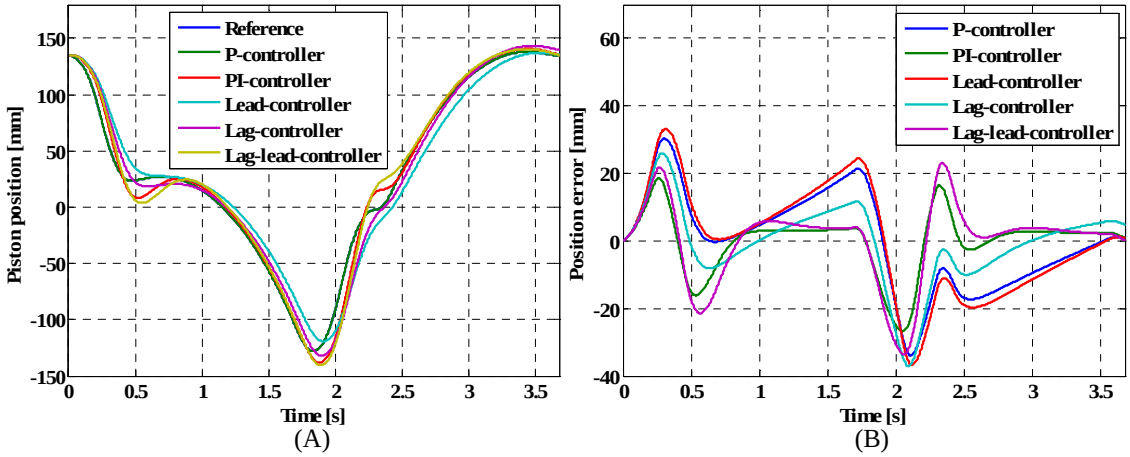

Figure 5.3: Trajectory tracking for HSS II. (A) Trajectory tracking. (B) Tracking errors

5.7.1 Tracking Errors (RECT)

In table 5.1 the tracking error, both peak and rms, are summarized.

Compensator	$\lvert e_{maxI} \rvert$ $[mm]$	e_{rmsI} $[mm]$	$\lvert e_{maxII} \rvert$ $[mm]$	e_{rmsII} $[mm]$
P	67.55	35.15	33.90	14.16
PI	60.30	34.65	26.70	8.83
Lead	70.20	35.09	36.64	16.01
Lag	50.80	30.78	28.60	11.64
Lag-Lead	70.50	32.04	29.50	11.55

Table 5.1: Tracking error values for controllers tested on the rectangular trajectory.

The simulation results for the IOT, along with their errors are found in appendix L.

5.8 Summary

In this chapter different compensators have been designed by use of frequency responses to meet the design specifications of GM and PM, and the designed compensators have subsequently been adjusted to have satisfactory responses when subjected to step-, ramp and parabolic inputs. It is found that these classic linear controllers provide poor tracking performance for the position servo, experiencing large maximum- and rms values of the tracking errors. This calls for additional controllers in order to decrease the errors, which is carried out in the following chapter. Due to the poor tracking performance, the controllers designed in this chapter are not implemented on the physical robot manipulator.

Chapter 6

Linear Control Extensions

Contents

This chapter serves as an extension to chapter 5 and the classical linear feedback control. Here velocity feedforward compensators are introduced, both with passive and active gains in the feedforward loops, and their effects are evaluated.

6.1 Introduction

The controllers designed previously are especially suited for regulator problems, and have poor performance regarding the position servo problems of this thesis, when tracking a trajectory where the reference is continuously changing with time. An effort that can be made to achieve improved performance is to implement a velocity feedforward compensation (henceforward designated VFC) in combination with the previously designed controllers. In the following the index i is omitted.

The nomenclature of this chapter, not previously defined, is shown below.

K:	system gain	$[-]$
T_n:	time constant	$[s]$
ζ:	damping ratio	$[-]$
F_D:	disturbance	$[N]$

6.2 Velocity Feedforward Compensation

The general idea of implementing this type of compensation is to feed forward the ideal servo valve gain, and from knowledge of the system and of the velocity trajectory, it is possible to establish this feed forward control signal. As the desired displacement flow is proportional to the velocity of the piston, based on information of the relationship between the spool position of the servo valve, the velocity of the piston, and piston velocity

reference trajectory it is possible to realize this compensation.

As mentioned above the VFC provides the main or ideal part of the reference tracking signal, and hence only additional transients deviating from the reference trajectory are needed to be regulated. By applying VFC, the feedforward compensated system transforms the servo problem into a regulator problem, for which the previously designed linear feedback controllers are suited. Therefore combining the VFC with a feedback controller, dramatically increases the tracking performance, as it will be shown in section 6.3. It is noted that the error will not be eliminated completely by applying VFC, as this only acts as a pre-filter and does not alter the closed loop system.

In the following a VFCP (VFC with passive valve gain) is designed and implemented in combination with the previously designed feedback controllers. Furthermore, based on knowledge of the load pressure, also an active feed forward gain (VFCA) is designed.

6.2.1 VFCP - Passive Gain

The ideal gain for the VFCP is calculated based on knowledge of the system, and it is possible to obtain the passive valve gain as the inverse gain of the transfer function describing the individual servo systems. The passive valve gain Γ_{VFCP} is hence found as [Mohieddine Jelali, 2004]:

$$\Gamma_{VFCP} = \left.\frac{T_n^2 s^2 + 2\zeta T_n s + 1}{K}\right|_{s=0} = \frac{1}{K} \tag{6.1}$$

The implementation of the VFCP on the SISO systems is shown in figure 6.1.

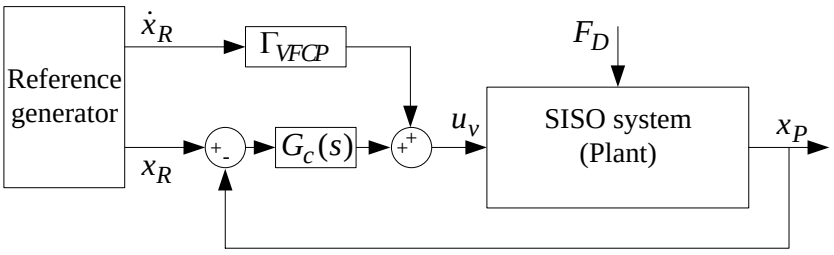

Figure 6.1: VFCP compensated system.

It is noted that the VFCP essentially results in a pre-filtering of the reference input to the system. The applied velocity reference corresponds to applying a zero to the position reference, and hence multiplying the reference signal with a differentiating first order filter, before the input is given to the closed loop system. The filtering effect is shown in figure 6.2 (equivalent to figure 6.1).

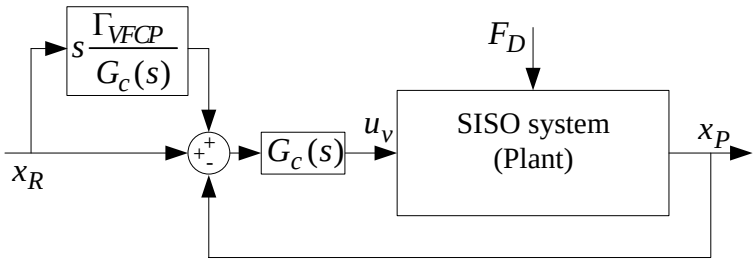

Figure 6.2: VFCP compensated system.

Closing the loop made up of the feed forward contribution, the pre-filter is obtained as:

$$\frac{s\Gamma_{VFCP}}{G_c(s)} + 1 = s\frac{\Gamma_{VFCP}}{G_c(s)} + \frac{G_c(s)}{G_c(s)} = \frac{s\Gamma_{VFCP} + G_c(s)}{G_c(s)} \tag{6.2}$$

As the VFCP acts as a pre-filter, this does not affect the stability of the closed loop system.

6.2.2 VFCA - Active Gain

In the previous section a VFC was established using the passive valve gain - however, this valve gain does only comply with the actual valve gain at the operating point of the linear model. Hence, it will be appreciable to extend the VFC to be valid for all operating points, and hence establish an active feedforward compensation (VFCA). In the following it is assumed that the pressure dynamics and the leakage flow can be neglected, and hence from the orifice equation, the load flow is given by (see appendix C):

$$q_L = A\dot{x}_P = K_v u_v \sqrt{\frac{P_S - P_T - P_L}{2}} \tag{6.3}$$

Isolating u_{vi}, yields:

$$u_v = \frac{A\sqrt{2}}{K_v\sqrt{P_S - P_T - P_L}}\dot{x}_P \tag{6.4}$$

Using the above expression, the VFCA is implemented as shown in figure 6.3, where the load pressure is fed back to continuously update the feedforward gain.

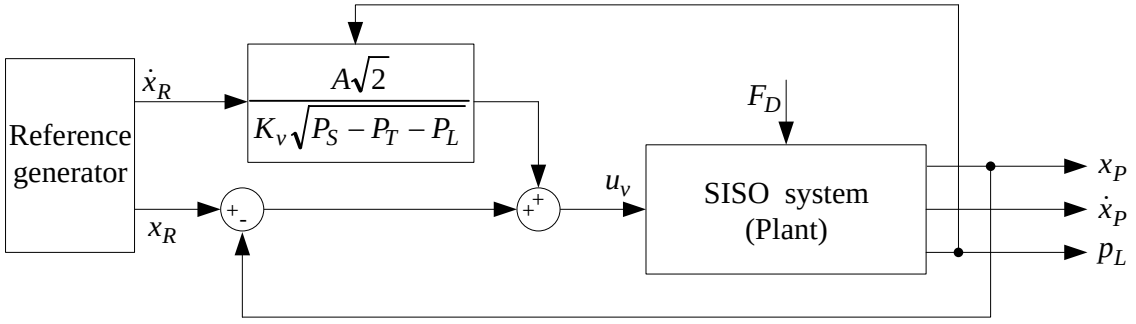

Figure 6.3: Velocity feedforward compensated HSS, using pressure feedback.

In order to evaluate the effect of the pressure feedback loop on the system, the linearized orifice equation is considered.

$$q_L = A\dot{x}_P = K_q u_v + K_{qp} p_L \tag{6.5}$$

Again by isolating u_v in the above expression, yields:

$$u_v = \frac{A}{K_q}\dot{x}_P - \frac{K_{qp}}{K_q} p_L \tag{6.6}$$

Hence the feedforward compensator in linearized form has been obtained. Implementing this feedforward compensator on the linear model results in the feedforward compensated HSS shown in figure 6.4.

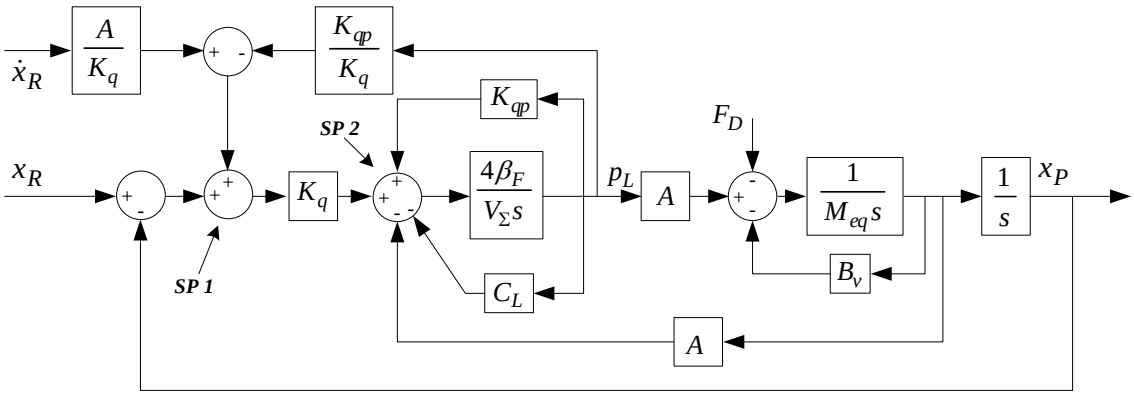

Figure 6.4: Velocity feedforward compensated system, using pressure feedback.

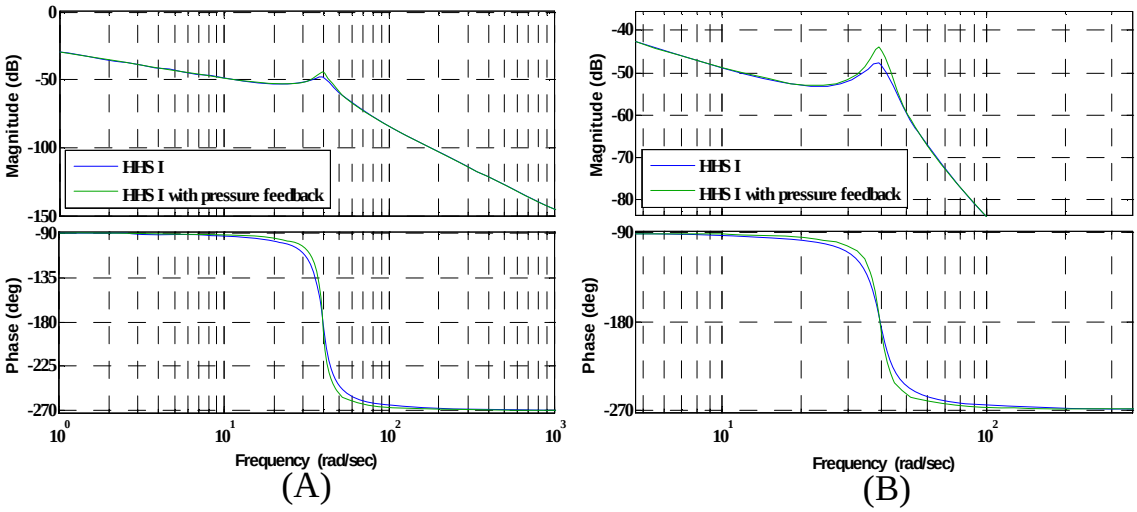

Figure 6.5: (A) Bode diagram for the non-compensated/compensated system. (B) Zoom of the bode diagram for non-compensated/compensated system. (in this case HSS I - similar effects occur on HSS II).

It is seen that the first term of the right hand side of expression 6.6, when implemented on the linear model, acts as a pre-filter to the reference input, and hence does not affect the closed loop stability of the system. However, the last term introduces an additional

loop to the system due to the pressure feedback. Moving the pressure feedback loop from summation point 1 (SP 1) to summation point 2 (SP 2), results in a loop where $K_{qp}p_L$ is fed back with negative sign - opposite to the feedback loop already in the linear model, where $K_{qp}p_L$ is fed back with positive sign, resulting in $(K_{qp} - K_{qp})p_L = 0$. From this it is found that this pressure feedback loop decreases the damping of the system. To further evaluate the effect of the pressure feedback loop, the bode diagram of HSS I is shown in figure 6.5.

It is seen from figure 6.5 that applying the pressure feedback to the velocity feedforward compensator, decreases the damping of the system, thereby allowing a smaller gain to the additional controller - however as the pressure feedback allows the feedforward gain to be more accurate in all of the working area, increased tracking performance should be achieved. To evaluate the increased tracking performance, the two HSS's are implemented with a feedback controller with unity gain and feed forward contribution, with passive and active VFC gain. See figure (6.6).

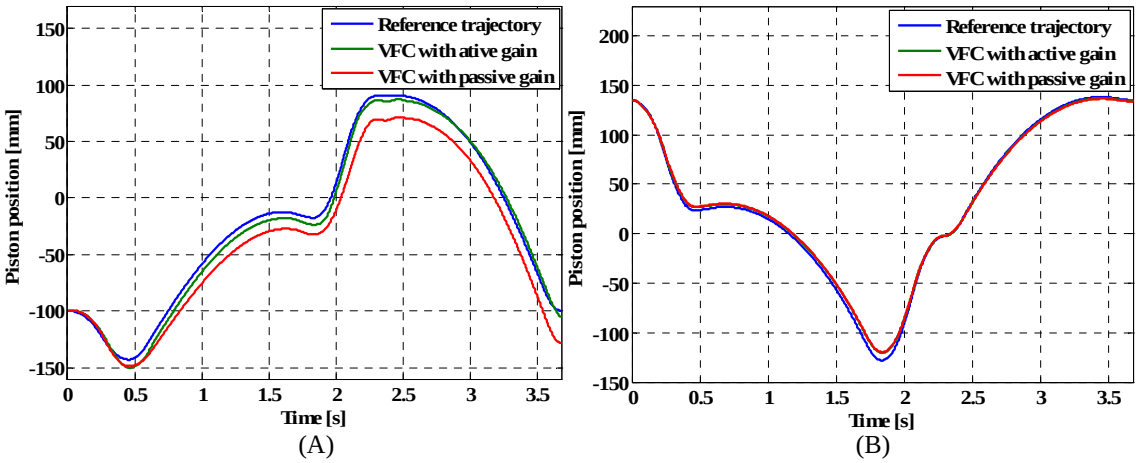

Figure 6.6: Active and passive gain VFC compensated systems. (A) HSS I. (B) HSS II.

It is seen from figure 6.6 (A) that a dramatic increase in the tracking performance is achieved by applying the VFCA on HSS I. However, as seen in figure 6.6 (B), the VFCA does not have any significant effect on the tracking performance of HSS II. The reason for this is that the inertia mass of HSS II is nearly constant, and hence the load pressure is nearly constant.

6.3 Simulation Results - VFCP

The trajectory tracking of the compensated systems configured with the different controllers are presented in the following, along with their tracking errors.

It is seen from figures 6.7 and 6.8 that adding a feed forward contribution with passive gain increases the performance dramatically, due to the fact that the feedforward provides the ideal valve gain throughout the trajectory.

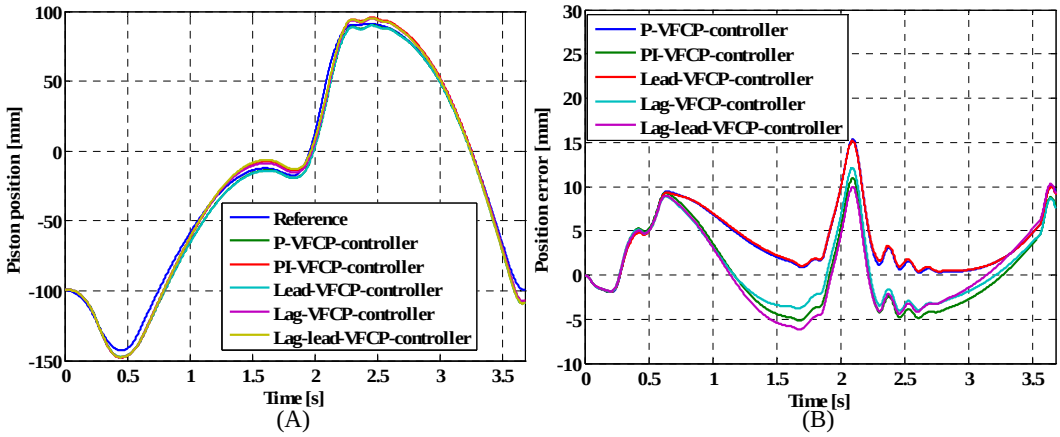

Figure 6.7: Trajectory tracking with VFCP for HSS I. (A) Trajectory tracking. (B) Tracking errors.

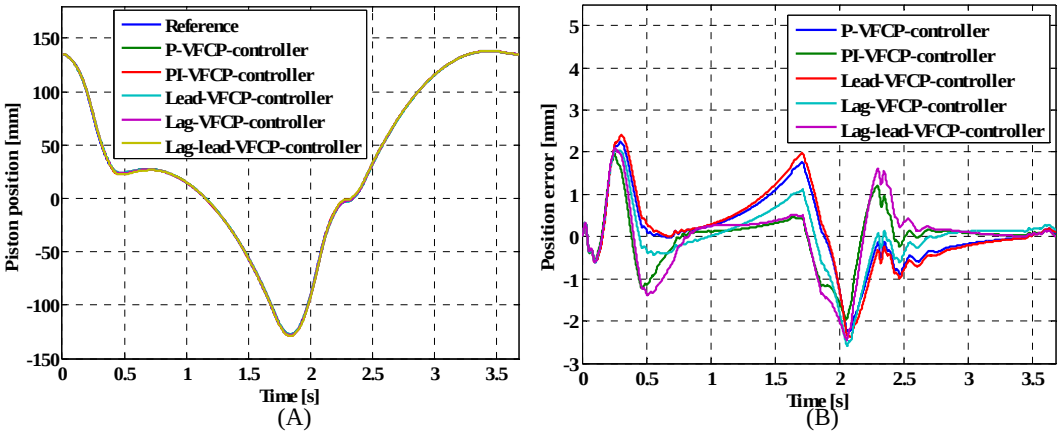

Figure 6.8: Trajectory tracking with VFCP for HSS II. (A) Trajectory tracking. (B) Tracking errors.

In the table below the tracking errors when implementing a VFCP in combination with the previously designed linear feedback controllers are shown.

Tracking Errors (RECT)

Compensator	$\lvert e_{maxI} \rvert$ $[mm]$	e_{rmsI} $[mm]$	$\lvert e_{maxII} \rvert$ $[mm]$	e_{rmsII} $[mm]$
P-VFCP	15.37	5.26	2.25	0.83
PI-VFCP	10.97	4.58	1.95	0.63
Lead-VFCP	15.22	5.27	2.39	0.92
Lag-VFCP	12.13	4.33	2.58	0.74
Lag-Lead-VFCP	10.29	4.61	2.44	0.80

Table 6.1: Tracking error values for controllers tested on the rectangular trajectory.

The simulation results for the IOT along with their errors are found in appendix L.

6.4 Simulation Results - VFCA

To evaluate the effect of the VFCA, this is implemented in combination with P and PI controllers, and tested on the RECT and IOT. From figure 6.9 it is seen that the VFCA in combination with P and PI controllers decreases the errors significantly in comparison to the control systems using VFCP. Hence it is found that the VFCA enhances the transient performance of the control system, but deteriorates the steady state performance.

Regarding HSS II, it is found from figure 6.10, that the VFCA has no significant influence on the tracking performance compared to the VCFP. As mentioned earlier, this was expected due to the nearly constant inertia load on HSS II.

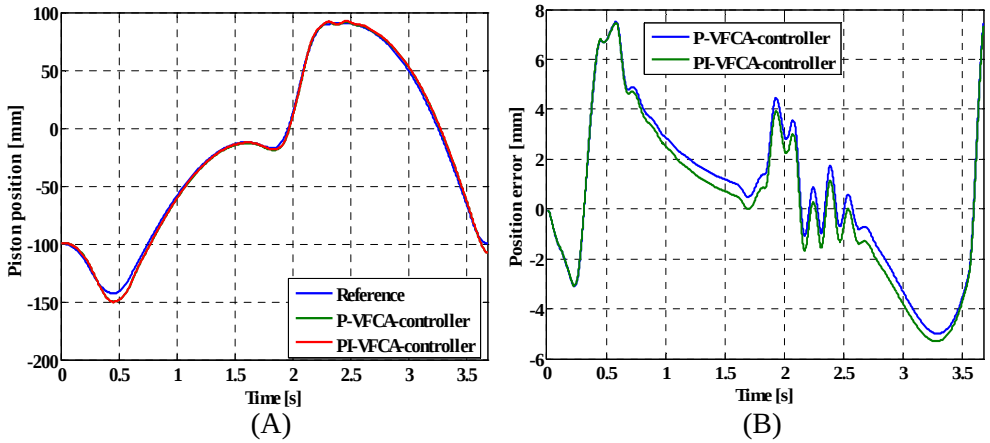

Figure 6.9: Trajectory tracking with VFCA for HSS I. (A) Trajectory tracking. (B) Tracking errors.

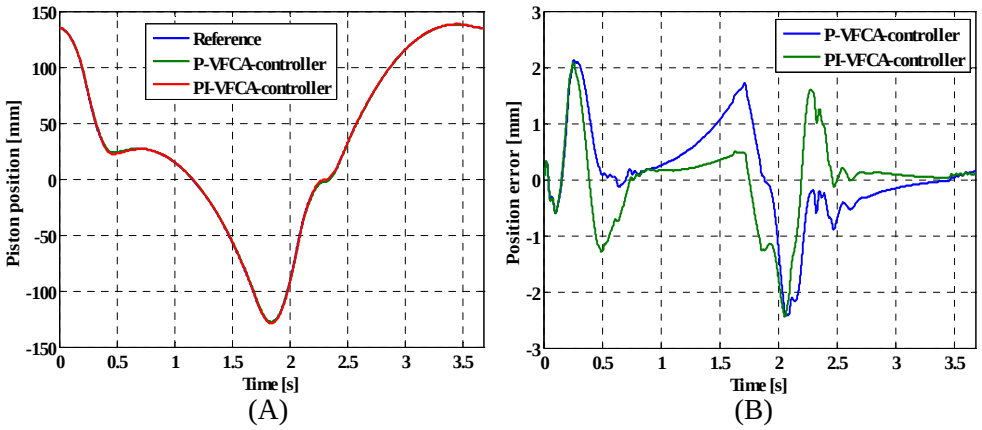

Figure 6.10: Trajectory tracking with VFCA for HSS II. (A) Trajectory tracking. (B) Tracking errors.

6.4.1 Tracking Errors (RECT)

The tracking errors are summarized in table 6.2.

The simulation results for the IOT, along with their errors are found in appendix L.

Compensator	$\lvert e_{maxI} \rvert$ $[mm]$	e_{rmsI} $[mm]$	$\lvert e_{maxII} \rvert$ $[mm]$	e_{rmsII} $[mm]$
P-VFCA	7.51	3.25	2.40	0.83
PI-VFCA	7.44	3.24	2.05	0.74

Table 6.2: Tracking error values for controllers tested on the rectangular trajectory.

6.5 Experimental Results

From the experimental results shown in figures 6.11 and 6.12 it is found that these resembles those of the simulation, however with a slight increase in the errors. This deviation in errors may be caused by inaccuracies in the nonlinear model. However, it is found the linear controllers implemented in combination with the VFCP on the physical system achieves fairly good performance.

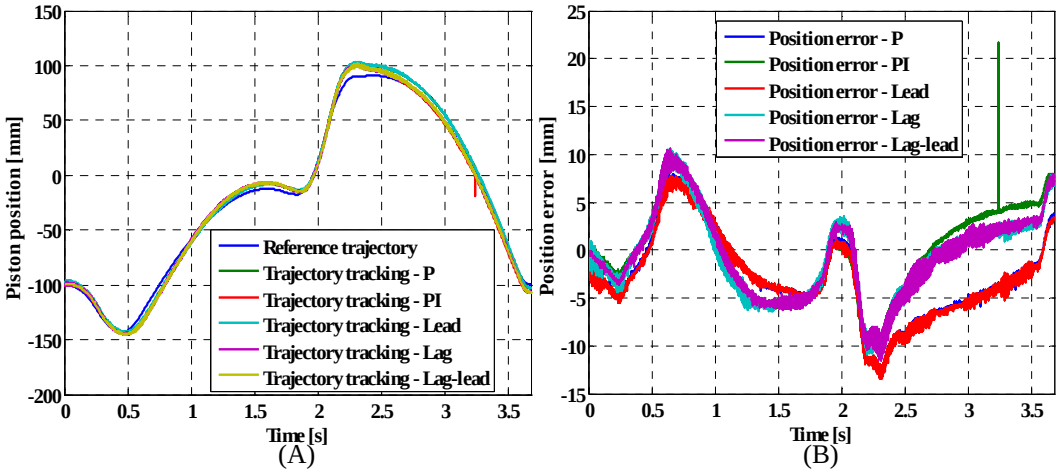

Figure 6.11: Trajectory tracking for HSS I. (A) Trajectory tracking. (B) Tracking errors.

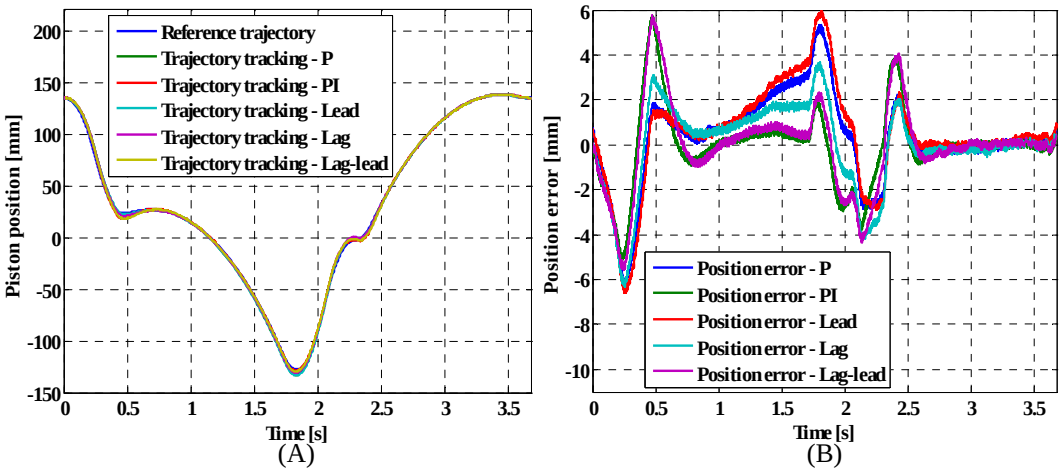

Figure 6.12: Trajectory tracking for HSS II. (A) Trajectory tracking. (B) Tracking errors.

6.5.1 Tracking Errors

Compensator	$\lvert e_{maxI} \rvert$ $[mm]$	e_{rmsI} $[mm]$	$\lvert e_{maxII} \rvert$ $[mm]$	e_{rmsII} $[mm]$
P-VFCP	12.46	5.29	6.15	2.01
PI-VFCP	10.01	4.73	5.58	1.73
Lead-VFCP	12.72	5.34	6.51	2.25
Lag-VFCP	10.04	4.55	6.13	1.87
Lag-Lead-VFCP	10.03	4.57	5.54	1.91

Table 6.3: Tracking error values for controllers tested on the rectangular trajectory.

6.6 Summary

In this chapter the performance of the linear controllers were augmented by adding extensions in the for of feed forward compensation, both passive and active. The passive feed forward gain has been found by use of the inverse dynamics of the linear system representation, and the active feed forward gain were established by use of a pressure feedback, updating the feed forward gain.

It was found that utilizing a feed forward gain, boosted controller performance regarding tracking errors. It was also found that the effect of the VFCA was most pronounced on the HSS I, since the inertia mass of HSS II is nearly constant, and the load pressure therefore also is nearly constant.

Chapter 7

Linear Control Design in State Space

Contents

In this chapter a compensator is developed based on a state space representation of the linear system. More specifically a state feedback gain compensator is developed using the pole assignment technique, in order to achieve certain system specifications. Furthermore a modification is made to this compensator regarding feedforward contribution.

7.1 Introduction

The pole assignment technique could be advantageous to use in the compensator design, for a compensator usable for trajectory tracking. The general idea of applying this method is to alter the properties of the system, by displacing the poles of the uncompensated system to desired locations of the compensated system. As the servo systems are poorly damped, and have slow transient response due to the free integrator, this method might prove usable, and will be used in this chapter. The nomenclature of this chapter is given below (not notations introduced previously).

$\underline{x}_i$:	state vector	[−]
$\underline{\dot{x}}_i$:	time derivative of state vector	[−]
$\underline{\underline{A}}_i$:	system matrix	[−]
$\underline{\underline{B}}_i$:	input matrix	[−]
$\underline{\underline{C}}_i$:	output matrix	[−]
y:	output	[−]
x_1, x_2, x_3:	states	[−]
$\underline{\underline{K}}$:	state feedback gain matrix	[−]
k_1, k_2, k_3:	elements of the state feedback gain matrix	[−]

7.2 State Space Model Representation

In the following a state space representation of the two servo systems is established, and the generalized form of this representation is given by:

$$\underline{\dot{x}_i} = \underline{\underline{A_i} x_i} + \underline{B_i} u \quad , \quad y = \underline{\underline{C_i} x_i} \tag{7.1}$$

The control design method considered in this chapter enables the possibility of considering the complete system as a MIMO HSS in the state space representation - however it has been decided by the project group to consider the system as two separate SISO systems. The describing equations are (valid for both systems):

$$q_{Li} = A_i \dot{x}_{Pi} + \frac{V_{\Sigma i}}{4\beta_{Fi}} \dot{p}_{Li} + C_{Li} p_{Li} \tag{7.2}$$

$$q_{Li} = K_{qi} u_{vi} + K_{qpi} p_{Li} \tag{7.3}$$

$$M_{eqi} \ddot{x}_{Pi} = p_{Li} A_i - B_{vi} \dot{x}_{Pi} \tag{7.4}$$

As the two SISO systems algebraically are similar to each other, the following is valid for both systems, and hence in the following the index i is omitted. The states of the system are defined as the piston position and velocity and the load pressure, which yields:

$$x_1 = x_P \quad , \quad x_2 = \dot{x}_P = \dot{x}_1 \quad , \quad x_3 = p_L \tag{7.5}$$

Combining equations 7.2 and 7.3, and isolating the state time derivatives of the describing equations, yields:

$$\dot{p}_L = \frac{4\beta_F}{V_\Sigma} (K_q u_v + (K_{qp} - C_L) p_L - A \dot{x}_P) \tag{7.6}$$

$$\ddot{x}_P = \frac{1}{M_{eq}} p_L - B_v \dot{x}_P \tag{7.7}$$

The system matrix, input matrix and the output matrix are the given as:

$$\underline{\underline{A}} = \begin{bmatrix} 0 & 1 & 0 \\ 0 & \frac{A}{M_{eq}} & -\frac{B_v}{M_{eq}} \\ 0 & -\frac{4\beta_F}{V_\Sigma} A & \frac{4\beta_F}{V_\Sigma}(K_{qp} - C_L) \end{bmatrix} \quad , \quad \underline{B} = \begin{bmatrix} 0 \\ 0 \\ \frac{4\beta_F}{V_\Sigma} K_q \end{bmatrix} \quad , \quad \underline{\underline{C}} = \begin{bmatrix} 1 & 0 & 0 \\ 0 & 1 & 0 \\ 0 & 0 & 1 \end{bmatrix}$$

7.3 State Controllability

To be able to apply the pole assignment technique, the system must be completely controllable. The HSS is completely controllable if the controllability matrix has full rank [Ogata, 2002]. It can be shown that:

$$[\underline{B} \;\; \underline{\underline{A}}\underline{B} \;\; \underline{\underline{A}}^2 \underline{B}] = 3 = \text{full rank} \tag{7.8}$$

As the controllability matrix has full rank, the system states are completely controllable, and hence the system can be subjected to control design by use of the pole assignment technique.

7.4 Compensation by Pole Assignment

In this section a compensator is developed by use of the pole assignment technique. This is motivated by the fact that this technique enables the possibility of altering the position of the poles to a specified position by use of a *state feedback gain matrix* (henceforward designated GFM). The state feedback gain matrix is defined aos[Ogata, 2002]:

$$\underline{\underline{K}} = [k_1 \ k_2 \ k_3 \ ] \tag{7.9}$$

The state feedback control scheme appears as shown in figure 7.1.

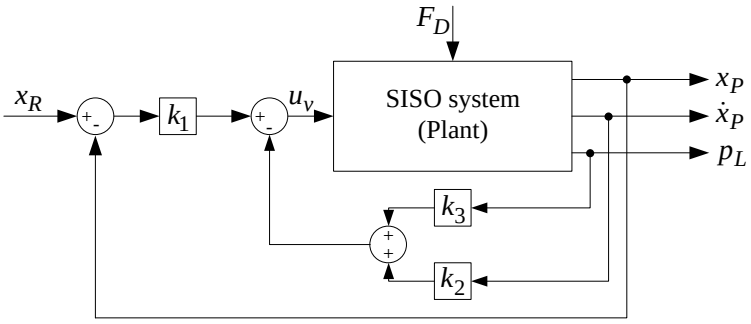

Figure 7.1: State feedback control scheme.

The compensated system dynamics are described in the following state space form:

$$\dot{\underline{x}} = (\underline{\underline{A}} - \underline{B}\underline{K})\underline{x} + \underline{B}k_1 u \tag{7.10}$$

With the reference control signal given by:

$$u = -\underline{K}\underline{x} + k_1 u = -(k_2 x_2 + k_3 x_3) + k_1(x_R - x_1) \tag{7.11}$$

Then by proper chosen $\underline{K}$, it is possible to design the control scheme such that the closed loop poles are placed in desired positions.

As the HSS's are poorly damped, and has slow transient performance, the desired closed loop poles are chosen such that the damping ratios and the speed of the HSS's are increased. Figure 7.2 shows how the damping ratio and the natural frequency is related to the poles.

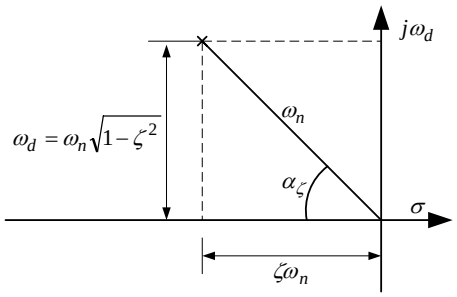

Figure 7.2: Relationship between the poles and the damping ratio and natural frequency .

The damping ratio ζ increases as α_ζ decreases - to ensure a properly damped system, the poles should be chosen such that $\alpha_\zeta \approx 45°$ ($\zeta \approx 0.7$). It is clear that this is achieved by letting both the real and complex part of the pole take the same value. Furthermore to increase the speed of the system, the pole at the origin (the free integrator), should be displaced towards left, to decrease the dominance of this, as the free integrator slows the system - by doing so corresponds to replacing the free integrator by a first order integrating system. Another initiative to increase the speed of the system, is to place the complex poles further to the left, thereby achieving a higher natural frequency. The approach for this compensator will be to displace the the real pole of the origin to the left, but at the same time maintain some level of integrating effect, by still letting this be the dominant pole of the system. The proper damping is achieved by letting $\alpha_\zeta = 45°$. Furthermore the complex poles are displaced as far to the left as possible, and at the same time assuring that no valve saturation is present, when completing the trajectories. The obtained poles of the compensated systems are (for HSS I and II, respectively):

$$s_I = -150 \pm j150 \quad \wedge \quad s_I = -25 \quad \text{and} \quad s_{II} = -350 \pm j350 \quad \wedge \quad s_{II} = -35 \tag{7.12}$$

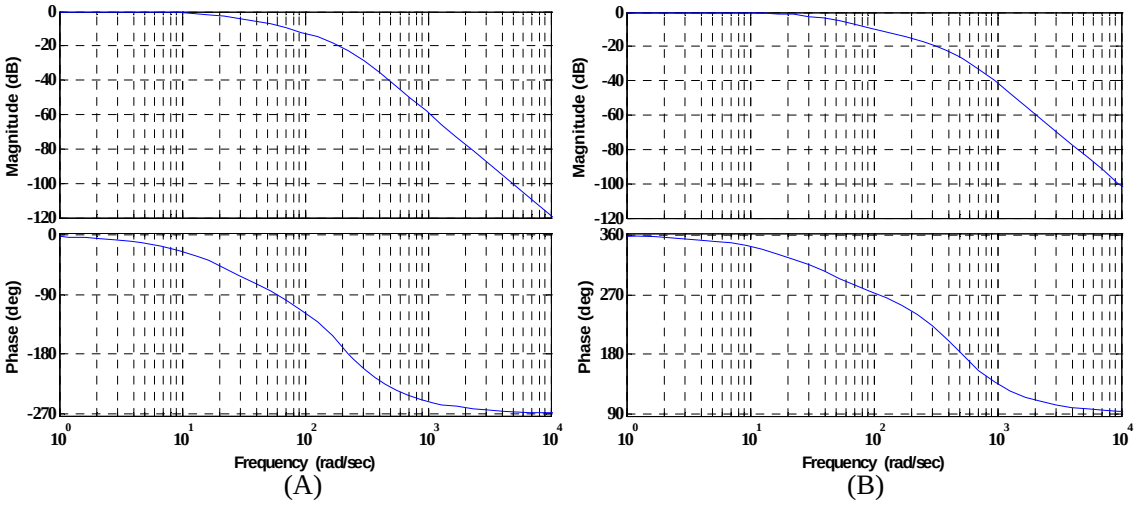

Figure 7.3: Bode diagrams for the GFM compensated systems. (A) HSS I. (B) HSS II.

From figure 7.3 it is clearly seen that the damping ratios of the systems are increased.

In order to increase the tracking performance, as for the classical linear controllers, a velocity feed forward compensation can be applied. In this case this is found in a way similar to the the VFCP. However, as the system has now been altered, one must take into account the velocity and pressure loops introduced by the GFM. Hence by closing the velocity and pressure feedback loops provided by the GFM, and disregarding the position feedback loop, the compensated system can be considered as an *open loop system*, as shown in figure 7.4.

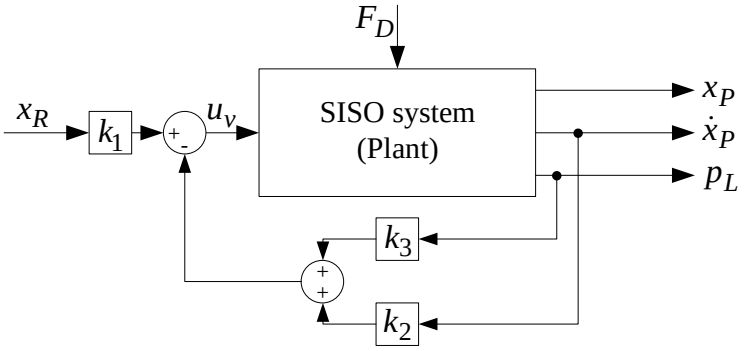

Figure 7.4: Open loop compensated system.

Now the passive feed forward gain is obtained similar to the one of expression 6.1. By letting the system gain of the *compensated open loop system* be denoted K_G, then the feed forward gain Γ_{VFCP_G} is obtained as:

$$\Gamma_{VFCP_G} = \frac{1}{K_G} \tag{7.13}$$

As mentioned earlier the feedforward compensation acts as a pre-filter and hence does not affect closed loop stability of the systems. Hence no further analysis is necessary regarding the feedforward contribution.

7.5 Simulation Results

In the following the simulation results when implemented on the nonlinear model, are presented for the GFM compensated system. The compensated systems are first subjected to the rectangular trajectory (RECT), and following this the IOT.

7.5.1 Simulation Results

In the following the simulation results for the rectangular trajectory tracking are presented. It is noted that the GFM compensated systems with feedforward compensation, is not shown for the RECT, as this experiences valve saturation in this situation.

It is seen from figures 7.5 and 7.6 that compensation by use of a state gain feedback matrix provides fairly good tracking performance for HSS II - however for HSS I relatively

large tracking error occurs. It has not been possible to implement the feed forward compensation in this situation, as the valve in this case reaches the saturation limits, when completing the RECT. It is seen that applying multiple feedback loops (as the GFM compensation does) causes the systems to track their trajectories without oscillations in the tracking error, as is experienced with the classic linear controllers.

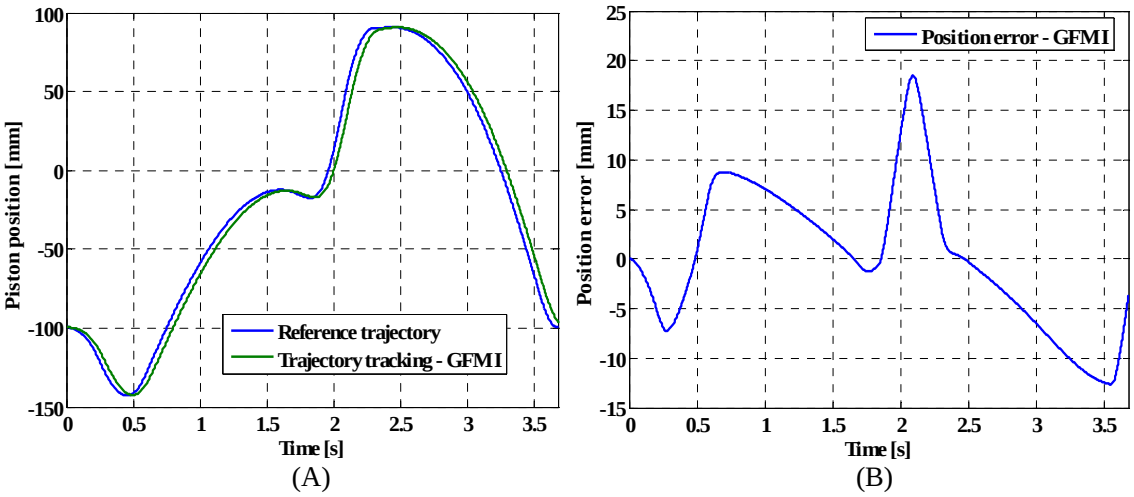

Figure 7.5: Simulation results for the GFM controller, applied on HSS I. (A) Trajectory tracking. (B) Tracking error.

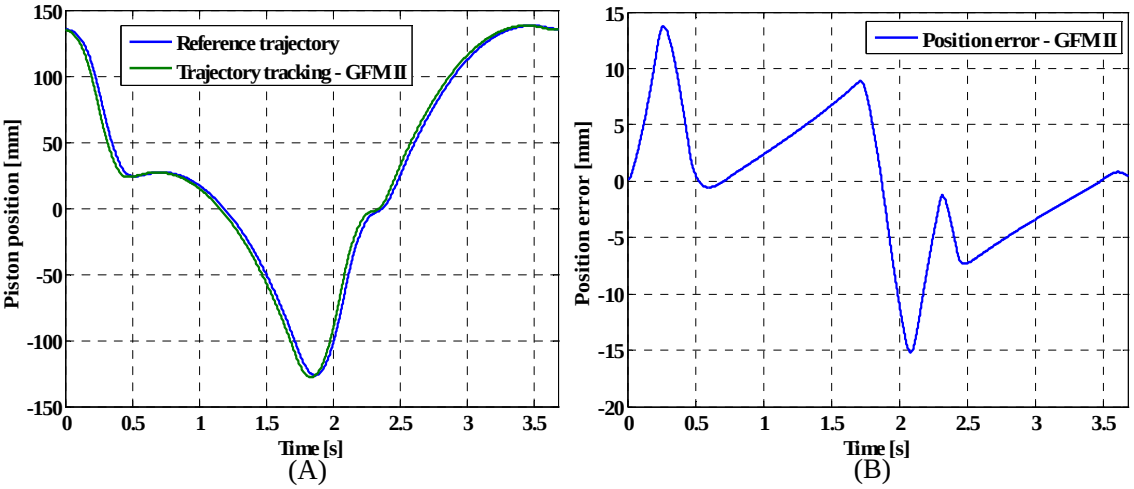

Figure 7.6: Simulation results for the GFM control scheme, applied on HSS II. (A) Trajectory tracking. (B) Tracking error.

7.5.2 Tracking Errors (RECT)

Compensator	$\lvert e_{maxI} \rvert$ $[mm]$	e_{rmsI} $[mm]$	$\lvert e_{maxII} \rvert$ $[mm]$	e_{rmsII} $[mm]$
GFM	18.54	7.22	15.18	5.90

The simulation results for the IOT, along with their errors are found in appendix L.

7.6 Summary

In this chapter state space representation is utilized for controller development. Here both a state feedback gain compensator and an augmentation of the same compensator by applying feed forward contributions is developed by use of the pole placement technique. The augmented state feedback gain compensator could unfortunately not be tested on the system using RECT, as this caused valve saturation. However, the augmented state feedback gain compensator could be tested for the system using IOT, which yielded a dramatically increased tracking performance compared to the pure GFM compensated system.

Part III

Advanced Control Schemes

Chapter 8

Simplified Actuator Model

This chapter concerns the establishment of a simplified actuator model, suitable for use in the development of the adaptive control schemes. This simplified model will be based on the existing model of the hydraulic actuators.

Before initiating the process of establishing the adaptive control laws, a simplified model used to represent the system is determined - this will be carried out considering the individual servo systems, hence the simplified model is established as a SISO system.

In general, hydraulic systems include various time variant parameters, which are difficult to describe. To be able to establish the adaptive controllers, as for the linear controllers, a mathematical model is needed. In this case, it is desirable to have a simplified lower order model, rather than having a complex relative high order model as that used in the linear control design. In order to establish this simplified lower order model, the following assumptions are made:

- The forces applied by the load pressure is strictly larger than the inertia load and the friction forces counteracting this - hence the force equilibrium is omitted in the simplified model
- The hydraulic oil is infinitely stiff - hence the pressure dynamics are omitted

Due to the less accurate simplified model based on the above mentioned assumption, the modeling error has increased compared to the linear model obtained previously - hence in the simplified model, a modeling error which is considered unknown, is introduced.

To provide further justification for using the simplified model in the control design, the previously obtained linear actuator model representation is considered:

$$G_{Pi}(s) = \frac{K_i}{(T_{ni}^2 s^2 + 2\zeta_i T_{ni} s + 1)s} = \frac{K_i}{\left(\frac{1}{\omega_{ni}^2} s^2 + 2\zeta_i \frac{1}{\omega_{ni}} s + 1\right) s} \tag{8.1}$$

It is seen that for large values of the natural frequency and damping ratio, which occurs for small values of the equivalent mass, it is reasonable to consider the dynamic model as consisting of the system gain and the pure integrator - hence, as mentioned before, when assuming that the forces applied by the load pressure is strictly larger than the inertia load, this is a valid simplification.

It is assumed that the stiffness of the hydraulic oil is infinite, thereby neglecting the pressure dynamics. When also neglecting the inertia load, the friction forces, and when also omitting the leakage flow, the describing equations for the actuators are reduced to:

$$Q_L = K_{vi} u_{vi} \sqrt{\frac{P_S - P_T - sign(u_{vi}) P_{Li}}{2}} \quad , \quad Q_L = A_i s x_{Pi} \quad \Rightarrow \tag{8.2}$$

$$A_i s x_{Pi} = K_{vi} u_{vi} \sqrt{\frac{P_S - P_T - sign(u_{vi}) P_{Li}}{2}} \quad \Rightarrow \tag{8.3}$$

$$\frac{x_{Pi}}{u_{vi}} = \frac{K_{vi} \sqrt{\frac{P_S - P_T - sign(u_{vi}) P_{Li}}{2}}}{A_i} \frac{1}{s} \tag{8.4}$$

Hence the simplified dynamic model is given by:

$$G_{si} = \frac{\Gamma_p}{s} \quad \text{where,} \quad \Gamma_p = \frac{K_{vi} \sqrt{\frac{P_S - P_T - sign(u_{vi}) P_{Li}}{2}}}{A_i} = \frac{K_{vi} \sqrt{P_S - P_T - sign(u_{vi}) P_{Li}}}{\sqrt{2} A_i} \tag{8.5}$$

Rewriting the dynamic model to express the valve input, introducing the modeling error ν (due to the neglected terms following from the made assumptions), the simplified dynamic model is given by:

$$\Gamma(t) \dot{x}_P(t) + \nu(t) = u(t) \quad \text{where,} \quad \Gamma(t) = \frac{1}{\Gamma_p} \tag{8.6}$$

This simplified model is a time variant function, representing the individual servo systems, thereby meaning a hydraulic cylinder and a servo valve.

Contents

Chapter 9

Adaptive Control Schemes

This chapter concerns the establishment and implementation of adaptive control schemes. First a derivation of a Robust Model based Controller (RMC) control law is carried out, which will form the base for the adaptive control laws. Hereafter the adaptive control laws are chosen and proved stable, and finally these are implemented and tested in simulations and in experiments.

9.1 Introduction

The adaptive control schemes developed and implemented in this chapter, based on the simplified model are:

- Adaptive Inverse Dynamics Controller (AIDC)
- Modified Adaptive Inverse Dynamics Controller (MAIDC)
- Augmented Adaptive Controller (AAC)
- Modified Augmented Adaptive Controller (MAAC)
- Robust Adaptive Inverse Dynamics Controller (RAIDC)
- Robust Augmented Adaptive Controller (RAIDC)

The approach will be to establish a control law that will enable the closed loop system to track a position reference, when assuming non varying system states, and thereby no

parameter variation (Robust Model based Controller)[Andersen, 1996]. In reality this is not the case, as parameters will vary, and to take these variations into account, adaption laws are introduced, enabling the possibility of updating the control parameters continuously over time, increasing the tracking performance. In each of these adaptive control schemes it will be necessary to prove that the chosen control law will cause the closed loop system to remain stable, and that the position error will converge to zero. For the stability proofs Lyapunov theory is used.

In the following (t) and the index i is omitted for reasons of clarity. Furthermore vector notation is omitted.

9.2 Robust Model Based Controller (RMC)

In this thesis the adaptive control scheme will basically be constituted by two elements - a gain in the feedforward path of the closed loop system stabilizing the error tracking system, and a feedforward contribution using the inverse dynamic expression in the feedforward loop, which as previously mentioned will provide the necessary valve input for trajectory tracking, and thereby increase tracking performance.

The robust control scheme is suggested as[Andersen, 1996]:

$$\hat{\Gamma}(\dot{x}_R - k_p e) + \hat{\nu} = u \tag{9.1}$$

With the $\hat{\Gamma}$ and $\hat{\nu}$ representing the control parameter estimates. This control scheme is motivated by the fact that it can be shown that, in the ideal case with known parameters and no disturbances, the system error dynamics will converge to zero, as time goes to infinity, which is found from the following. The simplified model and ideal case control law is given by:

$$\Gamma\dot{x}_P + \nu = u \quad ; \quad \Gamma(\dot{x}_R - k_p e) + \nu = u \quad ; \quad e = x_P - x_R \tag{9.2}$$

From the above expressions, the closed loop dynamics is given by:

$$\Gamma\dot{x}_P + \nu = \Gamma(\dot{x}_R - k_p e) + \nu \tag{9.3}$$
$$\Gamma\dot{x}_P + \nu = \Gamma\dot{x}_R - \Gamma k_p e + \nu \tag{9.4}$$
$$\Gamma(\dot{x}_P - \dot{x}_R) = -\Gamma k_p e \tag{9.5}$$
$$\Gamma\dot{e} + \Gamma k_p e = 0 \tag{9.6}$$
$$\dot{e} + k_p e = 0 \tag{9.7}$$

It is found that the error dynamics will converge to zero as time goes to infinity, and thereby the closed loop system is asymptotically stable (for proper values of k_p).

In reality however, the ideal case with known parameters an no disturbances does not occur, and hence it is needed to show that the closed loop system with estimated control parameters $\hat{\Gamma}$ and $\hat{\nu}$ are stable, which is shown in the following. The closed loop control

system with estimated control parameters is given by:

$$\Gamma\dot{x}_P + \nu = \hat{\Gamma}(\dot{x}_R - k_p e) + \hat{\nu} \tag{9.8}$$
$$\tag{9.9}$$

Subtracting $\Gamma\dot{x}_R$ on both sides, yields:

$$\Gamma\dot{x}_P + \nu - \Gamma\dot{x}_R = \hat{\Gamma}(\dot{x}_R - k_p e) + \hat{\nu} - \Gamma\dot{x}_R \tag{9.10}$$
$$\Gamma\dot{e} + \nu = \hat{\Gamma}\dot{x}_R - \hat{\Gamma}k_p e + \hat{\nu} - \Gamma\dot{x}_R \tag{9.11}$$
$$\Gamma\dot{e} = (\hat{\Gamma} - \Gamma)\dot{x}_R - \hat{\Gamma}k_p e + \hat{\nu} - \nu \tag{9.12}$$

Defining the error estimates $\tilde{\Gamma} = \hat{\Gamma} - \Gamma$ and $\tilde{\nu} = \hat{\nu} - \nu$[Slotine E J-J, 1991], yields:

$$\Gamma\dot{e} = \tilde{\Gamma}\dot{x}_R - \hat{\Gamma}k_p e + \tilde{\nu} \tag{9.13}$$
$$\hat{\Gamma}\dot{e} - \tilde{\Gamma}\dot{e} = \tilde{\Gamma}\dot{x}_R - \hat{\Gamma}k_p e + \tilde{\nu} \tag{9.14}$$
$$\hat{\Gamma}\dot{e} + \hat{\Gamma}k_p e = \tilde{\Gamma}\dot{x}_R + \tilde{\Gamma}\dot{e} + \tilde{\nu} \tag{9.15}$$
$$\hat{\Gamma}(\dot{e} + k_p e) = \tilde{\Gamma}\dot{x}_R + \tilde{\Gamma}\dot{x}_P - \tilde{\Gamma}\dot{x}_R + \tilde{\nu} \tag{9.16}$$
$$\hat{\Gamma}(\dot{e} + k_p e) = \tilde{\Gamma}\dot{x}_P + \tilde{\nu} \tag{9.17}$$
$$\dot{e} + k_p e = \hat{\Gamma}^{-1}\tilde{\Gamma}\dot{x}_P + \hat{\Gamma}^{-1}\tilde{\nu} \tag{9.18}$$

Using $\dot{e} = \dot{x}_P - \dot{x}_R$, yields:

$$\dot{e} + k_p e = \hat{\Gamma}^{-1}\tilde{\Gamma}\dot{e} + \hat{\Gamma}^{-1}\tilde{\Gamma}\dot{x}_R + \hat{\Gamma}^{-1}\tilde{\nu} \tag{9.19}$$
$$\dot{e} - \hat{\Gamma}^{-1}\tilde{\Gamma}\dot{e} + k_p e = \hat{\Gamma}^{-1}\tilde{\Gamma}\dot{x}_R + \hat{\Gamma}^{-1}\tilde{\nu} \tag{9.20}$$
$$\dot{e}(1 - \hat{\Gamma}^{-1}\tilde{\Gamma}) + k_p e = \hat{\Gamma}^{-1}\tilde{\Gamma}\dot{x}_R + \hat{\Gamma}^{-1}\tilde{\nu} \tag{9.21}$$

Using $\tilde{\Gamma} = \hat{\Gamma} - \Gamma \Rightarrow \Gamma = \hat{\Gamma} - \tilde{\Gamma} \Rightarrow \hat{\Gamma}^{-1}\Gamma = 1 - \hat{\Gamma}^{-1}\tilde{\Gamma}$, yields:

$$\dot{e}\hat{\Gamma}^{-1}\Gamma + k_p e = \hat{\Gamma}^{-1}\tilde{\Gamma}\dot{x}_R + \hat{\Gamma}^{-1}\tilde{\nu} \tag{9.22}$$
$$\dot{e} + \hat{\Gamma}\Gamma^{-1}k_p e = \hat{\Gamma}\Gamma^{-1}\hat{\Gamma}^{-1}\tilde{\Gamma}\dot{x}_R + \hat{\Gamma}\Gamma^{-1}\hat{\Gamma}^{-1}\tilde{\nu} \tag{9.23}$$
$$\dot{e} + \hat{\Gamma}\Gamma^{-1}k_p e = \Gamma^{-1}\tilde{\Gamma}\dot{x}_R + \Gamma^{-1}\tilde{\nu} \tag{9.24}$$
$$\dot{e} + \hat{\Gamma}\Gamma^{-1}k_p e = \Gamma^{-1}(\tilde{\Gamma}\dot{x}_R + \tilde{\nu}) \tag{9.25}$$

Addition of $k_p e$ on both sides yields:

$$\dot{e} + k_p e + \hat{\Gamma}\Gamma^{-1}k_p e = \Gamma^{-1}(\tilde{\Gamma}\dot{x}_R + \tilde{\nu}) + k_p e \tag{9.26}$$
$$\dot{e} + k_p e = \Gamma^{-1}(\tilde{\Gamma}\dot{x}_R + \tilde{\nu}) + k_p e - \hat{\Gamma}\Gamma^{-1}k_p e \tag{9.27}$$
$$\dot{e} + k_p e = \Gamma^{-1}(\tilde{\Gamma}\dot{x}_R + \tilde{\nu}) + (1 - \hat{\Gamma}\Gamma^{-1})k_p e \tag{9.28}$$

Defining $\xi = \Gamma^{-1}(\tilde{\Gamma}\dot{x}_R + \tilde{\nu}) + (1 - \hat{\Gamma}\Gamma^{-1})k_p e$, yields:

$$\dot{e} + k_p e = \xi \tag{9.29}$$

It is seen that the above expression represents a linear differential equation given by:

$$se + k_p e = \xi \tag{9.30}$$

$$(s + k_p)e = \xi \tag{9.31}$$

$$\frac{e}{\xi} = \frac{1}{s + k_p} = h(s) \quad \Rightarrow \quad h(t) = e^{-k_p t} \tag{9.32}$$

The function norm in appendix H.5 is used to give $h(s)$ a bound. The function norm says that for any fixed $p \in [1, \infty]$, if $f : \Re^n \rightarrow \Re$ belongs to L_p if $\int_0^\infty |f(t)|^p dt < \infty$. This means that if $\|h(s)\|_\infty$ has a finite positive value, then $h(s)$ is bounded (according to the function norm). This yields:

$$\|h(s)\|_\infty = \int_0^\infty |e^{-k_p t}| dt = \frac{1}{k_p} \tag{9.33}$$

From the above it is then found that $h(s)$ is bounded since $\|h(s)\|_\infty < \infty$. It is not possible to conclude whether ξ is bounded - however by using the truncated L_∞ norm, ξ can be given a bound in some limited time interval $0 < t < T$, where $T < \infty$. Then for zero initial conditions it is possible to give the error a bound as[Andersen, 1996]:

$$\|e\|_{T\infty} \leq \frac{1}{k_p} \|\xi\|_{T\infty} \tag{9.34}$$

Defining $\alpha_1 = \|\Gamma^{-1}(\tilde{\Gamma}\dot{x}_R + \tilde{\nu})\|_{T\infty}$ and $\alpha_2 = \|(1 - \hat{\Gamma}\Gamma^{-1})k_p\|_{T\infty}$, expression 9.34 is written as:

$$\|e\|_{T\infty} \leq \frac{1}{k_p}\alpha_1 + \frac{1}{k_p}\alpha_2 \|e\|_{T\infty} \quad \Rightarrow \tag{9.35}$$

$$\|e\|_{T\infty} \leq \frac{\frac{1}{k_p}\alpha_1}{1 - \frac{1}{k_p}\alpha_2} \tag{9.36}$$

To ensure that e is bounded ($e \in L_\infty$), the right hand side of expression 9.36 must have a finite value, which implies that:

$$\frac{1}{k_p}\alpha_2 < 1 \tag{9.37}$$

$$\frac{1}{k_p}\|(1 - \hat{\Gamma}\Gamma^{-1})k_p\|_{T\infty} < 1 \tag{9.38}$$

$$\|1 - \hat{\Gamma}\Gamma^{-1}\|_{T\infty} < 1 \tag{9.39}$$

Using expression 8.5 and disregarding $sign(u_{vi})$, yields:

$$1 - \hat{\Gamma}\Gamma^{-1} = 1 - \hat{\Gamma}\frac{K_{vi}\sqrt{P_s - P_T - P_{Li}}}{\sqrt{2}A_i} < 1 \tag{9.40}$$

The estimate $\hat{\Gamma}$ is chosen as:

$$\hat{\Gamma} = \frac{\sqrt{2}A_i}{K_{vi}\sqrt{P_s - P_T}} \tag{9.41}$$

Substituting into expression 9.40, yields:

$$1 - \frac{\sqrt{2}A_i}{K_{vi}\sqrt{P_s - P_T}} \frac{K_{vi}\sqrt{P_s - P_T - P_{Li}}}{\sqrt{2}A_i} < 1 \tag{9.42}$$

$$1 - \frac{\sqrt{P_s - P_T - P_{Li}}}{\sqrt{P_s - P_T}} < 1 \tag{9.43}$$

As the trajectories are planned such that the necessary supply pressure does not exceed $P_{Li} = 2/3P_s$ in order to have have enough power for control, the inequality of expression 9.43 will always be satisfied. Then the robustness of the controller is assured if the following conditions are satisfied[Andersen, 1996].

$$\hat{\Gamma}(t) \text{ exists} \quad , \quad k_p > 0 \quad , \quad \|1 - \hat{\Gamma}\Gamma^{-1}\|_{T\infty} < 1 \tag{9.44}$$

$$e = 0 \text{ for } t = 0 \quad , \quad \dot{x}_R \text{ is bounded} \quad , \quad \nu \text{ is bounded} \tag{9.45}$$

If these conditions are satisfied, then the system is stable, with:

$$\|e\|_{T\infty} \leq \frac{\frac{1}{k_p}\alpha_1}{1 - \frac{1}{k_p}\alpha_2} \tag{9.46}$$

It has now been shown that the suggested control law implemented in the system is stable, and this control law will form the base of the following adaptive control schemes.

9.3 Adaptive Inverse Dynamics Controller (AIDC)

The AIDC is derived based on the RMC control law, and in addition to this an adaption law is added, which will adapt the estimated control parameters continuously over time to achieve increased tracking performance. The stability for this set of differential equations which constitutes the control- and adaption laws, is proved by use of Lyapunov theory. By use of the simplified model and the control law, the closed loop system is given by:

$$\Gamma\dot{x}_P + \nu = \hat{\Gamma}(\dot{x}_R - k_p e) + \hat{\nu} \tag{9.47}$$

Subtracting $\Gamma\dot{x}_R$ on both sides yields:

$$\Gamma\dot{x}_P + \nu - \Gamma\dot{x}_R = \hat{\Gamma}(\dot{x}_R - k_p e) + \hat{\nu} - \Gamma\dot{x}_R \tag{9.48}$$

$$\Gamma\dot{e} + \nu = \hat{\Gamma}(\dot{x}_R - k_p e) + \hat{\nu} - \Gamma\dot{x}_R \tag{9.49}$$

Using the error estimates $\tilde{\Gamma} = \hat{\Gamma} - \Gamma$ and $\tilde{\nu} = \hat{\nu} - \nu$, yields:

$$\Gamma\dot{e} = \hat{\Gamma}(\dot{x}_R - k_p e) + \tilde{\nu} - \Gamma\dot{x}_R \tag{9.50}$$

$$\Gamma\dot{e} = \tilde{\Gamma}(\dot{x}_R - k_p e) + \Gamma(\dot{x}_R - k_p e) + \tilde{\nu} - \Gamma\dot{x}_R \tag{9.51}$$

$$\Gamma\dot{e} = \tilde{\Gamma}(\dot{x}_R - k_p e) + \Gamma\dot{x}_R - \Gamma k_p e + \tilde{\nu} - \Gamma\dot{x}_R \tag{9.52}$$

$$\Gamma\dot{e} = \tilde{\Gamma}(\dot{x}_R - k_p e) - \Gamma k_p e + \tilde{\nu} \tag{9.53}$$

$$\Gamma\dot{e} + \Gamma k_p e = \tilde{\Gamma}(\dot{x}_R - k_p e) + \tilde{\nu} \tag{9.54}$$

$$\Gamma(\dot{e} + k_p e) = \tilde{\Gamma}(\dot{x}_R - k_p e) + \tilde{\nu} \tag{9.55}$$

The following vectors are defined:

$$Y = \begin{bmatrix} \dot{x}_R - k_p e & 1 \end{bmatrix} \quad \text{and} \quad \tilde{a} = \begin{bmatrix} \tilde{\Gamma} \\ \tilde{\nu} \end{bmatrix} \tag{9.56}$$

Substituting these vectors into expression (9.55), the system is rewritten to:

$$\Gamma(\dot{e} + k_p e) = Y\tilde{a} \tag{9.57}$$
$$\dot{e} + k_p e = \Gamma^{-1} Y\tilde{a} \tag{9.58}$$
$$\dot{e} = -k_p e + \Gamma^{-1} Y\tilde{a} \tag{9.59}$$

Written by use of the laplace transform, this yields:

$$\dot{e} + k_p e = \Gamma^{-1} Y\tilde{a} \tag{9.60}$$
$$e(s + k_p) = \Gamma^{-1} Y\tilde{a} \tag{9.61}$$
$$e = \frac{1}{s + k_p}\Gamma^{-1} Y\tilde{a} \tag{9.62}$$

From lemma I in appendix H.2 it is seen, that the adaption parameters will adapt such that $e \to 0$ for $t \to \infty$, if the adaption law is chosen as:

$$\dot{\tilde{a}} = -\gamma Y^T e \quad ; \quad \gamma > 0 \tag{9.63}$$

Here γ is the adaption gain. In the following, the stability of the AIDC will be shown using Lyapunov theory.

9.3.1 Stability Proof (AIDC)

The Lyapunov candidate is chosen to be[Andersen, 1996]:

$$V(e, \tilde{a}) = \frac{1}{2}e^2 + \frac{1}{2}\gamma^{-1}\Gamma^{-1}\tilde{a}^T\tilde{a} \tag{9.64}$$

Taking the time derivative yields:

$$\dot{V}(e, \tilde{a}) = \dot{e}e + \frac{1}{2}\gamma^{-1}(\dot{\Gamma}^{-1}\tilde{a}^T\tilde{a} + 2\Gamma^{-1}\tilde{a}^T\dot{\tilde{a}}) \tag{9.65}$$

Substituting the error dynamics (expression 9.59), yields:

$$\dot{V}(e, \tilde{a}) = (-k_p e + \Gamma^{-1} Y\tilde{a})e + \frac{1}{2}\gamma^{-1}(\dot{\Gamma}^{-1}\tilde{a}^T\tilde{a} + 2\Gamma^{-1}\tilde{a}^T\dot{\tilde{a}}) \tag{9.66}$$
$$= -k_p e^2 + \Gamma^{-1} Y\tilde{a}e + \frac{1}{2}\gamma^{-1}\dot{\Gamma}^{-1}\tilde{a}^T\tilde{a} + \gamma^{-1}\Gamma^{-1}\tilde{a}^T\dot{\tilde{a}} \tag{9.67}$$

Assuming that $\|\dot{\Gamma}\| << \|\dot{\tilde{a}}\|$, yields:

$$\dot{V}(e, \tilde{a}) = -k_p e^2 + \Gamma^{-1} Y\tilde{a}e + \gamma^{-1}\Gamma^{-1}\tilde{a}^T\dot{\tilde{a}} \tag{9.68}$$

Using that $Y\tilde{a} = \tilde{a}^T Y^T$, yields:

$$\dot{V}(e,\tilde{a}) = -k_p e^2 + \Gamma^{-1}\tilde{a}^T(Y^T e + \gamma^{-1}\dot{\hat{a}}) \tag{9.69}$$

Substituting the adaption law, yields:

$$\begin{aligned}
\dot{V}(e,\tilde{a}) &= -k_p e^2 + \Gamma^{-1}\tilde{a}^T(Y^T e + \gamma^{-1}(-\gamma Y^T e)) && (9.70)\\
&= -k_p e^2 + \Gamma^{-1}\tilde{a}^T(Y^T e - \gamma^{-1}\gamma Y^T e) && (9.71)\\
&= -k_p e^2 + \Gamma^{-1}\tilde{a}^T(Y^T e - Y^T e) && (9.72)\\
&= -k_p e^2 \quad \Rightarrow && (9.73)\\
\dot{V}(e,\tilde{a}) &= -k_p e^2 \leq 0 && (9.74)
\end{aligned}$$

It is seen that $\dot{V}(e,\tilde{a})$ is negative semi-definite as the inequality is satisfied, independent of the value of $\tilde{a}$. This indicates that $e \in L_2 \cap L_\infty$ and $\tilde{a} \in L_\infty$. Then by considering 9.59, and noting that $\dot{x}_R$, $\tilde{a}$ and Γ are bounded, it is found that $\dot{e}$ is bounded and $\dot{e} \in L_\infty$. The following can now be stated:

$$V(e,\tilde{a}) > 0 \quad ; \quad \dot{V}(e,\tilde{a}) \leq 0 \quad ; \quad (e,\tilde{a}) \neq 0 \tag{9.75}$$

According to the Lyapunov-like lemma in appendix H.4, if 9.75 is satisfied, and $\dot{V}(e,\tilde{a})$ is uniformly continuous, then $e \to 0$ for $t \to \infty$. Barbalats lemma (appendix H.3) states, that a sufficient condition for a differentiable function to be uniformly continuous, is that its derivative is bounded. This means that it is needed to show that $\ddot{V}(e,\tilde{a})$ is bounded. Taking the time derivative of $\dot{V}(e,\tilde{a})$, yields:

$$\ddot{V}(e,\tilde{a}) = -2k_p e\dot{e} \tag{9.76}$$

From the above expression it is seen, that as e and $\dot{e}$ are bounded, then $\ddot{V}(e,\tilde{a})$ is bounded, and hence $\dot{V}(e,\tilde{a})$ is uniformly continuous, according to Barbalats lemma. It can then, according to the Lyapunov-like lemma, be concluded that $e \to 0$ as $t \to \infty$, yielding that e is asymptotically stable.

The control- and adaption laws of the AIDC can now formally be written, noting that $\dot{\tilde{a}} = \dot{\hat{a}}$, when considering a as a true slow varying parameter.

AIDC control law:

$$\hat{\Gamma}(\dot{x}_R - k_p e) + \hat{\nu} = u \quad ; \quad e = x_P - x_R \quad ; \quad k_p > 0 \tag{9.77}$$

AIDC adaption law:

$$\dot{\tilde{a}} = \dot{\hat{a}} = -\gamma Y^T e = \begin{bmatrix} \dot{\hat{\Gamma}} \\ \dot{\hat{\nu}} \end{bmatrix} = \begin{bmatrix} -\gamma_1(\dot{x}_R - k_p e)e \\ -\gamma_2 e \end{bmatrix} \quad ; \quad \gamma_1, \gamma_2 > 0 \tag{9.78}$$

9.4 Modified Adaptive Inverse Dynamics Controller (MAIDC)

The MAIDC is similar to the AIDC, but with a modified adaption law - instead of only having the integral part, also a proportional part is added to the adaption law. The model and control law is, as for the AIDC:

$$\Gamma\dot{x}_P + \nu = u \quad \text{and} \quad \hat{\Gamma}(\dot{x}_R - k_p e) + \hat{\nu} = u \quad ; \quad e = x_P - x_R \tag{9.79}$$

And the modified adaption law is given by[Hansen, 1997]:

$$\dot{\tilde{a}} = -\gamma Y^T e - \alpha \frac{d}{dt}(Y^T e) \quad ; \quad \gamma,\ \alpha > 0 \tag{9.80}$$

9.4.1 Stability Proof (MAIDC)

The Lyapunov candidate is chosen as[Hansen, 1997]:

$$V(e, \tilde{I}) = \frac{1}{2}e^2 + \frac{1}{2}\gamma\Gamma^{-1} I^T I \tag{9.81}$$

Where $I = \int (Y^T e)dt$. Taking the time derivative and assuming that $\|\dot{\Gamma}\| << \|\dot{\tilde{a}}\|$, yields:

$$\dot{V}(e, I) = \dot{e}e + \gamma\Gamma^{-1}\dot{I}^T I \tag{9.82}$$

Substituting the error dynamics (expression (9.59)), yields:

$$\begin{aligned}
\dot{V}(e, I) &= (-k_p e + \Gamma^{-1} Y\tilde{a})e + \gamma\Gamma^{-1}\dot{I}^T I && (9.83)\\
&= -k_p e^2 + \Gamma^{-1} Y\tilde{a}e + \gamma\Gamma^{-1}\dot{I}^T I && (9.84)\\
&= -k_p e^2 + \Gamma^{-1}\dot{I}^T\tilde{a} + \gamma\Gamma^{-1}\dot{I}^T I && (9.85)
\end{aligned}$$

Using the modified adaption law:

$$\begin{aligned}
\dot{\tilde{a}} &= -\gamma Y^T e - \alpha \frac{d}{dt}(Y^T e) && (9.86)\\
&= -\gamma\dot{I} - \alpha\ddot{I} \quad \Rightarrow && (9.87)\\
\tilde{a} &= -\gamma I - \alpha\dot{I} \quad \Rightarrow && (9.88)\\
I &= \gamma^{-1}(-\tilde{a} - \alpha\dot{I}) && (9.89)
\end{aligned}$$

And inserting, yields:

$$\begin{aligned}
\dot{V}(e, I) &= -k_p e^2 + \Gamma^{-1}\dot{I}^T\tilde{a} + \gamma\Gamma^{-1}\dot{I}^T\gamma^{-1}(-\tilde{a} - \alpha\dot{I}) && (9.90)\\
&= -k_p e^2 + \Gamma^{-1}\dot{I}^T\tilde{a} + \Gamma^{-1}\dot{I}^T(-\tilde{a} - \alpha\dot{I}) && (9.91)\\
&= -k_p e^2 + \Gamma^{-1}\dot{I}^T\tilde{a} - \Gamma^{-1}\dot{I}^T\tilde{a} - \alpha\Gamma^{-1}\dot{I}^T\dot{I} && (9.92)\\
&= -k_p e^2 - \alpha\Gamma^{-1}\dot{I}^T\dot{I} && (9.93)\\
&= -(k_p e^2 + \alpha\Gamma^{-1}\dot{I}^T\dot{I}) && (9.94)
\end{aligned}$$

The terms e^2 and $\dot{I}^T\dot{I}$ will always be positive, and as Γ is positive it is found that $\dot{V}(e, I)$ is negative semi-definite, for positive values of k_p and α. As $\dot{V}(e, I)$ is negative semi-definite

and $V(e,I) > 0$, it is found that e and $\dot{I}$ are bounded. Furthermore, by considering expression 9.59 it is found that $\dot{e}$ is bounded and $\dot{e} \in L_\infty$. Then if $\dot{V}(e,I)$ is uniformly continuous, $e \to 0$ for $t \to \infty$ (Lyapunov-like lemma, appendix H.4), and e will hence be asymptotically stable. Taking the time derivative of $\dot{V}(e,I)$, yields:

$$\ddot{V}(e,I) = -2k_p e\dot{e} - 2\alpha\Gamma^{-1}\dot{I}^T\ddot{I} \tag{9.95}$$

Substituting $\dot{\hat{a}} = -\gamma\dot{I} - \alpha\ddot{I} \;\Rightarrow\; \ddot{I} = -\gamma\dot{I}/\alpha - \dot{\hat{a}}/\alpha$, yields:

$$\ddot{V}(e,I) = -2k_p e\dot{e} - 2\alpha\Gamma^{-1}\dot{I}^T(-\gamma\dot{I}/\alpha - \dot{\hat{a}}/\alpha) \tag{9.96}$$

$$= -2k_p e\dot{e} - 2\Gamma^{-1}\dot{I}^T(-\gamma\dot{I} - \dot{\hat{a}}) \tag{9.97}$$

As e, $\dot{e}$ and $\dot{I}$ are found to be bounded, and as $\dot{\hat{a}}$ is bounded, it is found that $\ddot{V}(e,I)$ is bounded, and consequently that $\dot{V}(e,I)$ is uniformly continuous. From the Lyapunov-like lemma it is found that $e \to 0$ for $t \to \infty$. The control- and adaption laws of the MAIDC are formally written as shown below.

MAIDC control law:

$$\hat{\Gamma}(\dot{x}_R - k_p e) + \hat{\nu} = u \quad ; \quad e = x_P - x_R \quad ; \quad k_p > 0 \tag{9.98}$$

MAIDC adaption law:

$$\dot{\hat{a}} = \dot{\hat{a}} = \begin{bmatrix} \dot{\hat{\Gamma}} \\ \dot{\hat{\nu}} \end{bmatrix} = \begin{bmatrix} -\gamma_1(\dot{x}_R - k_p e)e - \alpha_1 \frac{d}{dt}((\dot{x}_R - k_p e)e) \\ -\gamma_2 e - \alpha_2 \frac{d}{dt} e \end{bmatrix} \quad ; \quad \gamma_1, \gamma_2, \alpha_1, \alpha_2 > 0$$

9.5 Augmented Adaptive Controller (AAC)

The AAC control scheme is similar to that of the AIDC, however in the AAC an additional proportional+integral term is added in the control law - the motivation for applying this control scheme is an initiative to decrease the error further than that of the AIDC. The control law is given by[Andersen, 1996]:

$$\hat{\Gamma}(\dot{x}_R - k_p e) + \hat{\nu} - k_{PI}\bar{x} = u \quad ; \quad \bar{x} = e + k_p \int_0^t e(\tau)d\tau \quad ; \quad e = x_P - x_R \tag{9.99}$$

First it is shown that this control structure will in fact cause the error to converge to zero, when the control parameters are known (as also carried out for the RMC control law used for the AIDC and MAIDC). Using the simplified model, and the AAC control

scheme with known parameters, the closed loop dynamics is given by:

$$\Gamma\dot{x}_P + \nu = \Gamma(\dot{x}_R - k_p e) + \nu - k_{PI}\bar{x} \tag{9.100}$$
$$\Gamma\dot{x}_P + \nu = \Gamma\dot{x}_R - \Gamma k_p e + \nu - k_{PI}\bar{x} \tag{9.101}$$
$$\Gamma\dot{x}_P = \Gamma\dot{x}_R - \Gamma k_p e - k_{PI}\bar{x} \tag{9.102}$$
$$\Gamma\dot{x}_P - \Gamma\dot{x}_R + \Gamma k_p e = -k_{PI}\bar{x} \tag{9.103}$$

Using the expression for $\bar{x}$, yields:

$$\Gamma(\dot{e} + k_p e) = -k_{PI}\bar{x} \tag{9.104}$$
$$\Gamma\dot{\bar{x}} = -k_{PI}\bar{x} \tag{9.105}$$
$$\Gamma\dot{\bar{x}} + k_{PI}\bar{x} = 0 \tag{9.106}$$

The chosen Lyapunov candidate is[Andersen, 1996]:

$$V(\bar{x}) = \frac{1}{2}\Gamma\bar{x}^2 \tag{9.107}$$

Taking the time derivative, yields:

$$\dot{V}(\bar{x}) = \Gamma\bar{x}\dot{\bar{x}} \tag{9.108}$$

Substituting $\dot{\bar{x}} = -\Gamma^{-1}k_{PI}\bar{x}$, yields:

$$\dot{V}(\bar{x}) = \Gamma\bar{x}(-\Gamma^{-1}k_{PI}\bar{x}) \tag{9.109}$$
$$\dot{V}(\bar{x}) = -k_{PI}\bar{x}^2 \tag{9.110}$$
$$\dot{V}(\bar{x}) \leq 0 \tag{9.111}$$

It is seen that $\dot{V}(\bar{x})$ is negative semi definite, and as $V(\bar{x}) > 0$ it is found that $\bar{x}$ is bounded and $\bar{x} \in L_2 \cap L_\infty$. From this it follows by considering expression (9.106), that $\dot{\bar{x}}$ is bounded and $\dot{\bar{x}} \in L_\infty$. Then if $\dot{V}(\bar{x})$ is uniformly continuous, $\bar{x} \to 0$ for $t \to 0$. Taking the time derivative of $\dot{V}(\bar{x})$, yields:

$$\ddot{V}(\bar{x}) = -2k_{PI}\bar{x}\dot{\bar{x}} \tag{9.112}$$

As $\bar{x}$ and $\dot{\bar{x}}$ are bounded, $\ddot{V}(\bar{x})$ is bounded, and hence $\dot{V}(\bar{x})$ is uniformly continuous. According to the Lyapunov-like lemma, this implies that $\bar{x} \to 0$ for $t \to \infty$. This however, does not imply whether e converges to zero, only that $\bar{x}$ does - to determine whether e does in fact converge to zero the expression for $\bar{x}$ is considered. Taking the time derivative and the laplace transform, yields:

$$s\bar{x} = se + k_{PI}e \tag{9.113}$$
$$s\bar{x} = (s + k_{PI})e \Rightarrow \tag{9.114}$$
$$e = \frac{s}{s + k_{PI}}\bar{x} \tag{9.115}$$

From the above expression it is found that for positive values of k_{PI} and if $\bar{x} \to 0$ for $t \to \infty$ (which is the case), then e is stable and $e \to 0$ for $t \to \infty$. From this it is found that the error will in fact converge to zero with an additional PI term in the control law.

As mentioned earlier there is not perfect knowledge of the control law parameters, and it is now shown that the e is asymptotically stable when using the adaption law to estimate the control parameters.

9.5.1 Stability Proof (AAC)

The control law is given by:

$$\hat{\Gamma}(\dot{x}_R - k_p e) + \hat{\nu} - k_{PI}\bar{x} = \begin{bmatrix} \dot{x}_R - k_p e & 1 \end{bmatrix} \begin{bmatrix} \tilde{\Gamma} \\ \tilde{\nu} \end{bmatrix} - k_{PI}\bar{x} = Y\underline{\hat{a}} - k_{PI}\bar{x} = u \tag{9.116}$$

With the adaption law[Andersen, 1996]:

$$\dot{\hat{a}} = -\gamma Y^T \bar{x} \tag{9.117}$$

The Lyapunov-like candidate is chosen as[Andersen, 1996]:

$$V(\bar{x}, \tilde{a}) = \frac{1}{2}\Gamma\bar{x}^2 + \frac{1}{2}\gamma^{-1}\tilde{a}^T\tilde{a} \tag{9.118}$$

Taking the time derivative, yields:

$$\dot{V}(\bar{x}, \tilde{a}) = \frac{1}{2}\dot{\Gamma}\bar{x}^2 + \Gamma\bar{x}\dot{\bar{x}} + \gamma^{-1}\tilde{a}^T\dot{\tilde{a}} \tag{9.119}$$

Using:

$$\Gamma\dot{\bar{x}} = \Gamma\dot{e} + \Gamma k_p e = u - \nu - \Gamma\dot{x}_R + \Gamma k_p e \tag{9.120}$$

Yields:

$$\dot{V}(\bar{x}, \tilde{a}) = \frac{1}{2}\dot{\Gamma}\bar{x}^2 + \bar{x}(u - \nu - \Gamma\dot{x}_R + \Gamma k_p e) + \gamma^{-1}\tilde{a}^T\dot{\tilde{a}} \tag{9.121}$$

Assuming $\|\dot{\Gamma}\| << \|\dot{\tilde{a}}\|$, gives:

$$\dot{V}(\bar{x}, \tilde{a}) = \bar{x}(u - \nu - \Gamma\dot{x}_R + \Gamma k_p e) + \gamma^{-1}\tilde{a}^T\dot{\tilde{a}} \tag{9.122}$$

$$= \bar{x}(u - \nu - \Gamma(\dot{x}_R + k_p e)) + \gamma^{-1}\tilde{a}^T\dot{\tilde{a}} \tag{9.123}$$

Using the control law:

$$\hat{\Gamma}(\dot{x}_R - k_p e) + \hat{\nu} - k_{PI}\bar{x} = u \tag{9.124}$$

And substituting, gives:

$$\dot{V}(\bar{x}, \tilde{a}) = \bar{x}(u - \nu - \Gamma(\dot{x}_R + k_p e)) + \gamma^{-1}\tilde{a}^T\dot{\tilde{a}} \tag{9.125}$$

$$= \bar{x}((\hat{\Gamma}(\dot{x}_R - k_p e) + \hat{\nu} - k_{PI}\bar{x}) - \nu - \Gamma(\dot{x}_R + k_p e)) + \gamma^{-1}\tilde{a}^T\dot{\tilde{a}} \tag{9.126}$$

$$= \bar{x}(\tilde{\Gamma}(\dot{x}_R - k_p e) + \tilde{\nu} - k_{PI}\bar{x}) + \gamma^{-1}\tilde{a}^T\dot{\tilde{a}} \tag{9.127}$$

$$= \bar{x}(Y\tilde{a} - k_{PI}\bar{x}) + \gamma^{-1}\tilde{a}^T\dot{\tilde{a}} \tag{9.128}$$

Using the adaption law, and assuming that a is a slow varying parameter:

$$\dot{\tilde{a}} = \dot{\hat{a}} = -\gamma Y^T \bar{x} \tag{9.129}$$

Yields:

$$\begin{aligned} \dot{V}(\bar{x}, \tilde{a}) &= \bar{x}(Y\tilde{a} - k_{PI}\bar{x}) + \gamma^{-1}\tilde{a}^T\dot{\tilde{a}} && (9.130)\\ &= \bar{x}(Y\tilde{a} - k_{PI}\bar{x}) + \gamma^{-1}\tilde{a}^T(-\gamma Y^T\bar{x}) && (9.131)\\ &= \bar{x}(Y\tilde{a} - k_{PI}\bar{x}) - \tilde{a}^T Y^T\bar{x} && (9.132) \end{aligned}$$

Using that $\tilde{a}^T Y^T = Y\tilde{a}$, yields:

$$\begin{aligned} \dot{V}(\bar{x}, \tilde{a}) &= \bar{x}(Y\tilde{a} - k_{PI}\bar{x}) - Y\tilde{a}\bar{x} && (9.133)\\ &= Y\tilde{a}\bar{x} - k_{PI}\bar{x}^2 - Y\tilde{a}\bar{x} && (9.134)\\ &= -k_{PI}\bar{x}^2 && (9.135) \end{aligned}$$

It is seen that $\dot{V}(\bar{x}, \tilde{a})$ is negative semi-definite. As expression 9.135 is identical to expression 9.110, then using the same argumentation it can be shown that $\bar{x} \to 0$ for $t \to \infty$, hence $e \to 0$ for $t \to \infty$. Thereby it is found that the e is asymptotically stable. The AAC can now formally be written as:

AAC control law:

$$\hat{\Gamma}(\dot{x}_R - k_p e) + \hat{\nu} - k_{PI}\bar{x} = u \quad ; \quad e = x_P - x_R \quad ; \quad k_p, k_{PI} > 0 \tag{9.136}$$

AAC adaption law:

$$\dot{\tilde{a}} = \dot{\hat{a}} = \begin{bmatrix} \dot{\hat{\Gamma}} \\ \dot{\hat{\nu}} \end{bmatrix} = \begin{bmatrix} -\gamma_1(\dot{x}_R - k_p e)\bar{x} \\ -\gamma_2\bar{x} \end{bmatrix} \quad ; \quad \gamma_1, \gamma_2 > 0 \tag{9.137}$$

Where:

$$\bar{x} = e + k_p \int_0^t e(\tau)d\tau \tag{9.138}$$

9.6 Modified Augmented Adaptive Controller (MAAC)

The MAAC is similar to the AAC but instead of using only integral terms in the adaption law, also a proportional term is added (as also done in the MAIDC). The control law and belonging adaption law is given as[Andersen, 1996]:

$$\hat{\Gamma}(\dot{x}_R - k_p e) + \hat{\nu} - k_{PI}\bar{x} = u \quad ; \quad \bar{x} = e + K_p \int_0^t e(\tau)d\tau \quad ; \quad e = x_P - x_R \tag{9.139}$$

$$\dot{\hat{a}} = -\gamma Y^T \bar{x} - \alpha \frac{d}{dt}(Y^T \bar{x}) \quad ; \quad \gamma,\ \alpha > 0 \tag{9.140}$$

To ensure that this control law is stable with the modified adaption law, again Lyapunov theory is used. Previous to the stability proof, $\dot{\bar{x}}$ is obtained by use of the simplified closed loop system.

$$\Gamma \dot{x}_P + \nu = \hat{\Gamma}(\dot{x}_R - k_p e) + \hat{\nu} - k_{PI}\bar{x} \tag{9.141}$$

Subtracting $\Gamma \dot{x}_R$ on both sides, yields:

$$\Gamma \dot{x}_P + \nu - \Gamma \dot{x}_R = \hat{\Gamma}(\dot{x}_R - k_p e) + \hat{\nu} - k_{PI}\bar{x} - \Gamma \dot{x}_R \tag{9.142}$$

$$\Gamma \dot{e} + \nu = \hat{\Gamma}(\dot{x}_R - k_p e) + \hat{\nu} - k_{PI}\bar{x} - \Gamma \dot{x}_R \tag{9.143}$$

$$\Gamma \dot{e} = \hat{\Gamma}(\dot{x}_R - k_p e) + \tilde{\nu} - k_{PI}\bar{x} - \Gamma \dot{x}_R \tag{9.144}$$

$$\tag{9.145}$$

Using $\hat{\Gamma} = \tilde{\Gamma} + \Gamma$, yields:

$$\Gamma \dot{e} = \tilde{\Gamma}(\dot{x}_R - k_p e) + \Gamma(\dot{x}_R - k_p e) + \tilde{\nu} - k_{PI}\bar{x} - \Gamma \dot{x}_R \tag{9.146}$$

$$\Gamma \dot{e} = \tilde{\Gamma}(\dot{x}_R - k_p e) + \Gamma \dot{x}_R - \Gamma k_p e + \tilde{\nu} - k_{PI}\bar{x} - \Gamma \dot{x}_R \tag{9.147}$$

$$\Gamma \dot{e} = \tilde{\Gamma}(\dot{x}_R - k_p e) - \Gamma k_p e + \tilde{\nu} - k_{PI}\bar{x} \tag{9.148}$$

$$\Gamma \dot{e} + \Gamma k_p e = \tilde{\Gamma}(\dot{x}_R - k_p e) + \tilde{\nu} - k_{PI}\bar{x} \tag{9.149}$$

$$\Gamma \dot{e} + \Gamma k_p e = Y\tilde{a} - k_{PI}\bar{x} \tag{9.150}$$

Using that $\dot{\bar{x}} = \dot{e} + k_p e$, yields:

$$\Gamma \dot{\bar{x}} = Y\tilde{a} - k_{PI}\bar{x} \tag{9.151}$$

$$\dot{\bar{x}} = \Gamma^{-1} Y\tilde{a} - \Gamma^{-1} k_{PI}\bar{x} \tag{9.152}$$

The error dynamics has now been derived using the closed loop dynamics, and the stability proof can be carried out.

9.6.1 Stability Proof (MAAC)

The Lyapunov candidate is chosen as[Hansen, 1997]:

$$V(\bar{x}, \tilde{I}) = \frac{1}{2}\bar{x}^2 + \frac{1}{2}\gamma \Gamma^{-1} I^T I \tag{9.153}$$

Where $I = \int (Y^T \bar{x}) dt$. Taking the time derivative and assuming that $\|\dot{\Gamma}\| << \|\dot{\hat{a}}\|$, yields:

$$\dot{V}(\bar{x}, I) = \dot{\bar{x}}\bar{x} + \gamma \Gamma^{-1} \dot{I}^T I \tag{9.154}$$

Substituting the expression 9.151, yields:

$$\dot{V}(\bar{x}, I) = (\Gamma^{-1} Y\tilde{a} - \Gamma^{-1} k_{PI}\bar{x})\bar{x} + \gamma \Gamma^{-1} \dot{I}^T I \tag{9.155}$$

$$= \Gamma^{-1} Y\tilde{a}\bar{x} - \Gamma^{-1} k_{PI}\bar{x}^2 + \gamma \Gamma^{-1} \dot{I}^T I \tag{9.156}$$

Using the modified adaption law:

$$\dot{\tilde{a}} = -\gamma Y^T \bar{x} - \alpha \frac{d}{dt}(Y^T \bar{x}) = -\gamma \dot{I} - \alpha \ddot{I} \quad \Rightarrow \tag{9.157}$$

$$\tilde{a} = -\gamma I - \alpha \dot{I} \quad \Rightarrow \quad I = \gamma^{-1}(-\tilde{a} - \alpha \dot{I}) \tag{9.158}$$

And inserting, yields:

$$\dot{V}(\bar{x}, I) = \Gamma^{-1} Y \tilde{a} \bar{x} - \Gamma^{-1} k_{PI} \bar{x}^2 + \gamma \Gamma^{-1} \dot{I}^T I \tag{9.159}$$

$$= \Gamma^{-1} Y \tilde{a} \bar{x} - \Gamma^{-1} k_{PI} \bar{x}^2 + \gamma \Gamma^{-1} \dot{I}^T (\gamma^{-1}(-\tilde{a} - \alpha \dot{I})) \tag{9.160}$$

$$= \Gamma^{-1} Y \tilde{a} \bar{x} - \Gamma^{-1} k_{PI} \bar{x}^2 - \Gamma^{-1} \dot{I}^T \tilde{a} - \alpha \Gamma^{-1} \dot{I}^T \dot{I} \tag{9.161}$$

$$= \Gamma^{-1} Y \tilde{a} \bar{x} - \Gamma^{-1} k_{PI} \bar{x}^2 - \Gamma^{-1} Y \tilde{a} \bar{x} - \alpha \Gamma^{-1} \dot{I}^T \dot{I} \tag{9.162}$$

$$= -\Gamma^{-1} k_{PI} \bar{x}^2 - \alpha \Gamma^{-1} \dot{I}^T \dot{I} \tag{9.163}$$

$$= -\Gamma^{-1}(k_{PI} \bar{x}^2 + \alpha \dot{I}^T \dot{I}) \leq 0 \tag{9.164}$$

It is seen that $\dot{V}(\bar{x}, I)$ is negative semi-definite, and as $V(\bar{x}, I) > 0$, then according to the Lyapunov-like lemma, if $\dot{V}(\bar{x}, I)$ is uniformly continuous, $\bar{x}$ will converge to zero as time goes to infinity. The argumentation that $\dot{V}(\bar{x}, I)$ is uniformly continuous is similar to that of the MAIDC, and it is found that $\bar{x} \to 0$ for $t \to \infty$, and consequently that $e \to 0$ for $t \to \infty$. Thereby it is found that e is asymptotically stable. The control- and adaption laws of the MAAC are given as shown below.

MAAC control law:

$$\hat{\Gamma}(\dot{x}_R - k_p e) + \hat{\nu} - k_{PI} \bar{x} = u \quad ; \quad e = x_P - x_R \quad ; \quad k_p, k_{PI} > 0 \tag{9.165}$$

MAAC adaption law:

$$\dot{\tilde{a}} = \dot{\hat{a}} = \begin{bmatrix} \dot{\hat{\Gamma}} \\ \dot{\hat{\nu}} \end{bmatrix} = \begin{bmatrix} -\gamma_1(\dot{x}_R - k_p e)\bar{x} - \alpha_1 \frac{d}{dt}((\dot{x}_R - k_p e)\bar{x}) \\ -\gamma_2 \bar{x} - \alpha_2 \frac{d}{dt} \bar{x} \end{bmatrix} \quad ; \quad \gamma_1, \gamma_2, \alpha_1, \alpha_2 > 0$$

Where:

$$\bar{x} = e + k_p \int_0^t e(\tau) d\tau \tag{9.166}$$

9.7 RAIDC & RAAC

In this section robust versions of the adaption law of the AIDC and AAC are presented (Robust Adaptive Inverse Dynamics Controller and Robust Augmented Adaptive Controller).

These adaption laws are accounted for, but not proved by Lyapunov theory as the previous controllers presented in this chapter. For stability proofs, there is referred to

[Andersen, 1996].

The AIDC and AAC adaption laws consists of pure integral parts, and it was assumed that the system could be represented by the simplified first order model - however, the system is of higher order which introduces dynamics that is not taken into account in the simplified model, and hence un-modeled high frequency dynamics might cause instability to the physical system. Furthermore, on the physical robot manipulator, the control schemes are implemented in a discrete way, using feedback signals containing some level of noise. This may also cause instability in the system if for example the adaption law adapts the control parameters using signals overlayed with noise. The mentioned elements acts as disturbances to the system, which calls for robust versions of the adaption laws, enabling the control schemes to cope with these disturbances.

In the robust adaption laws, instead of letting these consist of pure integral terms, a first order integrating system is put instead of the integrator. This corresponds to applying a first order filter in the adaption law, enabling the possibility to avoid these disturbances to some extend, making the parameter adaption more robust. As this is equivalent to applying a feedback loop in the adaption law, this ensures that the adapted parameters remain bounded provided that the input signals to the adaption algorithm are bounded.

It is noted that the adaption laws for the AIDC and AAC are similar to each other, and hence the following robust adaption law goes for both control schemes, seen from an algebraic point of view. The robust adaption laws are given by[Andersen, 1996]:

$$\dot{\hat{a}} = \dot{\hat{a}} = -\sigma\hat{a} - \gamma Y^T e \quad ; \quad \gamma,\ \sigma > 0 \tag{9.167}$$

From the following, it is found that the $\sigma\hat{a}$ term in the above expression does correspond to applying a first order filter to the adaption algorithm, instead of a pure integrator. Laplace transforming, yields:

$$\hat{a}s = -\sigma\hat{a} - \gamma Y^T e \tag{9.168}$$

$$\hat{a}s + \sigma\hat{a} = -\gamma Y^T e \tag{9.169}$$

$$(s+\sigma)\hat{a} = -\gamma Y^T e \tag{9.170}$$

$$\hat{a} = -\frac{\gamma}{s+\sigma} Y^T e \tag{9.171}$$

$$\tag{9.172}$$

It is seen that including the $\sigma\hat{a}$ term does have a filter effect in the adaption algorithm, with filter time constant determined by σ.

The RAIDC- and RAAC control schemes are given in the following:

RAIDC control law:

$$\hat{\Gamma}(\dot{x}_R - k_p e) + \hat{\nu} = u \quad ; \quad e = x_P - x_R \quad ; \quad k_p > 0 \tag{9.173}$$

RAIDC adaption law:

$$\dot{\tilde{a}} = \dot{\hat{a}} = \begin{bmatrix} \dot{\hat{\Gamma}} \\ \dot{\hat{\nu}} \end{bmatrix} = \begin{bmatrix} -\sigma\gamma_1 \int_t ((\dot{x}_R - k_p e)e)dt - \gamma_1(\dot{x}_R - k_p e)e \\ -\sigma\gamma_2 \int_t (e)dt - \gamma_2 e \end{bmatrix} \quad ; \quad \sigma, \gamma_1, \gamma_2 > 0 \tag{9.174}$$

RAAC control law:

$$\hat{\Gamma}(\dot{x}_R - k_p e) + \hat{\nu} - k_{PI}\bar{x} = u \quad ; \quad e = x_P - x_R \quad ; \quad k_p, k_{PI} > 0 \tag{9.175}$$

RAAC adaption law:

$$\dot{\tilde{a}} = \dot{\hat{a}} = \begin{bmatrix} \dot{\hat{\Gamma}} \\ \dot{\hat{\nu}} \end{bmatrix} = \begin{bmatrix} -\sigma\gamma_1 \int_t ((\dot{x}_R - k_p e)\bar{x})dt - \gamma_1(\dot{x}_R - k_p e)\bar{x} \\ -\sigma\gamma_2 \int_t (\bar{x})dt - \gamma_2 \bar{x} \end{bmatrix} \quad ; \quad \sigma, \gamma_1, \gamma_2 > 0 \tag{9.176}$$

Where:

$$\bar{x} = e + k_p \int_0^t e(\tau)d\tau \tag{9.177}$$

9.8 Parameters for Adaptive Control Schemes

In the following the control parameters obtained, when implementing the MAIDC- and MAAC schemes, will be presented. The AIDC-, AAC, RAIDC and RAAC control schemes are presented in appendix I. When implementing the adaptive control schemes, it is necessary to consider the initial values of the adapted parameters and in particular $\hat{\Gamma}$ - in the case of large deviations in the initial value of $\hat{\Gamma}$ compared to Γ, the parameter adaption might experience large transient periods, as this may not be able to adapt the parameters with sufficient speed. However, by using proper initial values of the adaption parameters, close to the actual values of these parameters, the transient period of the parameter adaption will be decreased.

The parameters used during simulations are presented in appendix J. It is noted that these has been found by trial and error, as no method for this purpose is available.

9.9 Simulation Results

In the following the simulation results for the MAIDC and the MAAC are presented.

From figures 9.1 and 9.5 it is found that the MAIDC and MAAC when implemented on HSS I increases tracking performance compared to the classic linear controllers, especially when completing the parabolic-like segments of the trajectory. From figures 9.2 and 9.6 no visible improvement is found, compared to the classic linear controllers - however, from table 9.1 it is clear that both maximum- and RMS errors are decreased compared to the classic linear controllers.

It is found from figures 9.3, 9.4, 9.7, 9.8, that when choosing proper initial values for the adapted parameters and properly tuned controller parameters, the adapted parameters $\hat{\Gamma}_i$ are able to *track* fluctuations in the Γ_i to some extend.

9.9.1 MAIDC

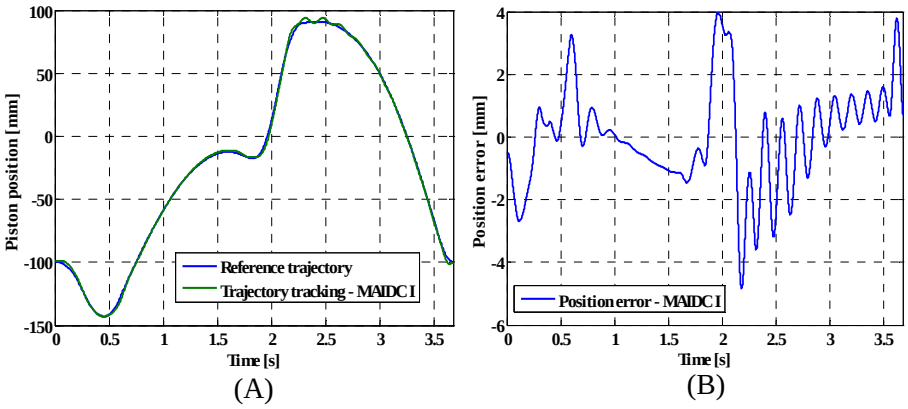

Figure 9.1: MAIDC scheme implemented on HSS I. (A) Trajectory tracking. (B) Tracking error.

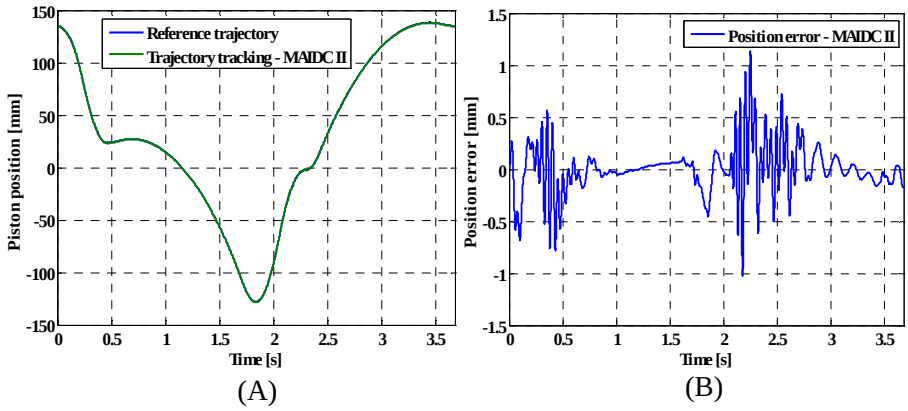

Figure 9.2: MAIDC scheme implemented on HSS II. (A) Trajectory tracking. (B) Tracking error.

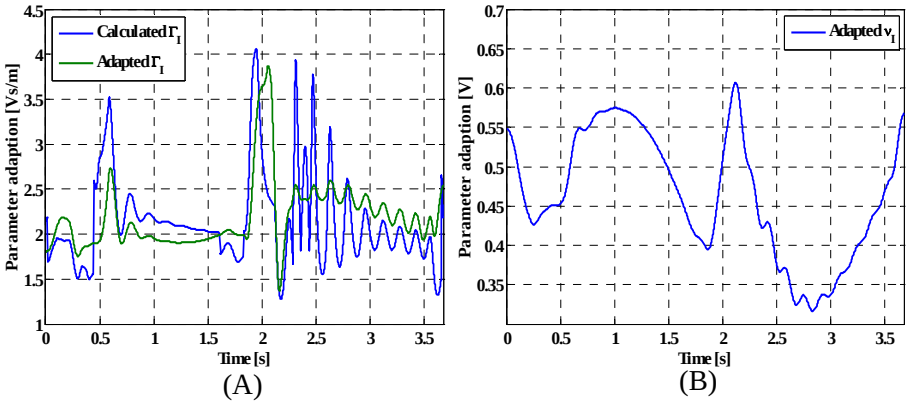

Figure 9.3: MAIDC scheme implemented on HSS I. (A) Adaption of $\hat{\Gamma}_I$. (B) Adaption of $\hat{\nu}_I$.

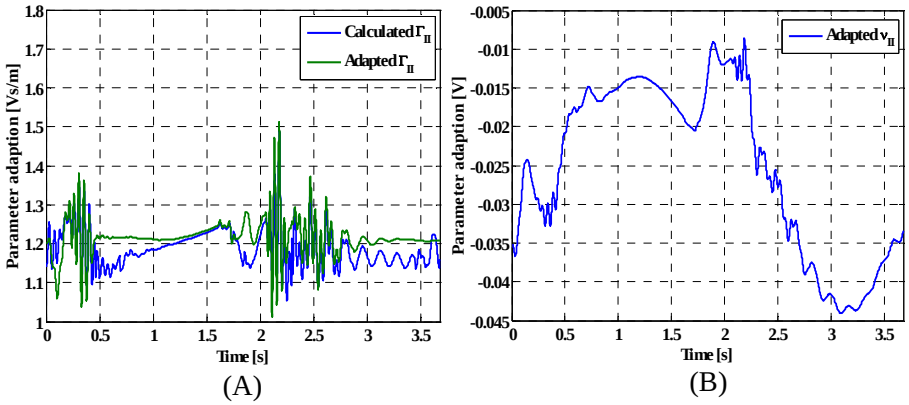

Figure 9.4: MAIDC scheme implemented on HSS II. (A) Adaption of $\hat{\Gamma}_{II}$. (B) Adaption of $\hat{\nu}_{II}$.

9.9.2 MAAC

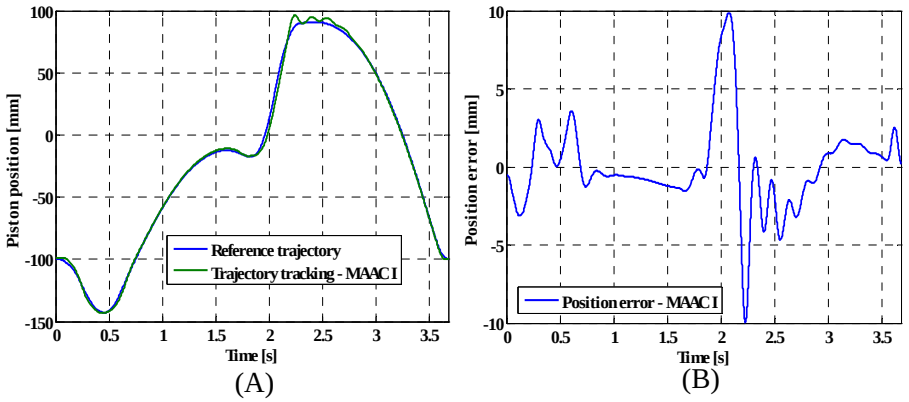

Figure 9.5: MAAC scheme implemented on HSS I. (A) Trajectory tracking. (B) Tracking error.

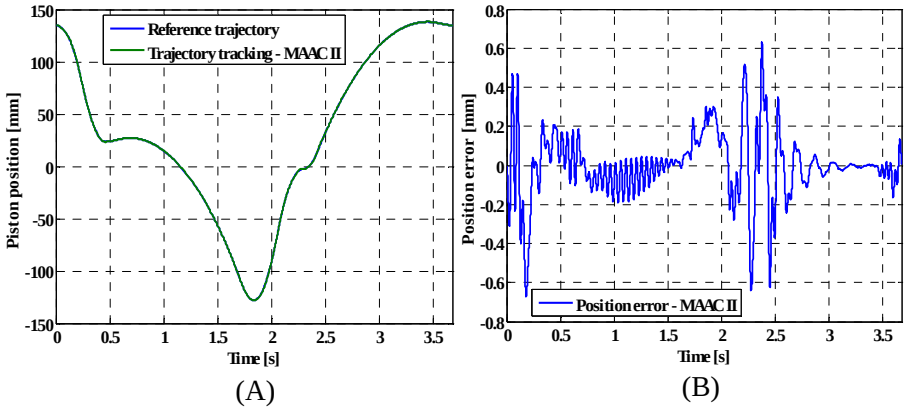

Figure 9.6: MAAC scheme implemented on HSS II. (A) Trajectory tracking. (B) Tracking error.

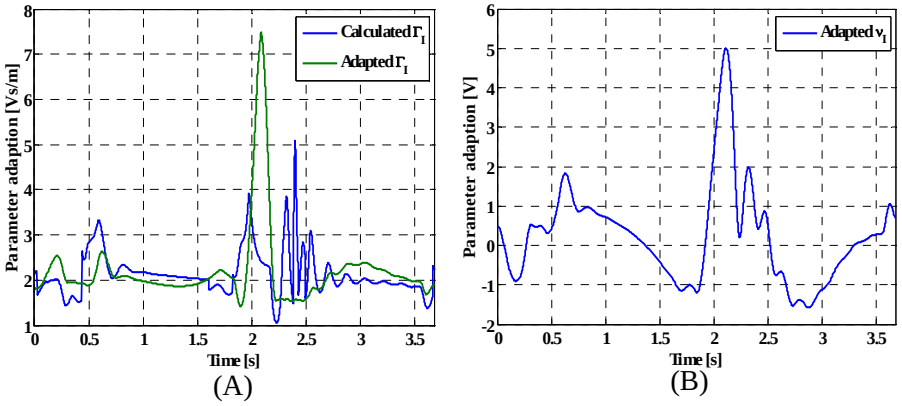

Figure 9.7: MAAC scheme implemented on HSS I. (A) Adaption of $\hat{\Gamma}_I$. (B) Adaption of $\hat{\nu}_I$.

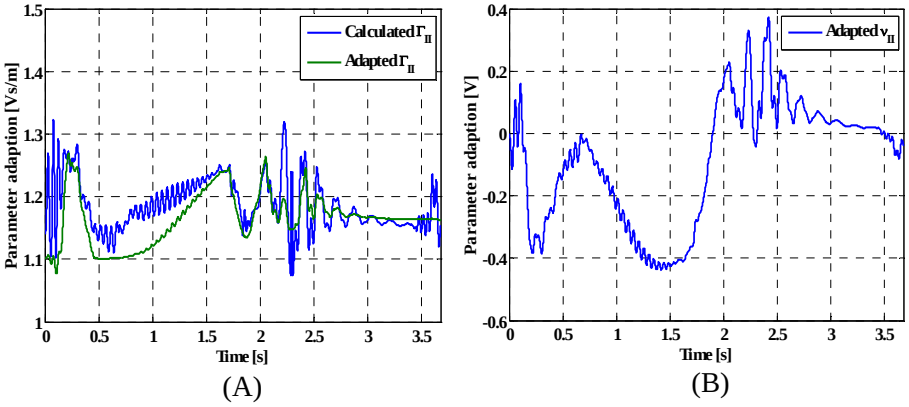

Figure 9.8: MAAC scheme implemented on HSS II. (A) Adaption of $\hat{\Gamma}_{II}$. (B) Adaption of $\hat{\nu}_{II}$.

9.9.3 Tracking errors - (RECT)

Compensator	$\lvert e_{maxI} \rvert$ $[mm]$	e_{rmsI} $[mm]$	$\lvert e_{maxII} \rvert$ $[mm]$	e_{rmsII} $[mm]$
MAIDC	4.00	1.59	1.15	0.23
MAAC	10.00	2.82	0.65	0.17

Table 9.1: Tracking error values for controllers tested on the rectangular trajectory.

The simulation results for the IOT, along with their errors are found in appendix M.

9.10 Experimental Results

When implemented on the physical system, the tuned controller parameters obtained on the on linear model have been scaled down in order to make the controllers function. This may be due to possibly un-modeled higher order dynamics, which effects are not shown when simulating the model. When implementing the MAIDC and MAAC it is found from figures 9.9, 9.10, 9.11 and 9.12 that the results resembles those of the simulations, however with increased errors. Particularly the experiments regarding actuator II shows decreased tracking performance. The project group considers this, to a large extend, to be due parameter tuning, and it is found that it may be possible to achieve increased performance, if more time is used on parameter tuning.

9.10.1 MAIDC

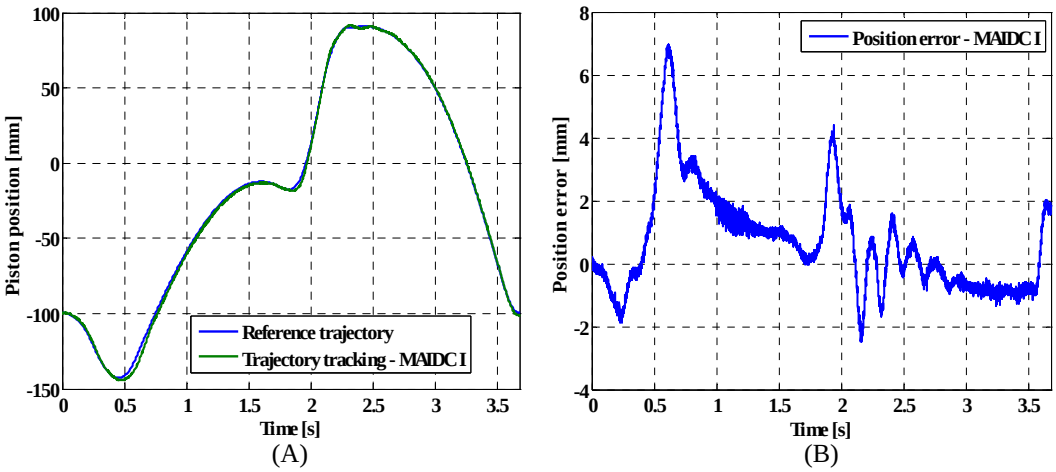

Figure 9.9: MAIDC scheme implemented on HSS I. (A) Trajectory tracking. (B) Tracking error.

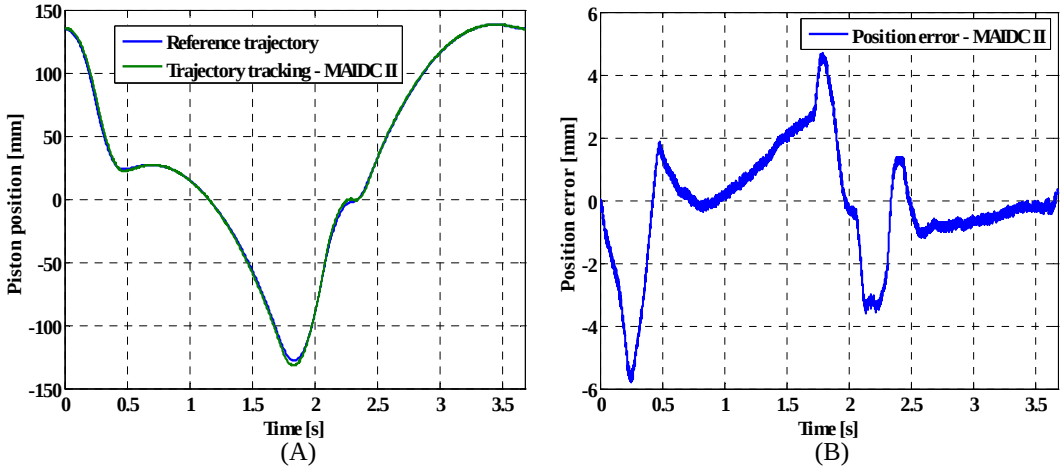

Figure 9.10: MAIDC scheme implemented on HSS II. (A) Trajectory tracking. (B) Tracking error.

9.10.2 MAAC

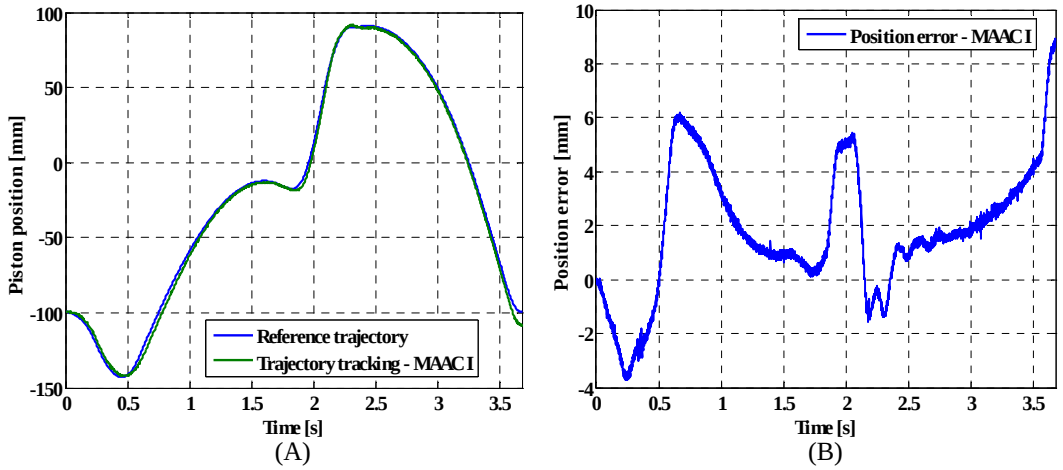

Figure 9.11: MAAC scheme implemented on HSS I. (A) Trajectory tracking. (B) Tracking error.

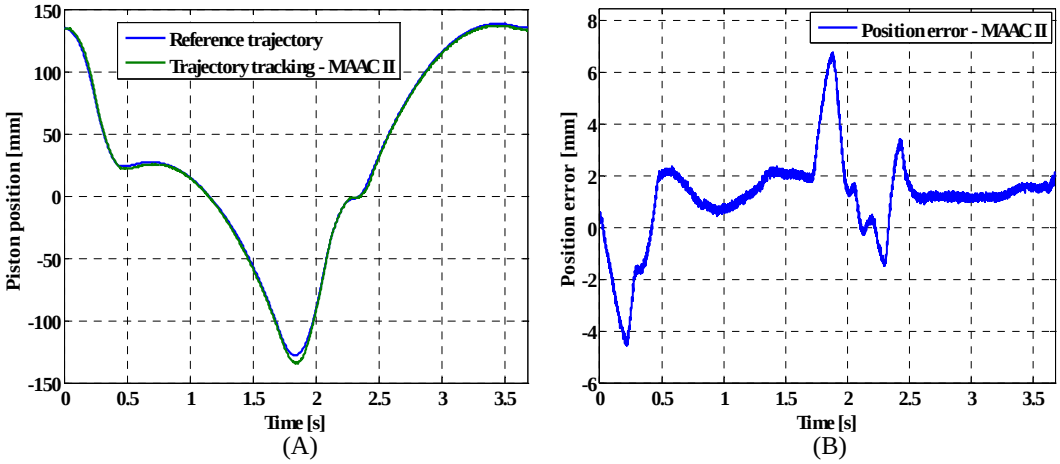

Figure 9.12: MAAC scheme implemented on HSS II. (A) Trajectory tracking. (B) Tracking error.

9.10.3 Tracking Errors - (RECT)

Compensator	$\lvert e_{maxI} \rvert$ $[mm]$	e_{rmsI} $[mm]$	$\lvert e_{maxII} \rvert$ $[mm]$	e_{rmsII} $[mm]$
MAIDC	6.97	1.80	5.77	1.82
MAAC	8.73	3.03	6.62	2.05

Table 9.2: Tracking error values for controllers tested on the rectangular trajectory.

9.11 Summary

In this chapter first a non-adaptive robust model based controller (RMC) has been presented and proved stable. This was hence used as base for the adaptive control schemes. Then various control and adaptive laws has been presented and proved stable, and robust adaption laws were presented, but not proved stable. The adaptive control schemes AIDC, MAIDC and RAIDC utilizes the same control law as the RMC. In the augmented adaptive control schemes AAC, MAAC and RAAC, the control law of the RMC were altered such that an extra proportional + integral term were added. All controllers established in this chapter has been implemented in simulation (except the RMC), and the MAIDC and MAAC has also been implemented on the physical system. When implemented on the physical system, the MAIDC and MAAC showed performance similar to the simulations. However, in general, when implemented on the physical system, slightly decreased performance were achieved compared to simulation, and this is found to be due to various modeling errors and parameter tuning.

Chapter 10

Adaptive Robust Control Scheme (ARC)

Contents

This chapter concerns the establishment of an adaptive robust controller (ARC) suitable to take into account the effect of various uncertainties, disturbances etc.

10.1 Introduction

On the physical system, both parametric uncertainties such as varying inertia load, variations of bulk modulus due to temperature changes and varying pressure, and uncertain non-linearities, such as external disturbances, un-modeled leakage and friction, occurs. In the design phase of this ARC, an initiative to compensate for these uncertainties is carried out. The controller established is a modified version of an ARC, called a discontinuous projection based adaptive robust controller[Yao et al., 2001]. The controller is established based on the complete hydraulic actuator model, and the design approach used is partly adaptive backstepping control design. In the following the index i is omitted.

10.2 Model used in Design Phase

In the model used in the design phase, proposed by [Yao et al., 2001], the servo valve dynamics is described by a third order system, where the complex conjugated poles are sufficiently fast to be neglected. However, for the servo valves implemented on the physical system object for this thesis, the servo valve dynamics is approximated by a second system, constituted by poles sufficiently fast to be neglected in the control design phase. In order to avoid redoing the proof developed by [Yao et al., 2001], it is assumed that the first order dynamics for the servo valve is present.

In the treatment of the ARC controller, the inertia load dynamics of the system is described by equation 10.1, where $\tilde{f}(t, x_P, \dot{x}_P)$ represents the external disturbances and un-modeled friction forces.

$$M_{eq}\ddot{x}_P = P_L A - b\dot{x}_P - F_C(\dot{x}_P) + \tilde{f}(t, x_P, \dot{x}_P) \tag{10.1}$$

The actuator dynamics is described by equation 10.2:

$$\frac{V_t}{4\beta_F}\dot{P}_L = -A\dot{x}_P - C_L P_L + Q_L \tag{10.2}$$

The load flow Q_L is given by 10.3:

$$Q_L = C_d w x_v \sqrt{\frac{P_S - sign(x_v)P_L}{\rho}} \tag{10.3}$$

The relation between the spool valve displacement and the input voltage is given by equation 10.4.

$$\tau_v \dot{x}_v = -x_v + K_v u_v \tag{10.4}$$

As seen from equation 10.4 the spool valve / input voltage relation is described by a first order system where τ_v and K_v is the servo valve time constant and gain, respectively. When implementing the controller for simulation purposes numerical errors may arise according to [Yao et al., 2001], and in order to minimize this phenomena scaling factors are used to scale the valve opening and the load pressure, by $\bar{x}_v = \frac{x_v}{S_c 4}$ and $\bar{P}_L = \frac{P_L}{S_c 3}$, respectively. By including the scaling factors and rewriting the system equations the equations take the form of 10.5:

$$\begin{aligned}
\ddot{x}_P &= \frac{AS_{c3}}{M_{eq}}\left(\bar{P}_L - \frac{b}{AS_{c3}}\dot{x}_P - \frac{F_C(x_P)}{AS_{c3}}\right) + d(t, x_P, \dot{x}_P) \\
\dot{\bar{P}}_L &= \frac{4\beta_F}{V_t}\frac{S_{c4}}{\sqrt{S_{c3}}}\frac{C_d w}{\sqrt{\rho}}\left(-\frac{A}{S_{c4}\sqrt{S_{c3}}}\frac{\sqrt{\rho}}{C_d w}\dot{x}_P - \frac{\sqrt{S_{c3}}}{S_{c4}}\frac{\sqrt{\rho}}{C_d w}C_L\bar{P}_L + g_3(\bar{P}_L, \bar{x}_v)\bar{x}_v\right) \\
\dot{\bar{x}}_v &= -\frac{1}{\tau_v}x_4 + \frac{K_v}{S_{c4}\tau_v}u_v
\end{aligned} \tag{10.5}$$

Where, $d = \frac{1}{M_{eq}}\tilde{f}(t, x_P, \dot{x}_P)$, $g_3(\bar{P}_L, \bar{x}_v) = \sqrt{\bar{P}_S - sign(x_v)\bar{P}_L}$ and $\bar{P}_S = \frac{P_S}{S_{c3}}$. The system is now formulated in state space, with the states defined as:

$$x_1 = x_P \quad , \quad x_2 = \dot{x}_P \quad , \quad x_3 = \bar{P}_L \quad , \quad x_4 = \bar{x}_v \tag{10.6}$$

Hence the state space representation of the system, is given as:

$$\dot{x}_1 = x_2 \tag{10.7}$$

$$\begin{aligned}
\dot{x}_2 &= \frac{AS_{c3}}{m}(x_3 - \bar{b}x_2 - \bar{F}_C) + d(t, x_1, x_2) \\
\dot{x}_3 &= \frac{4\beta_F}{V_t}\frac{S_{c4}}{\sqrt{S_{c3}}}\frac{C_d w}{\sqrt{\rho}}[-\bar{A}x_2 - \bar{C}_L x_3 + g_3 x_4]
\end{aligned} \tag{10.8}$$

$$\dot{x}_4 = -\frac{1}{\tau_v}x_4 + \frac{\bar{K}_v}{\tau_v}u_v$$

Where:

$$\bar{b} = \frac{1}{AS_{c3}}b \quad , \quad \bar{F}_C = \frac{1}{AS_{c3}}F_C \quad , \quad \bar{A} = \frac{1}{S_{c4}\sqrt{S_{c3}}}\frac{\sqrt{\rho}}{C_d w}A \quad , \tag{10.9}$$

$$\bar{C}_L = \frac{\sqrt{S_{c3}}}{S_{c4}}\frac{\sqrt{\rho}}{C_d w}C_L \quad , \quad \bar{K}_v = \frac{1}{S_{c4}}K_v \tag{10.10}$$

In order to reduce parametric uncertainties of bulk modlus β_F, the inertia load M_{eq} and the nominal value of the disturbance d (henceforward designated d_n), the state space equations in 10.7 are linearized and parameterized. The unknown parameter set $\theta = [\theta_1, \theta_2, \theta_3]^T$ is defined as:

$$\theta_1 = \frac{AS_{c3}}{m} \quad , \quad \theta_2 = d_n \quad , \quad \theta_3 = \frac{4\beta_F}{V_t}\frac{S_{c4}}{\sqrt{S_{c3}}}\frac{C_d w}{\sqrt{\rho}} \tag{10.11}$$

The state space equations resulting from the linearization, parameterization and defining $\tilde{d} = d(t, x_1, x_2) - d_n$, is given by:

$$\dot{x}_1 = x_2 \tag{10.12}$$

$$\dot{x}_2 = \theta_1(x_3 - \bar{b}x_2 - \bar{F}_C(x_2)) + \theta_2 + \tilde{d}(t, x_1, x_2) \tag{10.13}$$

$$\dot{x}_3 = \theta_3[-\bar{A}x_2 - \bar{C}_L x_3 + g_3(x_3, x_4)x_4] \tag{10.14}$$

$$\dot{x}_4 = -\frac{1}{\tau_v}x_4 + \frac{\bar{K}_v}{\tau_v}u \tag{10.15}$$

It is assumed that the bounds of 10.16 holds true.

$$\theta \in \Omega_\theta = \{\theta : \theta_{min} < \theta < \theta_{max}\} \tag{10.16}$$
$$\mid \tilde{d}(t, x_1, x_2) \mid \leq \delta_d(x_1, x_2, t)$$

where: $\theta_{min} = [\theta_{1min}, \theta_{2min}, \theta_{3min}]^T$, $\theta_{max} = [\theta_{1max}, \theta_{2max}, \theta_{3max}]^T$ and $\delta_d(t, x_1, x_2)$ are known. The adaption law proposed by [Yao et al., 2001], is given by:

$$\dot{\hat{\theta}} = Proj_{\hat{\theta}}(\Gamma\tau) \tag{10.17}$$

where $\Gamma > 0$ describes a constant diagonal matrix, τ is an adaption function and $Proj$ is a discontinuous projection given by:

$$Proj_{\hat{\theta}}(\bullet) = \begin{cases} 0 \;\; if \;\; \hat{\theta}_i = \theta_{imax} \;\; and \;\; \bullet > 0 \\ 0 \;\; if \;\; \hat{\theta}_i = \theta_{imin} \;\; and \;\; \bullet < 0 \\ \bullet \;\; otherwise \end{cases} \tag{10.18}$$

Here $\hat{\theta}$ is the estimate of θ, and $\tilde{\theta}$ is the estimation error given by $\tilde{\theta} = \hat{\theta} - \theta$. Bounds on the projection $Proj_{\hat{\theta}}$ are given by (according to [Yao et al., 2001]):

$$\hat{\theta} \in \bar{\Omega}_\theta = \{\hat{\theta} : \theta_{min} \leq \hat{\theta} \leq \theta_{max}\} \tag{10.19}$$

$$\tilde{\theta}^T(\Gamma^{-1}Proj_{\hat{\theta}}(\Gamma\tau) - \tau) \leq 0, \;\; \forall\tau \tag{10.20}$$

The parts of $\dot{x}_2$ and $\dot{x}_3$ that can be calculated are given by $\hat{\dot{x}}_2$ and $\hat{\dot{x}}_3$, respectively, and given by expressions 10.21.

$$\begin{aligned}\hat{\dot{x}}_2 &= \hat{\theta}_1(x_3 - \bar{b}x_2 - \bar{F}_C(x_2)) + \hat{\theta}_2 \\ \hat{\dot{x}}_3 &= \hat{\theta}_3[-\bar{A}x_2 - \bar{C}_L x_3 + g_3(x_3, x_4)x_4]\end{aligned} \tag{10.21}$$

10.3 Control Design

In the following the control design will be accounted for. This is carried out according to [Yao et al., 2001]. The control design is carried out in three steps - first a Lyapunov function is established for the first two states x_1 and x_2 directly. Following this, Lyapunov functions are established first, and the control laws are thus found in a way similar to the backstpping design approach[Yao et al., 2001]. In the following, notations ($\bullet$) will be omitted.

10.3.1 Step 1

The error dynamics denoted by z_2 is given by equation 10.22:

$$z_2 = \dot{e}_1 + k_p e_1 \tag{10.22}$$

Where $e_1 = x_1 - x_{1R}$ is the tracking position error. x_1 is the actual position, x_{1R} is the desired position and k_p is a positive feedback gain. Defining $x_{2eq} = \dot{x}_{1R} - k_p e_1$, the error dynamics is rewritten as:

$$z_2 = x_2 - x_{2eq} \tag{10.23}$$

Laplace transforming equation 10.22 yields,

$$\begin{aligned} z_2 &= \dot{e}_1 + k_p e_1 \\ z_2 &= e_1 s + k_p e_1 \\ z_2 &= e_1(s + k_p) \\ \frac{e_1(s)}{z_2(s)} &= \frac{1}{s + k_p} \end{aligned} \tag{10.24}$$

Since 10.24 is a stable transfer function, then if the input z_2 is bounded the output e_1 will also be bounded. Hence if the input converges to zero the output will also converge to zero as time goes to infinity. Then in the following the objective will be to make z_2 become as small as possible, in order to make the error e_1 as small as possible.

Differentiating 10.23 and substituting equation 10.13, yields:

$$\dot{z}_2 = \dot{x}_2 - \dot{x}_{2eq} = \theta_1(x_3 - \bar{b}x_2 - \bar{F}_C) + \theta_2 + \tilde{d} - \dot{x}_{2eq} \ , \ \dot{x}_{2eq} = \ddot{x}_{1R} - k_p \dot{e}_1 \tag{10.25}$$

A virtual control law α making z_2 small can be chosen for x_3 (according to [Yao et al., 2001]),

and is given by 10.26:

$$\alpha_2(x_1, x_2, \hat{\theta}_1, \hat{\theta}_2, t) = \alpha_{2a} + \alpha_{2s} = \alpha_{2a} + \alpha_{2s1} + \alpha_{2s2} \tag{10.26}$$

Where:

$$\alpha_{2a} = \bar{b}x_2 + \bar{F}_C + \frac{1}{\hat{\theta}_1}(\dot{x}_{2eq} - \hat{\theta}_2) \quad , \quad \alpha_{2s1} = -k_{2s1}z_2 \quad , \quad \alpha_{2s2} = -\frac{h_2}{2\theta_{1min}\varepsilon_2}z_2 \tag{10.27}$$

For a more detailed description of the elements of the control law in expression 10.26, see appendix N.1.

Defining the input discrepancy between x_3 and the control function α_2 by $z_3 = x_3 - \alpha_2$, and substituting into expression 10.25, yields:

$$\begin{aligned}
\dot{z}_2 &= \theta_1(x_3 - \bar{b}x_2 - \bar{F}_C) + \theta_2 + \tilde{d} - \dot{x}_{2eq} \\
&= \theta_1 x_3 - \theta_1\bar{b}x_2 - \theta_1\bar{F}_C + \theta_2 + \tilde{d} - \dot{x}_{2eq} \\
&= \theta_1(z_3 + \alpha_2) - \theta_1\bar{b}x_2 - \theta_1\bar{F}_C + \theta_2 + \tilde{d} - \dot{x}_{2eq} \\
&= \theta_1(z_3 + \alpha_{2a} + \alpha_{2s}) - \theta_1\bar{b}x_2 - \theta_1\bar{F}_C + \theta_2 + \tilde{d} - \dot{x}_{2eq} \\
&= \theta_1 z_3 + \theta_1\alpha_{2s} + \theta_1(\alpha_{2a} - \bar{b}x_2 - \bar{F}_C) + \theta_2 + \tilde{d} - \dot{x}_{2eq}
\end{aligned} \tag{10.28}$$

Noting that $\tilde{\theta} = \hat{\theta} - \theta \Rightarrow \theta = \hat{\theta} - \tilde{\theta}$, yields:

$$\dot{z}_2 = \theta_1 z_3 + \theta_1\alpha_{2s} + \hat{\theta}_1(\alpha_{2a} - \bar{b}x_2 - \bar{F}_C) - \tilde{\theta}_1(\alpha_{2a} - \bar{b}x_2 - \bar{F}_C) + \theta_2 + \tilde{d} - \dot{x}_{2eq} \tag{10.29}$$

Knowing that α_{2a} is given as $\alpha_{2a} = \bar{b}x_2 + \bar{F}_C + \frac{1}{\hat{\theta}_1}(\dot{x}_{2eq} - \hat{\theta}_2)$, yields:

$$\begin{aligned}
\dot{z}_2 &= \theta_1 z_3 + \theta_1\alpha_{2s} + \hat{\theta}_1(\frac{1}{\hat{\theta}_1}(\dot{x}_{2eq} - \hat{\theta}_2)) - \tilde{\theta}_1(\alpha_{2a} - \bar{b}x_2 - \bar{F}_C) + \theta_2 + \tilde{d} - \dot{x}_{2eq} \\
&= \theta_1 z_3 + \theta_1\alpha_{2s} - \hat{\theta}_2 - \tilde{\theta}_1(\alpha_{2a} - \bar{b}x_2 - \bar{F}_C) + \theta_2 + \tilde{d}
\end{aligned} \tag{10.30}$$

Knowing that $\alpha_{2s} = \alpha_{2s1} + \alpha_{2s2}$ where $\alpha_{2s1} = -k_{2s1}z_2$, yields:

$$\dot{z}_2 = \theta_1 z_3 + \theta_1(\alpha_{2s2} - k_{2s1}z_2) - \tilde{\theta}_2 - \tilde{\theta}_1(\alpha_{2a} - \bar{b}x_2 - \bar{F}_C) + \theta_2 + \tilde{d} \tag{10.31}$$

The following vector is defined:

$$\phi_2 = \begin{bmatrix} \alpha_{2a} - \bar{x}_2 - \bar{F}_C \\ 1 \\ 0 \end{bmatrix} \tag{10.32}$$

Then $\dot{z}_2$ can be written as:

$$\dot{z}_2 = \theta_1 z_3 + \theta_1\alpha_{2s2} - \theta_1 k_{2s1}z_2 - \tilde{\theta}^T\phi_2 + \tilde{d} \tag{10.33}$$

Now a positive semi-definite Lyapunov function V_2 is defined.

$$V_2 = \frac{1}{2} w_2 z_2^2 \quad ; \quad w_2 > 0 \tag{10.34}$$

With the time derivative:

$$\dot{V}_2(z_2) = w_2 z_2 \dot{z}_2 \tag{10.35}$$

Substituting expression 10.28, yields:

$$\begin{aligned} \dot{V}_2 &= w_2 z_2 \dot{z}_2 \\ &= w_2 z_2 (\theta_1 z_3 + \theta_1 \alpha_{2s2} - \theta_1 k_{2s1} z_2 - \tilde{\theta}^T \phi_2 + \tilde{d}) && (10.36) \\ &= w_2 \theta_1 z_2 z_3 + w_2 z_2 (\theta_1 \alpha_{2s2} - \tilde{\theta}^T \phi_2 + \tilde{d}) - w_2 \theta_1 k_{2s1} z_2^2 && (10.37) \end{aligned}$$

The above Lyapunov function is in itself not proved stable, but as it will be shown in the following, by establishing an overall Lyapunov function composed of the above expression and Lyapunov functions for the remaining states, it is possible to proof stability. Hence this step has been completed, and step 2 can be initiated.

10.3.2 Step 2

In this step a virtual control law for α_3 is developed for $\bar{Q}_L$ such that x_3 tracks the control function α_2 developed in Step 1. Like the control function α_2 in Step 1 the control function α_3 also consists of two parts as shown in equation 10.38, and is chosen according to [Yao et al., 2001]:

$$\alpha_3(\bar{x}_3, \hat{\theta}, t) = \alpha_{3a} + \alpha_{3s} \tag{10.38}$$

The time derivative of 10.38, is given by:

$$\begin{aligned} \dot{\alpha}_2 &= \dot{\alpha}_{2c} + \dot{\alpha}_{2u} \\ &= \frac{\partial \alpha_2}{\partial x_1} x_2 + \frac{\partial \alpha_2}{\partial x_2} \dot{x}_2 + \frac{\partial \alpha_2}{\partial \hat{\theta}} \dot{\hat{\theta}} + \frac{\partial \alpha_2}{\partial t} && (10.39) \\ &= \frac{\partial \alpha_2}{\partial x_1} x_2 + \frac{\partial \alpha_2}{\partial x_2} \dot{\hat{x}}_2 - \frac{\partial \alpha_2}{\partial x_2} \dot{\tilde{x}}_2 + \frac{\partial \alpha_2}{\partial \hat{\theta}} \dot{\hat{\theta}} + \frac{\partial \alpha_2}{\partial t} && (10.40) \end{aligned}$$

Here $\dot{\alpha}_{2c}$ is the calculable part and $\dot{\alpha}_{2u}$ is the incalculable part due to various uncertainties. Hence these are obtained as:

$$\dot{\alpha}_{2c} = \frac{\partial \alpha_2}{\partial x_1} x_2 + \frac{\partial \alpha_2}{\partial x_2} \dot{\hat{x}}_2 + \frac{\partial \alpha_2}{\partial t} \tag{10.41}$$

$$\dot{\alpha}_{2u} = \frac{\partial \alpha_2}{\partial x_2} (-\dot{\tilde{x}}_2) + \frac{\partial \alpha_2}{\partial \hat{\theta}} \dot{\hat{\theta}} = \frac{\partial \alpha_2}{\partial x_2} \tilde{\theta}_1 [-(x_3 - \bar{b} x_2 - \bar{F}_C) - \tilde{\theta}_2 + \tilde{d}] + \frac{\partial \alpha_2}{\partial \hat{\theta}} \dot{\hat{\theta}} \tag{10.42}$$

In the following an initiative to deal with the incalculable part $\dot{\alpha}_{2u}$, is taken. Taking the time derivative of the previously defined $z_3 = x_3 - \alpha_2$, yields:

$$\dot{z}_3 = \dot{x}_3 - \dot{\alpha}_2 \tag{10.43}$$

Substituting the state equation $\dot{x}_3 = \dot{P}_L$, yields:

$$\dot{z}_3 = \theta_3(-\bar{A}x_2 - \bar{C}_L x_3 + g_3 x_4) - \dot{\alpha}_{2c} - \dot{\alpha}_{2u} \tag{10.44}$$
$$= \theta_3(-\bar{A}x_2 - \bar{C}_L x_3 + \bar{Q}_L) - \dot{\alpha}_{2c} - \dot{\alpha}_{2u} \tag{10.45}$$

Defining $z_4 = \bar{Q}_L - \alpha_3 \;\Rightarrow\; \bar{Q}_L = z_4 + \alpha_3$, and substituting, yields:

$$\dot{z}_3 = \theta_3(-\bar{A}x_2 - \bar{C}_L x_3 + z_4 + \alpha_3) - \dot{\alpha}_{2c} - \dot{\alpha}_{2u} \tag{10.46}$$
$$= \theta_3 z_4 + \theta_3(-\bar{A}x_2 - \bar{C}_L x_3 + \alpha_3) - \dot{\alpha}_{2c} - \dot{\alpha}_{2u} \tag{10.47}$$

Now the Lyapunov candidate, regarding the third state equation, is established. The Lyapunov candidate is chosen as [Yao et al., 2001]:

$$V_3 = V_2 + \frac{1}{2} w_3 z_3^2 \quad ; \quad w_3 > 0 \tag{10.48}$$

Taking the time derivative, yields:

$$\dot{V}_3 = \theta_1 w_2 z_2 z_3 + \dot{V}_2|_{\alpha_2} + w_3 z_3 \tag{10.49}$$

Here $\dot{V}_2|_{\alpha_2}$ denotes $\dot{V}_2$ under the condition that $x_3 = \alpha_3$, which yields $z_3 = 0$. Substituting the expression for $\dot{z}_3$, yields:

$$\dot{V}_3 = \theta_1 w_2 z_2 z_3 + \dot{V}_2|_{\alpha_2} + w_3 z_3 \left(\theta_3 z_4 + \theta_3(-\bar{A}x_2 - \bar{C}_L x_3 + \alpha_3) - \dot{\alpha}_{2c} - \dot{\alpha}_{2u}\right) \tag{10.50}$$
$$= \theta_3 w_3 z_3 z_4 + \dot{V}_2|_{\alpha_2} + w_3 z_3 \left(\frac{w_2}{w_3}\theta_1 z_2 + \theta_3(-\bar{A}x_2 - \bar{C}_L x_3 + \alpha_3) - \dot{\alpha}_{2c} - \dot{\alpha}_{2u}\right)$$

Substituting the expression for $\dot{\alpha}_{2u}$, yields:

$$\dot{V}_3 = \theta_3 w_3 z_3 z_4 + \dot{V}_2|_{\alpha_2} + w_3 z_3 (\frac{w_2}{w_3}\theta_1 z_2 + \theta_3(-\bar{A}x_2 - \bar{C}_L x_3 + \alpha_3) - \dot{\alpha}_{2c} \tag{10.51}$$
$$- \frac{\partial \alpha_2}{\partial x_2}(-(x_3 - \bar{b}x_2 - \bar{F}_C)\tilde{\theta}_1 - \tilde{\theta}_2 + \tilde{d}) + \frac{\partial \alpha_2}{\partial \hat{\theta}}\dot{\hat{\theta}})$$
$$= \theta_3 w_3 z_3 z_4 + \dot{V}_2|_{\alpha_2} + w_3 z_3 \theta_3 \alpha_3 + w_3 z_3 (\frac{w_2}{w_3}\theta_1 z_2 + \theta_3(-\bar{A}x_2 - \bar{C}_L x_3) - \dot{\alpha}_{2c}$$
$$- \frac{\partial \alpha_2}{\partial x_2}(-(x_3 - \bar{b}x_2 - \bar{F}_C)\tilde{\theta}_1 - \tilde{\theta}_2 + \tilde{d}) + \frac{\partial \alpha_2}{\partial \hat{\theta}}\dot{\hat{\theta}})$$

Using the error estimate $\tilde{\theta} = \hat{\theta} - \theta \;\Rightarrow\; \theta = \hat{\theta} - \tilde{\theta}$, yields:

$$\dot{V}_3 = \theta_3 w_3 z_3 z_4 + \dot{V}_2|_{\alpha_2} + w_3 z_3 \theta_3 \alpha_3 + w_3 z_3 (\frac{w_2}{w_3}\hat{\theta}_1 z_2 + \hat{\theta}_3(-\bar{A}x_2 - \bar{C}_L x_3) \tag{10.52}$$
$$- \frac{w_2}{w_3}\tilde{\theta}_1 z_2 - \tilde{\theta}_3(-\bar{A}x_2 - \bar{C}_L x_3) - \dot{\alpha}_{2c} - \frac{\partial \alpha_2}{\partial x_2}(-(x_3 - \bar{b}x_2 - \bar{F}_C)\tilde{\theta}_1 - \tilde{\theta}_2 + \tilde{d}) + \frac{\partial \alpha_2}{\partial \hat{\theta}}\dot{\hat{\theta}})$$

Considering the third term of the right hand side of the above expression, and using that $\alpha_3 = \alpha_{3a} + \alpha_{3s}$, yields:

$$w_3 z_3 \theta_3 \alpha_3 = w_3 z_3 \theta_3 \alpha_{3s} + w_3 z_3 \theta_3 \alpha_{3a} \tag{10.53}$$

Using that $\theta = \hat{\theta} - \tilde{\theta}$, gives:

$$w_3 z_3 \theta_3 \alpha_3 = w_3 z_3 \theta_3 \alpha_{3s} + w_3 z_3 \hat{\theta}_3 \alpha_{3a} - w_3 z_3 \tilde{\theta}_3 \alpha_{3a} \tag{10.54}$$

Substituting into equation 10.52, yields:

$$\begin{aligned}\dot{V}_3 = {} & \theta_3 w_3 z_3 z_4 + \dot{V}_2|_{\alpha_2} + w_3 z_3 \theta_3 \alpha_{3s} + w_3 z_3 (\frac{w_2}{w_3}\hat{\theta}_1 z_2 + \hat{\theta}_3(-\bar{A}x_2 - \bar{C}_L x_3 + \alpha_{3a}) \\ & - \frac{w_2}{w_3}\tilde{\theta}_1 z_2 - \tilde{\theta}_3(-\bar{A}x_2 - \bar{C}_L x_3 - \alpha_{3a}) - \dot{\alpha}_{2c} - \frac{\partial \alpha_2}{\partial x_2}(-(x_3 - \bar{b}x_2 - \bar{F}_C)\tilde{\theta}_1 - \tilde{\theta}_2 \\ & + \tilde{d}) + \frac{\partial \alpha_2}{\partial \hat{\theta}}\dot{\hat{\theta}})\end{aligned} \tag{10.55}$$

Defining the expression:

$$\alpha_{3e} = \frac{w_2}{w_3}\hat{\theta}_1 z_2 + \hat{\theta}_3(-\bar{A}x_2 - \bar{C}_L x_3) - \dot{\alpha}_{2c} \tag{10.56}$$

And the vector:

$$\phi_3 = \begin{bmatrix} \frac{w_2}{w_3} z_2 - \frac{\partial \alpha_2}{\partial x_2}(-(x_3 - \bar{b}x_2 - \bar{F}_C) \\ -\frac{\partial \alpha_2}{\partial x_2} \\ -\bar{A}x_2 - \bar{C}_L x_3 + \alpha_{3a} \end{bmatrix} \tag{10.57}$$

Then expression 10.55 can be written as:

$$\begin{aligned}\dot{V}_3 = {} & \theta_3 w_3 z_3 z_4 + \dot{V}_2|_{\alpha_2} + w_3 z_3 \theta_3 \alpha_{3s} \\ & + w_3 z_3 \left(\hat{\theta}_3 \alpha_{3a} + \alpha_{3e} - \tilde{\theta}^T \phi_3 - \frac{\partial \alpha_2}{\partial x_2}\tilde{d} - \frac{\partial \alpha_2}{\partial \hat{\theta}}\dot{\hat{\theta}}\right)\end{aligned} \tag{10.58}$$

The control law α_3 is chosen as[Yao et al., 2001]:

$$\begin{aligned}\alpha_3 = \alpha_{3a} + \alpha_{3s} = \alpha_{3a} + \alpha_{3s1} + \alpha_{3s2} \qquad & \text{where,} \\ \alpha_{3a} = -\frac{1}{\hat{\theta}_3}\alpha_{3e} \quad , \quad \alpha_{3s1} = -K_{3s1} z_3 \quad , \quad & \alpha_{3s1} = -\frac{1}{2\theta_{3min}} h_3 z_3\end{aligned} \tag{10.59}$$

The coefficients of the above control law is accounted for according to [Yao et al., 2001], and are given in appendix N.2. Substituting into expression 10.58, yields:

$$\dot{V}_3 = \theta_3 w_3 z_3 z_4 + \dot{V}_2|_{\alpha_2} + w_3 z_3 \left(\theta_3 \alpha_{3s2} - \tilde{\theta}^T \phi_3 - \frac{\partial \alpha_2}{\partial x_2}\tilde{d}\right) - \theta_3 w_3 K_{3s1} z_3^2 - w_3 z_3 \frac{\partial \alpha_2}{\partial \hat{\theta}}\dot{\hat{\theta}} \tag{10.60}$$

The second step of the control design has now been completed, and the third step can be carried out.

10.3.3 Step 3

In this step, the control law for the valve input u_v is established. This is carried out such that $\bar{Q}_L$ tracks the control law established in step 2, and can be carried out by step 2, where the control law was determined based on the time derivative of the Lyapunov

candidate. However, as $\bar{Q}_L$ contains $sign(x_4)$, $\bar{Q}_L$ is not continuous at $x_4 = 0$, and hence is not differentiable. However, according to [Yao et al., 2001], it is possible to proceed the control design by noting that $\bar{Q}_L$ is differentiable anywhere except at the singular point of $x_4 = 0$ and is continuous anywhere.

Similar to the previous step, the positive semi-definite Lyapunov candidate is chosen as[Yao et al., 2001]:

$$V_4 = V_3 + \frac{1}{2} w_4 z_4^2 \quad ; \quad w_4 > 0 \tag{10.61}$$

Taking the time derivative, yields:

$$\dot{V}_4 = \theta_3 w_3 z_3 z_4 + \dot{V}_3|_{\alpha_3} + w_4 z_4 \dot{z}_4 \tag{10.62}$$

Using that:

$$z_4 = \bar{Q}_L - \alpha_3 \;\Rightarrow\; \dot{z}_4 = \dot{\bar{Q}}_L - \dot{\alpha}_3 \tag{10.63}$$

And substituting into 10.62, yields:

$$\dot{V}_4 = \theta_3 w_3 z_3 z_4 + \dot{V}_3|_{\alpha_3} + w_4 z_4 (\dot{\bar{Q}}_L - \dot{\alpha}_3) \tag{10.64}$$

$$= \dot{V}_3|_{\alpha_3} + w_4 z_4 (\theta_3 \frac{w_3}{w_4} z_3 + \dot{\bar{Q}}_L - \dot{\alpha}_3) \tag{10.65}$$

The time derivative of the control law α_3 is determined as:

$$\dot{\alpha}_3 = \dot{\alpha}_{3c} + \dot{\alpha}_{3u} \tag{10.66}$$

Where $\dot{\alpha}_{3c}$ and $\dot{\alpha}_{3u}$ are the calculable and the incalculable parts, respectively.

$$\dot{\alpha}_{3c} = \frac{\partial \alpha_3}{\partial x_1} x_2 + \frac{\partial \alpha_3}{\partial x_2} \dot{\hat{x}}_2 + \frac{\partial \alpha_3}{\partial x_3} \dot{\hat{x}}_3 + \frac{\partial \alpha_3}{\partial t} \tag{10.67}$$

$$\dot{\alpha}_{3u} = \frac{\partial \alpha_3}{\partial x_2}(-(x_3 - \bar{b}x_2 - \bar{F}_C)\tilde{\theta}_1 - \tilde{\theta}_2 + \tilde{d}) - \frac{\partial \alpha_3}{\partial x_3}(-\bar{A}x_2 - \bar{C}_L x_3 + g_3 x_4)\tilde{\theta}_3 + \frac{\partial \alpha_3}{\partial \hat{\theta}} \dot{\hat{\theta}}) \tag{10.68}$$

Substituting expressions 10.66 and 10.68 into expression 10.65, and using that $\dot{\bar{Q}}_L = \frac{\partial g_3}{\partial x_3} \dot{x}_3 x_4 + g_3 \dot{x}_4$, yields:

$$\dot{V}_4 = \dot{V}_3|_{\alpha_3} + w_4 z_4 (\theta_3 \frac{w_3}{w_4} z_3 + \frac{\partial g_3}{\partial x_3} \dot{x}_3 x_4 + g_3 \dot{x}_4 - \dot{\alpha}_{3c} - \frac{\partial \alpha_3}{\partial x_2}(-(x_3 - \bar{b}x_2 - \bar{F}_C)\tilde{\theta}_1 - \tilde{\theta}_2 + \tilde{d}) - \frac{\partial \alpha_3}{\partial x_3}(-\bar{A}x_2 - \bar{C}_L x_3 + g_3 x_4)\tilde{\theta}_3 + \frac{\partial \alpha_3}{\partial \hat{\theta}} \dot{\hat{\theta}})) \tag{10.69}$$

Substituting the third state equation $\dot{x}_3$ into the above expression gives:

$$\dot{V}_4 = \dot{V}_3|_{\alpha_3} + w_4 z_4 (\theta_3 \frac{w_3}{w_4} z_3 + \frac{\partial g_3}{\partial x_3} \theta_3 (-\bar{A}x_2 - \bar{C}_L x_3 + g_3 x_4) x_4 + g_3 \dot{x}_4 \tag{10.70}$$

Continued $\Rightarrow$

$$- \dot{\alpha}_{3c} - \frac{\partial \alpha_3}{\partial x_2}(-(x_3 - \bar{b}x_2 - \bar{F}_C)\tilde{\theta}_1 - \tilde{\theta}_2 + \tilde{d}) - \frac{\partial \alpha_3}{\partial x_3}(-\bar{A}x_2 - \bar{C}_L x_3 + g_3 x_4)\tilde{\theta}_3 + \frac{\partial \alpha_3}{\partial \hat{\theta}}\dot{\hat{\theta}}))$$

Using that $\theta = \hat{\theta} - \tilde{\theta}$, and inserting the expression for $\dot{x}_4$ yields:

$$\begin{aligned} \dot{V}_4 = \dot{V}_3|_{\alpha_3} + w_4 z_4(\hat{\theta}_3 \frac{w_3}{w_4} z_3 + \frac{\partial g_3}{\partial x_3}\hat{\theta}_3(-\bar{A}x_2 - \bar{C}_L x_3 + g_3 x_4)x_4 - \tilde{\theta}_3 \frac{w_3}{w_4} z_3 \\ - \frac{\partial g_3}{\partial x_3}\tilde{\theta}_3(-\bar{A}x_2 - \bar{C}_L x_3 + g_3 x_4)x_4 + g_3(-\frac{1}{\tau_v}x_4 + \frac{\bar{K}_v}{\tau_v}u) - \dot{\alpha}_{3c} - \frac{\partial \alpha_3}{\partial x_2}(-(x_3 - \bar{b}x_2 \\ - \bar{F}_C)\tilde{\theta}_1 - \tilde{\theta}_2 + \tilde{d}) - \frac{\partial \alpha_3}{\partial x_3}(-\bar{A}x_2 - \bar{C}_L x_3 + g_3 x_4)\tilde{\theta}_3 + \frac{\partial \alpha_3}{\partial \hat{\theta}}\dot{\hat{\theta}})) \end{aligned} \tag{10.71}$$

Defining expressions:

$$\alpha_{4e} = \hat{\theta}_3 \frac{w_3}{w_4} z_3 - g_3 \frac{1}{\tau_v} x_4 + \frac{\partial g_3}{\partial x_3}\dot{\hat{x}}_3 x_4 + \alpha_{4e} \tag{10.72}$$

$$\phi_4 = \begin{bmatrix} -\frac{\partial \alpha_3}{\partial x_2}(-(x_3 - \bar{b}x_2 - \bar{F}_C) \\ -\frac{\partial \alpha_3}{\partial x_2} \\ \frac{w_3}{w_4} z_3 - (\frac{\partial g_3}{\partial x_3}x_4 - \frac{\partial \alpha_3}{\partial x_3})\bar{A}x_2 - \bar{C}_L x_3 + \bar{Q}_L \end{bmatrix} \tag{10.73}$$

And noting the expression for $\dot{\hat{x}}_3$, expression 10.71 is written as:

$$\dot{V}_4 = \dot{V}_3|_{\alpha_3} + w_4 z_4(g_3 \frac{\bar{K}_v}{\tau_v} u + \alpha_{4e} - \tilde{\theta}\phi_4 + \frac{\partial \alpha_3}{\partial \hat{x_2}}\tilde{d} - \frac{\partial \alpha_3}{\partial \hat{\theta}}\dot{\hat{\theta}})$$

The control law for u_v is now chosen according to [Yao et al., 2001], as:

$$u_v(x, \hat{\theta}, t) = u_a + u_s = u_a + u_{s1} + u_{s2} \tag{10.74}$$

Where:

$$u_a = -\frac{\tau_v}{\bar{K}_v g_3}\alpha_{4e} \quad , \quad u_{s1} = -K_{4s1} z_4 \quad , \quad u_{s2} = -\frac{\tau_v}{2\bar{K}_v g_3 \varepsilon_4} h_4 z_4 \tag{10.75}$$

The constants of the above expression is presented in appendix N.3. Substituting expression 10.60 into expression 10.74, yields:

$$\begin{aligned} \dot{V}_4 = w_2 z_2 \left(\theta_1 \alpha_{2s2} - \tilde{\theta}^T \phi_2 + \tilde{d}\right) - \theta_1 w_2 K_{2s1} z_2^2 \\ + w_3 z_3 \left(\theta_3 \alpha_{3s2} - \tilde{\theta}^T \phi_3 - \frac{\partial \alpha_2}{\partial x_2}\tilde{d}\right) - \theta_3 w_3 K_{3s1} z_3^2 \\ + w_4 z_4(g_3 \frac{\bar{K}_v}{\tau_v} u_{s2} - \tilde{\theta}^T \phi_4 + \frac{\partial \alpha_3}{\partial x_2}\tilde{d}) - w_4 K_{4s1} z_4^2 \\ - (w_3 z_3 \frac{\partial \alpha_2}{\partial \hat{\theta}}\dot{\hat{\theta}} + w_4 z_4 \frac{\partial \alpha_3}{\partial \hat{\theta}}\dot{\hat{\theta}}) \end{aligned} \tag{10.76}$$

10.4 Stability Proof (ARC)

According to theorem 1 of appendix N.4, if the adaption law is chosen as:

$$\tau = \sum_{j=2}^{4} w_j z_j \phi_j \tag{10.77}$$

Then expression 10.76 can, according to [Yao et al., 2001], be rewritten to:

$$\dot{V}_4 \leq -\sum_{j=2}^{4} w_j k_j z_j^2 - \tilde{\theta}^T \tau \tag{10.78}$$

The following new Lyapunov function is defined:

$$V_\theta = V_4 + \frac{1}{2}\tilde{\theta}^T \Gamma^{-1} \tilde{\theta} \tag{10.79}$$

Taking the time derivative, yields:

$$\dot{V}_\theta = \dot{V}_4 + \tilde{\theta}^T \Gamma^{-1} \dot{\tilde{\theta}} \tag{10.80}$$

Considering θ a slow varying parameter, then $\dot{\tilde{\theta}} = \dot{\hat{\theta}}$. This gives:

$$\dot{V}_\theta = \dot{V}_4 + \tilde{\theta}^T \Gamma^{-1} \dot{\hat{\theta}} \tag{10.81}$$

Substituting expression 10.78, yields:

$$\dot{V}_\theta \leq -\sum_{j=2}^{4} w_j k_j z_j^2 - \tilde{\theta}^T \tau + \tilde{\theta}^T \Gamma^{-1} \dot{\hat{\theta}} \tag{10.82}$$

Using the projection bound of expression 10.20 and noting the adaption law of expression 10.17, yields:

$$\tilde{\theta}^T (\Gamma^{-1} Proj_{\hat{\theta}}(\Gamma\tau) - \tau) \leq 0 \tag{10.83}$$

$$\tilde{\theta}^T (\Gamma^{-1} \dot{\hat{\theta}} - \tau) \leq 0 \tag{10.84}$$

$$\tilde{\theta}^T \Gamma^{-1} \dot{\hat{\theta}} - \tilde{\theta}^T \tau \leq 0 \tag{10.85}$$

$$\tilde{\theta}^T \Gamma^{-1} \dot{\hat{\theta}} \leq \tilde{\theta}^T \tau \tag{10.86}$$

Substituting into expression 10.82, yields:

$$\dot{V}_\theta \leq -\sum_{j=2}^{4} w_j k_j z_j^2 \tag{10.87}$$

As w_j and k_j are positive constants, it is found that expression 10.87, which contains $\dot{V}_2$, $\dot{V}_3$ and $\dot{V}_4$, is negative semi-definite, indicating that z_2, z_3 and z_4 are bounded as $V_\theta > 0$. Then according to the Lyapunov-like lemma of appendix H.4, if $\dot{V}_\theta$ is uniformly

continuous, $z_2,\ z_3,\ z_4 \to 0$ for $t \to \infty$. Taking the time derivative of $\dot{V}_\theta$, yields:

$$\ddot{V}_\theta = -2(w_2 k_2 z_2 \dot{z}_2 + w_3 k_3 z_3 \dot{z}_3 + w_4 k_4 z_4 \dot{z}_4) \tag{10.88}$$

In the above it was found that $z_2,\ z_3,\ z_4$ are bounded, and according to [Yao et al., 2001] it can be shown that $\dot{z}_2,\ \dot{z}_3$ and $\dot{z}_4$ are bounded. Hence it is found that $\ddot{V}_\theta$ is bounded, and $\dot{V}_\theta$ is uniformly continuous. Then according to the Lyapunov-like lemma $z_2,\ z_3,\ z_4 \to 0$ for $t \to 0$. From the above, and noting expression 10.22, it is found that $e \to 0$ for $t \to 0$. The control- and adaption laws are summarized below.

ARC control law:

$$u_v = u_a + u_s \tag{10.89}$$

Where the terms u_a and u_s are synthesized as shown in the derivation.

ARC adaption law:

$$\dot{\hat{\theta}} = \Gamma\tau \quad ; \quad \Gamma > 0 \tag{10.90}$$

Where:

$$\Gamma\tau = \begin{cases} 0 \text{ if } \hat{\theta}_i = \theta_{imax} \text{ and } \Gamma\tau > 0 \\ 0 \text{ if } \hat{\theta}_i = \theta_{imin} \text{ and } \Gamma\tau < 0 \\ \Gamma\tau \text{ else} \end{cases} \tag{10.91}$$

And:

$$\tau = \sum_{j=2}^{4} w_j z_j \phi_j = w_2 z_2 \phi_2 + w_3 z_3 \phi_3 + w_4 z_4 \phi_4 \tag{10.92}$$

Due to the significant amount of parameters in the ARC, it has not been possible to obtain reasonable tracking performance in simulations within the time frame of this thesis. However, the project group will attempt to achieve reasonable results in order to present these at the thesis evaluation.

10.5 Summary

In this chapter an adaptive robust controller has been derived and proved stable, based on the theory of [Yao et al., 2001]. However, due to difficulties in the tuning phase, which were caused by the significant amount of unknown controller parameters, it has not been possible to obtain reasonable tracking performance within the time frame of this thesis. An initiative to improve performance of the ARC will be made in order to present reasonable result to the thesis evaluation.

Chapter 11

Learning Control Schemes

Contents

In this chapter learning control schemes are introduced. First a simple iterative learning controller (ILC) is established, followed by a robust and more complex discrete learning controller (RDLC). Finally, the two learning controllers are tested. This chapter is based on [Andersen, 1995]

11.1 Introduction

This type of control schemes is motivated by the possibility of implementing a learning or self-tuning law, accompanying the control law. The controllers treated cancels out the unknown repeatable dynamics of the system by adaptively altering the feed forward input to the plant. To be able to apply learning control it is a necessary condition that the control system is to track cyclic trajectories, thereby meaning that the control system has to track a given trajectory over and over again. The idea is then to improve tracking performance based on knowledge of the error experienced by the control system in the previous cycle. The error occurring in the previous cycle is recorded and used to compensate for the error in the present cycle. For both the controllers presented in this chapter, the control system appears as shown in figure 11.1 (n indicates the cycle number).

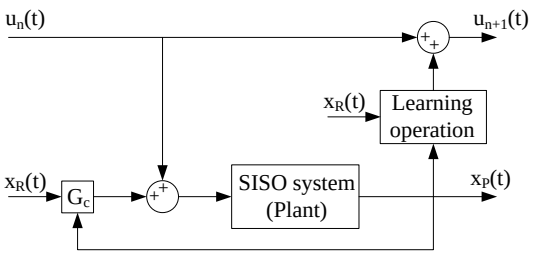

Figure 11.1: Control system implemented with learning controller.

In figure 11.1, $u_n(t)$ is the input trajectory. The learning operator $L()$ compares $x_P(t)$ and $x_R(t)$ and adds an update term to $u_n(t)$ resulting in an output $u_{n+1}(t)$.

11.2 Iterative Learning Controller (ILC)

The iterative learning control scheme introduced in this section, is derived based on the same simple first order dynamic model used to derive the adaptive control schemes of chapter 8. Hence the model used is given by:

$$u = \Gamma \dot{x}_P + \nu \tag{11.1}$$

The error dynamics is defined as (the index n denotes the n^{th} cycle):

$$\dot{e}_n + k_p e_n = \xi_L \tag{11.2}$$

The idea is then to add a term to the right hand side of expression 11.2, that reduces the right hand side of the above expression as close to zero as possible. Hence the error dynamic equation is given by:

$$\dot{e}_n + k_p e_n = \xi_n - u_n \cong 0 \tag{11.3}$$

Hence based on knowledge of ξ_{n-1}, u_n is updated such that $\xi_n - u_n$ approaches zero. For this to be possible, it is necessary that ξ_n is approximately the same during each cycle. Laplace transforming expression 11.3, yields:

$$s e_n + k_p e_n = \xi_n - u_n \tag{11.4}$$

$$e_n = \frac{1}{s + k_p}(\xi_n - u_n) \tag{11.5}$$

Defining:

$$H_L(s) = \frac{1}{s + k_p} \tag{11.6}$$

Yields:

$$e_n = H_L(s)(\xi_n - u_n) \tag{11.7}$$

The control law is chosen as[Andersen, 1995]:

$$u = \hat{\Gamma}(\dot{x}_R + k_p e_n + u_n) \tag{11.8}$$

Here the learning term u_n is chosen as:

$$u_{n+1} = u_n + L(s) e_n \tag{11.9}$$

Substituting expression 11.7 into expression 11.9, yields:

$$u_{n+1} = u_n + L(s) H_L(s)(\xi_n - u_n) \tag{11.10}$$

Defining $C_{L1} = L(s)H_L(s)$, yields:

$$u_{n+1} = u_n + C_{L1}(\xi_n - u_n) \tag{11.11}$$
$$= C_{L1}\xi_n + u_n(1 - C_{L1}) \tag{11.12}$$
$$\tag{11.13}$$

Letting $u_0 = 0$, expression 11.11 can be written as:

$$u_n = \sum_{i=1}^{n}((1 - C_{L1})^{n-i}C_{L1})\xi_n \tag{11.14}$$

Subtracting ξ_n on both sides of expression 11.14, gives:

$$u_n - \xi_n = \sum_{i=1}^{n}((1 - C_{L1})^{n-i}C_{L1})\xi_n - \xi_n \tag{11.15}$$
$$= (\sum_{i=1}^{n}((1 - C_{L1})^{n-i}C_{L1}) - 1)\xi_n \tag{11.16}$$

Defining $C_{L2} = 1 - C_{L1}$, yields:

$$u_n - \xi_n = (\sum_{i=1}^{n}(C_{L2}^{n-i}C_{L1}) - 1)\xi_n \tag{11.17}$$
$$= (\sum_{i=1}^{n}(C_{L2}^{n-i}(1 - C_{L2})) - 1)\xi_n \tag{11.18}$$

It is possible to write $\sum_{i=1}^{n}(C_{L2}^{n-i}(1-C_{L2})) = 1-C_{L2}^{n}$. Substituting into expression 11.17, yields:

$$u_n - \xi_n = ((1 - C_{L2}^{n}) - 1)\xi_n \tag{11.19}$$
$$= -C_{L2}^{n}\xi_n \tag{11.20}$$

Substituting $C_{L2} = 1 - C_{L1}$, yields:

$$u_n - \xi_n = -C_{L2}^{n}\xi_n \tag{11.21}$$
$$= -(1 - C_{L1})^{n}\xi_n \tag{11.22}$$

Applying the L_2 norm, yields:

$$\|u_n - \xi_n\|_2 \leq \| - (1 - C_{L1})^{n}\|_2\|\xi_n\|_2 \tag{11.23}$$

From expression 11.23, it is found that for u_n to converge to ξ_n, the following must be satisfied, noting that n represents the number of cycles, and hence always will be $0 \leq n$:

$$\| - (1 - C_{L1})\|_2 \leq 1 \quad \text{for} \quad \| - (1 - C_{L1})^{n}\|_2 \ \rightarrow \ 0 \tag{11.24}$$

Now choosing the learning operator $L(s)$ to $L(s) = s + (k_p - \mu)$[Andersen, 1995], yields:

$$1 - C_{L1} = 1 - L(s)H_L(s) = 1 - \frac{s + (k_p - \mu)}{s + k_p} \tag{11.25}$$

$$= \frac{s + k_p}{s + k_p} - \frac{s + (k_p - \mu)}{s + k_p} \tag{11.26}$$

$$= \frac{s + k_p - s - k_p + \mu}{s + k_p} \tag{11.27}$$

$$= \frac{\mu}{s + k_p} \tag{11.28}$$

Taking the L_2 norm (according to appendix H.7), yields:

$$\|1 - C_{L1}\|_2 = \left\| \frac{\mu}{s + k_p} \right\|_2 = \max_{\omega \in \Re} \left| \frac{\mu}{j\omega + k_p} \right| = \frac{\mu}{k_p} \tag{11.29}$$

Hence it is found that for $\|(1 - C_{L1})\|_2 \leq 1$ to be satisfied, the following must be satisfied:

$$0 < \mu < k_p \tag{11.30}$$

Hence by satisfying expression 11.30, it is found that u_n will approach ξ_n as the number of cycles progresses. From this it follows that the error will approach zero. Now the control- and learning update law can be written as shown below (here the learning update law is displaced one cycle back).

ILC control law:

$$u = \hat{\Gamma}(\dot{x}_R + k_p e + u_n) \tag{11.31}$$

ILC learning update law:

$$u_n = u_{n-1} + L(s)e_{n-1} = u_{n-1} + (s + (k_p - \mu))e_{n-1} \tag{11.32}$$

11.3 Robust Discrete Time Learning Controller (RDLC)

The controller presented in this section is a robust discrete time learning controller for non-linear time varying systems as the type described by the state space equations of expressions 11.33.

$$\begin{aligned} \dot{x}_n(t) &= f(x_n((t), t) + B(x_n((t), t)u_n(t) + \omega_n(t) \\ y_n(t) &= g(x_n((t), t) \end{aligned} \tag{11.33}$$

First there will be a motivation (according to [Andersen, 2004a]) for using the later proposed more general learning control law, following a presentation of the proposed control and learning laws proposed for the system at hand.

In the following a motivation for the later proposed learning control law is given. This is based on the same simplified model, used in the previous section (expression 11.1). The simplified model is rewritten to the following form:

$$\dot{x}_P(t) = \Gamma^{-1}(t)u(t) - \Gamma^{-1}(t)\nu(t) \tag{11.34}$$

It is seen that $-\Gamma^{-1}(t)\nu(t)$ is equivalent to the state error, and will in the following be denoted $\phi(t)$. Denoting the n^{th} work cycle, yields (in the following the subscript $_P$ is omitted):

$$\dot{x}_n(t) = \Gamma_n^{-1}(t)u_n(t) + \phi_n(t) \tag{11.35}$$

By utilizing Taylor expansion the output x_n at time $t + \Delta t$ can be described as:

$$x_n(t + \Delta t) = x_n(t) + \dot{x}_n(t)\Delta t = x_n(t) + [\Gamma_n^{-1}(t)u_n(t) + \phi_n(t)]\Delta t \tag{11.36}$$

The subsequent work cycle is denoted by $n + 1$ and an expression for the input is found as:

$$x_{n+1}(t + \Delta t) = x_{n+1}(t) + \dot{x}_{n+1}(t)\Delta t = x_{n+1}(t) + [\Gamma_{n+1}^{-1}(t)u_{n+1}(t) + \phi_{n+1}(t)]\Delta t \tag{11.37}$$

By substituting $x_{n+1}(t + \Delta t)$ with $x_d(t + \Delta t)$ the input signal $u_{n+1}(t)$ which causes $x_{n+1}(t + \Delta t)$ to approach $x_R(t + \Delta t)$ can be found if $\phi(t)$ is known. This is carried out in the following. Substituting $x_{n+1}(t + \Delta t)$ with $x_R(t + \Delta t)$, yields (x_R represents the desired, or reference position):

$$x_R(t + \Delta t) = x_{n+1}(t) + \dot{x}_{n+1}(t)\Delta t = x_{n+1}(t) + [\Gamma_{n+1}^{-1}(t)u_{n+1}(t) + \phi_{n+1}(t)]\Delta t \tag{11.38}$$

If the variation of $\phi(t)$ between two cycles is ignored, meaning that $\phi_n(t) = \phi_{n+1}(t)$,then $\phi_{n+1}(t)$ can be eliminated from equation 11.38, and an expression for $\phi(t)$ is subsequently derived by isolating in equation 11.36.

$$\begin{aligned} x_n(t + \Delta t) &= x_n(t) + [\Gamma_n^{-1}(t)u_n(t) + \phi_n(t)]\Delta t \quad \Rightarrow \\ x_n(t + \Delta t) - x_n(t) - \Gamma_n^{-1}(t)u_n(t)\Delta t &= \phi_n(t)\Delta t \quad \Rightarrow \\ \frac{x_n(t + \Delta t)}{\Delta t} - \frac{x_n(t)}{\Delta t} - \Gamma_n^{-1}(t)u_n(t) &= \phi_n(t) \end{aligned} \tag{11.39}$$

Inserting equation 11.39 into equation 11.38, yields:

$$\begin{aligned} x_R(t + \Delta t) &= x_{n+1}(t) + [\Gamma_{n+1}^{-1}(t)u_{n+1}(t) + \frac{x_n(t + \Delta t)}{\Delta t} - \frac{x_n(t)}{\Delta t} && (11.40) \\ &\quad - \Gamma_n^{-1}(t)u_n(t)]\Delta t \\ &= x_{n+1}(t) + \Gamma_{n+1}^{-1}(t)u_{n+1}(t)\Delta t + x_n(t + \Delta t) - x_n(t) && (11.41) \\ &\quad - \Gamma_n^{-1}(t)u_n(t)\Delta t \quad \Rightarrow \\ x_R(t + \Delta t) - x_n(t + \Delta t) &= x_{n+1}(t) - x_n(t) + [\Gamma_{n+1}^{-1}(t)u_{n+1}(t) - \Gamma_n^{-1}(t)u_n(t)]\Delta t && (11.42) \end{aligned}$$

Equation 11.42 can, by isolating $u_{n+1}(t)$ and ignoring the variation of Γ between the

cycles, be turned into a learning algorithm given by:

$$x_R(t+\Delta t) - x_n(t+\Delta t) = x_{n+1}(t) - x_n(t) + [\Gamma^{-1}u_{n+1}(t) - \Gamma^{-1}u_n(t)]\Delta t \quad \Rightarrow \quad (11.43)$$

$$\frac{x_R(t+\Delta t) - x_n(t+\Delta t) - x_{n+1}(t) + x_n(t)}{\Delta t} = [\Gamma^{-1}u_{n+1}(t) - \Gamma^{-1}u_n(t)] \quad (11.44)$$

Isolating $u_{n+1}(t)$ yields the motivational learning update law:

$$u_{n+1}(t) = u_n(t) + \Gamma\frac{[x_R(t+\Delta t) - x_n(t+\Delta t)] - [x_{n+1}(t) - x_n(t)]}{\Delta t} \quad (11.45)$$

A more general form of the learning law is proposed in equation 11.46[Andersen, 2004a]:

$$u_{n+1}(t) = (1-\gamma)u_n(t) + \gamma u_0(t) + L(x_n(t), t)\frac{[x_R(t+\Delta t) - x_n(t+\Delta t)] - [x_{n+1}(t) - x_n(t)]}{\Delta t} \quad (11.46)$$

Where, $L : R^m \times [0, T] \rightarrow R^{r\times m}$ is bounded, and the term γ is can be used to prevent input wandering at initial conditions and also function as a bias. The term $L(x_n(t), t)$ is a learning operator which in this thesis is considered constant. If the system described in equation 11.33 uses the learning law of equation 11.46, and satisfies assumptions $(A1) - (A5)$ listed in appendix K, then (according to [Andersen, 2004a]) given an obtainable x_R, and if:

$$\|(1-\gamma)I - L_n(g(x(t), t)\frac{1}{\Delta t}\int_t^{t+\Delta t} g_x(x, t)B(x, t)d\tau\| \leq \rho < 1 \quad (11.47)$$

And if the initial state error is bounded, then as n approaches infinity, the error between u_n and u_R is bounded,that is $\|x_R(0) - x_n(0)\| \leq b_{x0}$.

As the number of work cycles approaches infinity, then the error between u_n and u_R are bounded.

Where $\forall(x, t) \in \Re^n \times [0, T]$.

By choosing a small Δt the theorem of equation 11.47 is reduced to equation 11.48:

$$\|(1-\gamma)I - L_n(g(x(t), t)g_x(x, t)B(x, t)d\tau\| \leq \rho < 1 \quad (11.48)$$

Where $\forall(x, t) \in \Re^n \times [0, T]$.

The chosen control law is given as 11.49[Andersen, 2004a]:

$$u = \hat{\Gamma}(t)(\dot{x}(t) - k_P(x_R(t) - x(t))) + u^L \quad (11.49)$$

where u^L is the learning term.

A modified version of the learning law given in equation 11.46 is given by equation 11.50[Andersen, 2004a].

$$u^L_{n+1}(t) = u^L_n(t) + L(t)\frac{[x_R(t+\Delta t) - x_k(t+\Delta t)] - [x_{k+1}(t) - x_k(t)]}{\Delta t} \quad (11.50)$$

where the learning operator $L(t)$ represents Γ.

Also the state and output asymptotic errors are bounded, and these depend on the bound of the initial state error, the bound on the state disturbance and γ.

Given a desired input trajectory the output will eventually converge to the desired input trajectory which is implied by equation 11.47 if $\| 1 - L\frac{1}{\Delta t}\int_t^{t+\Delta t} g_x B d\tau \| \leq \rho < 1$. by regarding Δt as being small the above condition is reduced to $\| 1 - L\Gamma^{-1} \| \leq \rho < 1$.

From this expression it is seen that choosing $L \leq \Gamma$ will make the expression hold true. The control law and learning update law for the RDLC are given below.

RDLC control law:

$$u = \hat{\Gamma}(\dot{x}_R + k_p e + u_n) \tag{11.51}$$

RDLC learning update law:

$$u_n(t) = u_{n-1}(t) + \frac{L}{\Delta t}((x_R(t+\Delta t) - x_P(t+\Delta t))_{n-1} - (x_k(t) - x_{k-1}(t))) \tag{11.52}$$

11.4 Simulation results

Regarding the implementation of the learning controllers, the following must be taken into account. As the error reaches a minimum of what the controller can perform, the error over time will be oscillatory, as the output tracks about the reference. This will cause the learning part of the controller to accumulate these oscillations, and use this in the feed forward learning term. Hence the error will increase, yielding poor tracking performance. The same phenomena occurs if the feedback signal is overlayed with noise, which to some extend occurs on the physical system. Therefore it is necessary to define some limits that switches of, or scales down the learning term at a given error value.

11.4.1 Simulation results - ILC

As the ILC is not a robust controller, to ensure that disturbances are similar to each other during each cycle, and thereby evaluate the performance, the tracking performance is evaluated by testing the individual HSS's, while the other is kept in a fixed position.

Regarding the used parameters, the $\hat{\Gamma}$ values are chosen poorly, in order to observe the effect of the learning controller. The parameters used for the ILC's, are found in appendix J. It is noted that the learning operators are scaled down in order to be able to observe the learning effect over several cycles.

It is clear from figures 11.2 and 11.3, that the learning update term causes the effect of reducing the errors as the trajectory cycles progresses. It is also found from figures 11.2

and 11.3, that the oscillations begins to accumulate at the last cycles - hence the effect of the learning operator needs to be scaled down at this point.

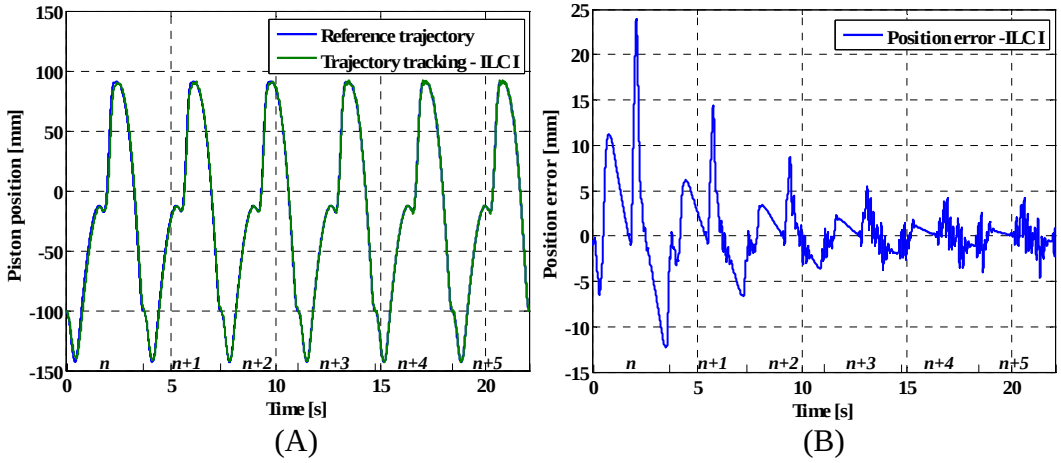

Figure 11.2: Learning controller implemented on HSS I. (A) Trajectory tracking. (B) Tracking error.

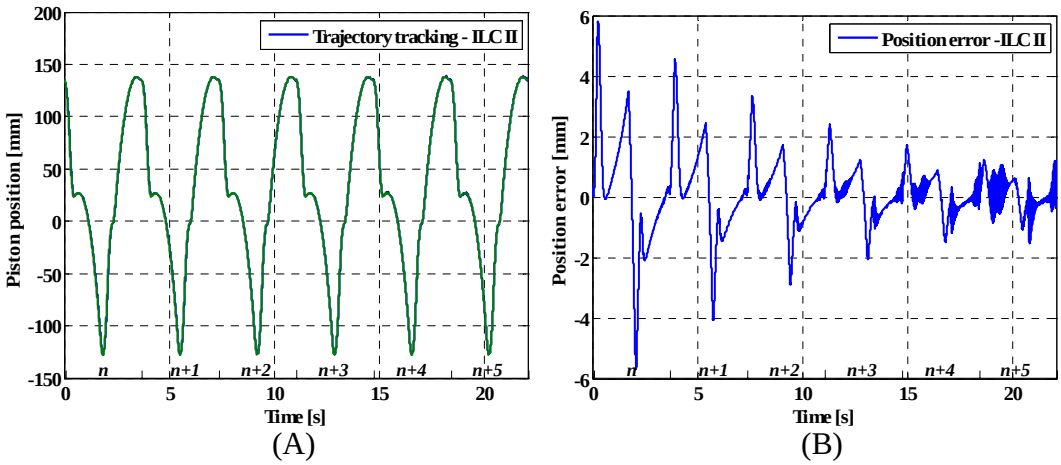

Figure 11.3: Learning controller implemented on HSS II. (A) Trajectory tracking. (B) Tracking error.

11.4.2 Simulation results - RDLC

The simulations for the RDLC control systems are carried out similar to the these of the ILC control systems, hence evaluating the tracking performance for the individual HSS's, while the other is kept in a fixed position.

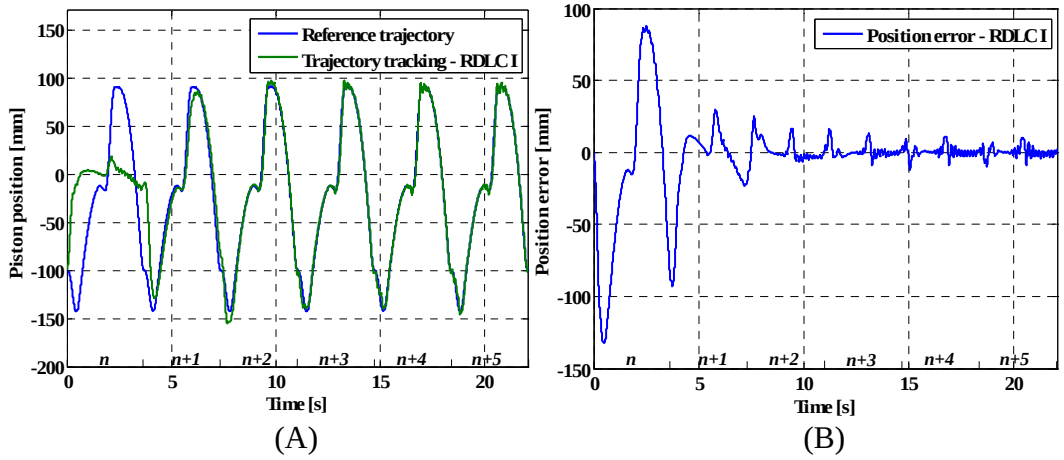

Figure 11.4: RDLC implemented on HSS I. (A) Trajectory tracking. (B) Tracking error.

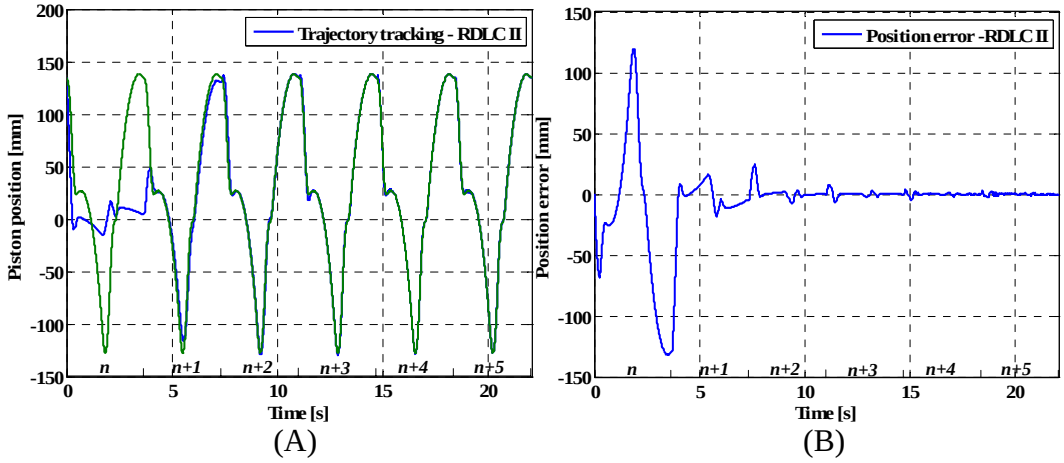

Figure 11.5: RDLC implemented on HSS II. (A) Trajectory tracking. (B) Tracking error.

The parameters used in the simulations of the RDLC, are as for the ILC, chosen poorly, in order to observe the effect of the learning operation. The parameters used for the RDLC's are found in appendix J.

It is clear from figures 11.2 and 11.5, that the learning update term causes the effect of reducing the errors as the trajectory cycles progresses. It is also found from figures 11.2 and 11.3, that the oscillations begins to accumulate at the last cycles - hence the effect of the learning operator needs to be scaled down at this point.

11.4.3 Tracking Errors - (RECT)

The maximum- and RMS errors are obtained for the trajectory cycles with best performance, and are given in the table below.

Compensator	$\lvert e_{maxI} \rvert$ $[mm]$	e_{rmsI} $[mm]$	$\lvert e_{maxII} \rvert$ $[mm]$	e_{rmsII} $[mm]$
ILC	5.79	1.72	1.64	0.49
RDLC	10.36	3.59	3.21	0.73

Table 11.1: Tracking error values for controllers tested on the rectangular trajectory.

The simulation results for the IOT, along with their errors are found in appendix M.

11.4.4 Summary

In this chapter two learning controllers, an ILC and a RDLC has been treated. Both learning controllers are established using the same simplified system model as for the adaptive controllers. A proof for the stability of the ILC is given and for the RDLC a motivation for using the learning law of the RDLC has been given. Both controllers have been implemented and tested in simulink. The controllers were however not implemented on the physical robot during this thesis, but an initiative to implement the controllers before the thesis evaluation will be carried out.

Part IV

Comparison of Control Schemes & Conclusions

Chapter 12

Comparison of Controllers

Contents

This chapter treats the comparison of the controllers in order to estimate which controllers yield the best performance when implemented on a hydraulic servo application as the servo robot in this thesis.

In order to estimate the performance of the various controllers, a set of evaluation criteria was setup in chapter 1. These where the maximum RMS error, maximum peak error and robustness towards disturbances.

Even though some of the controllers in the following will perform worse then others, it may still be justifiable to use them on a hydraulic servo robot, depending on the task that the robot is to perform. This means that the performance of the controllers might vary with the job that the robot is to carry out.

12.1 Robustness

As mentioned in section 1.5.3 the robustness of the controllers will also be investigated. The analysis of the robustness is carried out in order to be able to evaluate how robust the control systems tested in the thesis, are towards disturbances. In order to provide proper disturbances to the control systems, it will be appreciable to be able to apply a disturbance that excites all of the system dynamics. To do this an additional load is applied to the system at a given point of time during the trajectory - this is applied as a step to the mass of link II at the center of mass of this. Due to the sudden increase in the load, the pressure dynamics will be affected, hence affecting all of the hydraulic system. This analysis is carried only for the RECT, as this is the trajectory that provides the highest demands for the system. The applied mass will be 50 $[kg]$, and will be applied at time $t = 1$ $[s]$ for all control systems. This analysis will be carried out for the linear controllers with VFCP and VFCA, for the AIDC, MAIDC, RAIDC, AAC, MAAC, RAAC, and for the learning controllers ILC and RDLC. Regarding the learning controllers, the

disturbance is applied during the trajectory cycle with the best performance.

The analysis will be carried out by evaluating the error differences ($\Delta|e_{maxi}|$, Δe_{RMSi}) between the errors experienced for the control system without disturbance, and for the control systems with disturbance. Plots of the $\Delta|e_{maxi}|$ and for the trajectory tracking of the controllers when subjected to a disturbance, are found in appendix O.

The controllers are evaluated within each main group of controllers meaning linear, adaptive and learning. It should be noted that the performance of the controllers is dependent on the tuning of the belonging parameters, meaning that the controllers implemented in this thesis might perform better than illustrated below, given a different tuning.

All the controllers established and tested in this thesis are listed subsequently with indications on whether or not a given controller has been implemented on the physical robot, or only the model. An indication of the number and types of sensors needed for each controller is also given for the servo system.

Compensator	Implemented on physical robot	Number of sensors required	Types of sensors required
P-VFCP	x	1	Position
PI-VFCP	x	1	Position
Lead-VFCP	x	1	Position
Lag-VFCP	x	1	Position
Lag-Lead-VFCP	x	1	Position
P-VFCA	-	2	Position, Pressure
PI-VFCA	-	2	Position, Pressure
GFM	-	3	Position, Pressure, Velocity
GFM+VFCP	-	3	Position, Pressure, Velocity
MAIDC	x	1	Position
MAAC	x	1	Position
RAIDC	-	1	Position
RAAC	-	1	Position
AIDC	-	1	Position
AAC	-	1	Position
ILC	-	1	Position
RDLC	-	1	Position

Table 12.1: Controllers established in this thesis.

12.2 Linear Controllers

12.2.1 Performance for the RECT

As seen in table 12.2 the best performing controller, when running the RECT, regarding e_{max} and e_{rms} for link I is the PI-VFCA. Even though the feed forward gain of the PI-VFCA is continuously adjusted, and the controller also uses both pressure and position

sensors, it does not performing as well for link II, regarding e_{max} and e_{rms}, as the PI-VFCP controller. But as seen the difference between PI-VFCA and PI-VFCP in tracking error, for both e_{max} and e_{rms} for link II are small.

Compensator	$\lvert e_{maxI}\rvert$ $[mm]$	e_{rmsI} $[mm]$	$\lvert e_{maxII}\rvert$ $[mm]$	e_{rmsII} $[mm]$
P-VFCP	15.37	5.26	2.25	0.83
PI-VFCP	10.97	4.58	1.95	0.63
Lead-VFCP	15.22	5.27	2.39	0.92
Lag-VFCP	12.13	4.33	2.58	0.74
Lag-Lead-VFCP	10.29	4.61	2.44	0.80
P-VFCA	7.51	3.25	2.40	0.83
PI-VFCA	7.44	3.24	2.05	0.74
GFM	18.54	7.22	15.18	5.90
GFM+VFCP	–	–	–	–

Table 12.2: Tracking error values for controllers tested on the rectangular trajectory.(simulation)

Performance for Experimental Results for the RECT

Compensator	$\lvert e_{maxI}\rvert$ $[mm]$	e_{rmsI} $[mm]$	$\lvert e_{maxII}\rvert$ $[mm]$	e_{rmsII} $[mm]$
P-VFCP	12.46	5.29	6.15	2.01
PI-VFCP	10.01	4.73	5.58	1.73
Lead-VFCP	12.72	5.34	6.51	2.25
Lag-VFCP	10.04	4.55	6.13	1.87
Lag-Lead-VFCP	10.03	4.57	5.54	1.91

Table 12.3: Tracking error values for controllers tested on the rectangular trajectory(experimental).

In the table listing the experimental results it is seen that the tracking errors, both e_{max} and e_{rms}, are very similar for the PI-VFCP, Lag-VFCP and Lag-Lead-VFCP for link I. The peak tracking error for link II is smallest when using the Lag-Lead-VFCP, but the e_{rms} value is the smallest when using the PI-VFCP, which has a reasonable e_{max} value close to that of the Lag-Lead-VFCP. It is also seen that the controllers implemented on the physical system does perform better regarding e_{max} for link I, but worse for e_{rms} for both link I and II and also worse regarding e_{max} for link II. The difference in performance between the simulated and experimental results, is believed to be due to model uncertainties, and could probably be rectified, or improved, by additional tuning of the controller parameters on the physical system.

12.2.2 Performance for the IOT

Compensator	$\lvert e_{maxI}\rvert$ $[mm]$	e_{rmsI} $[mm]$	$\lvert e_{maxII}\rvert$ $[mm]$	e_{rmsII} $[mm]$
P-VFCP	11.61	6.97	1.88	1.18
PI-VFCP	14.08	8.83	0.92	0.41
Lead-VFCP	11.45	6.90	2.19	1.36
Lag-VFCP	12.28	7.85	1.49	0.82
Lag-Lead-VFCP	15.68	9.48	1.46	0.51
P-VFCA	14.44	6.39	3.37	1.87
PI-VFCA	21.06	7.67	1.48	0.52
GFM	13.43	10.90	9.02	7.36
GFM+VFCP	1.27	0.65	1.44	1.07

Table 12.4: Tracking error values for controllers tested on the out/in trajectory (simulation).

For the IOT trajectory the controller showing the least tracking error, both e_{max} and e_{rms} is clearly the GFM+VFCP, which is also the controller utilizing the most sensors. Unfortunately, as previously mentioned, the GFM+VFCP controller could not be tested on the RECT due to valve saturation, and it is therefore not possible to test wether or not that the GFM+VFCP controller would also have been the best performance for the RECT.

The e_{max} for link II is also the lowest when using the GFM+VFCP, but does not have nearly as good an e_{rms} performance as the PI-VFCA which also shows good performance regarding e_{max}.

Generally the GFM+VFCP controller performs well since it uses information from more states to generate the control input. On the other it also needs more sensors than the rest of the controllers.

12.2.3 Robustness of Linear Controllers

The difference in maximum errors $|\Delta e_{maxi}|$ and difference between the RMS errors Δe_{rmsI}, found from the Δe plots in appendix O, are presented in the table below.

Compensator	$\lvert \Delta e_{maxI}\rvert$ $[mm]$	Δe_{rmsI} $[mm]$	$\lvert \Delta e_{maxII}\rvert$ $[mm]$	Δe_{rmsII} $[mm]$
P-VFCP	10.85	2.19	1.05	0.03
PI-VFCP	9.54	1.50	0.67	0.04
Lead-VFCP	10.90	2.22	1.13	0.03
Lag-VFCP	9.75	1.55	0.79	0.05
Lag-Lead- VFCP	9.13	1.32	0.78	0.05
P-VFCA	11.71	1.28	0.62	0.12
PI-VFCA	11.45	1.98	0.57	0.38
GFM	2.49	0.42	1.27	0.006

Table 12.5: Difference in errors $|\Delta e_{maxi}|$ and Δe_{rmsI}, between control systems with and without disturbances (simulation).

It is found that all linear control systems, except the control system with GFM, are able to cope with the applied disturbance in a way similar to each other. However, even though it did not perform well in neither the RECT nor the IOT simulation, it is found that the most robust of the linear controllers clearly is the GFM control system which is due to a relative high damping of the compensated system.

12.3 Adaptive Controllers

12.3.1 Performance for the RECT

Compensator	$\lvert e_{maxI} \rvert$ $[mm]$	e_{rmsI} $[mm]$	$\lvert e_{maxII} \rvert$ $[mm]$	e_{rmsII} $[mm]$
MAIDC	4.00	1.59	1.15	0.23
MAAC	10.00	2.82	0.65	0.17
RAIDC	6.46	2.68	1.16	0.36
RAAC	6.82	2.48	2.03	0.60
AIDC	9.6	3.00	1.33	0.32
AAC	9.7	2.62	0.91	0.27

Table 12.6: Tracking error values for controllers tested on the rectangular trajectory (simulation).

As for the linear controllers, the best performing controllers are not the same for link I and link II. The MAIDC is clearly the best performing controller, both regarding e_{max} and e_{rms} for link I whereas the MAAC is the best performing controller for link II. Generally speaking, all the adaptive controllers perform rather well regarding e_{rms} for both link I and II, but with rather varying results on the e_{max} for link I. It would be expected that the MAIDC and MAAC controllers would be the best performing, since both of these have an integral part and a proportional part increasing the speed of the parameter adaption, whereas the remaining controllers only have an integral part. The difference in performance for the MAIDC and the MAAC on link I and II is assumed to be, in some degre, due to tuning of parameters and could probably be decreased if additional time was spent tuning these.

Performance for Experimental Results for the RECT

Compensator	$\lvert e_{maxI} \rvert$ $[mm]$	e_{rmsI} $[mm]$	$\lvert e_{maxII} \rvert$ $[mm]$	e_{rmsII} $[mm]$
MAIDC	6.97	1.80	5.77	1.82
MAAC	8.73	3.03	6.62	2.05

Table 12.7: Tracking error values for controllers tested on the rectangular trajectory.(experimantal)

The experimental results for the RECT shows reasonable performance for both the MAIDC and the MAAC controllers, but the MAIDC is the best performing of the two for both link I and link II, regarding e_{max} and e_{rms}. The difference in controller performance is to some extent assumed to be due to parameter tuning.

Performance for the IOT

Compensator	$\lvert e_{maxI} \rvert$ $[mm]$	e_{rmsI} $[mm]$	$\lvert e_{maxII} \rvert$ $[mm]$	e_{rmsII} $[mm]$
MAIDC	3.85	1.73	0.35	0.14
MAAC	7.20	2.17	0.31	0.11
RAIDC	3.02	1.31	0.55	0.16
RAAC	5.90	2.65	0.63	0.33
AIDC	3.21	1.48	0.61	0.16
AAC	6.86	3.66	1.00	0.64

Table 12.8: Tracking error values for controllers tested on the in/out trajectory (simulation).

For the IOT the RAIDC is the best performing controller for link I for both e_{max} and e_{rms}, while the MAAC, as for the RECT, is the best performing for link II regarding both e_{max} and e_{rms}. Since the IOT is a less demanding trajectory than the RECT regarding power consumption, the controllers which only utilizes an integral part does perform better than for the RECT. It is suspected that the MAIDC could also have been performing better if additional parameter tuning was applied.

12.3.2 Robustness

Compensator	$\lvert \Delta e_{maxI} \rvert$ $[mm]$	Δe_{rmsI} $[mm]$	$\lvert \Delta e_{maxII} \rvert$ $[mm]$	Δe_{rmsII} $[mm]$
MAIDC	15.65	3.39	1.70	0.04
MAAC	13.63	2.59	1.43	0.04
AIDC	12.01	1.89	1.42	0.03
AAC	11.13	1.70	1.71	0.06
RAIDC	12.89	1.75	1.93	0.05
RAAC	13.00	1.48	1.33	0.08

Table 12.9: Difference in errors $\lvert \Delta e_{maxi} \rvert$ and Δe_{rmsI}, between adaptive control systems with and without disturbances (simulation).

The adaptive controllers all show rather similar tendencies regarding robustness. The largest deviances between the controllers are found for link I for e_{rms}, which was to be expected since link I has larger variations in inertia mass than link II, and also less excess power for control.

12.4 Learning Controllers

12.4.1 Performance for the RECT

Compensator	$\lvert e_{maxI} \rvert$ $[mm]$	e_{rmsI} $[mm]$	$\lvert e_{maxII} \rvert$ $[mm]$	e_{rmsII} $[mm]$
ILC	5.79	1.72	1.64	0.49
RDLC	10.36	3.59	3.21	0.73

Table 12.10: Tracking error values for controllers tested on the rectangular trajectory (simulation).

It is seen for both the RECT and IOT that the best performing controller for link I and link II, regarding e_{max} and e_{rms}, is the ILC controller which may be due the tuning of the parameters.

12.4.2 Performance for the IOT

Compensator	$\lvert e_{maxI}\rvert$ $[mm]$	e_{rmsI} $[mm]$	$\lvert e_{maxII}\rvert$ $[mm]$	e_{rmsII} $[mm]$
ILC	1.23	0.35	0.68	0.32
RDLC	10.07	3.45	3.10	0.67

Table 12.11: Tracking error values for controllers tested on the in/out trajectory (simulation).

As for the RECT the ILC outperforms the the RDLC for link I and II regarding both e_{max} and e_{rms}, especially regarding the e_{max} for link I. Again this may be due to parameter tuning.

12.4.3 Robustness

The difference in maximum errors $|\Delta e_{maxi}|$ and difference between the RMS errors Δe_{rmsI}, are presented in the table below.

Compensator	$\lvert\Delta e_{maxI}\rvert$ $[mm]$	Δe_{rmsI} $[mm]$	$\lvert\Delta e_{maxII}\rvert$ $[mm]$	Δe_{rmsII} $[mm]$
ILC	7.88	0.81	0.88	0.03
RDLC	9.65	0.15	1.40	0.0002

Table 12.12: Difference in errors $|\Delta e_{maxi}|$ and Δe_{rmsI}, between nonlinear control systems with and without disturbances.(simulation)

The ILC controller is the most robust regarding Δe_{max}, whereas the RDLC controller shows the best robustness regarding Δe_{rms}.

Chapter 13

Conclusions & Perspectives

This thesis have been initiated in order to investigate the performances of an array of controllers, linear and non-linear, on an electro hydraulic servo system realized by an electro hydraulic robot manipulator, in order to decide which of the tested controllers were the most suited for implementation on such a system. The controllers investigated were classical linear controllers, linear controllers with extensions, adaptive, and learning controllers. The thesis has been divided into four parts were the tasks and outcome of each part is summarized subsequently.

Part I

In order to simulate the behavior of the electro hydraulic robot manipulator and test the controllers a dynamic non-linear model of the electro hydraulic robot manipulator has been established, both for the solid state and fluid mechanical parts of the overall system. The model has then subsequently been tested, by comparison of pressure data from the physical system, regarding both dynamics and gravitation, which has proved the model to be adequately accurate for the design and testing of controllers.

The non-linear model has then been linearized and a linear model of the robot manipulator has been developed. The linear model has been verified by applying small inputs to the servo valves near the operating point of the linear model and afterwards comparing the outputs of the linear model to those of the nonlinear model. From this comparison the linear model has been found sufficiently accurate, and has therefore been used for development of the linear controllers.

In order to have a common testing scenario for evaluating the performances of the controllers developed in the thesis, trajectories have been established. The limits for the trajectories have been set up as the physical system boundaries, taking into account the mechanical damping at the actuator endpoints in order to avoid undesired system behavior. Furthermore flow and pressure boundaries for the hydraulic part of the system have been taken into account. Two trajectory scenarios have been set up - a robot control scenario, and a servo control scenario. In the robot control scenario the tool center point is to track a rectangular trajectory which requires fairly large variations in the actuator

space trajectories over a specified period of time. In the servo control scenario both actuators are to track the same trajectory, which is constituted by a retraction and extension of the actuators, also over a specified period of time.

part II

As a base of comparison different linear controllers have been designed by use of frequency responses to meet the design specifications of GM and PM, and the designed compensators have subsequently been adjusted to have satisfactory responses when subjected to step-, ramp and parabolic inputs. It has been found that the classical linear controllers provided poor tracking performance for both trajectories, resulting in large rms and peak tracking errors. In order to augment the performance of the classical controllers, extensions has been added in the form of feed forward compensation, both passive and active. The passive feed forward gain has been found by use of the inverse dynamics of the linear system representation, and the active feed forward gain has been established by use of pressure feedback, updating the feed forward gain. It has been found that adding a feed forward gain boosted the performance of the controllers regarding tracking performance. It has also been found that the effect of adding the active feed forward gain was most pronounced on the HSS I, since this part of the system has the largest variations in inertia mass and thereby also the largest fluctuations in load pressure. As the inertia mass for HSS II is almost constant, resulting in nearly constant load pressure rendering the active feed forward gain nearly constant, and therefore without any noteworthy difference from the passive feed forward gain.

By use of state space representation and pole placement two versions of a controller have been developed - one with state feedback gain matrix, and an augmented version with feed forward contributions. The augmented state feedback gain compensator could unfortunately not be tested on the system using the rectangular trajectory, as this caused valve saturation. However, the augmented state feedback gain compensator could be tested for the system using IOT, which yielded a dramatically increased tracking performance in comparison with the controller without feed forward contributions.

Part III

A non-adaptive robust model based controller (RMC) has been presented and proved stable forming the base of for the adaptive control schemes AIDC, MAIDC and RAIDC which utilizes the same control law as the RMC, but uses adaption laws in order to continuously adapt the parameters of the control law. The augmented adaptive control schemes AAC, MAAC and RAAC uses an altered control law, where an extra proportional + integration term has been added. All adaptive control schemes have been implemented and tested in simulink, and the MAIDC and MAAC have also been implemented on the physical robot manipulator. Also an adaptive robust controller has been established and proved stable, based on the theory of [Yao et al., 2001]. It has however not been possible to obtain reasonable tracking performance for this controller within the time frame of this thesis due to difficulties in the tuning phase. An initiative will however be made to improve the performance of the ARC in order to present reasonable results at the thesis evaluation.

Furthermore in this part, two learning controllers, an ILC and a RDLC, have been established. Both learning controllers have been established using the same simplified system model as for the adaptive controllers, and were both tested on the in simulation. The controllers were however not implemented on the physical robot during this thesis, but an initiative to implement the controllers before the thesis evaluation will be carried out.

The controller parameters used in this part have all been found by trial and error, as no method for this task is available. The adaptive controllers all provided good tracking performance in simulation and when implemented on the physical system (For those implemented there). The learning function of the learning controllers has been found to perform reasonable, and it has been found that these controllers reduces tracking errors significantly as the trajectory cycles progresses. For the nonlinear controllers it is found that these may achieve even better tracking performance, if more time is spend on parameter tuning.

Part IV

In this part controllers have been evaluated by performance and robustness, but also the number of sensors necessary for implementing the controllers were taken into consideration. The controllers have been grouped into three categories - linear, adaptive and learning controllers, and within each category the controller performance has been tested on the rectangular- and in/out trajectories, and subsequently the robustness of the controllers has been tested by giving a mass step to the system at a given time during the rectangular trajectory. The peak and rms errors have then been compared to the peak and rms errors without the disturbance input, and Δ peak- and rms values have been found as an indicator of the robustness of the given compensated system towards disturbance in the form of a mass step.

It has been found that the performance of the controllers varied with the trajectory, and to which actuator they were applied, meaning that controllers showing good performance for one trajectory and actuator, could show a rather different performance for the other trajectory and actuator.

Performance of Controllers

Linear Controllers

It has been found that the best performing linear controller running the rectangular trajectory for actuator I was the PI-VFCA with a peak tracking error of 7.44 $[mm]$ and an rms error of 3.24 $[mm]$. The best performing linear controller for actuator II was the PI-VFCP with peak and rms errors of 1.95 $[mm]$ 0.63 $[mm]$ respectively. However, the difference in tracking error both rms and peak between the PI-VFCP and the PI-VFCA for link II was found to be rather small with differences of peak and rms error of 0.1 $[mm]$ and 0.11 $[mm]$, respectively.

When running the in/out trajectory in simulation, it has been found that the GFM+VFCP was the best performing linear controller for actuator I, with peak and rms errors of 1.27 $[mm]$ 0.65 $[mm]$, respectively. Unfortunately this controller could not be tested

for the RECT due to servo valve saturation. For actuator II the best performing controller was the PI-VFCP with peak and rms tracking errors of 0.92 [mm] and 0.41 [mm], respectively.

Of the linear controllers implemented on the physical system the best performance regarding peak error for actuator I, has been obtained with the PI-VFCP with an error of 10.01 [mm], whereas the best rms error performance was obtained with the Lag-VFCP, with an rms error of 4.55 [mm]. It was also noted that the difference in peak and rms errors for the PI-VFCP, Lag-VFCP and Lag-Lead-VFCP was rather small with the biggest differences being between PI-VFCP and Lag-VFCP, with differences in peak and rms errors of 0.03 [mm] and 0.18 [mm] respectively.

The peak tracking error for acuator II has been found to be smallest when using the Lag-Lead-VFCP, but the rms value is the smallest when using the PI-VFCP, which also has a peak value close to that of the Lag-Lead-VFCP. It is also seen that the controllers implemented on the physical system does perform better regarding peak error for actuator I, but generally worse regarding rms errors for both actuator I and II, and also worse regarding peak error for actuator II.

Adaptive Controllers

The adaptive controller performing the best for actuator I, running the rectangular trajectory, has been found to be the MAIDC with peak and rms errors of 4 [mm] and 1.59 [mm], respectively, and for actuator II the best performing controller is the MAAC with peak and rms errors of 0.65 [mm] 0.17 [mm], respectively. It was also noted that the difference in peak and rms error, for link II, using the MAIDC and MAAC was only 0.5 [mm] and 0.06 [mm] respectively.

The controller performance when running the in/out trajectory was found to be best for link I and II when utilizing the RAIDC and MAAC controllers respectively.

When implemented on the physical system the MAIDC performed the best for both actuator I and II with peak and rms errors of 6.97 [mm] and 1.80 [mm], respectively, for actuator I and 5.77 [mm] 1.82 [mm] respectively for actuator II.

Learning Controllers

The best performing learning controller for both the rectangular- and in/out trajectories, for both actuator I and II, was found to be the ILC. For the RECT the peak and rms errors for actuator I was 5.79 [mm] and 1.72 [mm], and for actuator II the peak and rms values was 1.64 [mm] 0.49 [mm] respectively. When running the IOT the peak and rms errors for actuator I was 1.23 [mm] and 0.35 [mm], and the peak and rms values for actuator II was 0.68 [mm] 0.32 [mm] respectively. The Difference in tracking performance between the ILC and RDLC, is assumed to be partially due to the parameter tuning for each of the controllers.

Robustness

The most robust of the tested controllers proved to be the GFM controller, which is due to the relative high damping of the compensated system. The remaining controllers showed rather similar tendencies regarding the robustness. Also it was noted that the adaptive controllers in general did not yield good robustness compared to the linear controllers, which is thought to be due to the parameter adaption not being fast enough, which was to be expected since the adaptive controllers are not meant for fast changing parameter variations.

The different tuning of the controller parameters makes the comparison difficult, since some of the controllers probably would be able to perform rather different given a better tuning. However, it can be concluded that the performance of the tested controllers varies with the trajectory, and also according to which of the actuators the controller is implemented on. Therefore the task of the servo system should be considered before choosing a controller, since this can make the difference on whether or not a given controller will yield a reasonable performance. It is also concluded that one of the best all-round performing controllers is the MAIDC, which provide reasonable good tracking performance for both the rectangular- and in/out trajectory in simulation and also for the rectangular trajectory, when implemented on the physical system.

Perspectives

During this thesis it was found that the tuning of the controller parameters naturally has great influence on the behavior of the compensated systems. For the linear controllers this did not pose a problem since it was possible to analyze the behavior of the compensated system and tune the parameters accordingly. For the non-linear controllers, it did however pose a problem since the non-linear controllers generally had more parameters which are difficult to determine, since no method for this is available. Because of this it was rather difficult to obtain consistent results, and the tuning also proved to be rather cumbersome for some of the controllers. It was also noted that some of the non-linear controllers might have performed better given a different tuning. Hence it might prove prudent to utilize optimization techniques for tuning of the parameters, and thus maybe obtain better controller performance, and a better basis of comparison of the controllers, since this process might help tuning the parameters to values closer to their optimal values.

Chapter 14

Abstract

This master thesis concerns the development and implementation of an array of controllers both linear and non-linear in order to investigate if there is something to gain by using more advanced control schemes instead of simple and linear schemes on an electro hydraulic servo system implemented by an hydraulic robot manipulator. It should be noted that this is considered mainly as a position servo.

In order to develop, test and tune the various controllers, a non-linear dynamic model of the hydraulic robot manipulator has been developed and verified by comparing pressure and position data for the physical robot manipulator, and the non-linear dynamic model. Afterwards the non-linear model has been linearized in order to obtain a linear model for tuning and analyzing the linear controllers. The linear model has been verified by comparison to the nonlinear model in a region near the operating point of the linear model.

Using the linear model for parameter tuning an array of linear controllers were developed, all including a feed forward gain contribution. Two versions of the feed forward gain have been tested, one with passive gain and one with an active gain utilizing the load pressure of the system. The controllers were added to the system yielding a compensated system which has been tuned by using frequency responses.

For establishment and testing of the more advanced non-linear controllers a simplified version of the linear model has been derived describing only a simplified version of the actuator dynamics of the system, since this was found to be the dominant part of the system. A term taking into account the modeling error, due to the simplification of the system, has also been added and the simplified system is ultimately given by a gain, an integrator, and the modeling error term.

Utilizing the simplified linear model, an array of adaptive controllers have been developed and proved stable. The adaptive controllers have been implemented on the non-linear model and the system behavior for the compensated systems have been simulated, and selected controllers have been implemented and tested on the physical system. Also two learning controllers have been developed, using the simplified linear model, and implemented and tested in the non-linear model.

The controllers treated in this thesis have been compared on peak and rms errors regarding the tracking of selected trajectories. It has been found that the performance of the

controllers to a wide extent varied depending on the chosen trajectory, indicating the importance to take into account the specific use of the hydraulic servo system when choosing a control strategy. Performance wise the comparisons showed reasonable performance for some controllers in both the linear, adaptive and learning category and it was seen that one of the best performing controllers for a specific trajectory was a state feedback gain matrix controller with an added feed forward gain. The controller with the best overall performance has been found to be a *Modified Adaptive Inverse Dynamic Controller* (MAIDC) which performed well on all tested trajectories, and also when implemented on the physical robot manipulator.

The robustness of the controllers have also been tested, by giving a disturbance input to the top link of the robot manipulator in the form of a mass step. The different tuning of the controller parameters made the comparison difficult, since some of the controllers probably would be able to perform rather different given a better tuning. However, it can be concluded that the performance of the tested controllers varies with the trajectory, and also according to which of the actuators the controller is implemented on. Therefore the task of the servo system should be considered before choosing a controller, since this can make the difference on whether or not a given controller will yield a reasonable performance.

Bibliography

[Andersen, 2003a] Andersen, T.O., H.-M. (2003a). *Fluid Power Systems, Modelling and Analysis, 2nd edition.* Institute of Energy Technology and Institute of Mechanical Engineering, Aalborg Universitet.

[Andersen, 2004a] Andersen, T.O., H.-M. (2004a). *Discrete Learning Control Application To Hydraulic Actuators.* Institute of Energy Technology and Institute of Mechanical Engineering, Aalborg Universitet.

[Andersen, 2004b] Andersen, J.A., L.-J. (2004b). *Advanced control of hydraulic servo systems.* Institut for Energiteknik, Aalborg Universitet. Master thesis.

[Andersen, 1995] Andersen, T. O. (1995). *Robust Control, Discrete Learning Control: Strategy, Convergence and Robustness.* Instituttet for Styreteknik, Danmarks Tekniske Universitet. Rapport nr. S95.51.

[Andersen, 1996] Andersen, T. O. (1996). *Adaptive Control of Hydraulic Actuators and Multivariable Hydraulic Systems.* Control Engineering Institute Technical University of Denmark.

[Andersen, 2003b] Andersen, T. O. (2003b). *Applied Nonlinear Control, Norms and Matrix Measures, Lyapunov Theory, Hyperstability.* Institut for Energiteknik, Aalborg Universitet.

[Craig, 2005] Craig, J. (2005). *Introduction to robotics - Mechanics and Control.* Prentice Hall, third edition. ISBN: 0-13-123629-6.

[Hansen, 1997] Hansen, P. E. (1997). *Autonomous and Adaptive Control of Hydraulic Actuator Systems.* Department of Control and Engineering Design, Technical University of Denmark. PhD Dissertation.

[Mohieddine Jelali, 2004] Mohieddine Jelali, A. K. (2004). *Hydraulic servo systems.* Springer, - edition. ISBN 1-85233-692-7.

[Ogata, 2002] Ogata, K. (2002). *Modern Control Engineering.* Prentice Hall, fourth edition edition. ISBN: 0-13-043245-8.

[Rasmussen, 1996] Rasmussen, W. (1996). *Hydraulik Ståbi.* Teknisk Forlag A/S, - edition. ISBN 87-571-1325-4.

[Slotine E J-J, 1991] Slotine E J-J, L. W. (1991). *Applied Nonlinear Control*. Prentice-Hall, Inc. New Jersey. ISBN: 0-13-040890-5.

[Yao et al., 2001] Yao, B., Bu, F., and Chui, G. T. (2001). *Non-linear adaptive robust control of electro-hydraulic systems driven by double-rod actuators*. International Journal of Control. ISSN 0020-7179.

Part V

Appendix

Appendix A

Dynamic Model

In this appendix, the kinematics and kinetics of the robot manipulator will be described. First the necessary kinematic constraints will be derived, followed by kinetic derivations. Finally, the dynamic model will be formulated mathematically, and the inertia, coriolis and gravitational are presented graphically. Values for characteristic lengths, masses, inertia etc. are given according to [Andersen, 2004b]

A.1 Kinematics

In this section necessary kinematic constraints for the model development is derived. This includes kinematic relations between the cylinder positions and joint angles, definition of lengths on cylinders and kinematic relations between the joint angles and the overall robot structure.

A.1.1 Kinematic Constraints Between Joint Angles & Cylinder Positions

From figure A.1 it is seen that the angle θ_I is found as:

$$\theta_I = \varphi_I - \varphi_O + \varphi_{OQ} \quad \Rightarrow \quad \varphi_I = \theta_I + \varphi_O - \varphi_{OQ} \tag{A.1}$$

The relationship between the joint angle θ_I and the total length of cylinder I and piston I, x_I, is found as:

$$\varphi_I = arccos\left(\frac{L_{OQ}^2 + L_{HO}^2 - x_I^2}{2L_{OQ}L_{HO}}\right) \tag{A.2}$$

From the above expression, x_I is determined as:

$$x_I = \sqrt{L_{OQ}^2 + L_{HO}^2 - 2L_{OQ}L_{HO}cos(\varphi_I)} \tag{A.3}$$

The velocity and acceleration are given by:

$$\dot{x}_I = \frac{2L_{OQ}L_{HO}sin(\varphi_I)\dot{\theta}_I}{2\sqrt{L_{OQ}^2 + L_{HO}^2 - 2L_{OQ}L_{HO}cos(\varphi_I)}} \tag{A.4}$$

$$\ddot{x}_I = \frac{2L_{OQ}L_{HO}cos(\varphi_I)\dot{\theta}_I^2 + sin(\varphi_I)\ddot{\theta}_I}{2\sqrt{L_{OQ}^2 + L_{HO}^2 - 2L_{OQ}L_{HO}cos(\varphi_I)}} - \frac{(2L_{OQ}L_{HO})^2 sin^2(\varphi_I)\dot{\theta}_I^2}{4(L_{OQ}^2 + L_{HO}^2 - 2L_{OQ}L_{HO}cos(\varphi_I))^{2/3}} \tag{A.5}$$

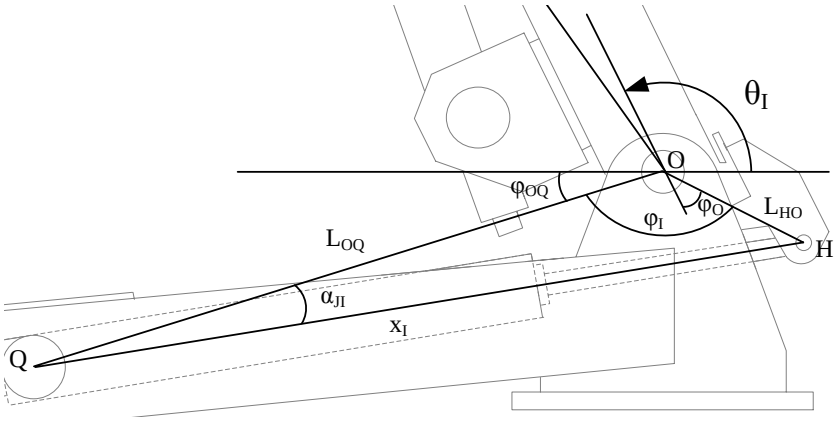

Figure A.1: Sketch forming the base for derivation of expressions describing the positions, velocities and accelerations internally on the robot manipulator.

From figure A.2 the angle θ_{II} is found as:

$$\varphi_{II1} - \varphi_B + \varphi_{BGO} = -\theta_{II} \quad \Rightarrow \quad \varphi_{II1} = -\theta_{II} + \varphi_B - \varphi_{BGO} \tag{A.6}$$

The the relationship between the joint angle θ_{II} and x_{II} is found as:

$$\varphi_{II1} = arccos\left(\frac{L_{BW}^2 + L_{BG}^2 - x_{II}^2}{2L_{BW}L_{BG}}\right) \tag{A.7}$$

From the above expression x_I is determined as:

$$x_{II} = \sqrt{L_{BW}^2 + L_{BG}^2 - 2L_{BW}L_{BG}cos(\varphi_{II1})} \tag{A.8}$$

Similar to the previous joint angle, the velocity and acceleration are given by:

$$\dot{x}_{II} = \frac{2L_{BW}L_{BG}sin(\varphi_{II1})\dot{\theta}_{II}}{2\sqrt{L_{BW}^2 + L_{BG}^2 - 2L_{BW}L_{BG}cos(\varphi_{II1})}} \tag{A.9}$$

$$\begin{aligned}\ddot{x}_{II} = &\frac{2L_{BW}L_{BG}cos(\varphi_{II1})\dot{\theta}_{II}^2 + sin(\varphi_{II1})\ddot{\theta}_{II}}{2\sqrt{L_{BW}^2 + L_{BG}^2 - 2L_{BW}L_{BG}cos(\varphi_{II1})}} \\ &- \frac{(2L_{BW}L_{BG})^2 sin^2(\varphi_{II1})\dot{\theta}_{II}^2}{4(L_{BW}^2 + L_{BG}^2 - 2L_{BW}L_{BG}cos(\varphi_{II1}))^{2/3}}\end{aligned} \tag{A.10}$$

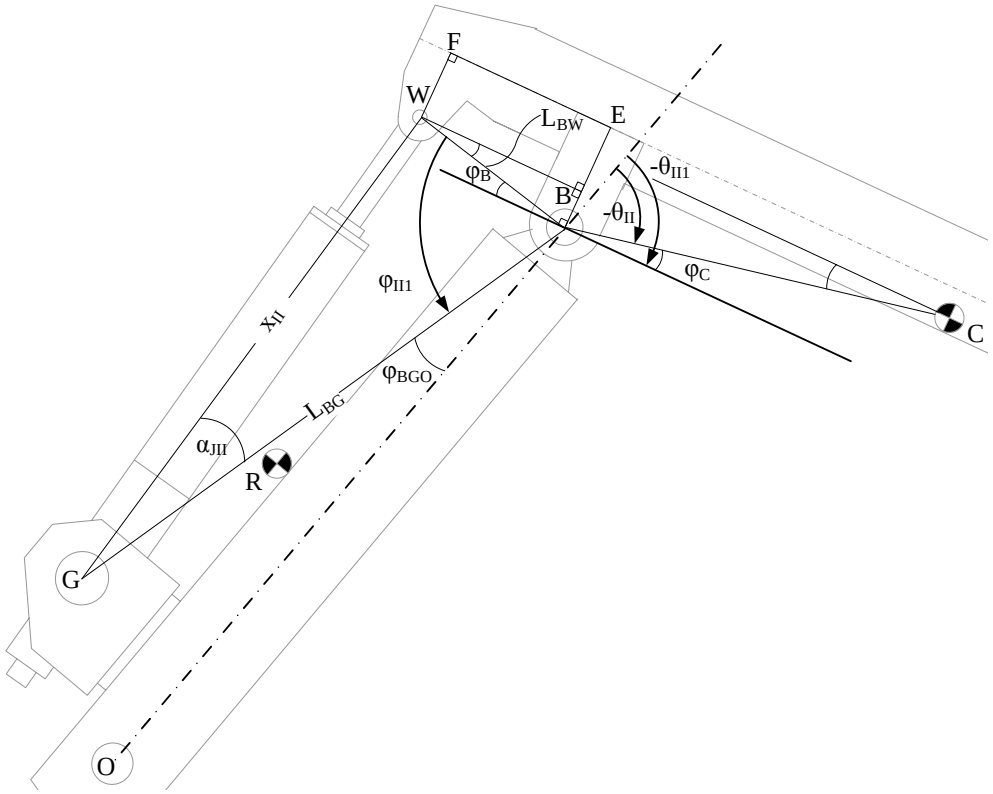

Figure A.2: Sketch forming the base for derivation of expressions describing the positions, velocities and accelerations internally on the robot manipulator.

A.1.2 Additional Necessary Constraints

Later in this appendix, some additional angles are needed in order to calculate the torque arms, relating the cylinder force to the joint torques. Hence the following angles α_{JI} and α_{JII} are obtained (see figures A.1 and A.2, respectively).

$$\alpha_{JI} = arccos\left(\frac{L_{OQ}^2 + x_I^2 - L_{HO}^2}{2L_{HO}x_{II}}\right) \tag{A.11}$$

$$\alpha_{JII} = arccos\left(\frac{L_{BG}^2 + x_{II}^2 - L_{BW}^2}{2L_{BG}x_{II}}\right) \tag{A.12}$$

A.1.3 Definition of x_I & x_{II}

The definitions for the cylinder positions are shown in figure A.3.

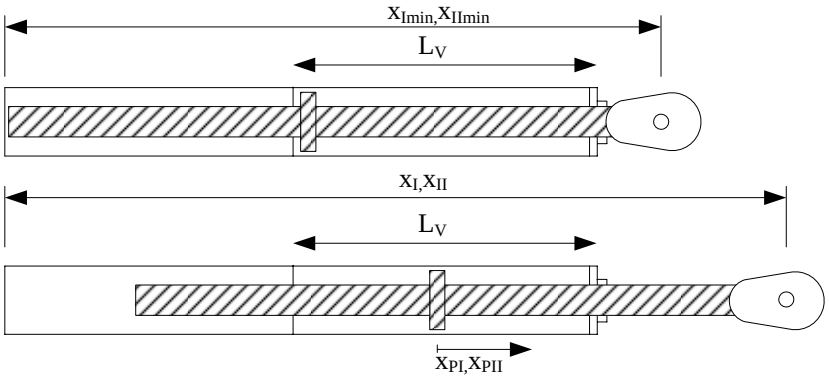

Figure A.3: Definition of cylinder lengths.

The nomenclature of figure A.3, is:

x_I, x_{II}:	total length of cylinder plus piston	$[m]$
x_{PI}, x_{PII}:	piston position	$[m]$
x_{Imin}, x_{IImin}:	minimum length of cylinder	$[m]$
L_V:	stroke length	$[m]$

As it is seen from the figure above, the reference point is defined at the center of the cylinders, and hence the total lengths of cylinders plus pistons are defined as:

$$x_I = xImin + L_V/2 + x_{PI} \quad \wedge \quad x_{II} = xIImin + L_V/2 + x_{PII} \tag{A.13}$$

A.2 Positions, Velocities & Accelerations of Point C

In this subsection the expressions describing the position, velocities and accelerations of key points internally on the robot manipulator will be derived. This derivation is based on figure A.4.

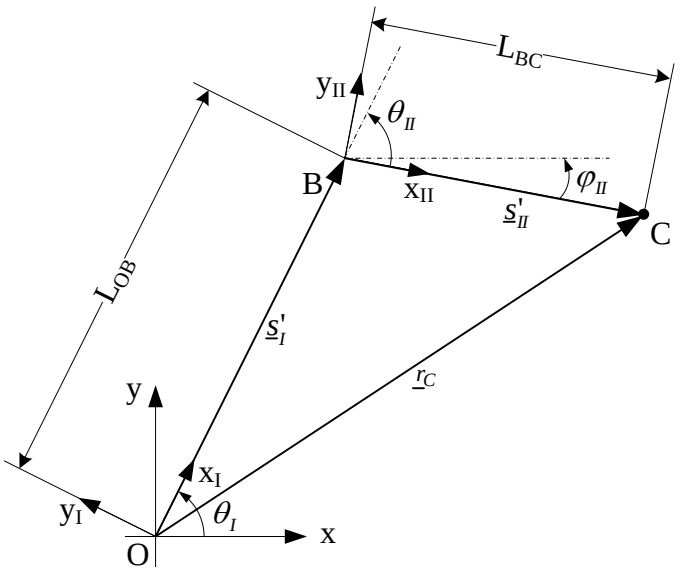

Figure A.4: Sketch forming the base for derivation of expressions describing the positions, velocities and accelerations internally on the robot manipulator.

The nomenclature of figure A.4, is:

x, y:	global coordinate system	$[-]$
x_I, y_I:	local coordinate system for link I	$[-]$
x_{II}, y_{II}:	local coordinate system for link II	$[-]$
$\underline{s}'_I$:	position B, relative to coordinate system I	$[m]$
$\underline{s}'_{II}$:	position C, relative to the local coordinate system II	$[m]$
$\underline{\underline{A}}_I$:	rotational matrix for link I relative to global	$[-]$
$\underline{\underline{A}}_{II}$:	rotational matrix for link II relative to global	$[-]$
θ_I:	angle between link I and global	$[rad]$
θ_{II}:	angle between link II and link I	$[rad]$
φ_{II}:	angle between link II and global	$[rad]$
L_{OB}:	length between point A and B	$[m]$
L_{BC}:	length between point B and G	$[m]$

First the different vectors and rotational matrices are established, and these are given by:

$$\underline{s}'_I = \begin{bmatrix} L_{OB} & 0 \end{bmatrix}^T \quad , \quad \underline{s}'_{II} = \begin{bmatrix} L_{BC} & 0 \end{bmatrix}^T \tag{A.14}$$

$$\underline{\underline{A}}_I = \begin{bmatrix} cos(\theta_I) & -sin(\theta_I) \\ sin(\theta_I) & cos(\theta_I) \end{bmatrix} \quad , \quad \underline{\underline{A}}_{II} = \begin{bmatrix} cos(\varphi_{II}) & -sin(\varphi_{II}) \\ sin(\varphi_{II}) & cos(\varphi_{II}) \end{bmatrix} \tag{A.15}$$

The position of the center of mass for link II can now be described as:

$$\underline{r}_C = \underline{\underline{A}}_I \underline{s}'_I + \underline{\underline{A}}_{II} \underline{s}'_{II} = \begin{bmatrix} cos(\theta_I)L_{OB} + cos(\varphi_G)L_{BC} \\ sin(\theta_I)L_{OB} + sin(\varphi_G)L_{BC} \end{bmatrix} \tag{A.16}$$

Taking the first time derivative of expression A.16, yields the velocity vector:

$$\underline{\dot{r}}_C = \begin{bmatrix} -sin(\theta_I)\dot{\theta}_I L_{OB} - sin(\varphi_{II})\dot{\varphi}_{II} L_{BC} \\ cos(\theta_I)\dot{\theta}_I L_{OB} + cos(\varphi_{II})\dot{\varphi}_{II} L_{BC} \end{bmatrix} \tag{A.17}$$

And the second time derivative of expression A.16, yields the acceleration vector:

$$\underline{\ddot{r}}_C = \begin{bmatrix} -cos(\theta_I)\dot{\theta}_I^2 L_{OB} - sin(\theta_I)\ddot{\theta}_I L_{OB} - cos(\varphi_{II})\dot{\varphi}_{II}^2 L_{BC} - sin(\varphi_{II})\ddot{\varphi}_{II} L_{BC} \\ -sin(\theta_I)\dot{\theta}_I^2 L_{OB} + cos(\theta_I)\ddot{\theta}_I L_{OB} - sin(\varphi_{II})\dot{\varphi}_{II}^2 L_{BC} + cos(\varphi_{II})\ddot{\varphi}_{II} L_{BC} \end{bmatrix} \tag{A.18}$$

A.3 Force & Torque Equilibriums for Link I

The kinetic diagram for link I is shown in figure A.5.

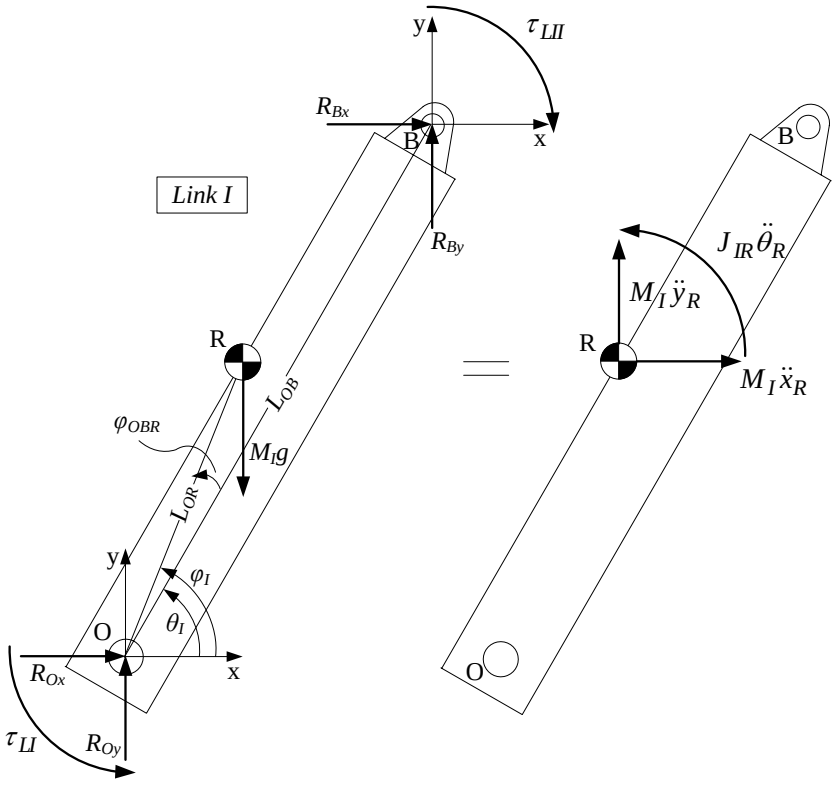

Figure A.5: Kinetic diagram for link I.

From figure A.5, the following force and torque equilibrium equations can be established:

$$\sum F_{Ix} = R_{Ox} + R_{Bx} = M_I \ddot{x}_R \tag{A.19}$$

$$\sum F_{Iy} = R_{Oy} + R_{By} - M_I g = M_I \ddot{y}_R \tag{A.20}$$

Taking the torque equilibrium about point O, yields:

$$\sum M_{IO} = \tau_{LI} - \tau_{LII} - R_{Bx}L_{OB}sin(\theta_I) + R_{By}L_{OB}cos(\theta_I) - M_I g L_{OR}cos(\varphi_I) \quad (A.21)$$

$$= J_{IO} \cdot \ddot{\theta}_I \quad (A.22)$$

Here $\varphi_I = \theta_I + \varphi_{OBR}$.

A.4 Force & Torque Equilibriums for Link II

The kinetic diagram for link II is shown in figure A.6.

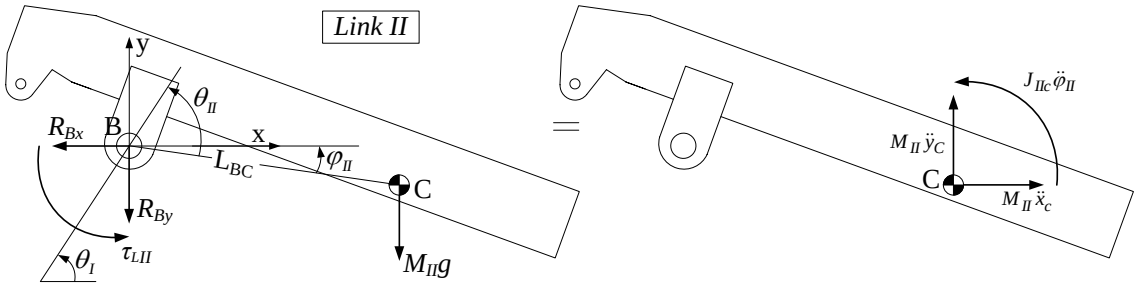

Figure A.6: Kinetic diagram for link II.

From figure A.6, the following force and torque equilibrium equations can be established:

$$\sum F_{IIx} = -R_{Bx} = M_{II}\ddot{x}_C \quad (A.23)$$

$$\sum F_{IIy} = -R_{By} - M_{II}g = M_{II}\ddot{y}_C \quad (A.24)$$

Here $\varphi_{II} = \theta_I - \theta_{II}$. Taking the torque equilibrium about point G, yields:

$$\sum M_{IIG} = \tau_{LII} + R_{Bx}L_{BC}sin(\varphi_{II}) + R_{By}L_{BC}cos(\varphi_{II}) = J_{IIG} \cdot \ddot{\varphi}_{II} \quad (A.25)$$

A.5 Mass Properties for Link I

In the following the total mass of link I, and the mass moment of inertia about point A are derived. Furthermore, due to the relative large masses of the hydraulic cylinders, the torque produced about point B due to the reaction forces at point F is derived.

A.5.1 Total Mass of Link I

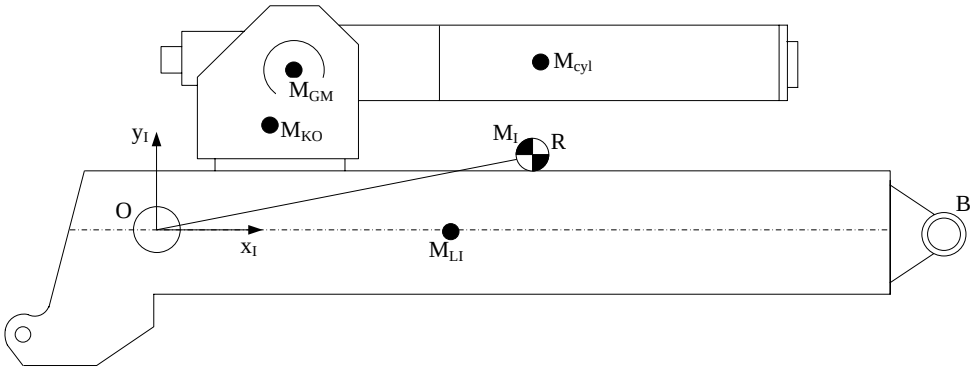

Figure A.7: Sketch forming the base for derivation of the center of mass for link I.

It is seen from figure A.7, that the total mass of link I is given by:

$$\sum M_{linkI} = M_I = M_{GM} + M_{KO} + M_{LI} + M_{cyl} \tag{A.26}$$

A.5.2 Mass Moment of Inertia for Link I

From figure A.7 (A) it is seen, that the mass moment of inertia of link I about point A, is given by:

$$J_{IO} = J_{IR} + M_I L_{OH}^2 \tag{A.27}$$

A.6 Mass Properties for Link II

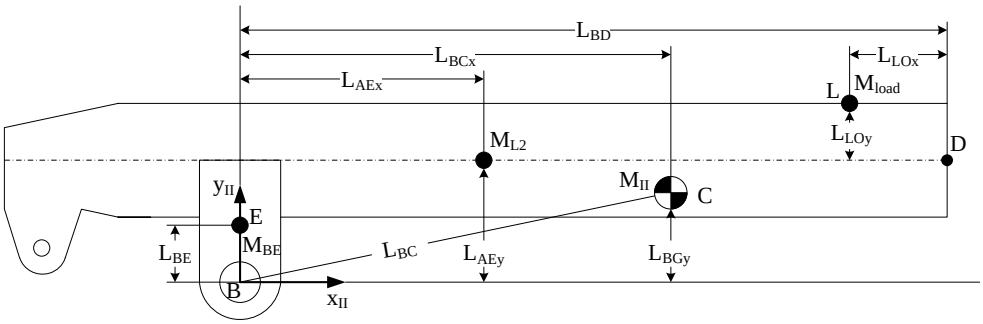

Figure A.8: Sketch forming the base for derivation of the center of mass for link II.

A.6.1 Center of Mass for Link II

The total mass of link II is given by:

$$\sum M_{linkII} = M_{II} = M_{L2} + M_{load} + M_{BE} \tag{A.28}$$

$$\tag{A.29}$$

Due to the fact that load can vary, the position of the center of mass can vary, and hence an expression for this position is described. Related to the local coordinate system for link II (x_{II}, y_{II}), the position of the center of mass is for the x_{II}-position:

$$\sum M_{linkII} L_{BCx} = M_{II} L_{BCx} = M_{L2} L_{AEx} + M_{load}(L_{BD} - L_{LOX}) \tag{A.30}$$

$$L_{BCx} = \frac{M_{L2} L_{AEx} + M_{load}(L_{BD} - L_{LOX})}{M_{II}} \tag{A.31}$$

And for the y_{II}-position:

$$\sum M_{linkII} L_{BCy} = M_{II} L_{BCy} = M_{L2} L_{AEy} + M_{load}(L_{AEy} + L_{LOy}) + M_{BE} L_{BE} \tag{A.32}$$

$$L_{BCy} = \frac{M_{L2} L_{AEy} + M_{load}(L_{AEy} + L_{LOy}) + M_{BE} L_{BE}}{M_{II}} \tag{A.33}$$

The length between point B and G is then given by:

$$L_{BC} = \sqrt{L_{BCx}^2 + L_{BCy}^2} \tag{A.34}$$

In the expressions above, the nomenclature is:

L_{BCx}:	length from point B to point G (x-direction)	0.353 / 0.632	$[m]$
L_{BCy}:	length from point B to point G (y-direction)	0.130 / 0.213	$[m]$
L_{BC}:	length from point B to point G	0.376 / 0.667	$[m]$
L_{AEx}:	length from point B to point K (x-direction)	0.420	$[m]$
L_{AEy}:	length from point B to point K (y-direction)	0.142	$[m]$
L_{BD}:	length from point B to point N	1.080	$[m]$
L_{LOx}:	length from point L to point N	0.200	$[m]$
L_{LOy}:	length from point K to point L	0.145	$[m]$
L_{BE}:	length from point B to point J	0.071	$[m]$
M_{BE}:	mass of bearing housing at point B	7.800	$[kg]$
M_{L2}:	mass of link II	38.000	$[kg]$
M_{load}:	mass of load	0.000 / 50	$[kg]$
M_{II}:	total mass of link II	45.800 / 95.800	$[kg]$

The above values has been obtained from [Andersen, 2004b]

A.6.2 Mass Moment of Inertia for Link II

The mass moment of inertia about point B is given by:

$$J_{IIC}^{C} = J_{L2}^{C} + J_{AEx}^{C} + J_{load}^{C} \tag{A.35}$$

Using the parallel axis theorem to find the mass moment of inertia about point G, yields:

$$J^B_{IIC} = J^C_{IIC} + M_{II}L^2_{BC} \tag{A.36}$$

A.7 Formulating the Describing Equations in Joint Space

In the following, the model will be established in cylinder space by use of the describing equations derived in the previous sections of the present appendix.

To be able to sustain the overview, the describing equations are presented again.

$$\ddot{x}_G = -cos(\theta_I)\dot{\theta}^2_I L_{OB} - sin(\theta_I)\ddot{\theta}_I L_{OB} - cos(\varphi_{II})\dot{\varphi}^2_{II} L_{BC} - sin(\varphi_{II})\ddot{\varphi}_{II} L_{BC} \tag{A.37}$$

$$\ddot{y}_G = -sin(\theta_I)\dot{\theta}^2_I L_{OB} + cos(\theta_I)\ddot{\theta}_I L_{OB} - sin(\varphi_{II})\dot{\varphi}^2_{II} L_{BC} + cos(\varphi_{II})\ddot{\varphi}_{II} L_{BC} \tag{A.38}$$

$$\tau_{LI} = J_{IA}\ddot{\theta}_I + \tau_{LII} + R_{Bx}L_{OB}sin(\theta_I) - R_{By}L_{OB}cos(\theta_I) + M_I g L_{OR}cos(\varphi_I) \tag{A.39}$$

$$\tau_{LII} = J_{IIG}\ddot{\varphi}_{II} - R_{Bx}L_{BC}sin(\varphi_{II}) - R_{By}L_{BC}cos(\varphi_{II}) \tag{A.40}$$

$$R_{Bx} = -M_{II}\ddot{x}_G \tag{A.41}$$

$$R_{By} = -M_{II}g - M_{II}\ddot{y}_G \tag{A.42}$$

The model is expressed by use of the Newton-Euler formulation, given by:

$$\underline{\tau_L} = [\tau_{LI}\ \tau_{LII}]^T = \underline{\underline{D}}(\underline{q})\ddot{\underline{q}} + \underline{H}(\underline{q}, \dot{\underline{q}}) + \underline{G}(\underline{q}) \tag{A.43}$$

Substituting the above equations and substituting $\varphi_{II} = \theta_I - \theta_{II}$, the Newton-Euler formulation is obtained. The elements of $\underline{\underline{D}}(\underline{q})$, $\underline{H}(\underline{q}, \dot{\underline{q}})$ and $\underline{G}(\underline{q})$ are found on the appended CD, in the Maple file *Newton Euler Joint Space*.

A.8 Formulating the Describing Equations in Actuator Space

In this section the dynamic equations are formulated in actuator space. Expression A.43 are related to the linear forces provided by the hydraulic actuators by the *drive jacobian* $\underline{\underline{J}}_d$, yielding:

$$\underline{\tau_L} = \underline{\underline{J}}^T_d \underline{F_L} \tag{A.44}$$

Where:

$$\underline{\tau_L} = [\tau_{LI}\ \tau_{LII}]^T \quad , \quad \underline{F_L} = [F_{LI}\ F_{LII}]^T \quad , \quad \underline{\underline{J}}^T_d = \begin{bmatrix} L_{OQ}sin(\alpha_{JI}) & 0 \\ 0 & -L_{BG}sin(\alpha_{JII}) \end{bmatrix}$$

Hence the non-linear dynamic model of the solid state part of the system compliant with the hydraulic system, is established as:

$$\underline{F_L} = \underline{\underline{J}}_d^{-T}\underline{\tau_L} = \underline{\underline{J}}_d^{-T}\underline{\underline{D}}(\underline{q})\ddot{\underline{q}} + \underline{J}_d^{-T}\underline{H}(\underline{q},\dot{\underline{q}}) + \underline{\underline{J}}_d^{-T}\underline{G}(\underline{q}) \tag{A.45}$$

The $\underline{\underline{J}}_d$ transpose provides the torque arms, and hence the perpendicular distance from the cylinder line of action, to the joints, relating the cylinder forces to the joint torques. In order to express equation B.3 in terms of the cylinder positions, the definition of the drive jacobian is used:

$$\underline{x}_P = \underline{\underline{J}}_d\underline{q} \tag{A.46}$$

The piston velocities $\dot{\underline{x}}_P$ and accelerations $\ddot{\underline{x}}_P$, are obtained as:

$$\dot{\underline{x}}_P = \underline{\underline{J}}_d\dot{\underline{q}} \quad , \quad \ddot{\underline{x}}_P = \dot{\underline{\underline{J}}}_d\dot{\underline{q}} + \underline{\underline{J}}_d\ddot{\underline{q}} \tag{A.47}$$

Isolating the last expression above, yields:

$$\underline{\underline{J}}_d\ddot{\underline{q}} = \dot{\underline{\underline{J}}}_d\dot{\underline{q}} - \dot{\underline{x}}_P \tag{A.48}$$

$$\ddot{\underline{q}} = \underline{\underline{J}}_d^{-1}\ddot{\underline{x}}_P - \underline{\underline{J}}_d^{-1}\dot{\underline{\underline{J}}}_d\dot{\underline{q}} \tag{A.49}$$

Substituting the expression for $\dot{\underline{q}}$, yields:

$$\underline{F_L} = \underline{\underline{J}}_d^{-T}\underline{\underline{D}}(\underline{q})(\underline{\underline{J}}_d^{-1}\ddot{\underline{x}}_P - \underline{\underline{J}}_d^{-1}\dot{\underline{\underline{J}}}_d\dot{\underline{q}}) + \underline{J}_d^{-T}\underline{H}(\underline{q},\dot{\underline{q}})\underline{\underline{J}}_d^{-1} + \underline{\underline{J}}_d^{-T}\underline{G}(\underline{q}) \tag{A.50}$$

$$= \underline{\underline{J}}_d^{-T}\underline{\underline{D}}(\underline{q})\underline{\underline{J}}_d^{-1}\ddot{\underline{x}}_P + (\underline{J}_d^{-T}\underline{H}(\underline{q},\dot{\underline{q}})\underline{\underline{J}}_d^{-1} - \underline{\underline{J}}_d^{-T}\underline{\underline{D}}(\underline{q})\underline{\underline{J}}_d^{-1}\dot{\underline{\underline{J}}}_d\dot{\underline{q}}) + \underline{\underline{J}}_d^{-T}\underline{G}(\underline{q}) \tag{A.51}$$

Hence the cylinder forces are expressed in terms of the piston velocities and accelerations. The inertia-, coriolis and gravitational terms are then given in actuator space, as:

$$\underline{\underline{M}}_{x_P}(\underline{q}) = \begin{bmatrix} M_{x_P11}(\underline{q}) & M_{x_P12}(\underline{q}) \\ M_{x_P21}(\underline{q}) & M_{x_P22}(\underline{q}) \end{bmatrix} = \underline{\underline{J}}_d^{-T}\underline{\underline{D}}(\underline{q})\underline{\underline{J}}_d^{-1} \tag{A.52}$$

$$\underline{V}_{x_P}(\underline{q},\dot{\underline{q}}) = \begin{bmatrix} V_{x_P11}(\underline{q}) & V_{x_P12}(\underline{q}) \\ V_{x_P21}(\underline{q}) & V_{x_P22}(\underline{q}) \end{bmatrix} = (\underline{J}_d^{-T}\underline{H}(\underline{q},\dot{\underline{q}})\underline{\underline{J}}_d^{-1} - \underline{\underline{J}}_d^{-T}\underline{\underline{D}}(\underline{q})\underline{\underline{J}}_d^{-1}\dot{\underline{\underline{J}}}_d\underline{\underline{J}}_d^{-1}) \tag{A.53}$$

$$\underline{G}_{x_P}(\underline{q}) = \begin{bmatrix} G_{x_P1}(\underline{q}) \\ G_{x_P2}(\underline{q}) \end{bmatrix} = \underline{\underline{J}}_d^{-T}\underline{G}(\underline{q}) \tag{A.54}$$

By substituting expressions $\underline{q}$, $\dot{\underline{q}}$ and $\ddot{\underline{q}}$, the formulation in actuator space is obtained as:

$$\underline{F_L} = \underline{\underline{M}}_{x_P}(\underline{x}_P)\ddot{\underline{x}}_P + \underline{\underline{V}}_{x_P}(\underline{x}_P,\dot{\underline{x}}_P) + \underline{G}_{x_P}(\underline{x}_P)\underline{x}_P \tag{A.55}$$

The model is now formulated in actuator space. However, friction phenomenons are present, hence coulomb and viscous friction elements are added, acting in the opposite direction of the cylinder force, which yields:

$$\underline{F_L} = \underline{\underline{M}}_{x_P}(\underline{x}_P)\ddot{\underline{x}}_P + \underline{\underline{V}}_{x_P}(\underline{x}_P,\dot{\underline{x}}_P) + \underline{G}_{x_P}(\underline{x}_P) + \underline{B}_v^T\dot{\underline{x}}_P + \underline{F}_c^T sign(\dot{\underline{x}}_P) \tag{A.56}$$

The inertia, coriolis and gravitational terms are shown in figures A.9, A.10, A.11, A.12 and A.13, respectively.

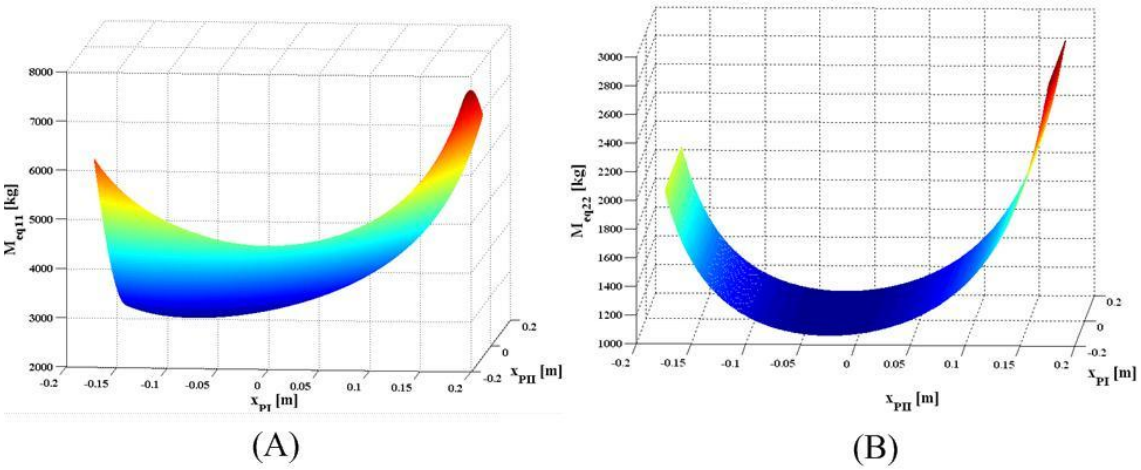

Figure A.9: (A) Equivalent mass for cylinder I, M_{eq11}. (B) Equivalent mass for cylinder II, M_{eq22}.

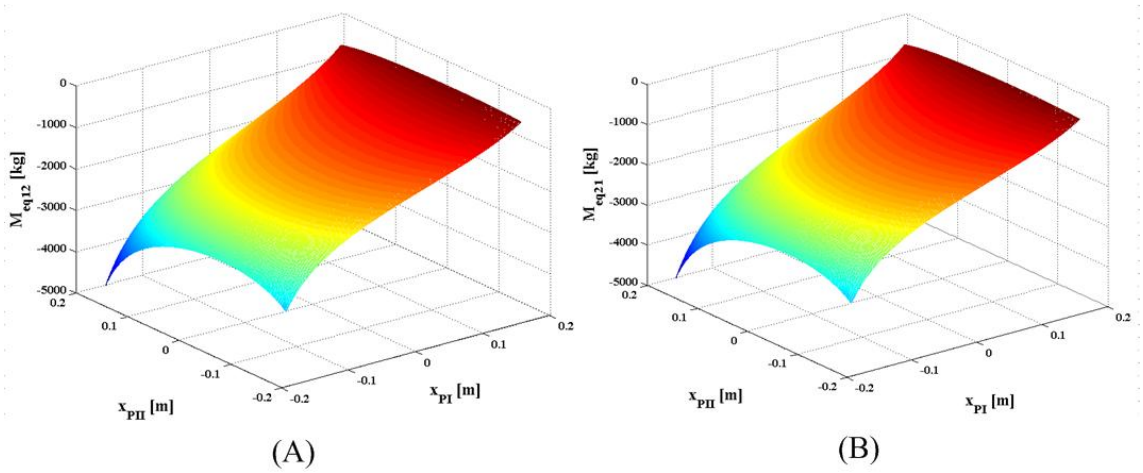

Figure A.10: (A) Equivalent mass representing the dynamic coupling between cylinders, M_{eq12}. (B) Equivalent mass representing the dynamic coupling between cylinders, M_{eq21}.

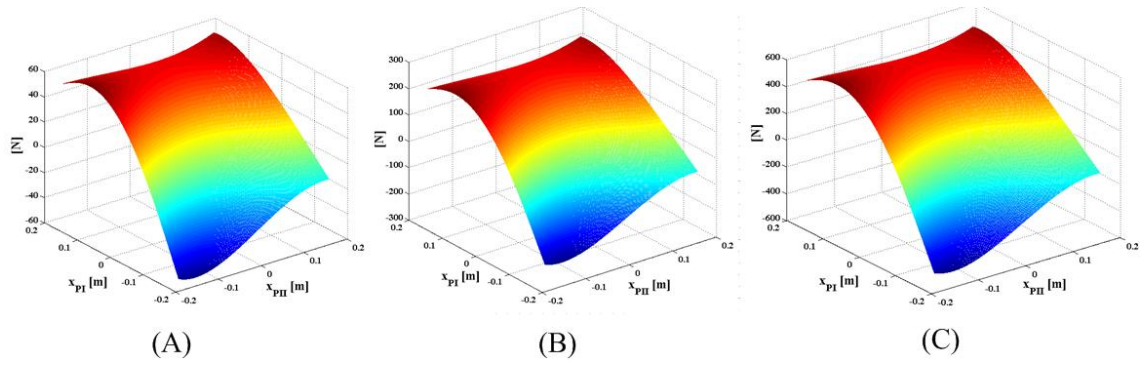

Figure A.11: Coriolis terms for cylinder I. (A) Tested with piston velocities $\dot{x}_I = \dot{x}_{II} = 0.25\ [m/s]$. (B) Tested with piston velocities $\dot{x}_I = \dot{x}_{II} = 0.50\ [m/s]$. (C) Tested with piston velocities $\dot{x}_I = \dot{x}_{II} = 0.75\ [m/s]$

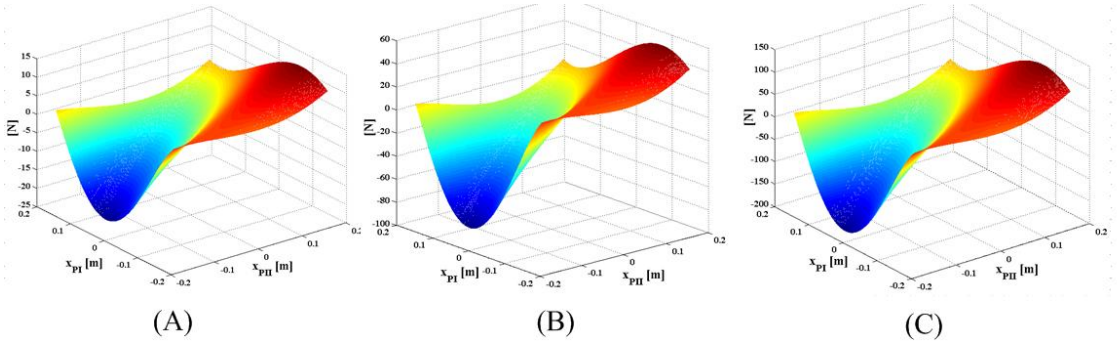

Figure A.12: Coriolis terms for cylinder II. (A) Tested with piston velocities $\dot{x}_I = \dot{x}_{II} = 0.25\ [m/s]$. (B) Tested with piston velocities $\dot{x}_I = \dot{x}_{II} = 0.50\ [m/s]$. (C) Tested with piston velocities $\dot{x}_I = \dot{x}_{II} = 0.75\ [m/s]$

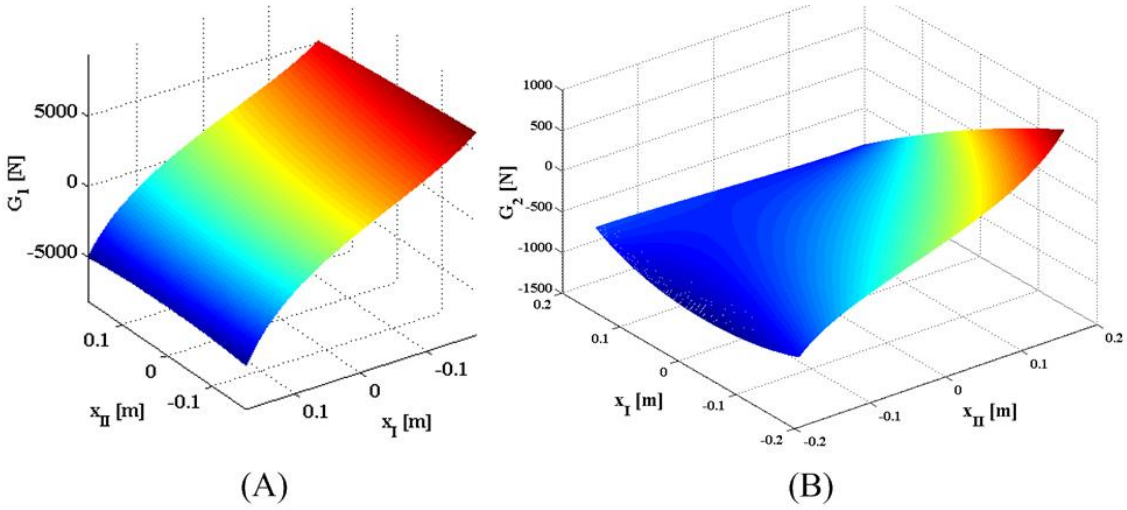

Figure A.13: (A) Gravitational term for cylinder I. (B) Gravitational term for cylinder II.

A.9 Hydraulic Model

In this section a non-linear model of the fluid mechanical system will be developed. First the fluid mechanical system will be described and the governing equations for describing the model will be deduced. This appendix takes base in [Andersen, 2003a]. The derivations takes base in figure A.14. In the following the index i can either denote actuator I or II.

A.9.1 Modeling of Cylinders

Since both cylinders on the robot have the same specifications the equation deduced in the following will be general and valid for both cylinders. The equations are deduced based on figure A.14.

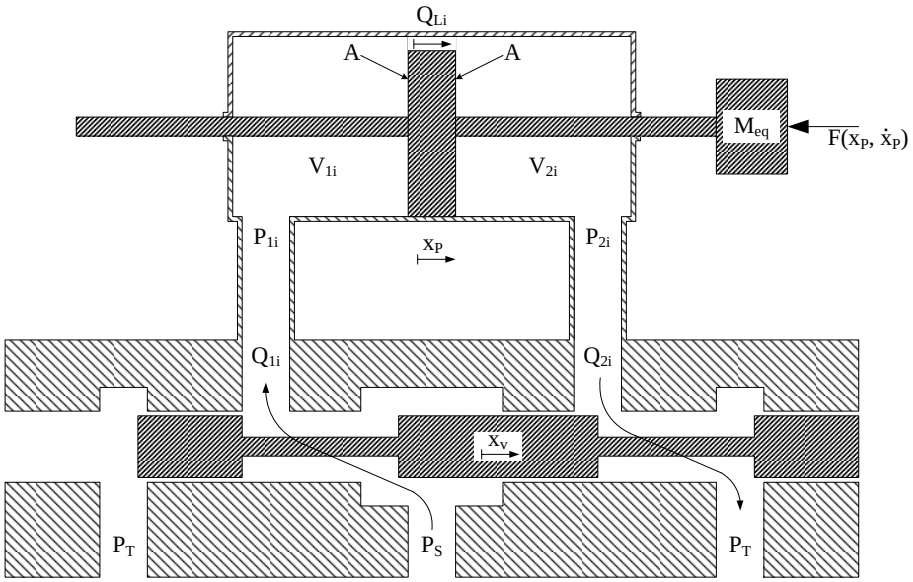

Figure A.14: Sketch of cylinder/servo valve setup

Equilibrium Equation

The force equilibrium equation is given by equation A.57

$$\sum F_x = M_{eqi} \cdot \ddot{x}_P = P_{1i} \cdot A - P_{2i} \cdot A - \alpha - B_{vi} \cdot \dot{x} - F_D(x_P, \dot{x}_P) \tag{A.57}$$

Where:

M_{eq}:	Equivalent mass	$[kg]$
$\ddot{x}_P$:	Acceleration of cylinder piston	$[m/s^2]$
P_{1i}:	Pressure on side 1	$[Pa]$
P_{2i}:	Pressure on side 2	$[Pa]$
A:	Piston area	$[m^2]$
α:	Coulomb friction	$[-]$
B_{vi}:	Viscous damping coefficient	$[-]$
$\dot{x}_P$:	Velocity of cylinder piston	$[m/s^2]$
$F(x_P, \dot{x}_P)$:	Force from robot acting on piston rod	$[m/s^2]$

Continuity Equations

The continuity equations are given by A.58 and A.59.

$$Q_{1i} - Q_{LEi} = \frac{dV_1}{dt} + \frac{V_{1i}}{\beta_{Fi}} \cdot \frac{dP_{1i}}{dt} \tag{A.58}$$

$$Q_{LEi} - Q_2 i = \frac{dV_2}{dt} + \frac{V_{2i}}{\beta_{Fi}} \cdot \frac{dP_{2i}}{dt} \tag{A.59}$$

Where:

Q_{1i}:	Flow into cylinder on side 1	$[m^3/s]$
Q_{2i}:	Flow out of cylinder on side 2	$[mm^3/s]$
Q_{LEi}:	Leakage flow between cylinder wall and piston	$[m^3/s]$
V_{1i}:	Chamber volume on side 1 of the cylinder	$[m^3]$
V_{2i}:	Chamber volume on side 2 of the cylinder	$[m^3]$
β_{Fi}:	Bulk modulus	$[bar]$
P_{1i}:	Pressure on side 1	$[Pa]$
P_{2i}:	Pressure on side 2	$[Pa]$

A.9.2 Modeling of Servo Valves

Subsequently the equations describing the flows through the servo valve are deduced. Equations A.60 and A.61 describe the flows when the servo valve plunger is displaced in the positive direction.

$$Q_{1i} = K_{vi} u_{vi} sign(P_S - P_{1i}) \sqrt{|P_S - P_{1i}|} \tag{A.60}$$

$$Q_{2i} = K_{vi} u_{vi} sign(P_{2i} - P_T) \sqrt{|P_{2i} - P_T|} \tag{A.61}$$

Equations A.62 and A.63 describe the flows when the servo valve plunger is displaced in the negative direction.

$$Q_{1i} = K_{vi} u_{vi} sign(P_{1i} - P_T) \sqrt{|P_{1i} - P_T|} \tag{A.62}$$

$$Q_{2i} = K_{vi} u_{vi} sign(P_S - P_{2i}) \sqrt{|P_S - P_{2i}|} \tag{A.63}$$

Where:

K_{vi}:	Flow value gain for the orifice	$[-]$
u_{vi}:	Servo valve input voltage	$[V]$
P_T:	Tank pressure	$[Pa]$
P_S:	Supply pressure	$[Pa]$

Establishment of Flow Value Gain K_{vi}

In the following values for the flow value gain for both the Rexroth and the Moog servo valves will be found. In figure A.15 a principal sketch of a servo valve at no load conditions is shown. Since the both servo valves are symmetrical valves it follows that K_{vi} goes for both orifices and thus the pressure drop over each of the orifices is given by $P_s - P_1 = P_2 - P_T = \Delta P$.This yields:

$$Q_{nom} = K_{vi} u_{vi} \sqrt{\Delta P} \tag{A.64}$$

Where:

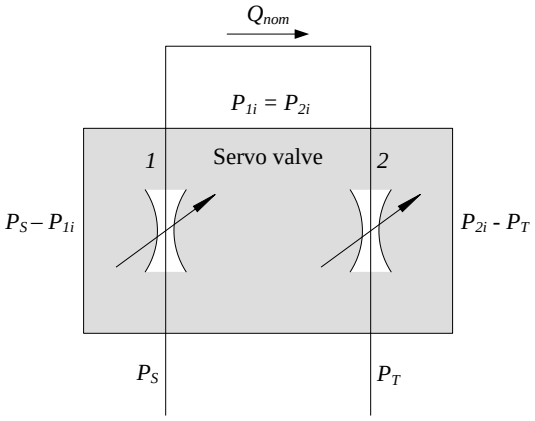

Figure A.15: Sketch of servo valve at no-load

Q_{nom}:	Nominal flow for arbitrary servo valve	$[-]$
K_{vi}:	Flow value gain for arbitrary symmetrical servo valve	$[-]$
δP:	Pressure drop over servo valve orifice	$[V]$

Isolating K_{vi} yields,

$$K_{vi} = \frac{Q_{nom}}{u_{vi}\sqrt{\delta P}} \tag{A.65}$$

The value of K_{vi} can now be found for both the Moog and the Rexroth servo valves. Since no data sheets for the exact model numbers of either of the servo valves were available at the time of writing, values for Q_nom, u_{vi} and ΔP was found in [Andersen, 2004b].

Servo Valve Dynamics

Usually the dynamics of a servo valve can be approximated with a second order system of the form of equation A.66, which is also assumed in this thesis. In order to describe the 2.order system the damping ζ and undamped natural frequency ω_n of the servo valve need to be found. This is also usually done by use of data sheets for the servo valves, however these values are also found in [Andersen, 2004b].

$$H(s) = \frac{\omega_n^2}{s^2 + 2\zeta\omega_n s + \omega_n^2} \tag{A.66}$$

Bulk Modulus

Since Bulk modulus varies with pressure, temperature and amount of air entrapped in the oil it is not desirable to use a constant bulk modulus but rather calculate and estimate continuously. According to [Mohieddine Jelali, 2004] most of the entrapped oil dissolves into the oil at higher pressures, and does therefore not affect the Bulk modulus. If assuming that the temperature of the oil is relative constant only the pressure is left to alter the value of Bulk modulus. In the Simulink model of the hydraulic system Bulk modulus is calculated by use of an empirical formula given by equation A.67, proposed

in [Mohieddine Jelali, 2004].

$$E'(p) = a_1 E_{max} log(a_2 \frac{p}{p_{max}} + a_3) \tag{A.67}$$

Where $a_1 = 0.5$, $a_2 = 90$, and $a_3 = 3$ are empirical values, and the maximum value of bulk modulus and the pressure are given as E_{max} and p_{max}, respectively.

A.10 Additional Verification Plots for the Nonlinear Model

In the following, addition verification plots for the nonlinear model is shown. Here the gravitation for link II is shown.

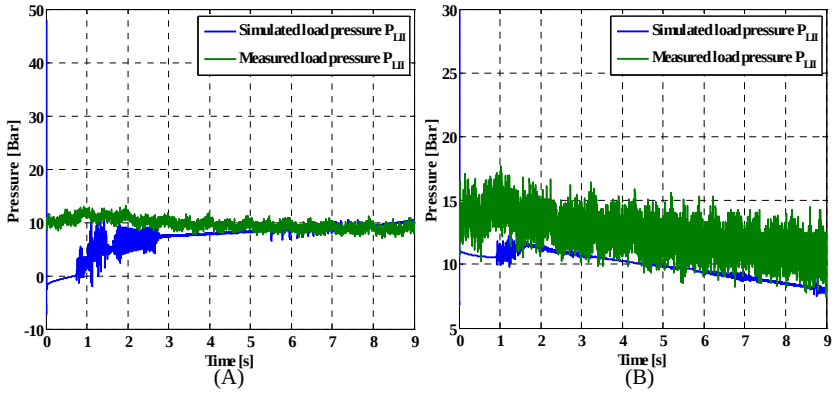

Figure A.16: (A) Load pressure P_{LII}. Both cylinder pistons are initially in retracted position. Cylinder II is extended, while cylinder I is kept in fixed position. (B) Load pressure P_{LII}. Cylinder I is initially in extended position, and cylinder II in retracted position. Cylinder II is extended, while cylinder I is kept in fixed position.

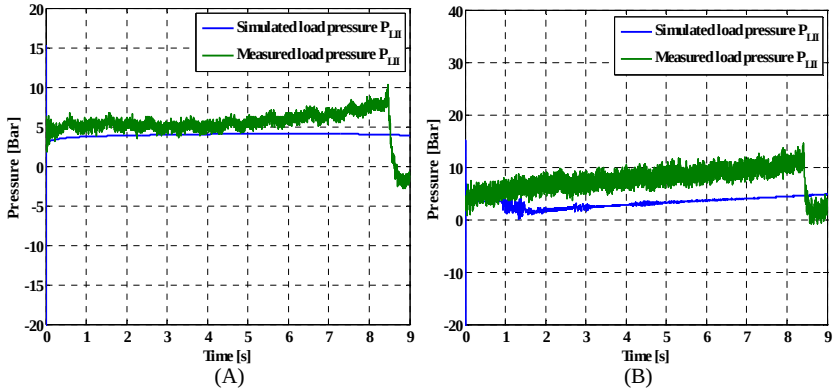

Figure A.17: (A) Load pressure P_{LII}. Cylinder I is initially in retracted position, and cylinder II in extended position. Cylinder II is retracted, while cylinder I is kept in fixed position. (B) Load pressure P_{LKII}. Both cylinder pistons are initially in extended position. Cylinder II is retracted, while cylinder I is kept in fixed position.

It is found from figures A.16 and A.17, that the data acquisition for the pressures of cylinder two is quite noisy. However, it is still possible to verify that the pressure levels,

and variations are similar when comparing the simulated and measured load pressures for cylinder II. Hence it is found that the part of the model concerning gravitation on cylinder II, is a sufficiently accurate rendering of the physical system.

Contents

Appendix B

Simulink Model of the Robot Manipulator

In this appendix, the simulink model of the robot manipulator is presented, along with its limitations.

The overall model of the system is shown in figure B.1.

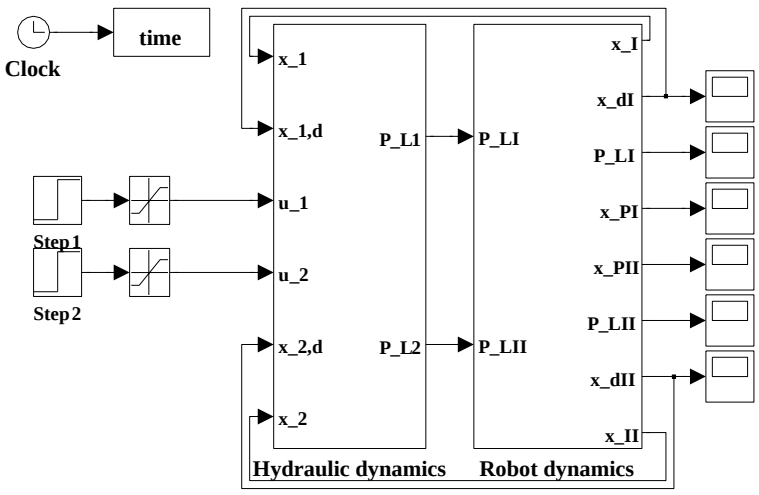

Figure B.1: Simulink model of the system.

B.1 Simulink Model of the Solid State Mechanical Subsystem

In figure B.2 the functions denoted *Angular Acceleration* contains the Newton Euler formulation in joint space. The accelerations are integrated by the double integrator, and the angular positions and velocities are then calculated and transformed into actuator space in order to calculate viscous and coulomb friction, torque arms etc.

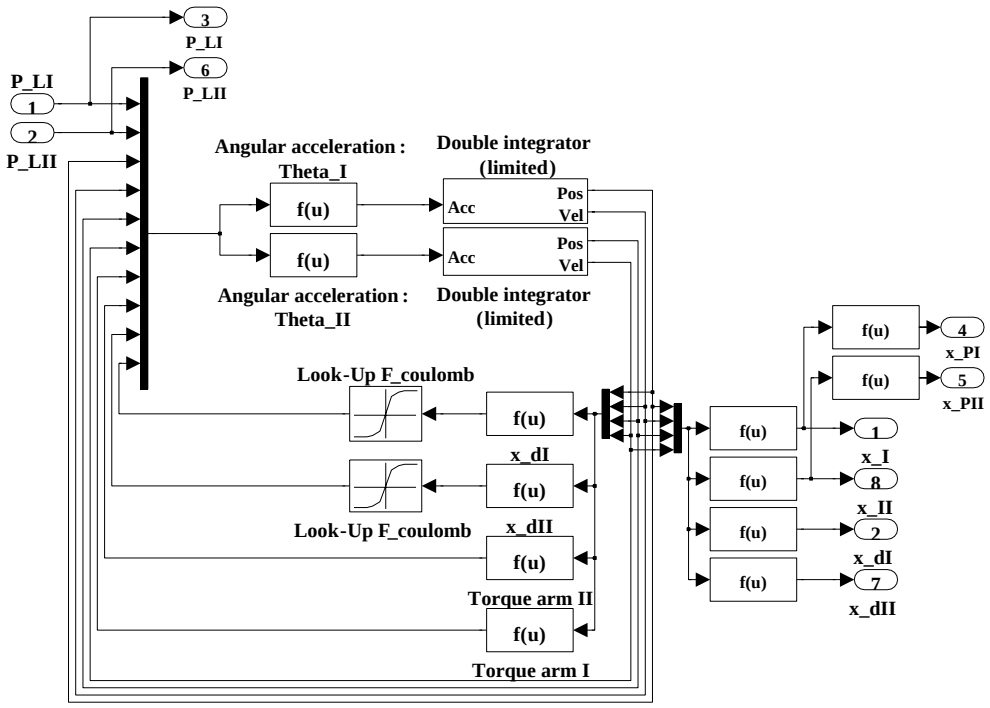

Figure B.2: Simulink model of the solid state part of the system.

B.2 Simulink Model of the Fluid Mechanical Subsystem

Figure B.3 shown the complete model of the hydraulic system.

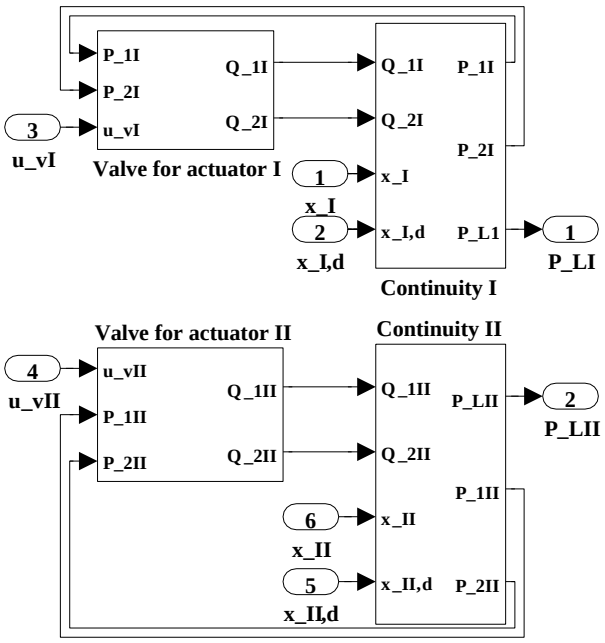

Figure B.3: Simulink model of the hydraulic part of the system.

The flow continuities and orifice equations are implemented in simulink as shown in figures B.4, B.5 and B.6.

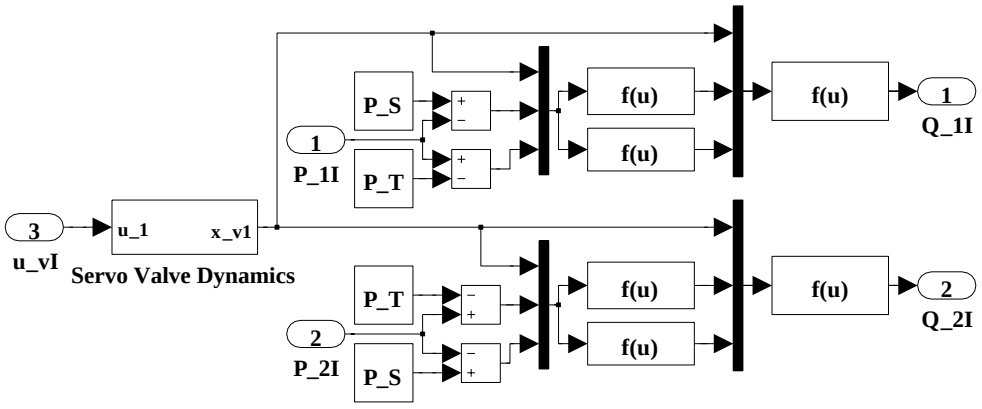

Figure B.4: Simulink model of servo valve.

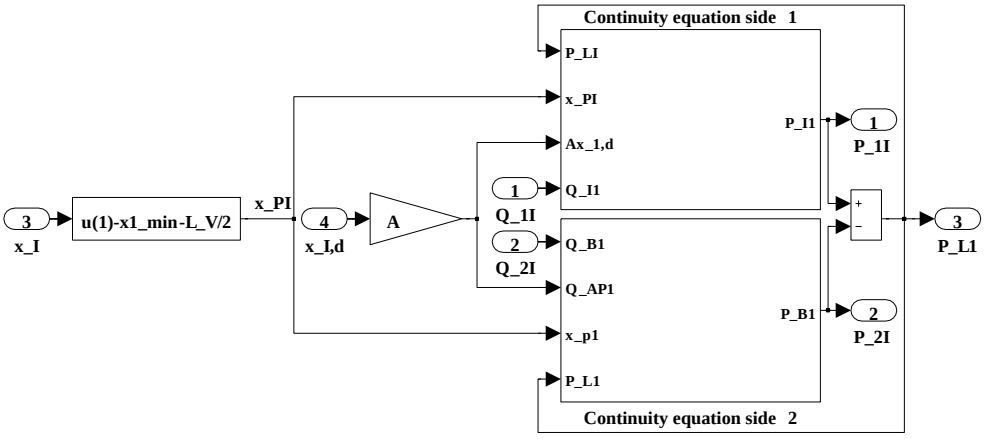

Figure B.5: Simulink model of flow continuities.

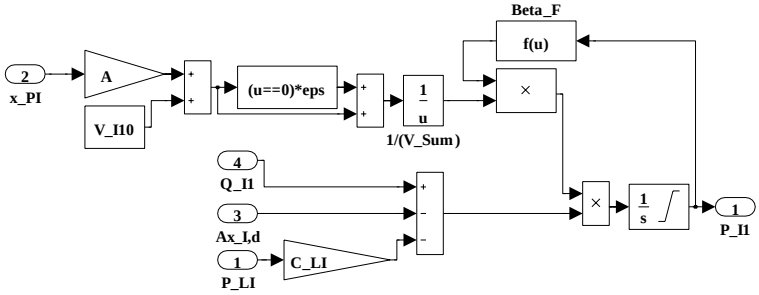

Figure B.6: Simulink sub model of flow continuity.

B.3 Limitations

As it from a model point of view is possible for the robot manipulator to reach singularity points, it is necessary to define limitations for the joint angles of model. Based on the saturation points of the hydraulic actuators, the limits of the joint angles are defined as:

$$\underline{q}_{min} < \underline{q} < \underline{q}_{max} \tag{B.1}$$

From this, the limits used in the limited double integrator block of the solid state mechanical subsystem of the simulink model are:

$$\underline{\dot{q}} = \begin{cases} 0, \text{ if } \underline{q} \geq \underline{q}_{max} \wedge \underline{\dot{q}} > 0 \\ 0, \text{ if } \underline{q} \leq \underline{q}_{min} \wedge \underline{\dot{q}} < 0 \\ \underline{\dot{q}}, \text{ else} \end{cases} \quad , \quad \underline{\ddot{q}} = \begin{cases} 0, \text{ if } \underline{q} \geq \underline{q}_{max} \wedge \underline{\dot{q}} > 0 \\ 0, \text{ if } \underline{q} \leq \underline{q}_{min} \wedge \underline{\dot{q}} < 0 \\ \underline{\ddot{q}}, \text{ else} \end{cases} \tag{B.2}$$

Further more initial conditions for the joint angles are calculated. The initial load pressures are calculated based on:

$$\underline{P_L} = [A_I \ A_{II}]^{-1} \underline{\underline{J}}_d^{-T} \underline{G}(\underline{q}) \tag{B.3}$$

Appendix C

Linear Model of Robot Manipulator

Contents

This appendix concerns the derivation of the linear SISO representation of the nonlinear dynamic model of the robot manipulator. The linear SISO model is derived for use in the development of classical linear SISO controllers applied on the individual servo loops.

C.1 Linearized & Reduced Describing Dynamic Equations

To be able to establish the linear models, the describing dynamic equations are simplified and linearized for a defined point of operation for the two servo loops, and following from this a block diagram and hence a transfer function can be established. Furthermore it is noticed that as the servo loops are similar to each other, both of the linear models are algebraically equal to each other, and hence the indices are $i = I \ \vee \ i = II$.

The assumptions used in this derivation are:

- The servo valves are constructed with ideal zero-lap spools
- Possible leakage flow in servo valves can be disregarded
- Supply pressure is constant
- Tank pressure is constant

Furthermore due to the high frequency of the servo valves compared to the frequency of the solid state part of the system, this is disregarded in the linear model as these are less dominating for the dynamic behavior.

C.1.1 Force Equilibrium

$$M_{PI}\ddot{x}_{PI} = P_{LI}A_I - B_{vI}\dot{x}_{PI} - F_{CI} - F_{extI} \tag{C.1}$$
$$- (M_{11}(\underline{x})\ddot{x}_{PI} + M_{12}(\underline{x})\ddot{x}_{PII} + V_1(\underline{x},\dot{\underline{x}})\dot{x}_{PI} + G_1(\underline{x}))$$
$$M_{PII}\ddot{x}_{PII} = P_{LII}A_{II} - B_{vII}\dot{x}_{PII} - F_{CII} - F_{extII} \tag{C.2}$$
$$- (M_{22}(\underline{x})\ddot{x}_{PII} + M_{21}(\underline{x})\ddot{x}_{PI} + V_2(\underline{x},\dot{\underline{x}})\dot{P}x_{II} + G_2(\underline{x}))$$

Due to the plots of the coriolis- and gravitation forces (figures A.11, A.12 and A.13), the project group considers it as a reasonable assumption to consider these as neglectable in comparison to the inertia load, and as the coulomb friction forces are considered constant these are disregarded in the linear model. Furthermore, as these linear models are to be obtained as SISO systems in order to be able to derive classical control algorithms from them, the inertia cross couplings are considered solely as the disturbance forces F_{DI} and F_{DII}, respectively. Hence the linear systems are considered as decoupled systems, and hence SISO systems. This reduces to:

$$M_{PI}\ddot{x}_{PI} + M_{11}(\underline{x})\ddot{x}_I = P_{LI}A_I - B_{vI}\dot{x}_{PI} - F_{DI} \tag{C.3}$$
$$M_{PII}\ddot{x}_{PII} + M_{22}(\underline{x})\ddot{x}_{II} = P_{LII}A_{II} - B_{vII}\dot{x}_{PII} - F_{DII} \tag{C.4}$$

Setting:

$$M_{eqI} = M_{PI} + M_{11} \quad \text{and} \quad M_{eqII} = M_{PII} + M_{22}(\underline{x}) \tag{C.5}$$

And applying the index i due to algebraically similarity, yields:

$$M_{eqi}\ddot{x}_{Pi} = P_{Li}A_i - B_{vi}\dot{x}_{Pi} - F_{Di} \tag{C.6}$$

Laplace transformation, yields:

$$M_{eqi}s^2x_{Pi} = P_{Li}A_i - B_{vi}sx_{Pi} - F_{Di} \tag{C.7}$$

C.1.2 Servo Valves

To simplify the linear model, the load pressure is introduced as the pressure difference between two chambers of the cylinders - in steady state, disregarding the compression of the oil, the oil flows in- and out of the cylinder chambers can be considered equal to each other, which from the orifice equations yields:

$$Q_{1i} = Q_{2i} = K_{vi}u_{vi}\sqrt{P_s - P_{1i}} = K_{vi}u_{vi}\sqrt{P_{2i} - P_T} \quad \Rightarrow \tag{C.8}$$
$$P_s - P_{1i} = P_{2i} - P_T \tag{C.9}$$

From the definition of the load pressure, the pressures P_{1i} and P_{2i}, are described as:

$$P_{Li} = P_{1i} - P_{2i} \quad , \dot{x}_i > 0 \quad \Rightarrow \tag{C.10}$$
$$P_{1i} = \frac{P_S + P_T + P_{Li}}{2} \quad , \quad P_{2i} = \frac{P_S + P_T - P_{Li}}{2} \tag{C.11}$$

Substituting the last expression of C.11 into the last expression of C.8, the orifice equation describing the load flow is given as:

$$Q_{Li} = Q_{2i} = K_{vi}u_{vi}\sqrt{\frac{P_S + P_T - P_{Li}}{2} - P_T} = K_i u_{vi}\sqrt{\frac{P_S - P_T - P_{Li}}{2}} \tag{C.12}$$

Due to the nonlinear expressions describing the load flow, this needs to be linearized. By use of taylor series, the linearized form of the load flow orifice equation is given by:

$$q_{Li} = K_{qi}u_{vi} + K_{qpi}p_{Li} \tag{C.13}$$

with the linearization coefficients:

$$K_{qi} = \left.\frac{\partial Q_{Li}}{\partial u_{vi}}\right|_{\bar{u}_{vi},\bar{P}_{Li}} = K_{vi}\sqrt{\frac{P_S - P_T - \bar{P}_{Li}}{2}} \quad , \quad K_{qpi} = \left.\frac{\partial Q_{Li}}{\partial P_{Li}}\right|_{\bar{u}_{vi},\bar{P}_{Li}} = \frac{-K_{vi}\bar{u}_{vi}}{2\sqrt{2}\sqrt{P_S - P_T - \bar{P}_{Li}}} \tag{C.14}$$

C.1.3 Flow Continuities

The flow continuity equations has previously been described, and are given as:

$$Q_{1i} - Q_{LEi} = Q_{1i} - C_{Li}P_{Li} = \frac{dV_{1i}}{dt} + \frac{V_{1i}}{\beta_{Fi}}\frac{dP_{1i}}{dt} \tag{C.15}$$

$$Q_{LEi} - Q_{2i} = C_{Li}P_{Li} - Q_{1i} = -\frac{dV_{2i}}{dt} + \frac{V_{2i}}{\beta_{Fi}}\frac{dP_{2i}}{dt} \tag{C.16}$$

As the volumes V_{1i} and V_{2i} are made up by initial volumes V_{10i} and V_{20i} plus the change in volume produced by the displacement of the piston. The volumes V_{1i} and V_{2i} can be expressed as:

$$V_{1i} = V_{10i} + A_i x_{Pi} \tag{C.17}$$

$$V_{Ar} = V_{20i} - A_i x_{Pi} \tag{C.18}$$

Thereby the continuity equations can be written as,

$$Q_{1i} - C_{Li}P_{Li} = \frac{dV_{1i}}{dt} + \frac{V_{10i}}{\beta}\frac{dP_{1i}}{dt} + \frac{A_i x_{Pi}}{\beta}\frac{dP_{1i}}{dt} \tag{C.19}$$

$$C_{Li}P_{Li} - Q_{2i} = -\frac{dV_{2i}}{dt} + \frac{V_{20i}}{\beta}\frac{dP_{2i}}{dt} - \frac{A_i x_{Pi}}{\beta}\frac{dP_{2i}}{dt} \tag{C.20}$$

As the linear model only concern the dynamics of the system, at a specific operating point, it is assumed that $V_{10i} >> A_i x_{Pi}$ and $V_{20i} >> A_i x_{Pi}$. This is assumed as the linear model is created for a specific operating point, hence the displacement of the piston about the operating point is considered to be small relative to the initial volumes. Thus it is found reasonable to neglect $A_i x_{Pi}$, resulting in the following simplified laplace

transformed continuity equations,

$$q_{1i} - C_{Li}p_{Li} = sA_ix_{Pi} + \frac{V_{10i}}{\beta}sp_{1i} \quad \Rightarrow \quad q_{1i} = sA_ix_{Pi} + \frac{V_{10i}}{\beta}sp_{1i} + C_{Li}p_{Li} \tag{C.21}$$

$$C_{Li}p_{Li} - q_{2i} = -sA_ix_{Pi} + \frac{V_{20i}}{\beta}sp_{2i} \quad \Rightarrow \quad -q_{2i} = -sA_ix_{Pi} + \frac{V_{20i}}{\beta}sp_{2i} - C_{Li}p_{Li} \tag{C.22}$$

Introducing the total volume $V_{1i} = V_{2i} = V_{\Sigma i}/2$ (center position of the cylinder), introducing the load flow as the average flow through the cylinder, yields:

$$q_{Li} = \frac{q_{1i} + q_{2i}}{2} = sA_ix_{Pi} + s\frac{V_{\sum i}}{4\beta_{Fi}}p_{Li} + C_{Li}p_{Li} \tag{C.23}$$

The above expression is obtained for the center position of the cylinder (which is the point with lowest possible natural frequency, and hence the operating point).

C.2 Transfer Function

Establishing the transfer block diagram based on the linear describing equations, yields the diagram of figure C.1.

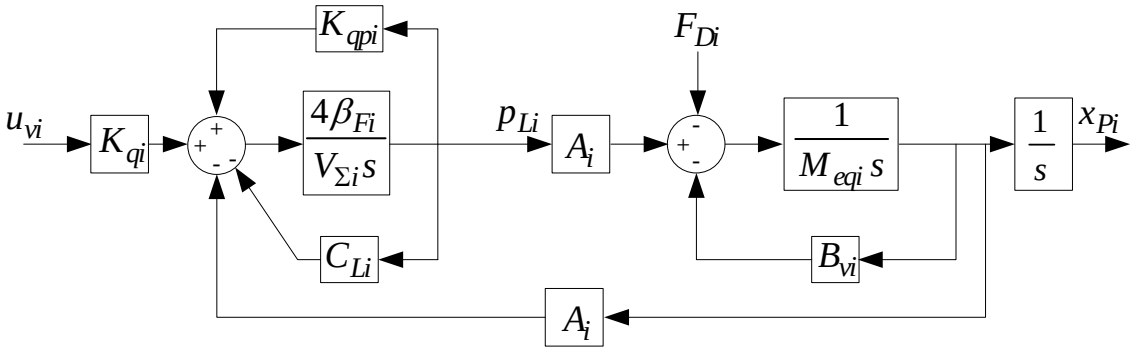

Figure C.1: Block diagram of HSS.

Reducing the block diagram of figure C.1, the transfer function is obtained to be:

$$G_i(s) = \frac{X_{Pi}(s)}{U_{vi}(s)} = \frac{K_i}{T_{ni}^2s^2 + 2\zeta_iT_{ni}s + 1}\frac{1}{s} \tag{C.24}$$

With the coefficients:

$$K_i = \frac{A_{Pi}K_{qi}}{(C_{Li} - K_{qpi})B_{vi} + A_{Pi}^2} \tag{C.25}$$

$$\omega_{ni} = \frac{1}{T_{ni}} = \sqrt{\frac{4\beta_{Fi}}{V_{\Sigma i}M_{eqi}}((C_{Li} - K_{qpi})B_{vi} + A_{Pi}^2)} \tag{C.26}$$

$$\zeta_i = \frac{4\beta_{Fi}(C_{Li} - K_{qpi})M_{eqi} + V_{\Sigma i}B_{vi}}{2T_{ni}(4\beta_{Fi}((C_{Li} - K_{qpi})B_{vi} + A_{Pi}^2))} \tag{C.27}$$

Now the linear model has been derived.

C.3 Assessment of Operating Point

Regarding an operating point for which the linear models must be valid, a critical point of operation must be chosen - regarding the cylinders the critical point of operation is where the lowest possible natural frequency occurs, which for symmetric actuators is at the center position. Due to the symmetry of the cylinders, this critical point occurs at the center stroke position.

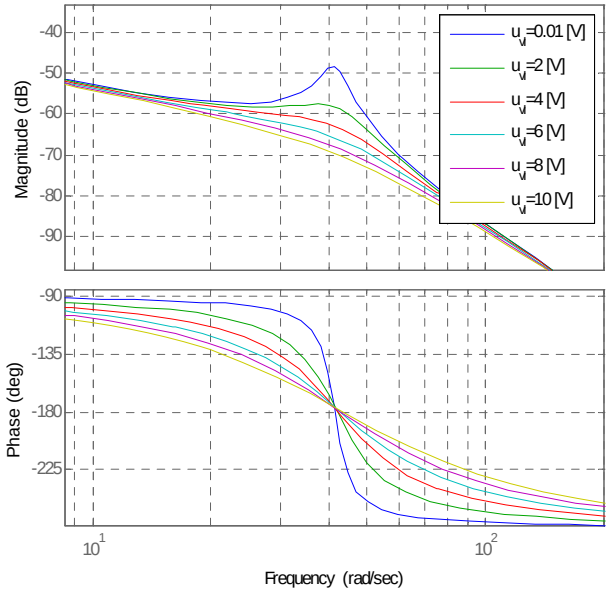

Figure C.2: Bode diagram of HSS I with different values for the input voltage at the operating point.

Regarding an operating point for the servo valves, the damping ratio of the transfer function is examined via its bode diagram, when varying the input signal in the linearization coefficients - it is seen from the bode diagram in figure C.2, that the critical point of operation is when the spool of the servo valve is slightly opened, due to the poor damping ratio.

Appendix D

Trajectory Profiles

Contents

I this appendix the expressions for the trajectory profiles a given.

$Time\ [s]$	$x_D\ [m]$	$\dot{x}_D\ [m/s]$	$\ddot{x}_D\ [m/s^2]$
$0 < t < t_{b1}$	$q_{0x} + 0.5\ddot{x}_D t^2$	$\ddot{x}_D t$	$\ddot{x}_D$
$t_{b1} < t < (t_{f1} - t_{b1})$	$\ddot{x}_D t_{b1} t - 0.5\ddot{x}_D t_{b1}^2 + q_{0x}$	$-\ddot{x}_D(t - (t_{f1} - t_{b1})) + \ddot{x}_D t_{b1}$	0
$(t_{f1} - t_{b1}) < t < t_{f1}$	$-0.5\ddot{x}_D(t - (t_{f1} - t_{b1}))^2 + \ddot{x}_D t_{b1} t - 0.5\ddot{x}_D t_{b1}^2 + q_{0x}$	$\ddot{x}_D(t - (t_{f1} - t_{b1}))$	$-\ddot{x}_D$
$t_{f1} < t < t_{f2}$	$-0.5\ddot{x}_D(t_{f1} - (t_{f1} - t_{b1}))^2 + \ddot{x}_D t_{b1} t_{f1} - 0.5\ddot{x}_D t_{b1}^2 + q_{0x}$	0	0
$t_{f2} < t < (t_{f2} + t_{b3})$	$q_{1x} - 0.5\ddot{x}_D(t - t_{f2})^2$	$-0.5\ddot{x}_D(t - t_{f2})$	$-\ddot{x}_D$
$(t_{f2} + t_{b3}) < t < (t_{f3} - t_{b3})$	$-\ddot{x}_D t_{b3}(t - t_{f2}) + 0.5\ddot{x}_D t_{b3}^2 + q_{1x}$	$-\ddot{x}_D t_{b3}$	0
$(t_{f3} - t_{b3}) < t < t_{f3}$	$0.5\ddot{x}_D(t - (t_{f3} - t_{b3}))^2 - \ddot{x}_D t_{b3}(t - t_{f2}) + 0.5\ddot{x}_D t_{b3}^2 + q_{1x}$	$\ddot{x}_D(t - (t_{f3} - t_{b3})) - \ddot{x}_D t_{b3}$	$\ddot{x}_D$
$t_{f3} < t < t_{f4})$	$0.5\ddot{x}_D(t_{f3} - (t_{f3} - t_{b3}))^2 - \ddot{x}_D t_{b3}(t_{f3} - t_{f2}) + 0.5\ddot{x}_D t_{b3}^2 + q_{1x}$	0	0

Table D.1: Position-, velocity- and acceleration profiles for the x_D-axis.

$Time\ [s]$	$y_D\ [m]$	$\dot{y}_D\ [m/s]$	$\ddot{y}_D\ [m/s^2]$
$0 < t < t_{f1}$	q_{0y}	0	0
$t_{f1} < t < t_{f1} + t_{b2}$	$q_{0y} + 0.5\ddot{y}_D(t - t_{f1})^2$	$\ddot{y}_D(t - t_{f1})$	$\ddot{y}_D$
$t_{f1} + t_{b2} < t < t_{f2} - t_{b2}$	$\ddot{y}_D t_{b2}(t - t_{f1}) - 0.5\ddot{y}_D t_{b2}^2 + q_{0y}$	$\ddot{y}_D t_b 2$	0
$t_{f2} - t_{b2} < t < t_{f2}$	$-0.5\ddot{y}_D(t - (t_{f2} - t_{b2}))^2 + \ddot{y}_D t_{b2}(t - t_{f1}) - 0.5\ddot{y}_D t_{b2}^2 + q_{0y}$	$-\ddot{y}_D(t - (t_{f2} - t_{b2})) + \ddot{y}_D t_{b2}$	$-\ddot{y}_D$
$t_{f2} < t < t_{f3}$	$-0.5\ddot{y}_D(t_{f2} - (t_{f2} - t_{b2}))^2 + \ddot{y}_D t_{b2}(t_{f2} - t_{f1}) - 0.5\ddot{y}_D t_{b2}^2 + q_{0y}$	0	0
$t_{b3} < t < t_{f3} + t_{b4}$	$q_{1y} - 0.5\ddot{y}_D(t - t_{f3})^2$	$-\ddot{y}_D(t - t_{b3})$	$-\ddot{y}_D$
$t_{f3} + t_{b4} < t < t_{f4} - t_{b4}$	$-\ddot{y}_D t_{b4}(t - t_{f3}) + 0.5\ddot{y}_D t_{b4}^2 + q_{1y}$	$-\ddot{y}_D t_{b4}$	0
$t_{f4} - t_{b4} < t < t_{f4}$	$0.5\ddot{y}_D(t - (t_{f4} - t_{b4}))^2 - \ddot{y}_D t_{b4}(t - t_{f3}) + 0.5\ddot{y}_D t_{b4}^2 + q_{1y}$	$\ddot{y}_D(t - (t_{f4} - t_{b4})) - \ddot{y}_D t_{b4}$	$\ddot{y}_D$

Table D.2: Position-, velocity- and acceleration profiles for the y_D-axis.

Appendix E

Linear Control - Bode Diagrams

This appendix presents the bode diagrams for the compensated systems, and compensators developed in the linear control design.

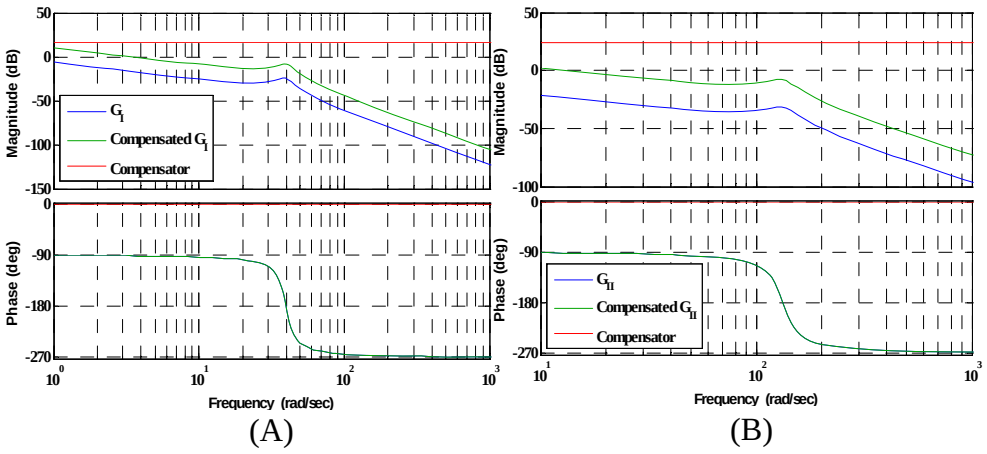

Figure E.1: Bode diagrams for P-compensated systems. (A) HSS I. (B) HSS II.

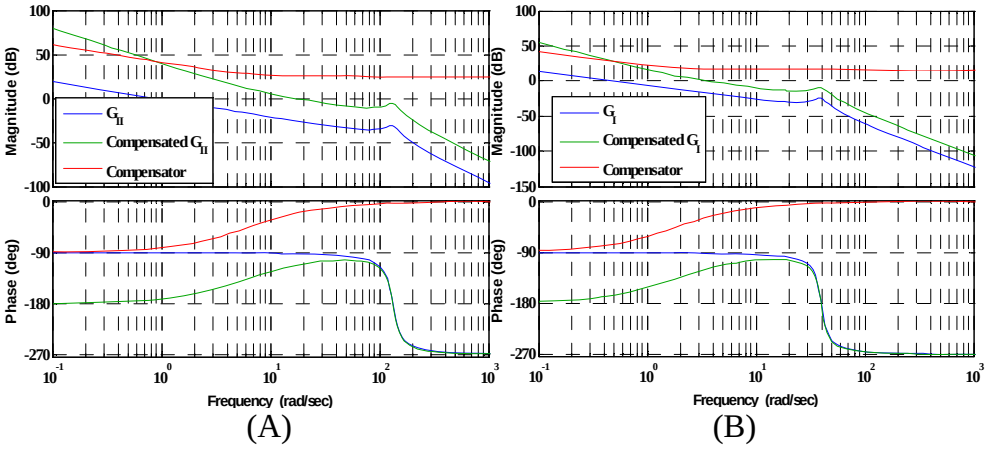

Figure E.2: Bode diagrams for PI-compensated systems. (A) HSS I. (B) HSS II.

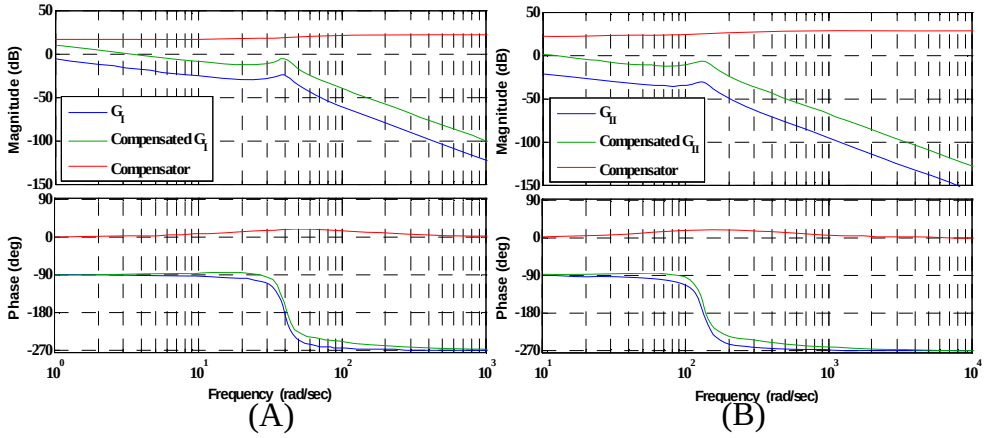

Figure E.3: Bode diagrams for lead-compensated systems. (A) HSS I. (B) HSS II.

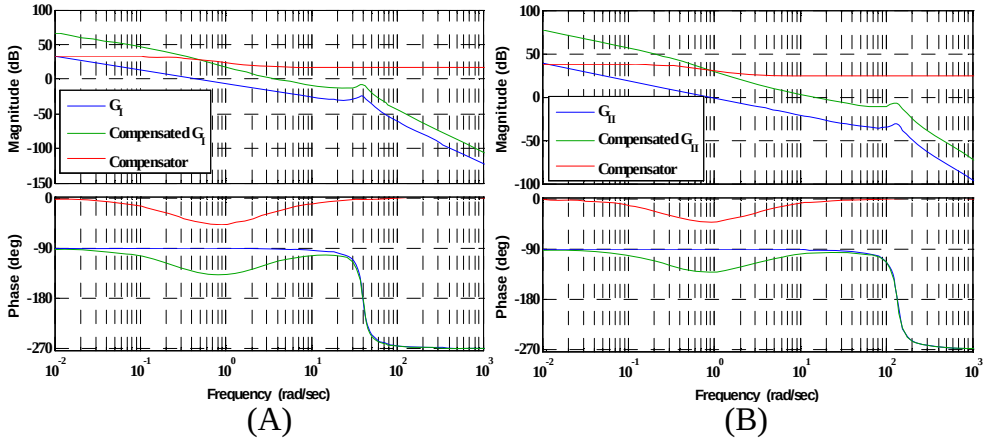

Figure E.4: Bode diagrams for lag-compensated systems. (A) HSS I. (B) HSS II.

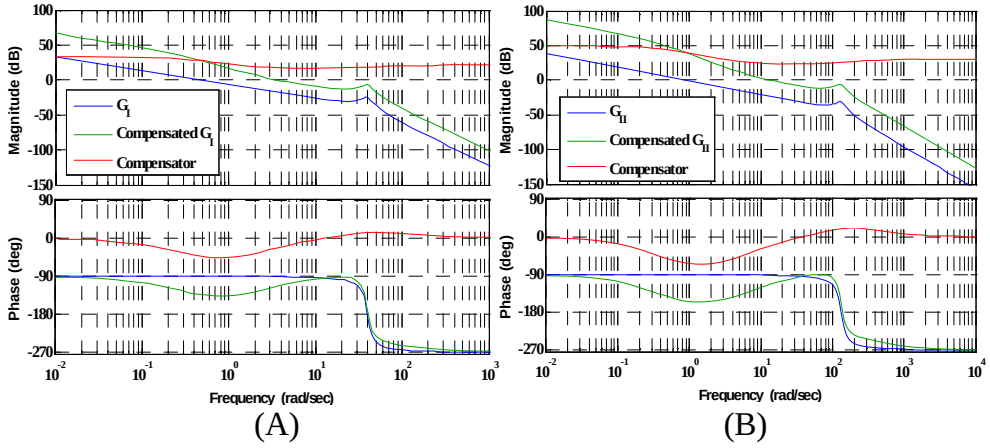

Figure E.5: Bode diagrams for lag-lead-compensated systems. (A) HSS I. (B) HSS II.

Appendix F

Linear Controller Parameters

In this appendix the controller parameters used for the linear controllers are presented.

The notation z and p refers to whether it is a time constant relating to a zero or a pole.

P - Controllers

$$K_{pI} = 6.84 \quad ; \quad K_{pII} = 15.00 \tag{F.1}$$

PI - Controllers

$$K_{pI} = 6.39 \quad , \quad T_{iI} = 0.55[s] \tag{F.2}$$
$$K_{pII} = 17.72 \quad , \quad T_{iII} = 0.16[s] \tag{F.3}$$

Lead - Controllers

$$K_{LeadI} = 6.67 \quad , \quad T_{zI} = 0.027[s] \quad , \quad T_{pI} = 0.014[s] \tag{F.4}$$
$$K_{LeadII} = 12.90 \quad , \quad T_{zII} = 0.0086[s] \quad , \quad T_{pII} = 0.0042[s] \tag{F.5}$$

Lag - Controllers

$$K_{LagI} = 45.50 \quad , \quad T_{zI} = 0.48[s] \quad , \quad T_{pI} = 3.1[s] \tag{F.6}$$
$$K_{LagII} = 78.342 \quad , \quad T_{zII} = 0.54[s] \quad , \quad T_{pII} = 2.6[s] \tag{F.7}$$

Lag-Lead - Controllers

$$K_{Lag-leadI} = 44.00 \quad , \quad T_{zI1} = 0.48[s], T_{zI2} = 0.028[s] \quad , \quad T_{pI1} = 3.2[s], T_{pI2} = 0.016[s] \tag{F.8}$$

$$K_{Lag-leadII} = 287.44 \quad , \quad T_{zII1} = 0.15[s], T_{zII2} = 0.0086[s] \quad , \quad T_{pII1} = 3.1[s], T_{pII2} = 0.0038[s] \tag{F.9}$$

Appendix G

Contents

Anti Wind Up

In this appendix, integrator antiwind up is briefly accounted for.

As long as the values of piston positions and valve spool positions are not in saturation, the feedback loop enables the system to correct the error. However, when the valve spool position and cylinder piston position saturates, the feedback loop looses its effect as the outputs of these are not influenced by their inputs. This can cause the destabilizing effect of the integrator to reach large values, as it keeps on accumulating the errors. At some point of time, when the integrator is accumulating the error, the output will become larger than the input to the system, hence the error changes its sign. At this point the integrator will begin to wind down. This will not happen unless the system overshoots its target value with a certain value. The initiative taken to avoid the integrator windup phenomenon, is to ensure that the integral has a reasonable value as the valve and cylinder saturates. By doing so, integral anti windup has been created. Integrator anti windup is implemented both in the software on the physical system, and in the simulation models. The anti windup implemented in the model is shown in figure G.1, and it is seen that if the controller output exceeds the saturation value of the limiter/saturator, the difference between the saturation value and the controller output value, is increased an subtracted from the input to the controller thereby correcting the controller to have a maximum value equal to the saturation value. This value will, at most, only exceed the saturation value momentarily, depending on the value of the constant in the anti wind-up feedback loop.

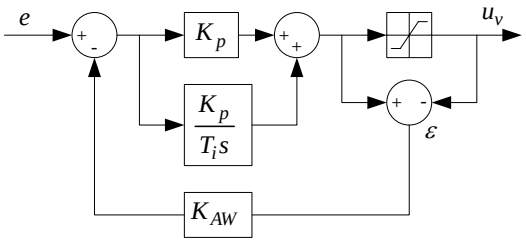

Figure G.1: Sketch of integrator anti wind up implemented in the model.

Appendix H

Lemmas, Theorems & Norms

This appendix presents the theorems, lemmas and function norms used in the stability proofs of the adaptive controllers.

H.1 Lyapunov's Stability Theorem

If there exists a function $V : \Re^n \rightarrow \Re$ which is positive definite, and if its derivative along $\frac{d\underline{x}}{dt} = f(\underline{x})$ is negative semi-definite, then the solution $\underline{x} = 0$ is stable. If $\frac{dV}{dt}$ is negative definite, then the solution is asymptotically stable. V is then referred to as a *Lyapunov function* for $\frac{d\underline{x}}{dt} = f(\underline{x})$.

H.2 Lemma I

(This lemma has been taken directly from [Slotine E J-J, 1991])

Consider two signals e and ϕ related by the following dynamic equation:

$$e(t) = H(s)(k\underline{\phi}^T(t)\underline{v}(t)) \tag{H.1}$$

Where:

$e(t)$:	scalar output signal	[−]
$H(s)$:	strictly positive real transfer function	[−]
k:	unknown constant with known sign	[−]
$\underline{\phi}(t)$:	$m \times 1$ vector function of time	[−]
$\underline{v}(t)$:	measurable $m \times 1$ vector	[−]

If the vector $\underline{\phi}$ varies according to:

$$\dot{\underline{\phi}} = -sign(k)\gamma e\underline{v}(t) \tag{H.2}$$

with γ being a positive constant, then $e(t)$ and $\underline{\phi}(t)$ are globally bounded. Furthermore if $\underline{v}(t)$ is bounded, then:

$$e \to 0 \quad \text{for} \quad t \to \infty \tag{H.3}$$

H.3 Lemma II - *Barbalats Lemma*

If g is a real function of a real variable t, defined and uniformly continuous for $t \geq 0$, and if the limit of the integral:

$$\int_0^t g(\tau)d\tau \tag{H.4}$$

Exists for $t \to \infty$ and is a finite number, then:

$$\lim_{t\to\infty} g(t) = 0 \tag{H.5}$$

Remark: A consequence of Barbalats Lemma is that if $g \in L_2$ and $\frac{dg}{dt}$ is bounded, then:

$$\lim_{t\to\infty} g(t) = 0 \tag{H.6}$$

Uniform Continuity

A sufficient condition for a differentiable function to be uniformly continuous is that its derivative is bounded.

H.4 Lemma III - *Lyapunov-like Lemma*

If a scalar function $V(\underline{x}, t)$ satisfies the following conditions:

- $V(\underline{x}, t)$ is lower bounded
- $\dot{V}(\underline{x}, t)$ is negative semi-definite
- $\dot{V}(\underline{x}, t)$ is uniformly continuous

Then:

$$\dot{V}(\underline{x}, t) \to 0 \quad \text{for} \quad t \to \infty \tag{H.7}$$

H.5 Function Norms

(Taken directly from [Andersen, 2003b])

For any fixed $p \in [1, \infty]$, if $f : \Re^n \to \Re$ belongs to L_p if $\int_0^\infty |f(t)|^p dt < \infty$. The associated norm is:

$$\|f_p\| = \left(\int_0^\infty |f(t)|^p dt \right)^{\frac{1}{p}} = \frac{1}{k_p} \tag{H.8}$$

In addition to the class of functions in L_p, this extended space also includes truncated functions of the form:

$$f_T(t) = \begin{cases} f(t) & t \leq T \\ 0 & t > T \end{cases} \tag{H.9}$$

Such that:

$$\|f_T\|_p < \infty \quad ; \quad \forall T \tag{H.10}$$

H.6 Induced Matrix Norms

(Taken directly from [Andersen, 2003b])

For a matrix $\underline{\underline{A}} \in \Re^{n \times n}$ a norm can be defined by,

$$\|\underline{\underline{A}}\|_p \hat{=} \sup_{x \neq 0} \frac{\|\underline{\underline{A}}\underline{x}\|_p}{\|\underline{x}\|_p}, \ \forall \underline{x} \in \Re^n \tag{H.11}$$

The norm is called the *induced (matrix) norm* of $\underline{\underline{A}}$ corresponding to the vector norm $\|\underline{x}\|_p$. For the induced norm it can be shown that,

$$\|\underline{\underline{A}}\underline{\underline{B}}\|_p \leq \|\underline{\underline{A}}\|_p \cdot \|\underline{\underline{B}}\|_p, \ \forall \underline{\underline{A}}, \ \underline{\underline{B}} \in \Re^{n \times n} \tag{H.12}$$

$$\|\underline{\underline{A}}\underline{x}\|_p \leq \|\underline{\underline{A}}\|_p \cdot \|\underline{x}\|_p, \ \forall \underline{\underline{A}} \in \Re^{n \times n}, \ \underline{x} \in \Re^n \tag{H.13}$$

For $p = 2$ the induced norm can be given as $\|\underline{\underline{A}}\|_2 = \sqrt{max_i \lambda_i (\underline{\underline{A}}^T \ \underline{\underline{A}})}$.

H.7 Gain of Linear Operators

(Taken directly from [Andersen, 2003b])

Let H be a causal operator $H : \ f \to g$. The L_p gain of H is denoted $\|H\|_p$ and is defined as the smalles value of γ such that:

$$\|g\|_p = \|Hf\|_p \leq \gamma \|f\|_p + \beta \ \forall f \in L_p \tag{H.14}$$

Consider the convolution-type operator $H: \ f \rightarrow g$ given by,

$$g(t) = \int_{-\infty}^{\infty} h(t-\tau)f(\tau)d\tau \ \forall t \in \Re \tag{H.15}$$

Then for $p = 2$ the L_2 gain is given by:

$$\|H\|_2 = \max_{\omega \in \Re} |\hat{h}(j\omega)| \tag{H.16}$$

Where $\hat{h}(s)$ is the laplace transform of the impulse response of H. For $p = \infty$ the L_∞ is given by:

$$\|H\|_\infty = \int_0^{\infty} |\hat{h}(t)|dt \tag{H.17}$$

Having defined the L_p spaces the following lemma is useful in analysing the input-output proporties of systems with exponentially stable transfer functions.

Lemma 1: (Desoer & Vidyasagar)

Let the transfer function $H(s)$ be exponentially stable and strictly proper. Then $f \in L_2$ implies that $g = H \cdot f \in L_2 \cap L_\infty, \ \dot{g} \in L_2$, g is continuous, and $g \rightarrow 0$ as $t \rightarrow \infty$. If, in addition $f \rightarrow 0$ as $t \rightarrow \infty$, then $\dot{g} \rightarrow 0$.

H.8 Normed Spaces

(Taken directly from [Andersen, 2003b])

A **normed space** is a vector space V with a given norm. A **norm** on a vector space V is a rule which, given any $x \in V$, specifies a real number $\|x\|$, such that,

(a) $\|x\| > 0$ if $x \neq 0$, and $\|0\| = 0$;
(b) $\|ax\| = |a| \cdot \|x\|$ for any $x \in V$ and any scalar a;
(c) $\|x + y\| \leq \|x\| + \|y\|$ for any $x, y \in V$ (the triangle inequality);

A normed vector space is called real or complex according to whether the underlying vector space V is real or complex. Subsequent only norms defined on $\Re^n$ are considered.

Examples of norms which satisfy the axioms of the norm are,

$$\|\underline{x}\|_1 \hat{=} \sum_{i=1}^{n} |x_i| \tag{H.18}$$

$$\|\underline{x}\|_p \hat{=} \left(\sum_{i=1}^{n} |x_i|^p \right)^{1/p} \tag{H.19}$$

$$\|\underline{x}\|_\infty \hat{=} \max_i |x_i| \tag{H.20}$$

$\|\underline{x}\|_2$ is the usual Euclidean of $\underline{x}$.

An important result is that all norms are equivalent in the sense that there exist positive numbers κ_1 and κ_2 such that,

$$\kappa_1 \|\underline{x}\|_a \leq \|\underline{x}\|_b \leq \kappa_2 \|\underline{x}\|_a, \forall \underline{x} \in \Re^n \tag{H.21}$$

This means that any norm can be used to show boundedness or convergence. Hence, often the symbol $\|\cdot\|$ is used without specifying exactly which norm is meant.

Appendix I

Simulation Results for AIDC, AAC, RAIDC & RAAC

Contents

I.1 Simulation Results - AIDC/AAC (RECT)

I.1.1 Results - AIDC

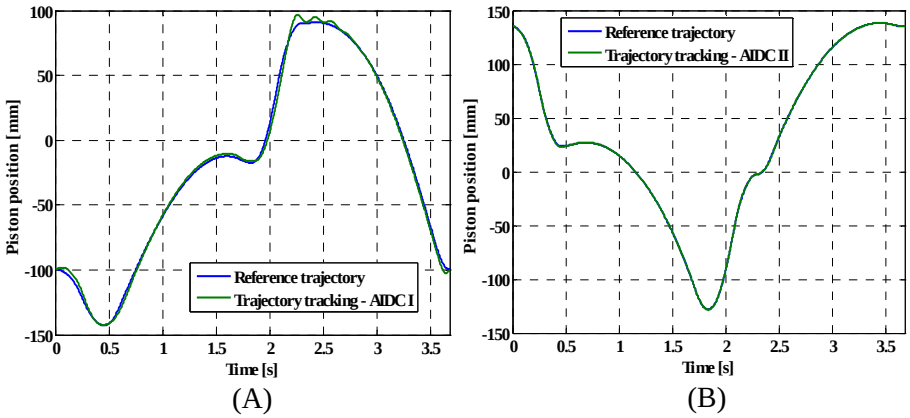

(A) (B)

Figure I.1: Trajectory tracking for AIDC control system. (A) HSS I. (B) HSS II.

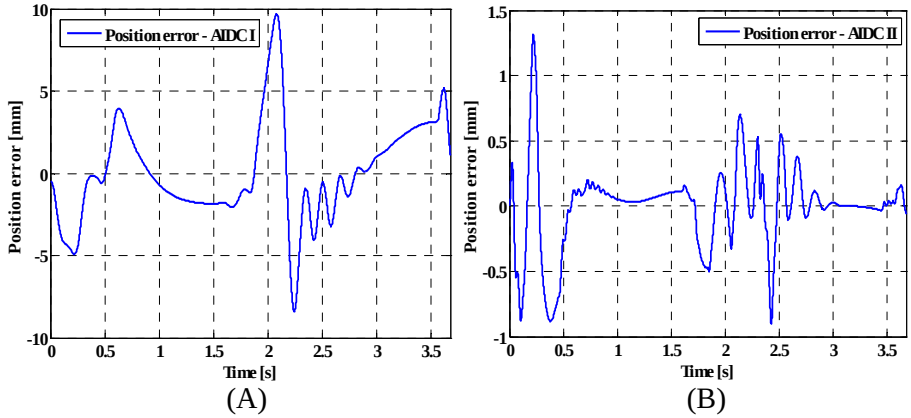

(A) (B)

Figure I.2: Tracking error for AIDC control system. (A) HSS I. (B) HSS II.

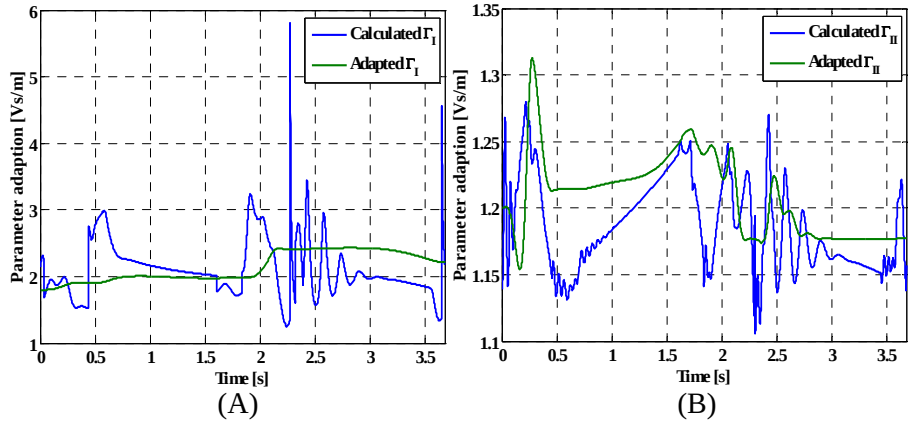

(A) (B)

Figure I.3: Γ adaption for AIDC control system. (A) HSS I. (B) HSS II.

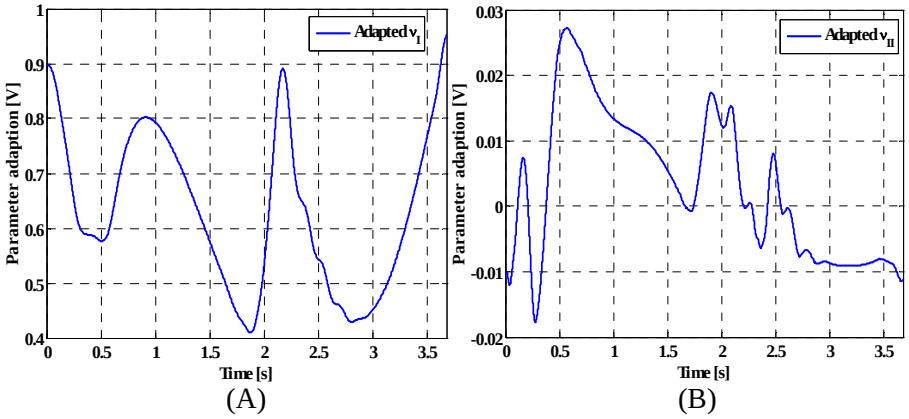

Figure I.4: ν adaption for AIDC control system. (A) HSS I. (B) HSS II.

I.1.2 Results - AAC

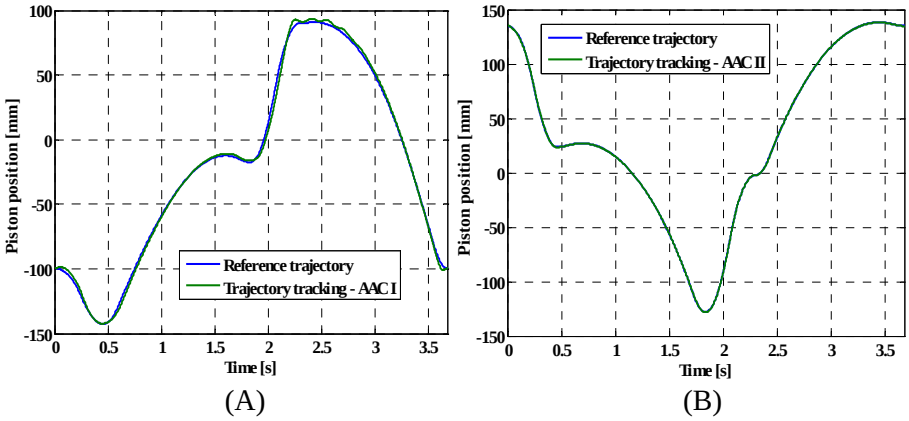

Figure I.5: Trajectory tracking for AAC control system. (A) HSS I. (B) HSS II.

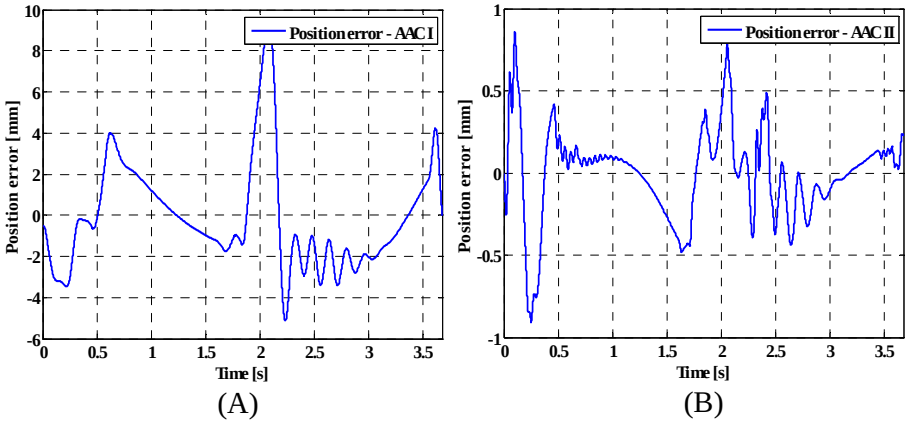

Figure I.6: Tracking error for AAC control system. (A) HSS I. (B) HSS II.

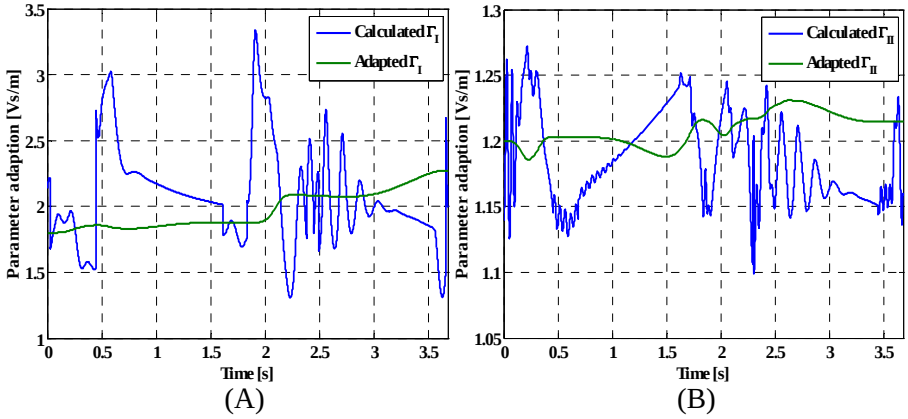

Figure I.7: Γ adaption for AAC control system. (A) HSS I. (B) HSS II.

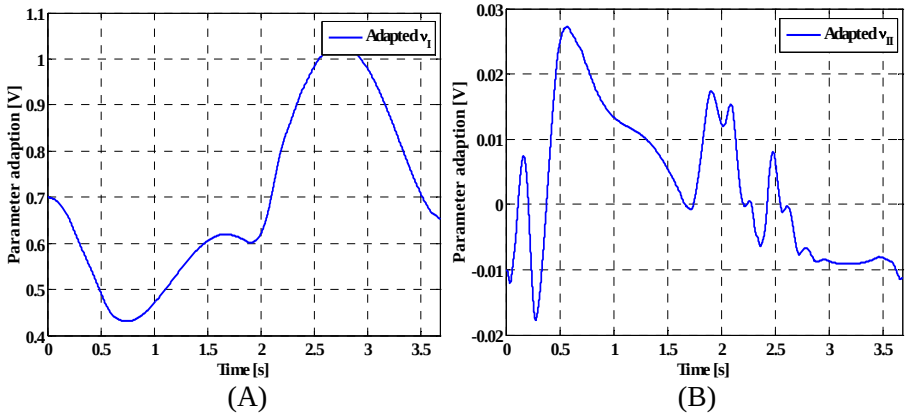

Figure I.8: ν adaption for AAC control system. (A) HSS I. (B) HSS II.

I.1.3 Tracking Errors - AIDC/AAC

Compensator	$\lvert e_{maxI} \rvert$ $[mm]$	e_{rmsI} $[mm]$	$\lvert e_{maxII} \rvert$ $[mm]$	e_{rmsII} $[mm]$
AIDC	9.6	3.00	1.33	0.32
AAC	9.7	2.62	0.91	0.27

Table I.1: Tracking error values for controllers tested on the rectangular trajectory.

I.2 Simulation Results - RAIDC/RAAC (RECT)

I.2.1 Results - RAIDC

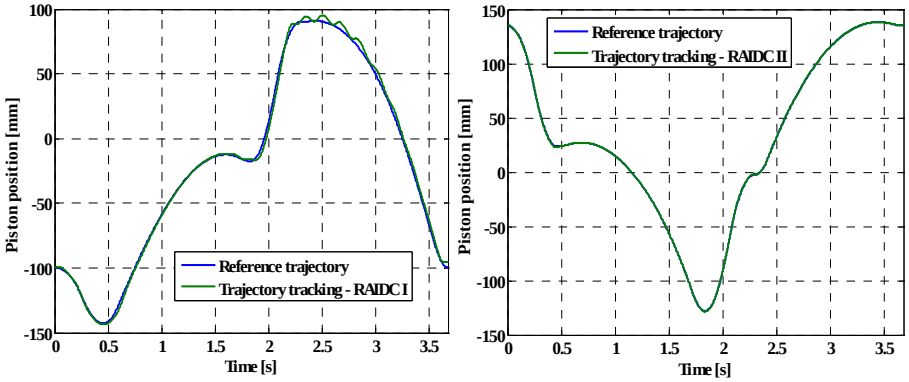

Figure I.9: Trajectory tracking for RAIDC control system. (A) HSS I. (B) HSS II.

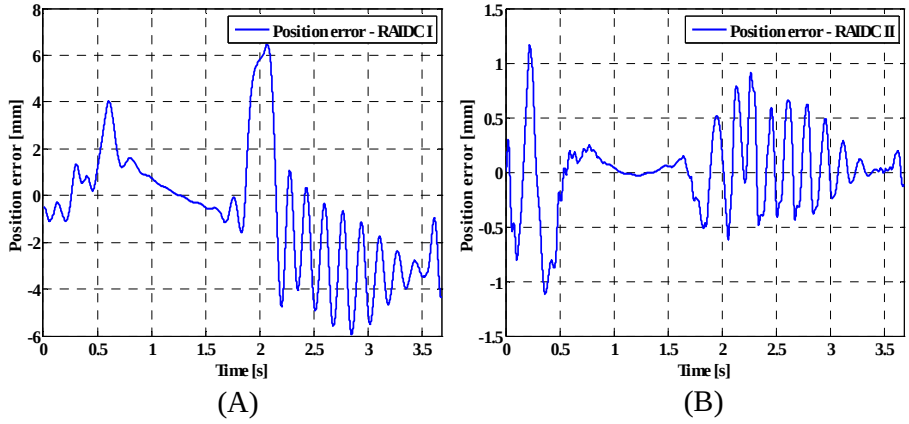

Figure I.10: Tracking error for RAIDC control system. (A) HSS I. (B) HSS II.

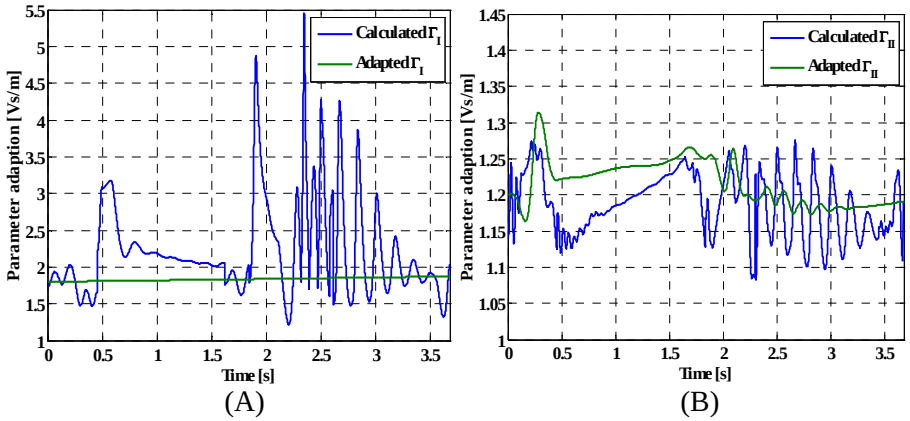

Figure I.11: Γ adaption for RAIDC control system. (A) HSS I. (B) HSS II.

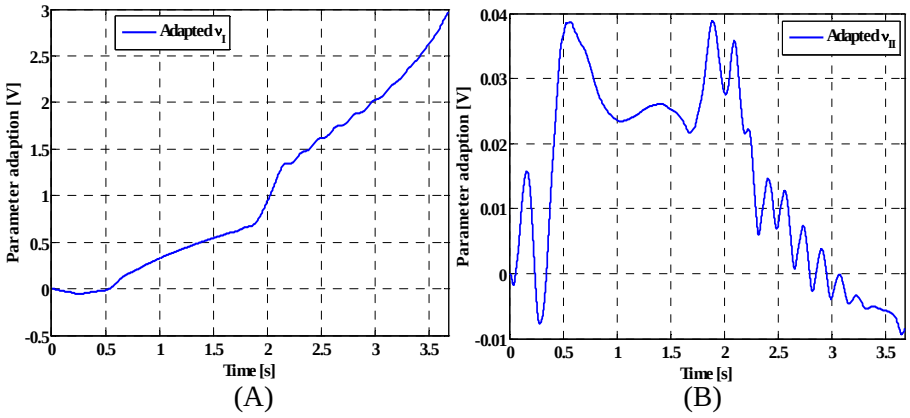

Figure I.12: ν adaption for RAIDC control system. (A) HSS I. (B) HSS II.

I.2.2 Results - RAAC

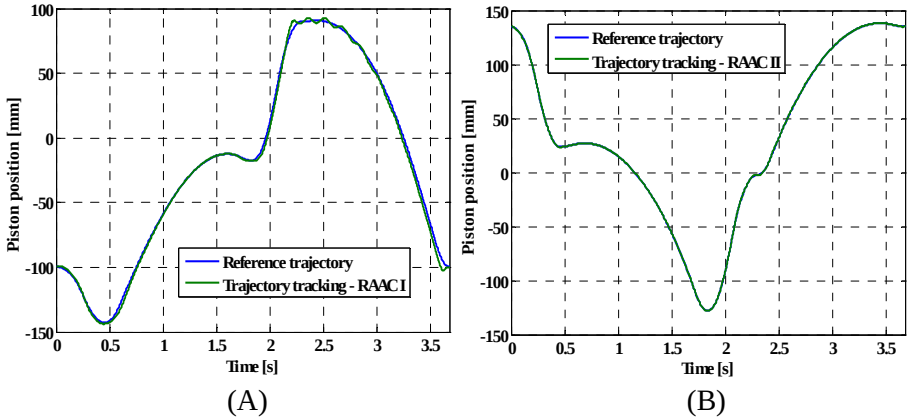

Figure I.13: Trajectory tracking for RAAC control system. (A) HSS I. (B) HSS II.

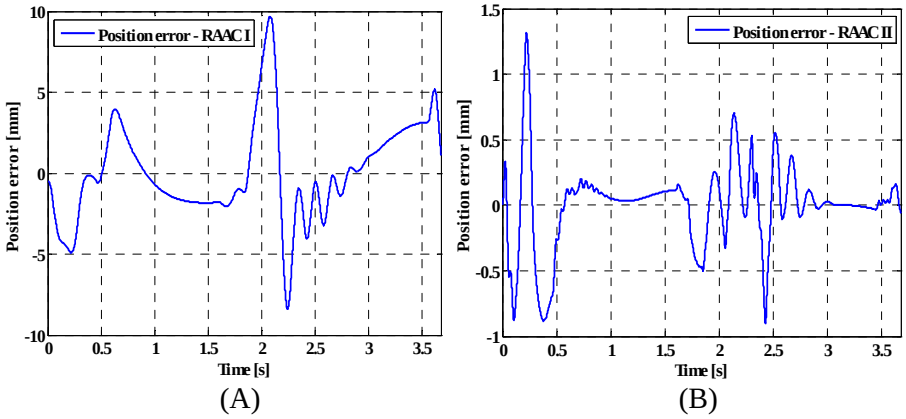

Figure I.14: Tracking error for RAAC control system. (A) HSS I. (B) HSS II.

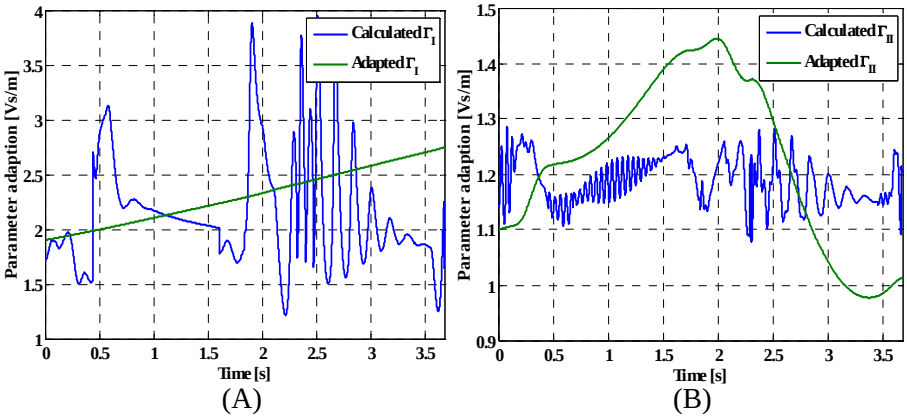

Figure I.15: Γ adaption for RAAC control system. (A) HSS I. (B) HSS II.

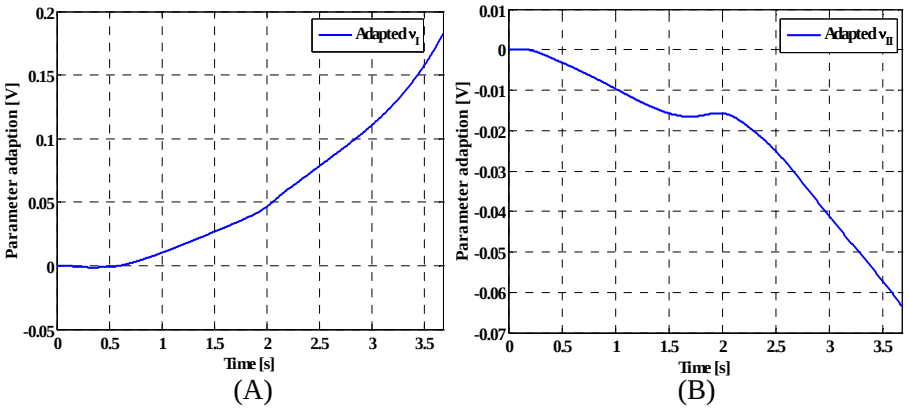

Figure I.16: ν adaption for RAAC control system. (A) HSS I. (B) HSS II.

I.2.3 Tracking Errors - RAIDC/RAAC

Compensator	$\lvert e_{maxI}\rvert$ $[mm]$	e_{rmsI} $[mm]$	$\lvert e_{maxII}\rvert$ $[mm]$	e_{rmsII} $[mm]$
RAIDC	6.46	2.68	1.16	0.36
RAAC	6.82	2.48	2.03	0.60

Table I.2: Tracking error values for controllers tested on the rectangular trajectory.

I.3 Simulation Results - AIDC/AAC (IOT)

In this section of the appendix, the simulation results regarding errors for the IOT are presented. The plots for the trajectory tracking and errors are found on the appended CD under *IOT plots*.

I.3.1 Tracking Errors - AIDC/AAC

Compensator	$\lvert e_{maxI}\rvert$ $[mm]$	e_{rmsI} $[mm]$	$\lvert e_{maxII}\rvert$ $[mm]$	e_{rmsII} $[mm]$
AIDC	3.21	1.48	0.61	0.16
AAC	6.86	3.66	1.00	0.64

Table I.3: Tracking error values for controllers tested on the in/out trajectory.

I.4 Simulation Results - RAIDC/RAAC (IOT)

The plots for the trajectory tracking and errors are found on the appended CD under *IOT plots*.

I.4.1 Tracking Errors - RAIDC/RAAC

Compensator	$\lvert e_{maxI}\rvert$ $[mm]$	e_{rmsI} $[mm]$	$\lvert e_{maxII}\rvert$ $[mm]$	e_{rmsII} $[mm]$
RAIDC	3.02	1.31	0.55	0.16
RAAC	5.90	2.65	0.63	0.33

Table I.4: Tracking error values for controllers tested on the in/out trajectory.

Appendix J

Controller Parameters - Nonlinear Controllers

Contents

In this appendix the parameters for the adaptive and learning controllers used during simulation are presented. Controller parameters for the AIDC, AAC, RAIDC and AAC are found on the appended CD.

J.1 Control Parameters used for MAIDC/MAAC

J.1.1 Control Parameters used for the RECT - MAIDC/MAAC

The control parameters used for the MAIDC and MAAC, when completing the rectangular trajectory are presented in table J.1.

Parameter	MAIDC	MAAC
k_{pI}	13.00	10.00
k_{pII}	15.00	38.00
k_{piI}	–	15.00
k_{piII}	–	13.00
γ_{1I}	0.01	0.50
γ_{1II}	20.00	0.80
γ_{2I}	20.00	2.10
γ_{2II}	20.00	0.80
α_{1I}	5.00	3.00
α_{1II}	1.00	0.80
α_{2I}	5	17.00
α_{2II}	0.10	17.00
$\hat{\Gamma}_{iniI}$	1.80	1.80
$\hat{\Gamma}_{iniII}$	1.20	1.10
$\hat{\nu}_{iniI}$	0.55	0.50
$\hat{\nu}_{iniII}$	0.03	0.00

Table J.1: Parameters used in the control- and adaption laws of the MAIDC and MAAC

J.1.2 Control Parameters used for the IOT - MAIDC/MAAC

The control parameters used for the MAIDC and MAAC, when completing the IOT are presented in table J.2.

Parameter	MAIDC	MAAC
k_{pI}	13.00	10.00
k_{pII}	15.00	38.00
k_{piI}	–	15.00
k_{piII}	–	13.00
γ_{1I}	0.01	0.50
γ_{1II}	20.00	0.80
γ_{2I}	20.00	2.10
γ_{2II}	20.00	0.10
α_{1I}	5.00	3.00
α_{1II}	5.00	0.30
α_{2I}	0.10	17.00
α_{2II}	0.10	17.00
$\hat{\Gamma}_{iniI}$	1.80	2.30
$\hat{\Gamma}_{iniII}$	1.20	1.13
$\hat{\nu}_{iniI}$	0.80	0.50
$\hat{\nu}_{iniII}$	0.025	0.05

Table J.2: Parameters used in the control- and adaption laws of the MAIDC and MAAC

J.2 Control Parameters used for ILC/RDLC

The control parameters used for the ILC and RDLC aresimilar for both trajectories.

J.2.1 Control Parameters used for ILC

$$\hat{\Gamma}_I = 1 \quad , \quad k_{pI} = 20 \quad , \quad \mu_I = 10 \tag{J.1}$$

$$\hat{\Gamma}_{II} = 1 \quad , \quad k_{pII} = 20 \quad , \quad \mu_{II} = 5 \tag{J.2}$$

J.2.2 Control Parameters used for RDLC

$$\hat{\Gamma}_I = 1 \quad , \quad k_{pI} = 1 \quad , \quad L_I = 0.011 \tag{J.3}$$

$$\hat{\Gamma}_{II} = 1 \quad , \quad k_{pII} = 1 \quad , \quad L_{II} = 0.011 \tag{J.4}$$

Here $\Delta t = 1/2000$ $[s]$.

Appendix K

Appendix for the RDLC

Contents

This appendix presents the bounds and assumptions used for the RDLC. This is taken directly from [Andersen, 2004a].

In the following the desired trajectory is denoted x_d, whereas the desired trajectory in this thesis is denoted x_R.

K.1 Bounds & Assumptions

The following has been scanned directly from [Andersen, 2004a].

The class of non-linear, time-varying systems considered is described by the following state-space equations:

$$\begin{aligned} \dot{x}_k(t) &= f(x_k(t),t) + B(x_k(t),t)\,u_k(t) + \omega_k(t) \\ y_k(t) &= g(x_k(t),t) \end{aligned} \tag{1}$$

where, for all $t \in [0,\ T]$, $x_k(t) \in \Re^n$, $u_k(t) \in \Re^r$, $y_k(t) \in \Re^m$, and $\omega_k(t) \in \Re^n$. The functions $f: \Re^n \times [0,\ T] \to \Re^n$ and $B: \Re^n \times [0,\ T] \to \Re^{n \times r}$ are piecewise continuous in t and $g: \Re^n \times [0,\ T] \to \Re^m$ is differentiable in x and t, with partial derivatives $g_x(\cdot,\cdot)$ and $g_t(\cdot,\cdot)$. The inputs considered, not necessarily continuous, are $u_k: [0,\ T] \to \Re^r$. Let Ω denote the mapping from $(x_k(0), u_k(t), t \in [0,T])$ to $x_k(t), t \in [0,T]$ as determined by the differential equation (1) with $\omega_k(t) \equiv 0$. Similarly, let Π denote the mapping from $(x_k(0), u_k(t), t \in [0,T])$ to $y_k(t), t \in [0,T]$. Thus, for a given initial condition and control input on $[0,T]$, $x_k(\cdot) = \Omega(u_k(\cdot),\ x_k(0))$ and $y_k(\cdot) = \Pi(u_k(\cdot),\ x_k(0))$. In addition, the following properties are assumed.

(A1) The mappings Ω and Π are one-to-one.
(A2) The disturbance $\omega_i(\cdot)$ is bounded by b_ω on $[0,\ T]$.
(i.e. $\|\omega_i(\cdot)\| \le b_\omega$ on the interval $[0,\ T]$).
(A3) The functions $f(\cdot,\cdot)$, $B(\cdot,\cdot)$, $g_x(\cdot,\cdot)$ and $g_t(\cdot,\cdot)$ are uniformly globally Lipschitz in x on the interval $[0,\ T]$. That is,
$\|h(x_1,t) - h(x_2,t)\| \le k_h \|x_1(t) - x_2(t)\|$ $\forall t \in [0,\ T]$ and
some $k_h < \infty \in R$ $(h \in \{f,\ B,\ g_x,\ g_t\})$
(A4) The operators $B(\cdot,\cdot)$ and $g_x(\cdot,\cdot)$ are bounded on $R^n \times [0,\ T]$.
(A5) All functions are assumed to be measurable and integrable.

Assumption (A1) implies that given an achievable, desired output trajectory (y_d) and initial state $(x_d(0))$, there exist unique input (u_d) and state (x_d) trajectories corresponding to this output trajectory. Assumption (A4) on $g_x(\cdot,\cdot)$ implies that g is uniformly globally Lipschitz in x on $[0,\ T]$. The function $\omega_k(t)$ represents both deterministic and random disturbances of the system. It may be stiction, non-reproducible friction, modelling errors, etc. This is important to include since these are present in physical systems. Assumption (A2) restricts these disturbances to be bounded, but they may discontinuous (e.g. stiction in mechanical systems).

Figure K.1: Extract from [Andersen, 2004a].

Appendix L

Simulation Results for the IOT - Linear Controllers

Contents

In this appendix the simulation results for linear controllers tested on the IOT are presented.

L.1 Simulation Results - Classic Linear Controllers

As shown in figures L.1 and L.2, it is clear that the tracking performance is similar to those of the RECT, despite the lesser demanding trajectory.

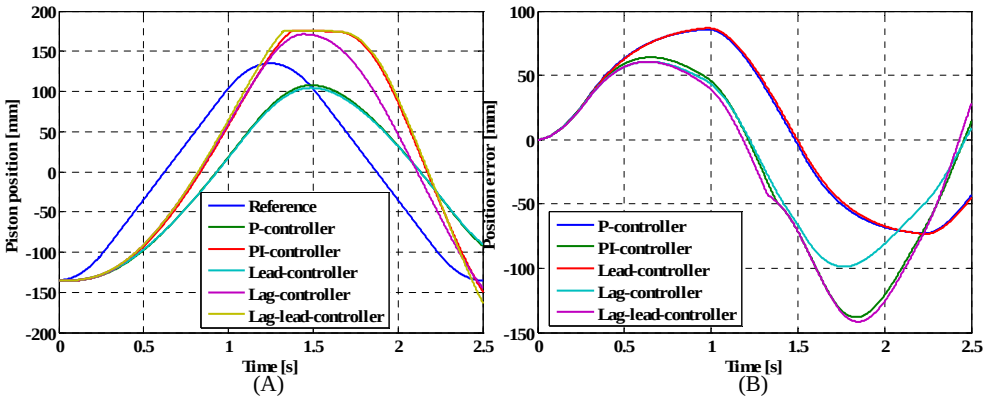

Figure L.1: (A) Trajectory position tracking, for the nonlinear model cylinder I. (B) Position tracking errors for the nonlinear model, cylinder I.

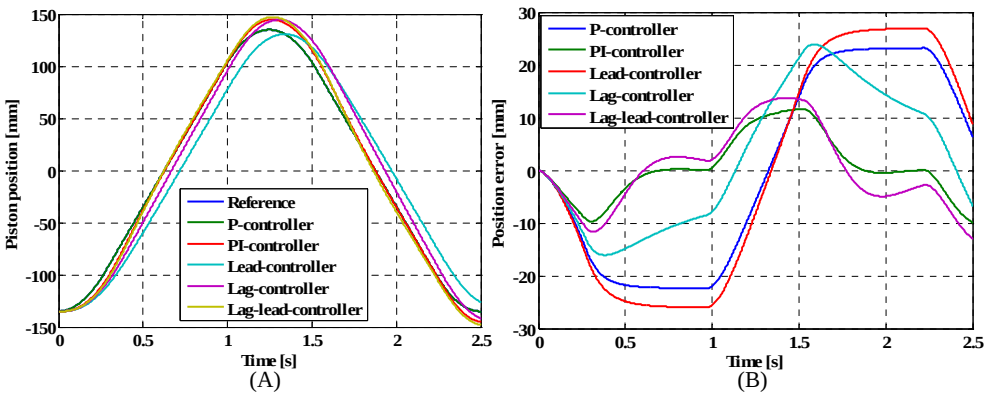

Figure L.2: (A) Trajectory position tracking, for the nonlinear model cylinderII. (B) Position tracking errors for the nonlinear model, cylinder II.

L.1.1 Tracking Errors (IOT)

As for the RECT, the tracking errors are summarized and shown in table L.1.

Compensator	$\lvert e_{maxI} \rvert$ $[mm]$	e_{rmsI} $[mm]$	$\lvert e_{maxII} \rvert$ $[mm]$	e_{rmsII} $[mm]$
P	85.81	59.06	23.21	18.53
PI	138.20	71.79	11.65	5.93
Lead	86.79	59.20	26.95	21.33
Lag	98.91	56.75	23.88	13.33
Lag-Lead	141.55	72.27	13.76	7.46

Table L.1: Tracking error values for controllers tested on the out/in trajectory.

L.2 Simulation Results - VFCP/VFCA

L.2.1 Simulation Results - VFCP

From figures L.3 and L.4 it is found that the performance is similar to the situation, where the compensated systems are subjected to the RECT.

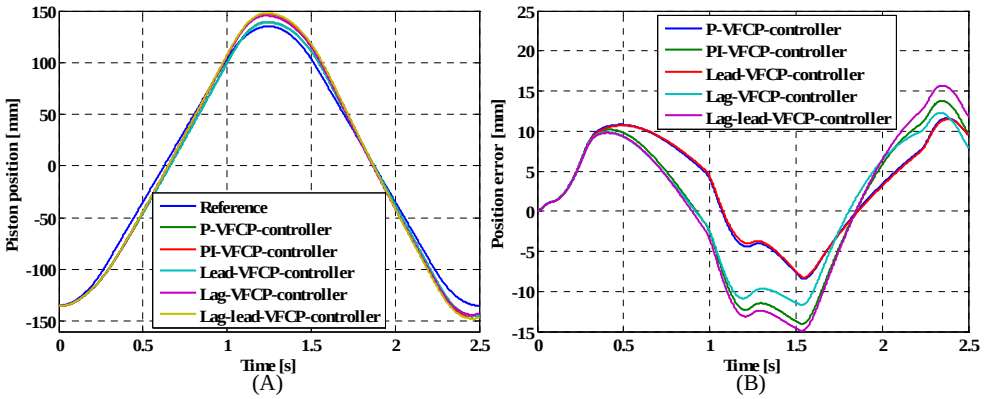

Figure L.3: (A) Trajectory position tracking, for HSS I. (B) Position tracking errors for HSS I.

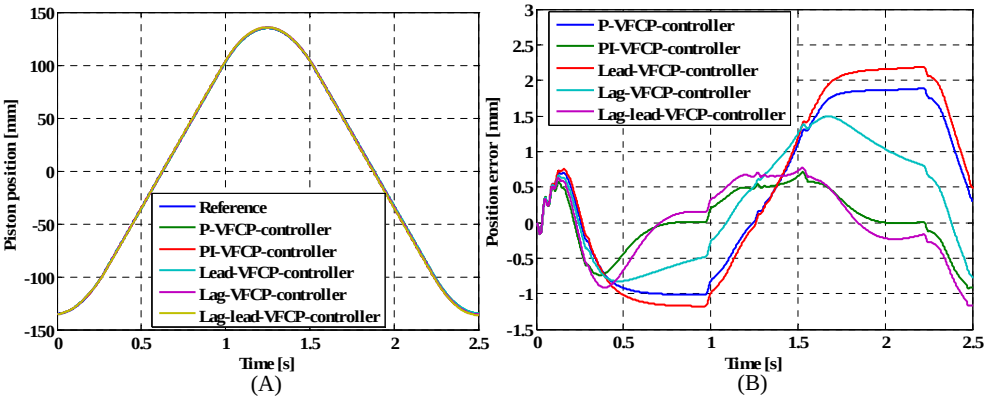

Figure L.4: (A) Trajectory position tracking, for HSS II. (B) Position tracking errors for HSS II.

Tracking Errors (IOT)

The tracking errors for the IOT are summarized in table L.2.

Compensator	$\lvert e_{maxI} \rvert$ $[mm]$	e_{rmsI} $[mm]$	$\lvert e_{maxII} \rvert$ $[mm]$	e_{rmsII} $[mm]$
P-VFCP	11.61	6.97	1.88	1.18
PI-VFCP	14.08	8.83	0.92	0.41
Lead-VFCP	11.45	6.90	2.19	1.36
Lag-VFCP	12.28	7.85	1.49	0.82
Lag-Lead-VFCP	15.68	9.48	1.46	0.51

Table L.2: Tracking error values for controllers tested on the out/in trajectory.

L.2.2 Simulation Results - VFCA

It is found from figures L.5 and L.6, that when testing a VFCA in combination with a P and PI controller, the tracking performance is decreased, compared to the tracking

performance obtained with the RECT. Especially in the second half of the IOT, the controllers are not able to track the reference position. This may by due to that the forces and hence the load pressures are reversed within as short period of time when the actuators are to retract. This may cause variations in the active feed forward gain to such an extend, that these are not corrected within the second half of the time period for the trajectory.

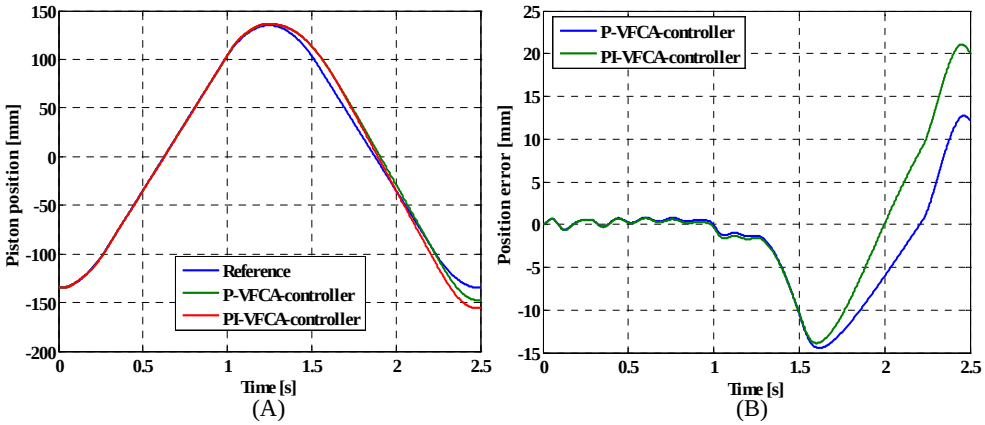

Figure L.5: Trajectory tracking with VFCA for HSS I. (A) Trajectory tracking. (B) Tracking errors.

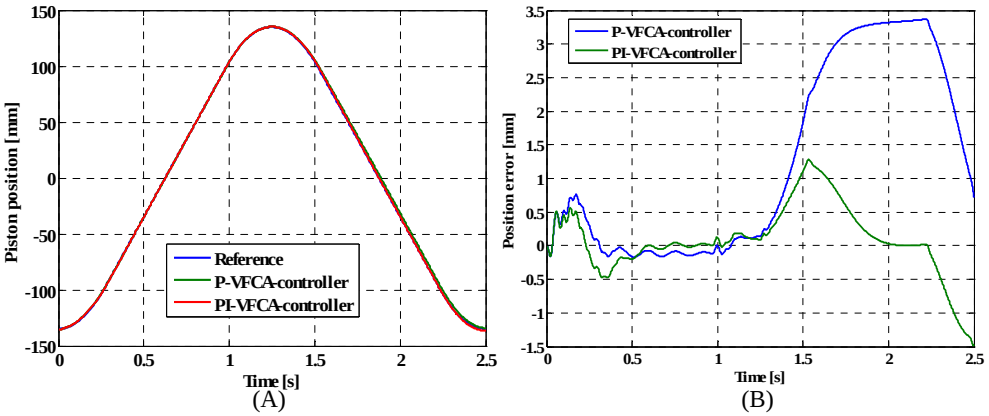

Figure L.6: Trajectory tracking with VFCA for HSS II. (A) Trajectory tracking. (B) Tracking errors.

Tracking Errors

Compensator	$\lvert e_{maxI} \rvert$ $[mm]$	e_{rmsI} $[mm]$	$\lvert e_{maxII} \rvert$ $[mm]$	e_{rmsII} $[mm]$
P-VFCA	14.44	6.39	3.37	1.87
PI-VFCA	21.06	7.67	1.48	0.52

Table L.3: Tracking error values for controllers tested on the in/out trajectory.

L.3 Simulation Results - GFM

In the following the simulation results for the in/out trajectory are presented. Here it is possible to apply the feed forward compensation, as the control valve input does not experience saturation with the IOT. It is found from figures L.7 and L.8 that the tracking performance for the IOT is similar to the tracking performance of the RECT. However, it is found that the maximum errors regarding the IOT are smaller compared to the RECT, and this improvement is caused by the lesser demands to the system when completing the IOT.

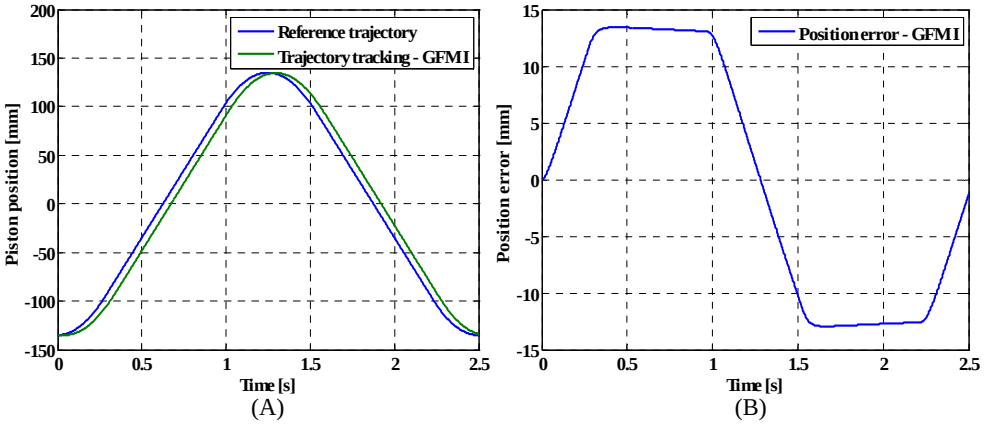

Figure L.7: Simulation results for the GFM control scheme applied on HSS I. (A) Trajectory tracking. (B) Tracking error.

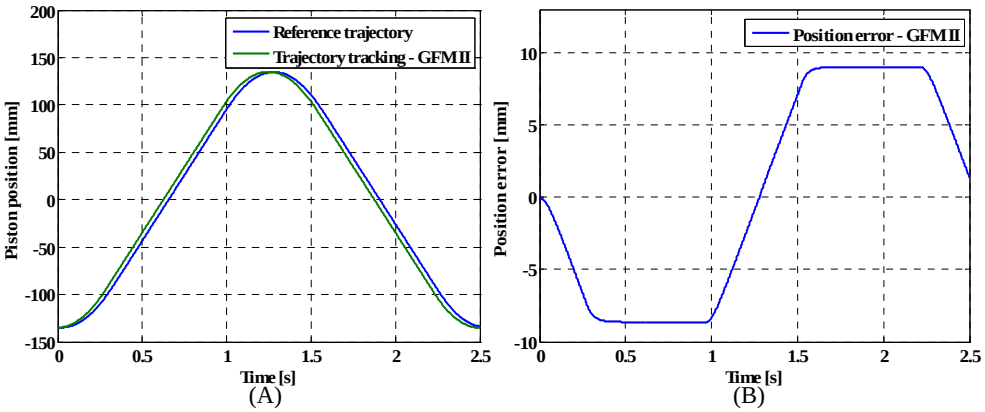

Figure L.8: Simulation results for the GFM control scheme applied on HSS II. (A) Trajectory tracking. (B) Tracking error.

From figures L.9 and L.10 it is seen that adding the feed forward contribution to the controller, dramatically increases the tracking performance.

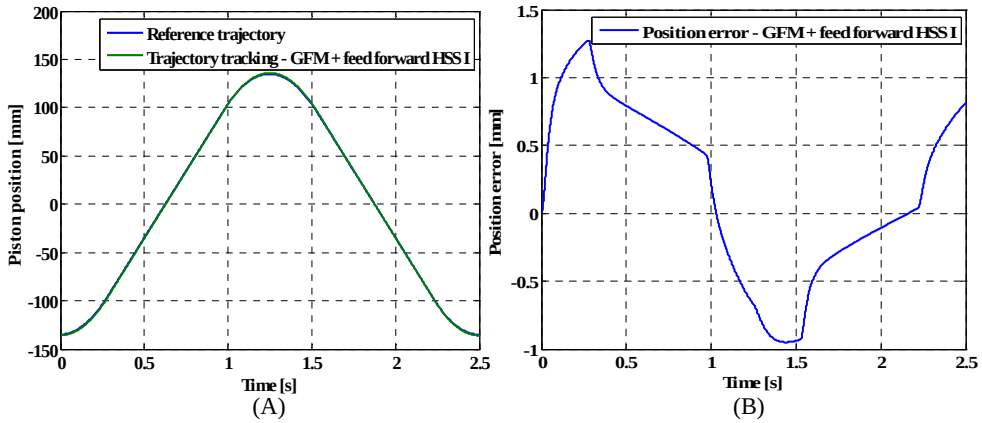

Figure L.9: Simulation results for the GFM+feed forward applied on HSS I. (A) Trajectory tracking. (B) Tracking error.

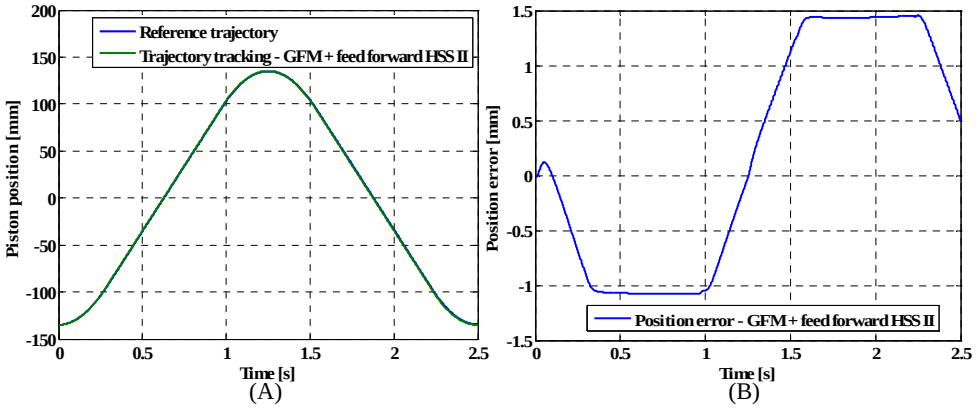

Figure L.10: Simulation results for the GFM+feed forward applied on HSS II. (A) Trajectory tracking. (B) Tracking error.

L.3.1 Tracking Errors (IOT)

Compensator	$\lvert e_{maxI} \rvert$ $[mm]$	e_{rmsI} $[mm]$	$\lvert e_{maxII} \rvert$ $[mm]$	e_{rmsII} $[mm]$
GFM	13.43	10.90	9.02	7.36
GFM+VFCP$_G$	1.27	0.65	1.44	1.07

Due to the fact that no velocity sensors are available on the physical system, this compensator has not been tested the test setup.

Appendix M

Simulation Results for the IOT - Nonlinear Controllers

Contents

In this appendix the simulation results for linear controllers tested on the IOT are presented.

The simulation results for the IOT, along with their errors are found in appendix M.

M.1 Simulation Results - Adaptive Controllers

In the following the simulation results for the MAIDC and the MAAC are presented.

It is found from figures M.1, M.2, M.5 and M.6, that when using MAIDC- and MAAC schemes to complete the IOT, tracking performance is similar to completing the RECT - however, with an increase in the tracking performance.

Regarding the parameter adaption, it is found from figures M.3, M.4, M.7 and M.8, that the adapted parameters $\hat{\Gamma}_i$ experiences increased tracking of the calculated Γ_i, along the ramp-like segments of the IOT.

M.1.1 MAIDC

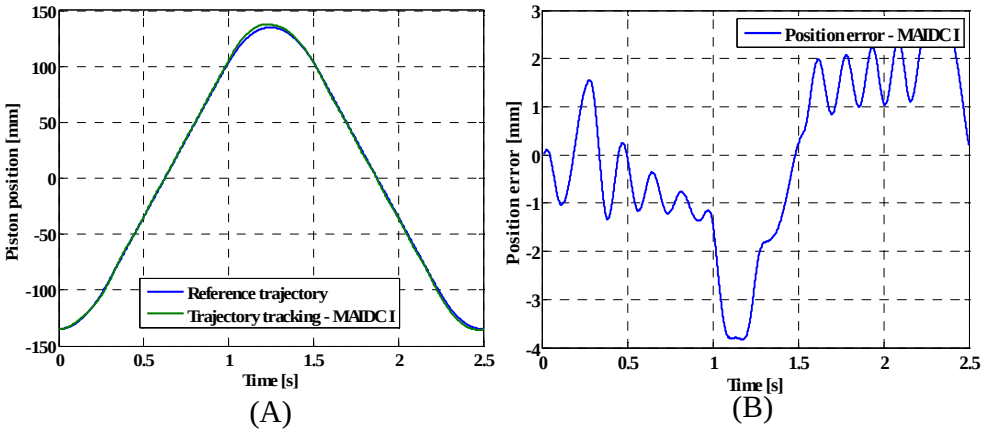

Figure M.1: MAIDC scheme implemented on HSS I. (A) Trajectory tracking. (B) Tracking error.

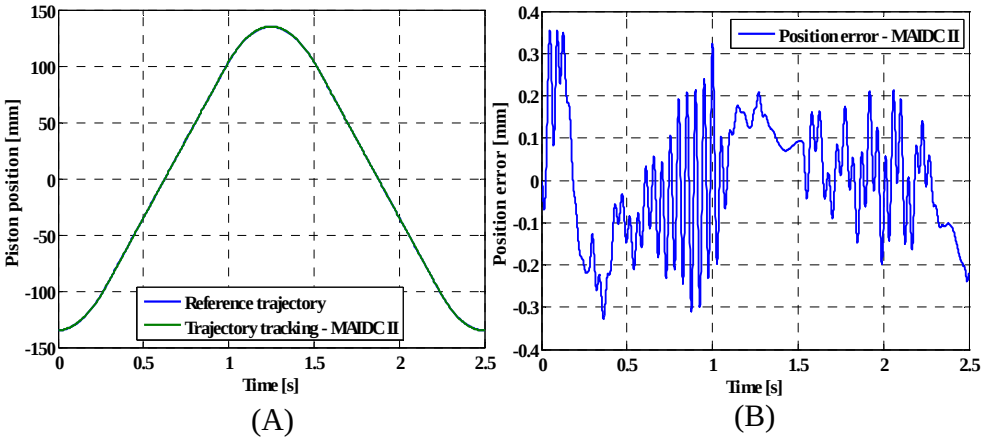

Figure M.2: MAIDC scheme implemented on HSS II. (A) Trajectory tracking. (B) Tracking error.

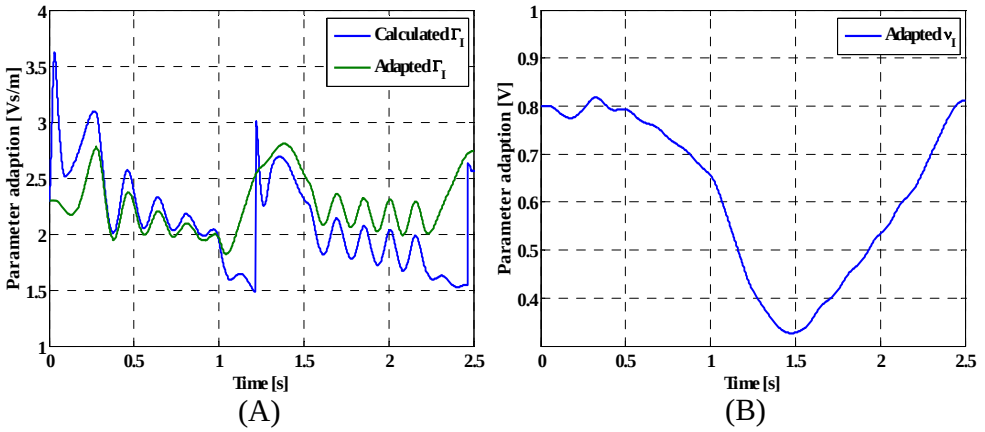

Figure M.3: MAIDC scheme implemented on HSS I. (A) Adaption of $\hat{\Gamma}_I$. (B) Adaption of $\hat{\nu}_I$.

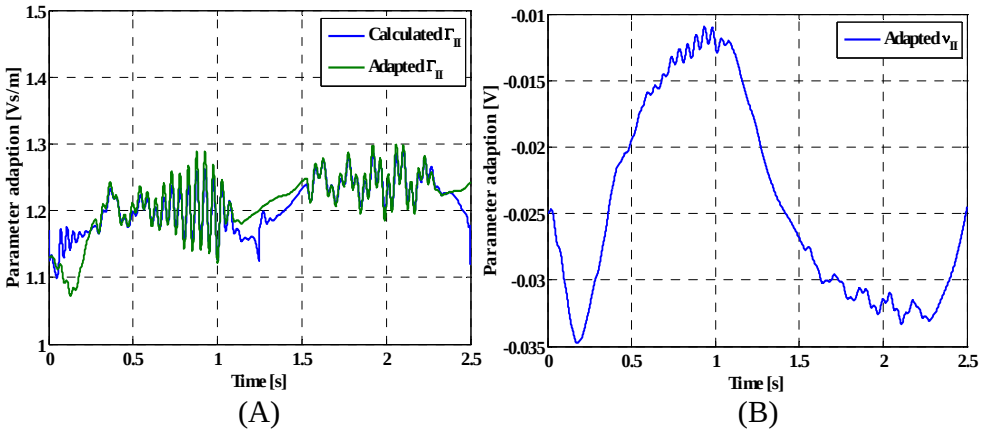

Figure M.4: MAIDC scheme implemented on HSS II. (A) Adaption of $\hat{\Gamma}_{II}$. (B) Adaption of $\hat{\nu}_{II}$.

M.1.2 MAAC

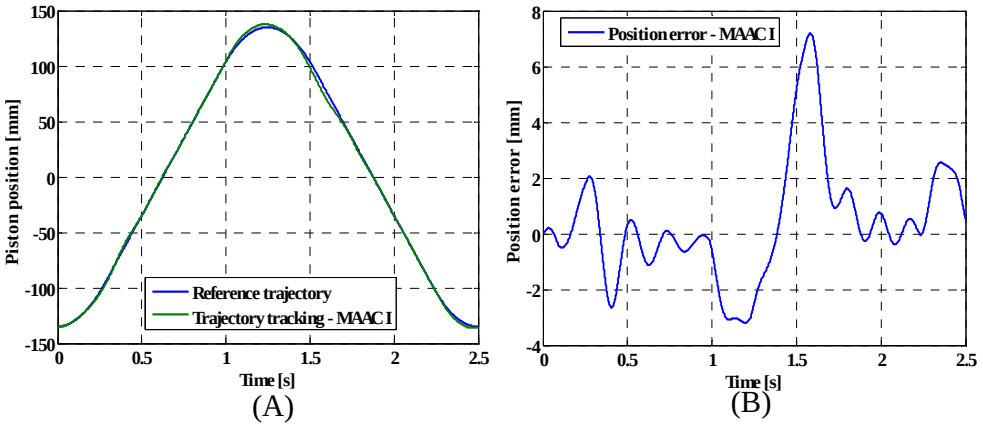

Figure M.5: MAAC scheme implemented on HSS I. (A) Trajectory tracking. (B) Tracking error.

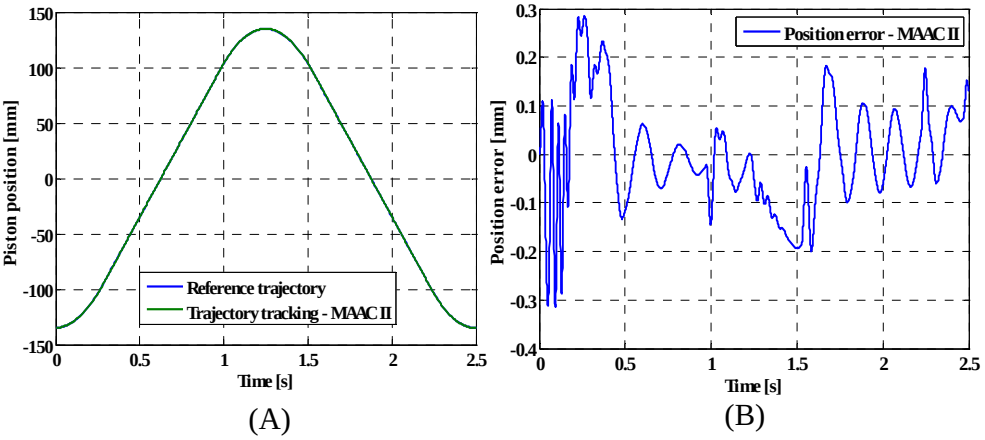

Figure M.6: MAAC scheme implemented on HSS II. (A) Trajectory tracking. (B) Tracking error.

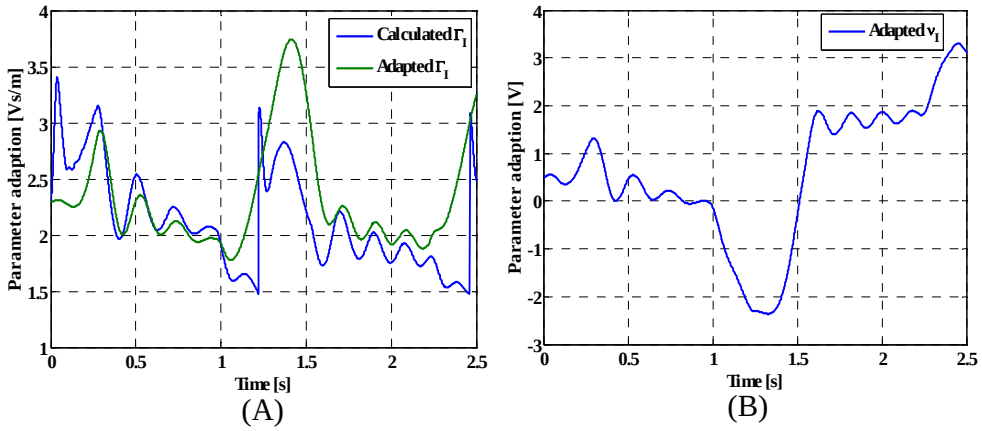

Figure M.7: MAAC scheme implemented on HSS I. (A) Adaption of $\hat{\Gamma}_I$. (B) Adaption of $\hat{\nu}_I$.

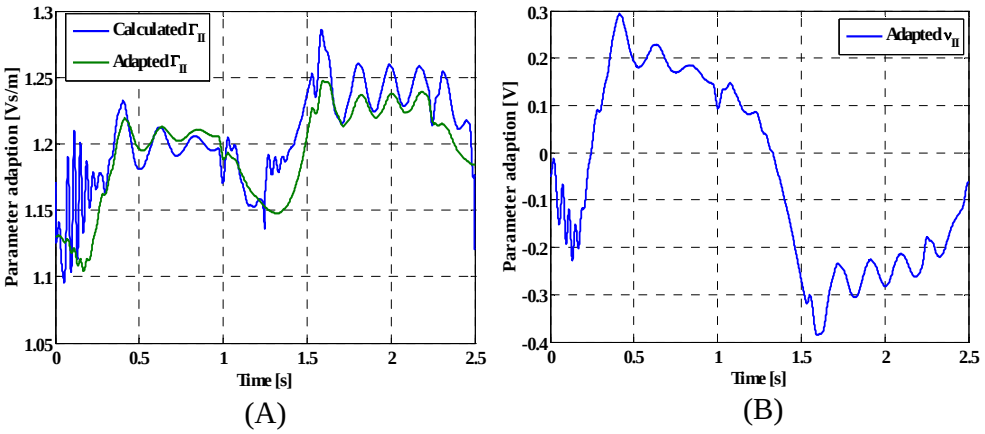

Figure M.8: MAAC scheme implemented on HSS II. (A) Adaption of $\hat{\Gamma}_{II}$. (B) Adaption of $\hat{\nu}_{II}$.

M.1.3 Tracking Errors - IOT

Compensator	$\lvert e_{maxI}\rvert$ $[mm]$	e_{rmsI} $[mm]$	$\lvert e_{maxII}\rvert$ $[mm]$	e_{rmsII} $[mm]$
MAIDC	3.85	1.73	0.35	0.14
MAAC	7.20	2.17	0.31	0.11

Table M.1: Tracking error values for controllers tested on the in/out trajectory.

M.2 Simulation Results - Learning Controllers

M.2.1 Simulation Results - RDLC

The parameters of the learning controllers used for the IOT are given below.

$$\hat{\Gamma}_I = 1 \quad , \quad k_{pI} = 1 \quad , \quad K_{LI} = 0.011 \tag{M.1}$$

$$\hat{\Gamma}_{II} = 1 \quad , \quad k_{pII} = 1 \quad , \quad K_{LII} = 0.011 \tag{M.2}$$

Regarding the IOT, simulation results are similar to the ones obtained for the RECT - however, due to the lesser demanding trajectory, the obtained minimum errors are smaller than the ones obtained for the RECT.

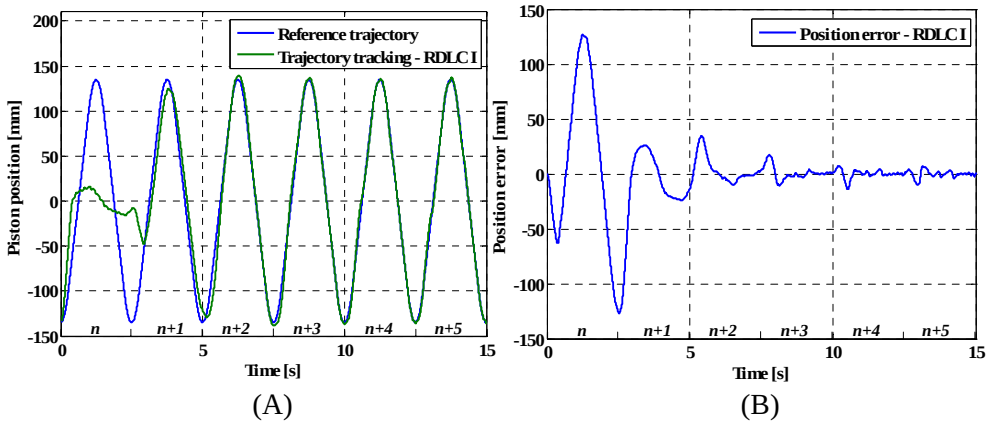

Figure M.9: RDLC implemented on HSS I. (A) Trajectory tracking. (B) Tracking error.

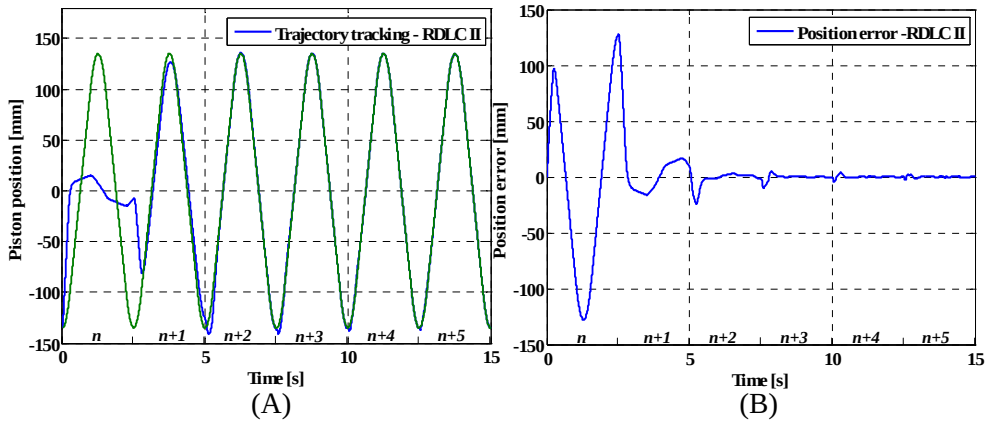

Figure M.10: RDLC implemented on HSS II. (A) Trajectory tracking. (B) Tracking error.

M.2.2 Tracking Errors - (IOT)

The maximum- and RMS errors are obtained for trajectory cycle with best performance, and are given in the tables below.

Compensator	$\lvert e_{maxI} \rvert$ $[mm]$	e_{rmsI} $[mm]$	$\lvert e_{maxII} \rvert$ $[mm]$	e_{rmsII} $[mm]$
RDLC	10.07	3.45	3.10	0.67

Table M.2: Tracking error values for controllers tested on the in/out trajectory.

It has not been possible to implement the learning controllers within the time frame of the thesis, hence no experimental results are presented. However, efforts to obtain

reasonable experimental results for the learning controllers will be made previous to the thesis evaluation, and the results will presented there.

M.2.3 Simulation Results - ILC

The parameters of the learning controllers used for the IOT are given below.

$$\hat{\Gamma}_I = 1 \quad , \quad k_{pI} = 20 \quad , \quad \mu_I = 8 \tag{M.3}$$

$$\hat{\Gamma}_{II} = 1 \quad , \quad k_{pII} = 20 \quad , \quad \mu_{II} = 8 \tag{M.4}$$

Regarding the IOT, simulation results are similar to the ones obtained for the RECT - however, due to the lesser demanding trajectory, the obtained minimum errors are smaller than the ones obtained for the RECT.

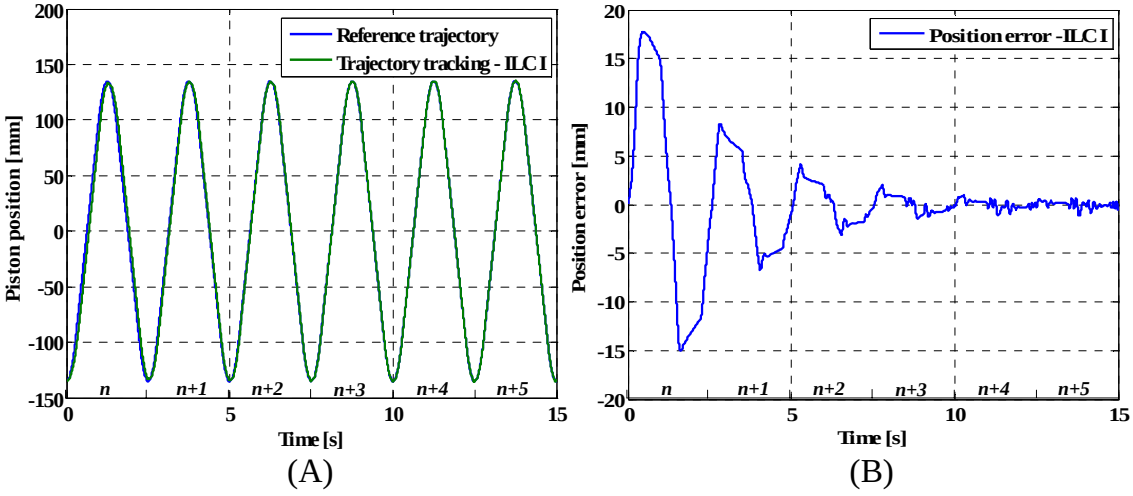

Figure M.11: Learning controller implemented on HSS I. (A) Trajectory tracking. (B) Tracking error.

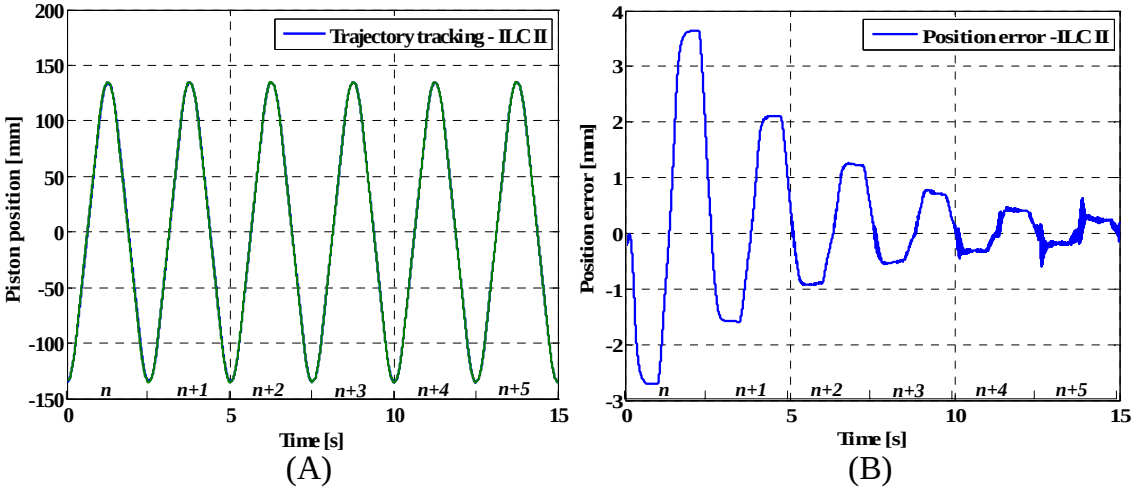

Figure M.12: Learning controller implemented on HSS II. (A) Trajectory tracking. (B) Tracking error.

M.2.4 Tracking Errors - (IOT)

Compensator	$\lvert e_{maxI} \rvert$ $[mm]$	e_{rmsI} $[mm]$	$\lvert e_{maxII} \rvert$ $[mm]$	e_{rmsII} $[mm]$
ILC	1.23	0.35	0.68	0.32

Table M.3: Tracking error values for controllers tested on the in/out trajectory.

Appendix N

Control Laws for ARC

Contents

This appendix presents the elements of the control laws for the ARC. This is taken directly from [Yao et al., 2001].

N.1 Control Law α_2

The following has been scanned directly from [Yao et al., 2001]. The following two figures (N.1, N.2 and N.3) are coherent.

$$k_{2s1} \geq \frac{1}{\theta_{1\min}}(k_2 + \|C_{\phi 2}\Gamma\phi_2\|^2) \Bigg\}$$

Figure N.1: Extract from [Yao et al., 2001].

The robust control function α_{2s2} is now chosen to satisfy the conditions

$$\left.\begin{array}{ll} \text{Condition i} & z_2[\theta_1\alpha_{2s2} - \tilde{\theta}^{\mathrm{T}}\phi_2 + \tilde{d}] \le \varepsilon_2 \\ \text{Condition ii} & z_2\theta_1\alpha_{2s2} \le 0 \end{array}\right\} \quad (19)$$

where ε_2 is a design parameter which can be arbitrarily small. Essentially, Condition i of (19) shows that α_{2s2} is synthesized to dominate the model uncertainties coming from both parametric uncertainties $\tilde{\theta}$ and uncertain nonlinearities $\tilde{d}$, and Condition ii is to make sure that α_{2s2} is dissipating in nature so that it does not interfere with the functionality of the adaptive control part α_{2a}. How to

Figure N.2: Extract from [Yao et al., 2001].

Remark 1: One example of a smooth α_{2s2} satisfying (19) can be found in the following way. Let h_2 be any smooth function satisfying

$$h_2 \ge \|\theta_M\|^2\|\phi_2\|^2 + \delta_d^2 \quad (20)$$

where $\theta_M = \theta_{\max} - \theta_{\min}$. Then, α_{2s2} can be chosen as

$$\alpha_{2s2} = -\frac{h_2}{2\theta_{1\min}\varepsilon_2} z_2 \quad (21)$$

It can be shown that (19) is satisfied (Yao and Tomizuka 1997). Other smooth or continuous examples of α_{2s2} can be found in Yao (1997) and Yao and Tomizuka (1997, 1999).

Figure N.3: Extract from [Yao et al., 2001].

N.2 Control Law α_3

The following has been scanned directly from [Yao et al., 2001].

$$k_{3s1} \geq \frac{1}{\theta_{3\min}}\left(k_3 + \left\| C_{\theta 3}\left(\frac{\partial \alpha_2}{\partial \hat{\theta}}\right)^{\mathrm{T}}\right\|^2 + \|C_{\phi 3}\Gamma\phi_3\|^2\right) \Bigg| \tag{31}$$

where $k_3 > 0$ is a constant, $C_{\theta 3}$ and $C_{\phi 3}$ are positive definite constant diagonal matrixes, and α_{3s2} is a robust control function satisfying the two conditions

$$\left.\begin{array}{ll} \text{Condition i} & z_3\left[\theta_3\alpha_{3s2} - \tilde{\theta}_1^{\mathrm{T}}\phi_3 - \dfrac{\partial \alpha_2}{\partial x_2}\tilde{d}\right] \leq \varepsilon_3 \\ \text{Condition ii} & z_3\theta_3\alpha_{3s2} \leq 0 \end{array}\right\} \tag{32}$$

where ε_3 is a design parameter. As in Remark 1, one example of α_{3s2} satisfying (32) is given by

$$\alpha_{3s2} = -\frac{1}{2\theta_{3\min}\varepsilon_3}h_3 z_3 \tag{33}$$

satisfying

$$h_3 \geq \|\theta_M\|^2\|\phi_3\|^2 + \left\|\frac{\partial \alpha_2}{\partial x_2}\right\|\delta_d^2 \tag{34}$$

Figure N.4: Extract from [Yao et al., 2001].

N.3 Control Law u_v

The following has been scanned directly from [Yao et al., 2001]. The following two figures (N.5 and N.6) are coherent.

$$k_{4s1} \geq \frac{\tau_v}{g_3\bar{K}_v}\left(k_4 + \left\| C_{\theta 4}\left(\frac{\partial \alpha_3}{\partial \hat{\theta}}\right)^{\mathrm{T}}\right\|^2 + \|C_{\phi 4}\Gamma\phi_4\|^2\right)$$

Figure N.5: Extract from [Yao et al., 2001].

$$\left.\begin{array}{ll} \text{Condition i} & z_4\left[\dfrac{\bar{K}_v}{\tau_v}g_3u_{s2} - \tilde{\theta}^{\mathrm{T}}\phi_4 - \dfrac{\partial\alpha_3}{\partial x_2}\tilde{d}\right] \le \varepsilon_4 \\ \text{Condition ii} & z_4\dfrac{g_3\bar{K}_v}{\tau_v}u_{s2} \le 0 \end{array}\right\} \tag{43}$$

in which ε_4 is a design parameter. As in Remark 1, one example of u_{s2} satisfying (43) is given by

$$u_{s2} = -\frac{\tau_v}{2\bar{K}_v g_3 \varepsilon_4}h_4 z_4 \tag{44}$$

in which h_4 is any continuous function satisfying

$$h_4 \ge \|\theta_M\|^2\|\phi_4\|^2 + \left\|\frac{\partial\alpha_3}{\partial x_2}\right\|\delta_d^2 \tag{45}$$

Figure N.6: Extract from [Yao et al., 2001].

N.4 Theorem 1

The following has been scanned directly from [Yao et al., 2001]. The following two figures (N.7 and N.8) are coherent.

Theorem 1: *Let the parameter estimates be updated by the adaptation law* (10) *in which* τ *is chosen as*

$$\tau = \sum_{j=2}^{4} w_j z_j \phi_j \tag{46}$$

By choosing non-linear controller gains k_{2s1}, k_{2s2} *and* k_{2s3} *large enough such that the inequality conditions in* (17), (31) *and* (42) *are satisfied for a set of*

$$C_{\theta j} = \text{diag}\{c_{\theta jl}, l = 1, 2, 3\}, j = 3, 4$$

and $C_{\phi k} = \text{diag}\{c_{\phi kl}\}, k = 2, 3, 4$ *with*

$$c_{\phi kl}^2 \geq \frac{3w_k}{4}\left(\frac{w_3}{c_{\theta 3l}{}^2} + \frac{w_4}{c_{\theta 4l}{}^2}\right), \quad \forall k, l$$

then, the control law (42) *with the adaptation law* (10) *guarantees that*

A. *In general, all signals are bounded. Furthermore,* V_4 *given by* (39) *is bounded above by*

$$V_4(t) \leq \exp(-\lambda_V t) V_4(0) + \frac{\varepsilon_V}{\lambda_V}[1 - \exp(-\lambda_V t)] \tag{47}$$

where $\lambda_V = 2\min\{k_2, k_3, k_4\}$ *and*

$$\varepsilon_V = w_2\varepsilon_2 + w_3\varepsilon_3 + w_4\varepsilon_4$$

B. *If after a finite time* t_0, $\tilde{d} = 0$, *i.e. in the presence of parametric uncertainties only, then, in addition to results in A, asymptotic output tracking (or zero final tracking error) is also achieved.*

Remark 2: Results in **A** of Theorem 1 indicate that the proposed controller has an exponentially converging transient performance with the exponentially converging rate λ_V and the final tracking error being able

Figure N.7: Extract from [Yao et al., 2001].

N.6) are coherent.

Theorem 1: *Let the parameter estimates be updated by the adaptation law* (10) *in which* τ *is chosen as*

$$\tau = \sum_{j=2}^{4} w_j z_j \phi_j \tag{46}$$

By choosing non-linear controller gains k_{2s1}, k_{2s2} *and* k_{2s3} *large enough such that the inequality conditions in* (17), (31) *and* (42) *are satisfied for a set of*

$$C_{\theta j} = \text{diag}\{c_{\theta jl}, l = 1,2,3\}, j = 3,4$$

and $C_{\phi k} = \text{diag}\{c_{\phi kl}\}, k = 2,3,4$ *with*

$$c_{\phi kl}^2 \geq \frac{3w_k}{4}\left(\frac{w_3}{{c_{\theta 3l}}^2} + \frac{w_4}{{c_{\theta 4l}}^2}\right), \quad \forall k, l$$

then, the control law (42) *with the adaptation law* (10) *guarantees that*

A. *In general, all signals are bounded. Furthermore,* V_4 *given by* (39) *is bounded above by*

$$V_4(t) \leq \exp(-\lambda_V t) V_4(0) + \frac{\varepsilon_V}{\lambda_V}[1 - \exp(-\lambda_V t)] \tag{47}$$

where $\lambda_V = 2\min\{k_2, k_3, k_4\}$ *and*

$$\varepsilon_V = w_2\varepsilon_2 + w_3\varepsilon_3 + w_4\varepsilon_4$$

B. *If after a finite time* t_0, $\tilde{d} = 0$, *i.e. in the presence of parametric uncertainties only, then, in addition to results in A, asymptotic output tracking (or zero final tracking error) is also achieved.*

Remark 2: Results in **A** of Theorem 1 indicate that the proposed controller has an exponentially converging transient performance with the exponentially converging rate λ_V and the final tracking error being able

Figure N.8: Extract from [Yao et al., 2001].

Appendix O

Robustness analysis

Contents

This appendix is a supplement to the chapter concerning the robustness of the control systems. Here the trajectory tracking of the control systems, when subjected to a disturbance, are presented.

O.1 Δ Error Plots for Linear Controllers

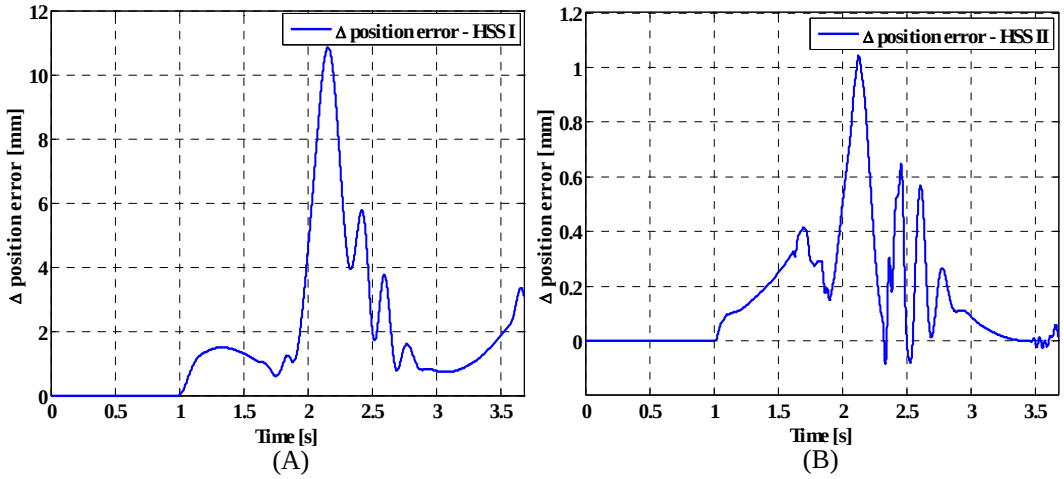

Figure O.1: Difference in error between P control system, with and without disturbance. (A) HSS I. (B) HSS II.

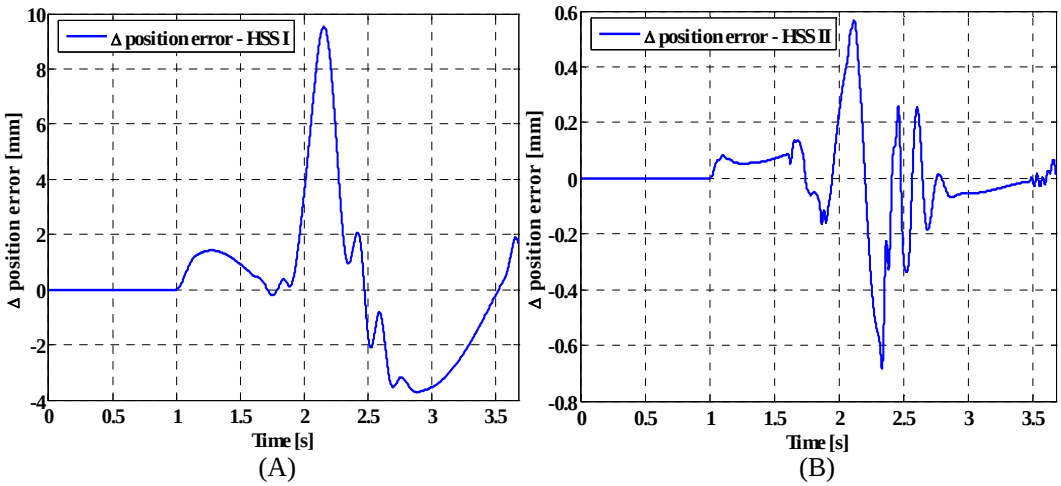

Figure O.2: Difference in error between PI control system, with and without disturbance. (A) HSS I. (B) HSS II.

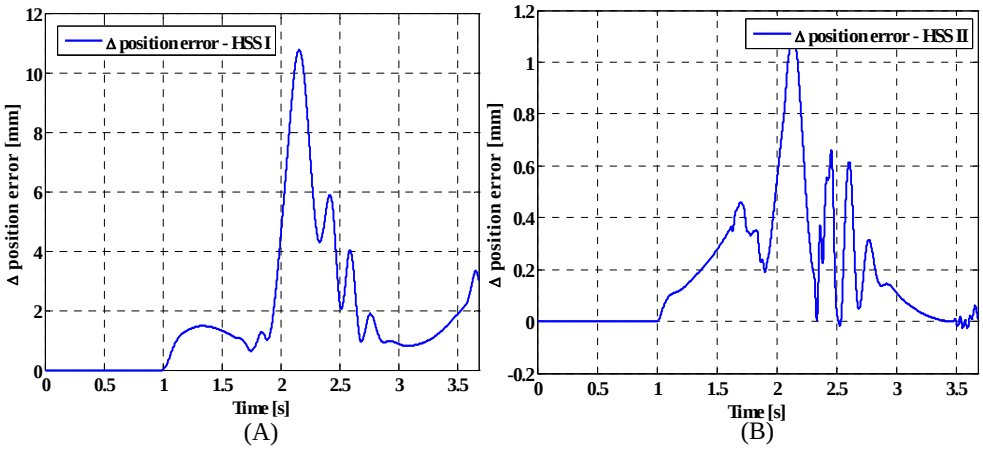

Figure O.3: Difference in error between Lead control system, with and without disturbance. (A) HSS I. (B) HSS II.

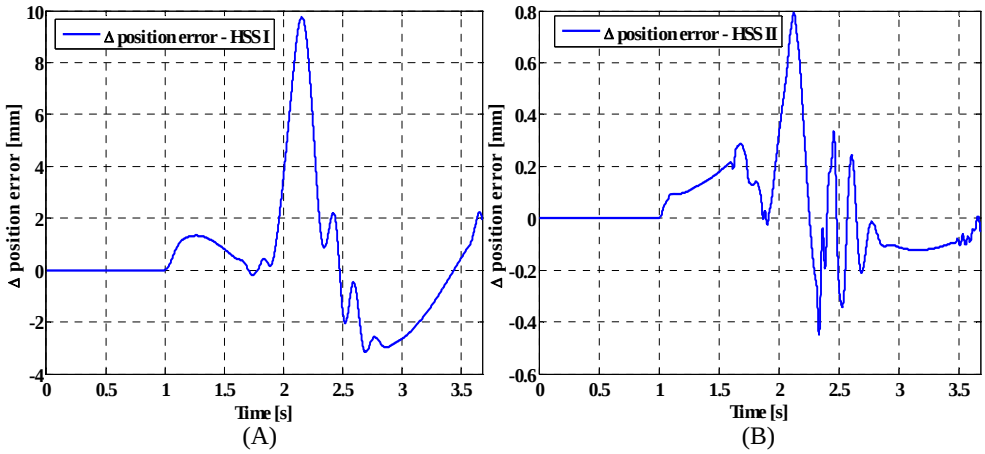

Figure O.4: Difference in error between Lag control system, with and without disturbance. (A) HSS I. (B) HSS II.

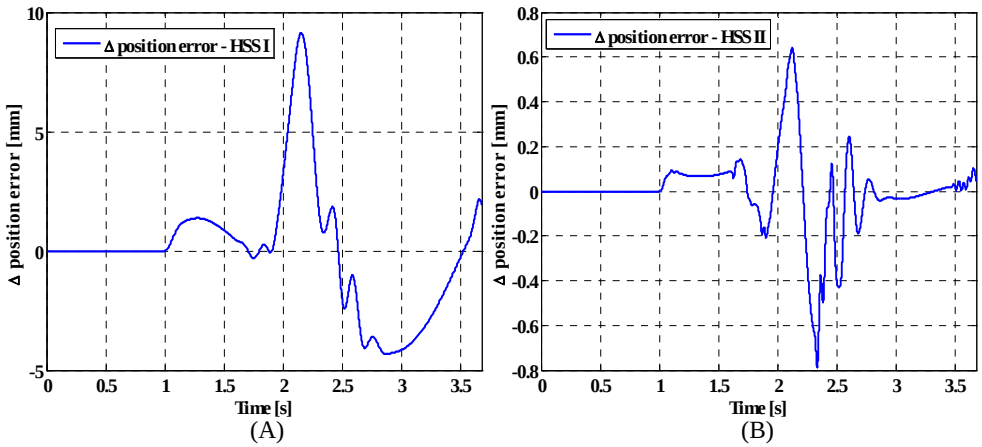

Figure O.5: Difference in error between Lag-Lead control system, with and without disturbance. (A) HSS I. (B) HSS II.

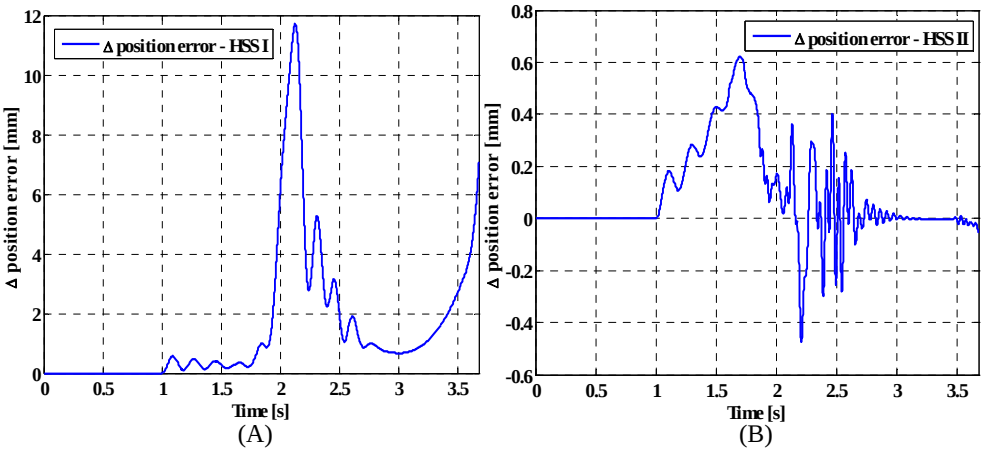

Figure O.6: Difference in error between P-VFCA control system, with and without disturbance. (A) HSS I. (B) HSS II.

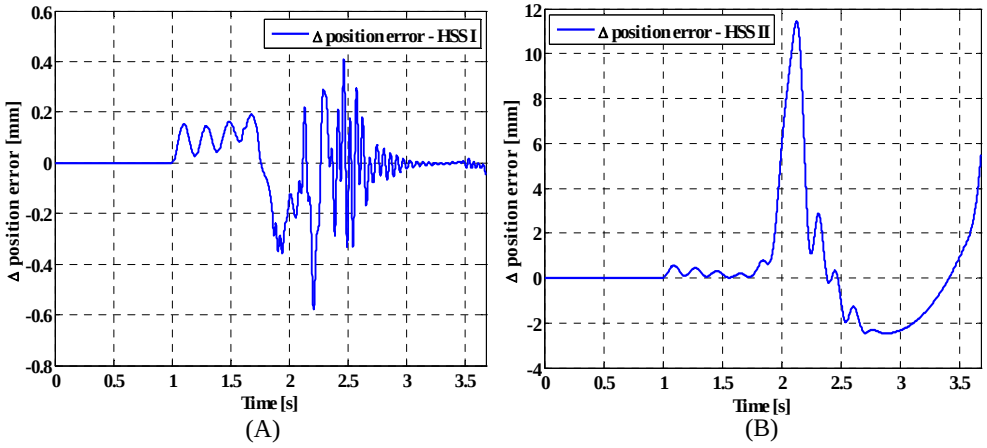

Figure O.7: Difference in error between PI-VFCA control system, with and without disturbance. (A) HSS I. (B) HSS II.

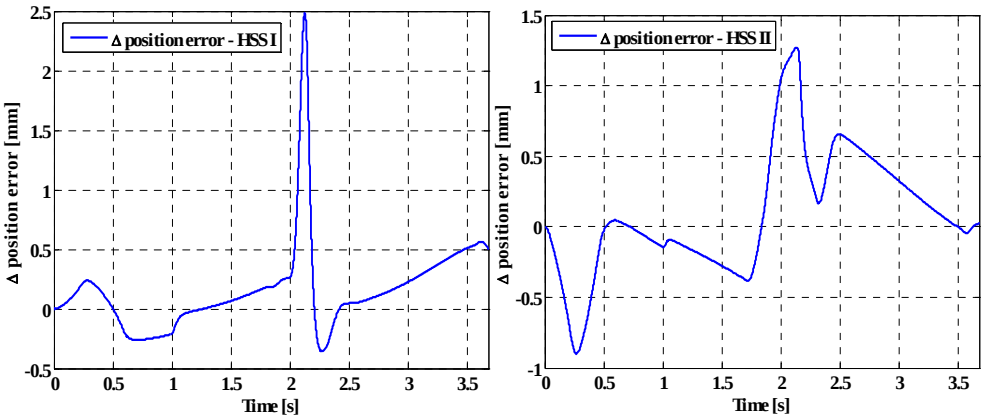

Figure O.8: Difference in error between GFM control system, with and without disturbance. (A) HSS I. (B) HSS II.

O.2 Δ Error Plots for Nonlinear controllers

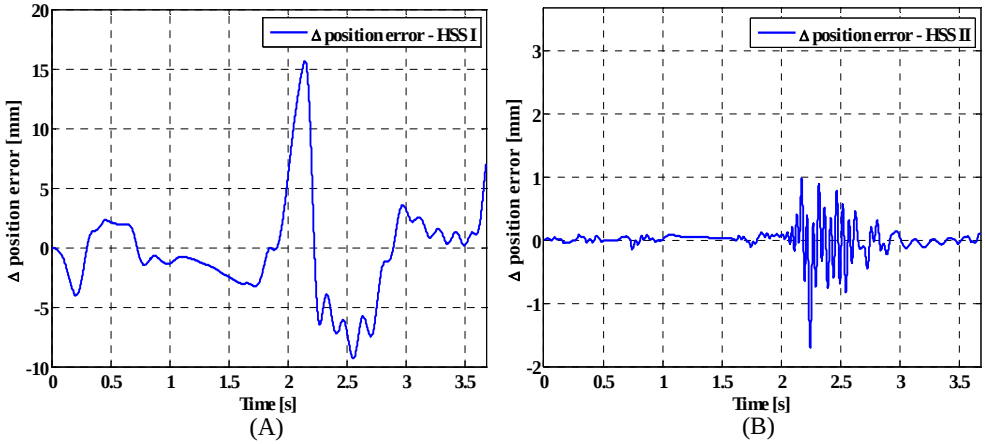

Figure O.9: Difference in error between MAIDC control system, with and without disturbance. (A) HSS I. (B) HSS II.

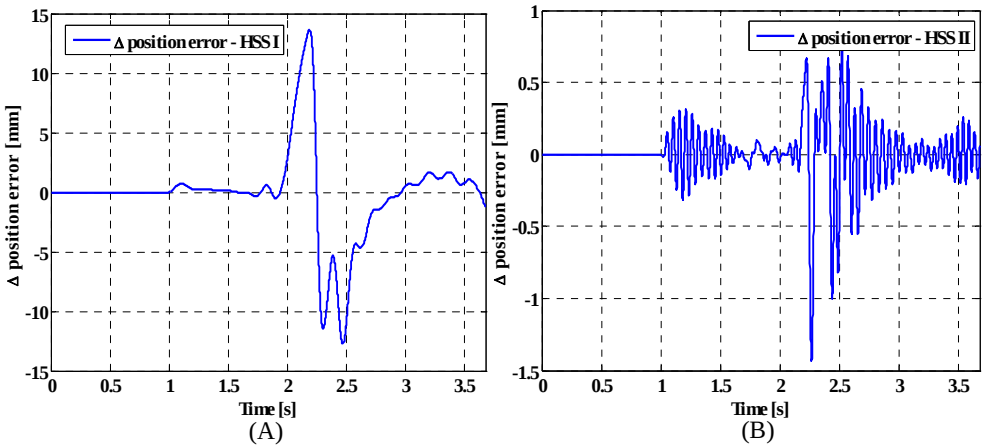

Figure O.10: Difference in error between MAAC control system, with and without disturbance. (A) HSS I. (B) HSS II.

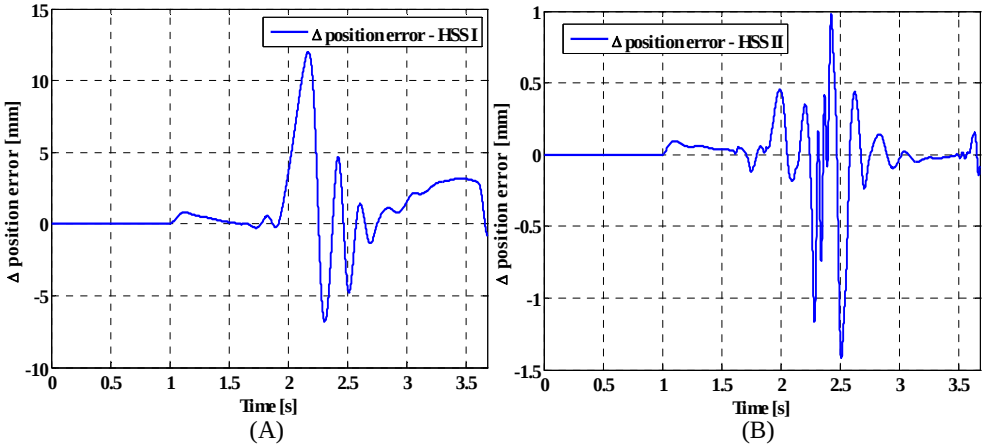

Figure O.11: Difference in error between AIDC control system, with and without disturbance. (A) HSS I. (B) HSS II.

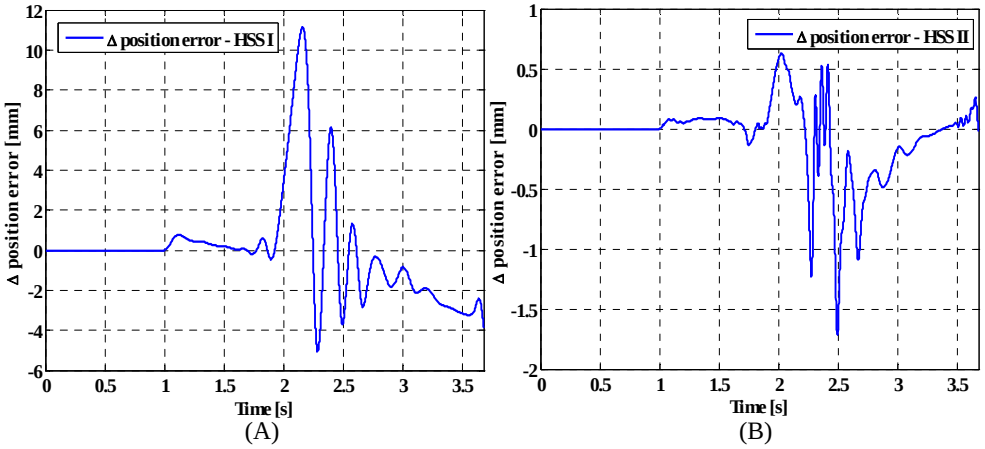

Figure O.12: Difference in error between AAC control system, with and without disturbance. (A) HSS I. (B) HSS II.

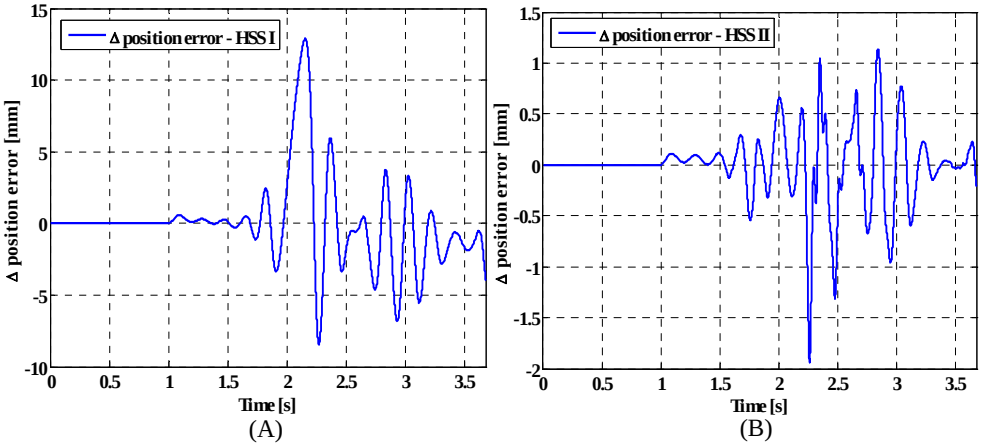

Figure O.13: Difference in error between RAIDC control system, with and without disturbance. (A) HSS I. (B) HSS II.

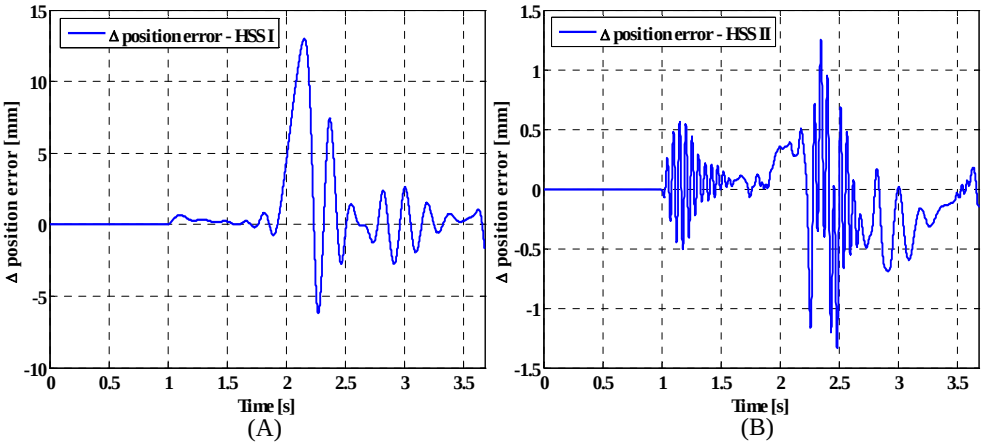

Figure O.14: Difference in error between RAAC control system, with and without disturbance. (A) HSS I. (B) HSS II.

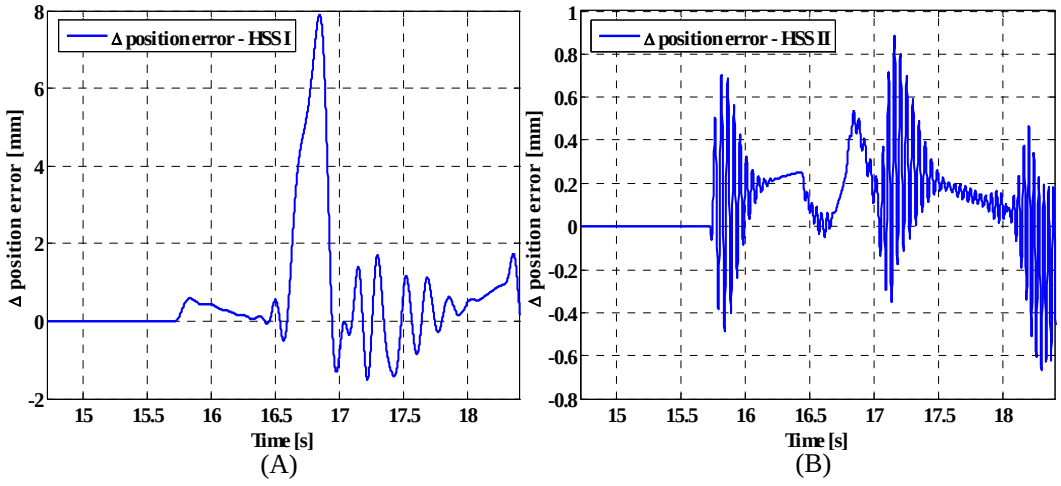

Figure O.15: Difference in error between ILC control system, with and without disturbance. (A) HSS I. (B) HSS II.

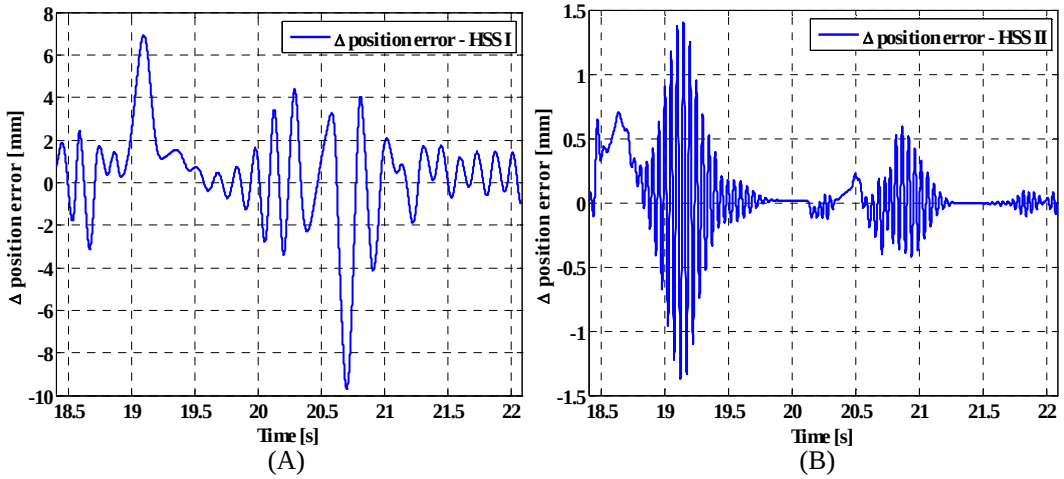

Figure O.16: Difference in error between ILC control system, with and without disturbance. (A) HSS I. (B) HSS II.

O.3 Trajectory tracking for linear controllers applied to a disturbance

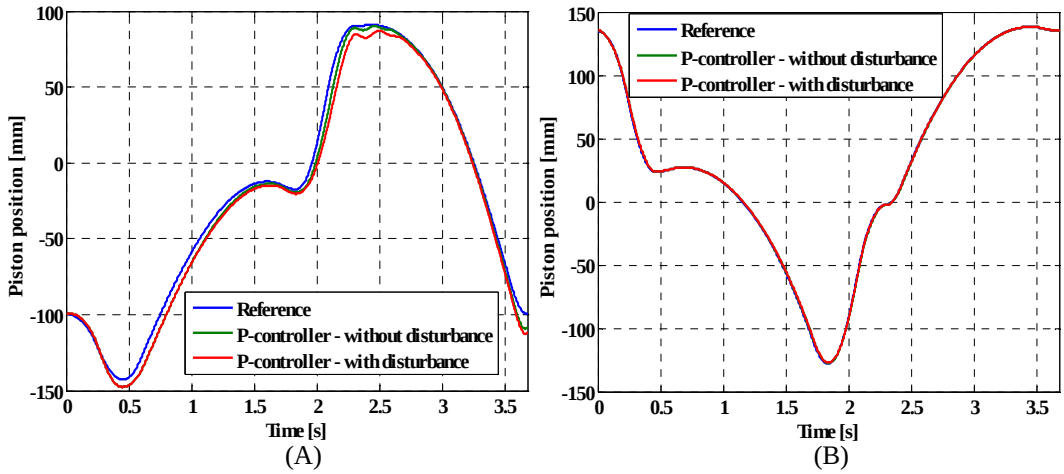

Figure O.17: Trajectory tracking P control system, with and without disturbance. (A) HSS I. (B) HSS II.

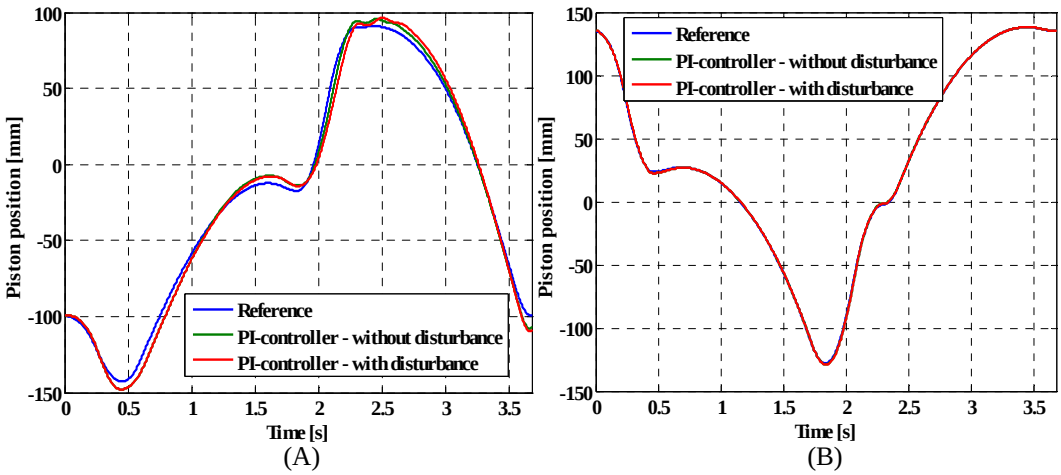

Figure O.18: Trajectory tracking PI control system, with and without disturbance. (A) HSS I. (B) HSS II.

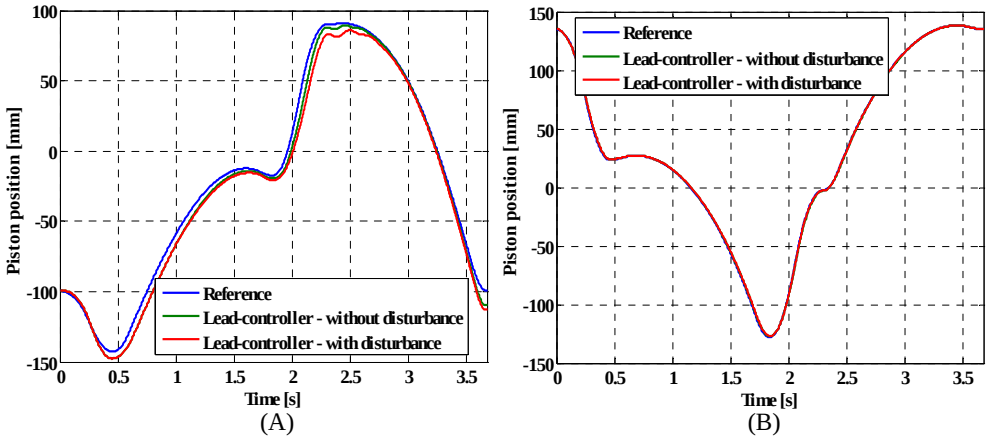

Figure O.19: Trajectory tracking Lead control system, with and without disturbance. (A) HSS I. (B) HSS II.

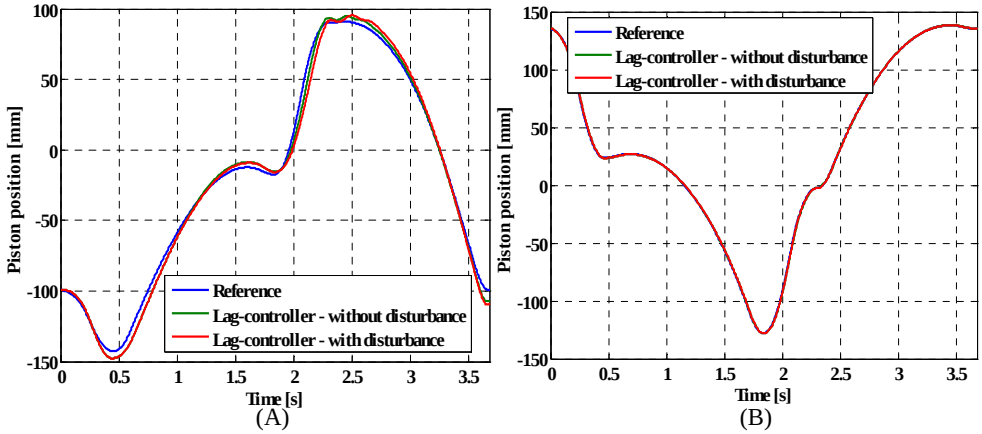

Figure O.20: Trajectory tracking Lag control system, with and without disturbance. (A) HSS I. (B) HSS II.

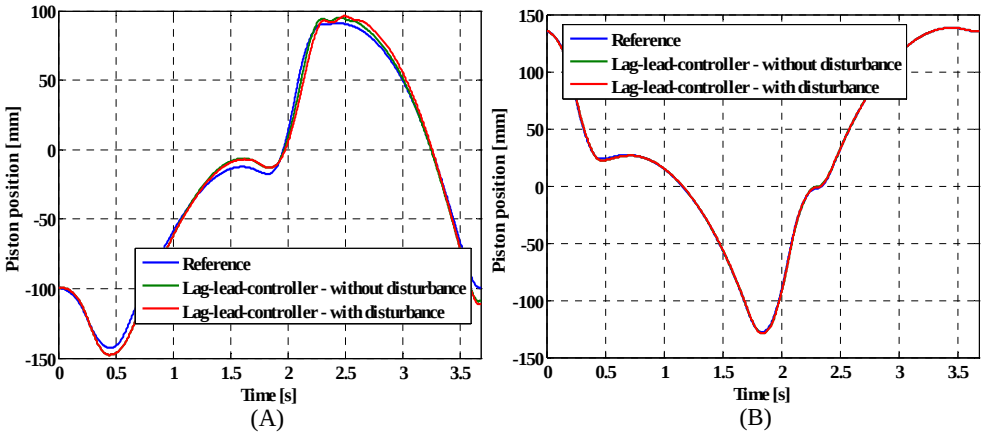

Figure O.21: Trajectory tracking Lag-Lead control system, with and without disturbance. (A) HSS I. (B) HSS II.

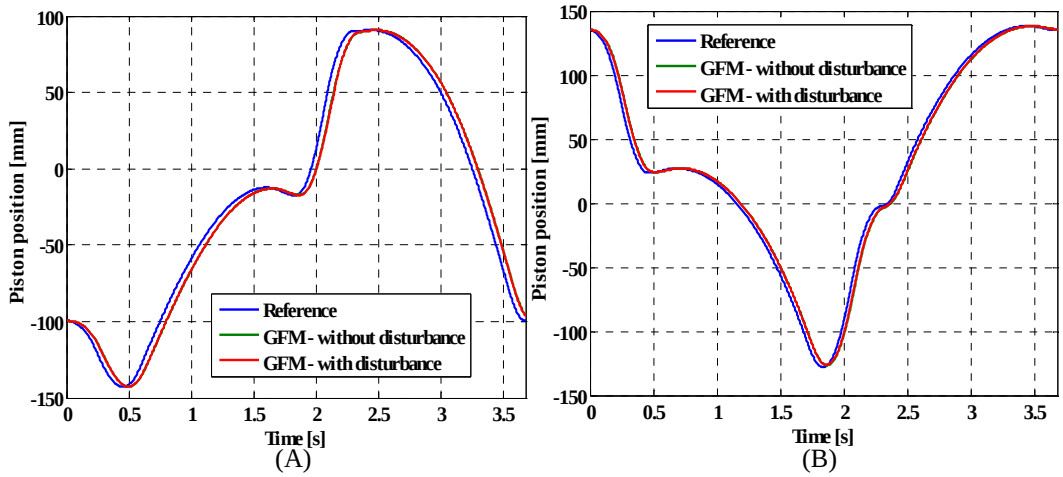

Figure O.22: Trajectory tracking GFM control system, with and without disturbance. (A) HSS I. (B) HSS II.

O.4 Trajectory tracking for nonlinear controllers applied to a disturbance

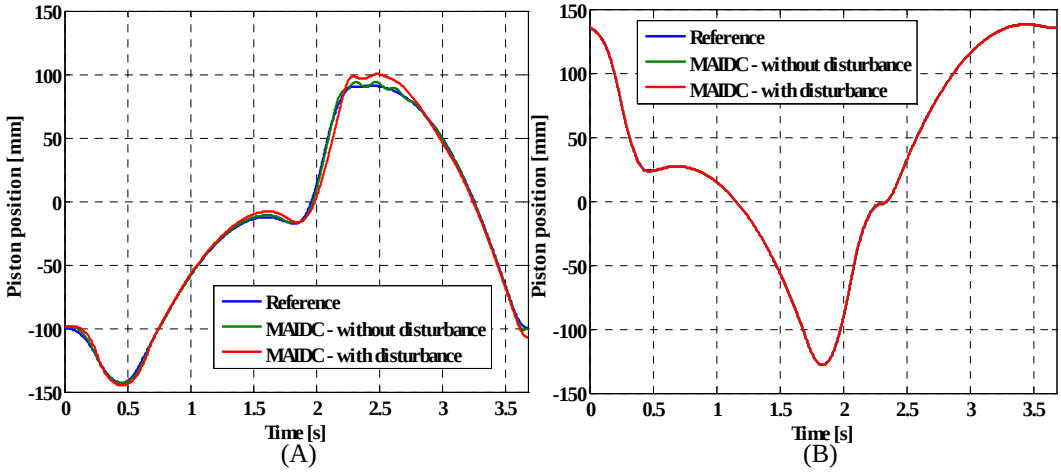

Figure O.23: Trajectory tracking MAIDC control system, with and without disturbance. (A) HSS I. (B) HSS II.

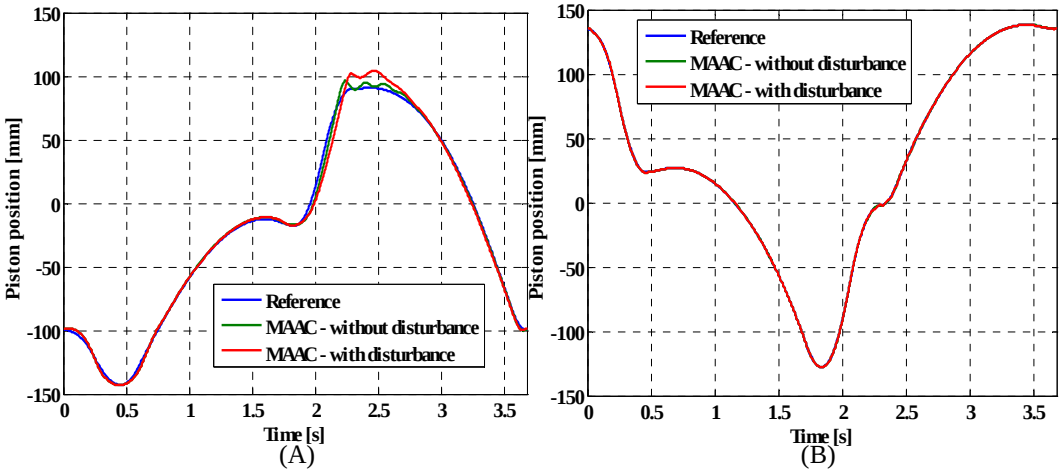

Figure O.24: Trajectory tracking MAAC control system, with and without disturbance. (A) HSS I. (B) HSS II.

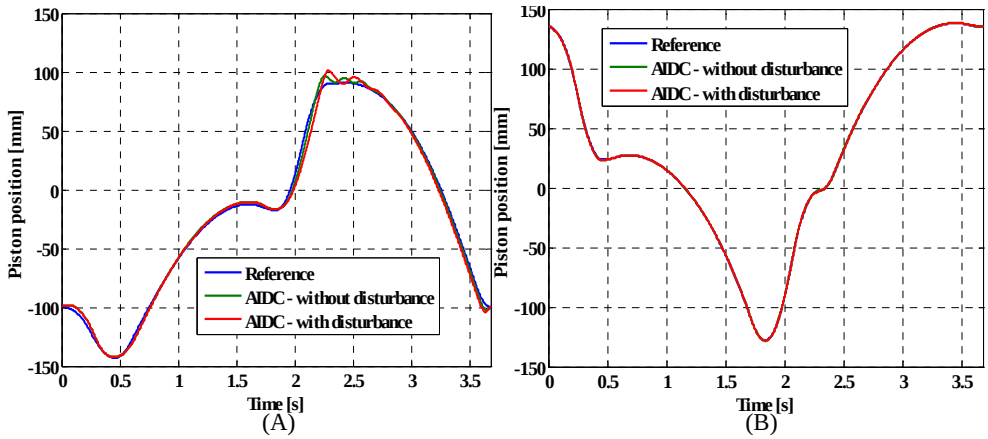

Figure O.25: Trajectory tracking AIDC control system, with and without disturbance. (A) HSS I. (B) HSS II.

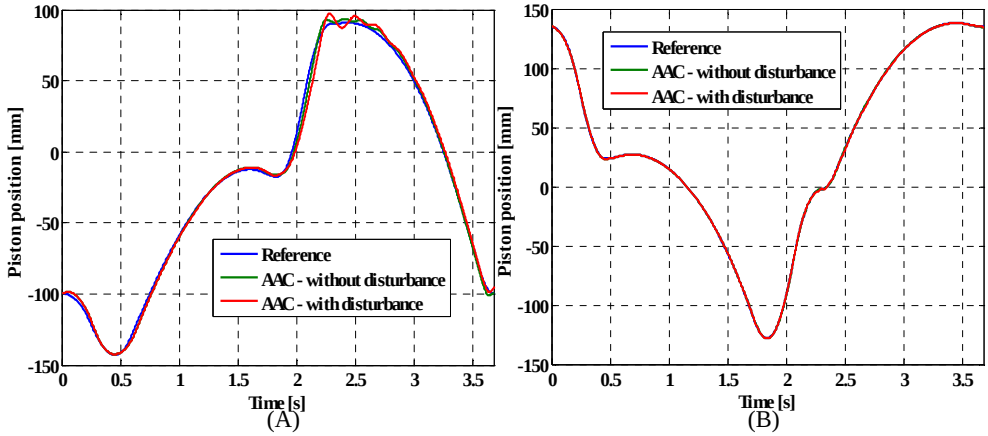

Figure O.26: Trajectory tracking AAC control system, with and without disturbance. (A) HSS I. (B) HSS II.

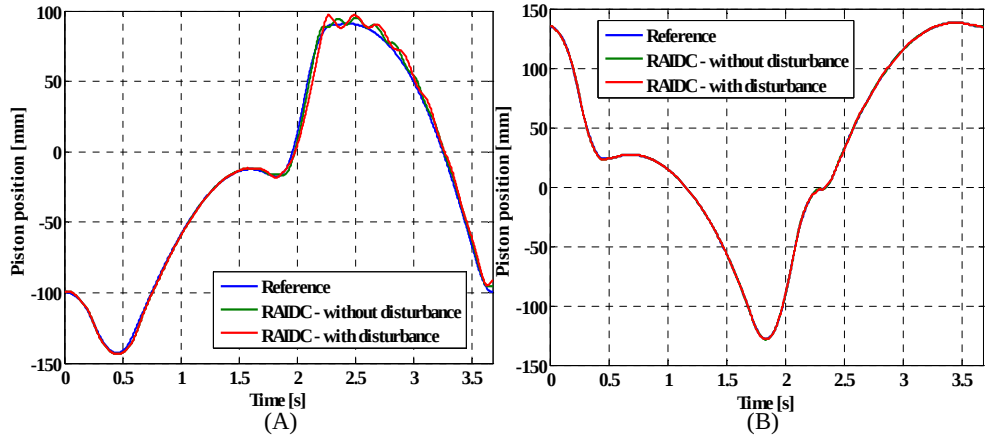

Figure O.27: Trajectory tracking RAIDC control system, with and without disturbance. (A) HSS I. (B) HSS II.

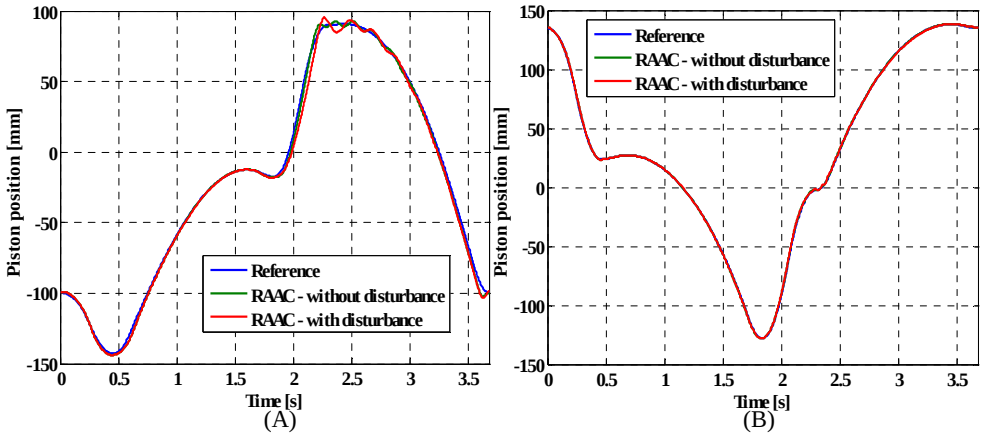

Figure O.28: Trajectory tracking RAAC control system, with and without disturbance. (A) HSS I. (B) HSS II.

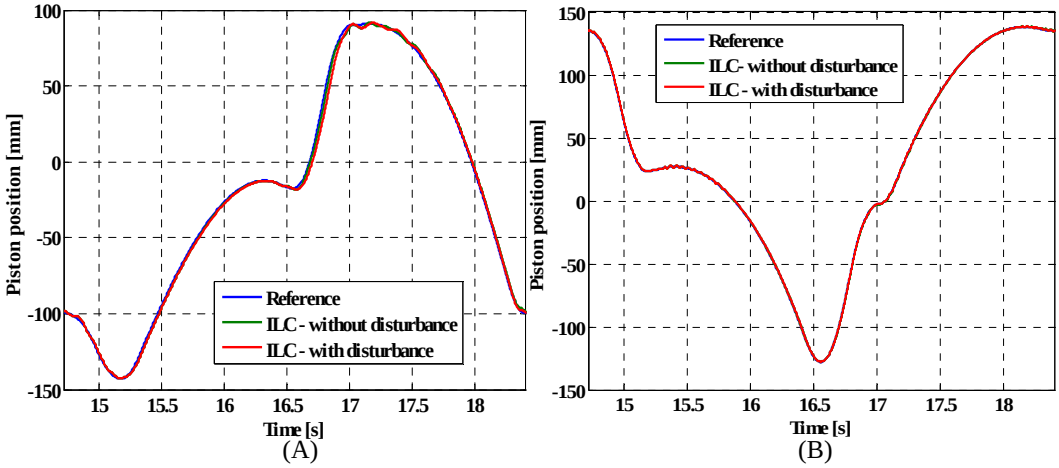

Figure O.29: Trajectory tracking between ILC control system, with and without disturbance. (A) HSS I. (B) HSS II.

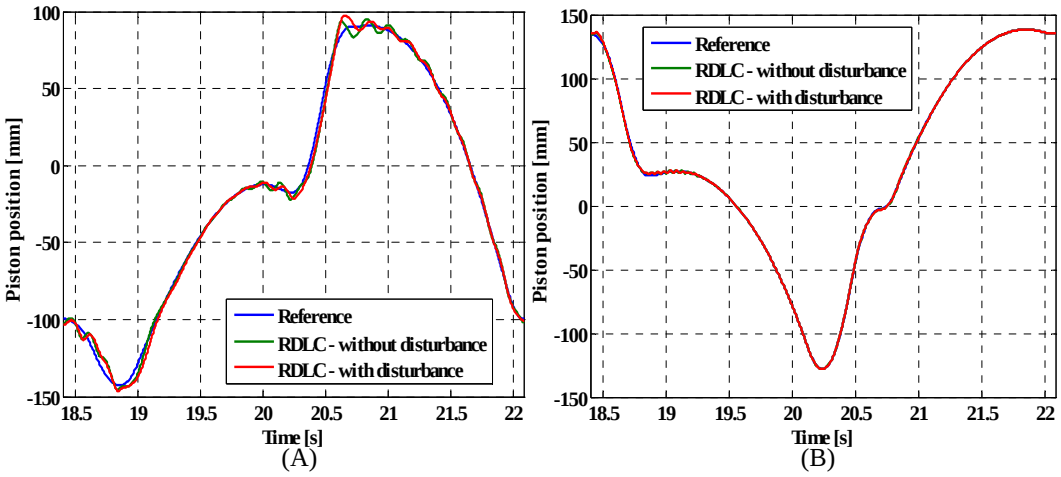

Figure O.30: Trajectory tracking between RDLC control system, with and without disturbance. (A) HSS I. (B) HSS II.

Contents

Appendix P

Laboratory Setup

In this appendix the laboratory equipment used for implementing and testing the controllers from the thesis is described

In the following is listed all the laboratory equipment used during this thesis along with and indication of where the belonging data sheets may be found. Afterwards a more detailed description of selected components are given along with a diagram showing the coupling of the various components.

- One servo valve, Moog, E760-942, El05(Data sheet on CD (not specific valve))
- One servo valve, Rexroth, 4WS 2 EE 10-40(Data sheet on CD(not specific valve))
- Two safety valves, Rexroth, 4 WE 6 Y51/AG24NZ4(No data sheet available)
- Two cylinders, Rexroth, STC 0331-10/, WLP350 17126, H05001(No data sheet available)
- Four pressure transducers, HBM P4A(Data sheet on CD)
- Two position transducers, Messotron WLP 350(Data sheet on CD)
- One pressure transducer amplifier, (No data sheet available)
- Two position transducer amplifiers, HBM, MVD2555(Data sheet on CD)
- One servo valve amplifier, Moog, Moog servo amp(No data sheet available)
- One servo valve amplifier, Rexroth, VT 1610(No data sheet available)
- Two DC power supplies(No data sheet available)
- One PC with DSP and DAQ card(No data sheet available)
- One DSP interface(No data sheet available)

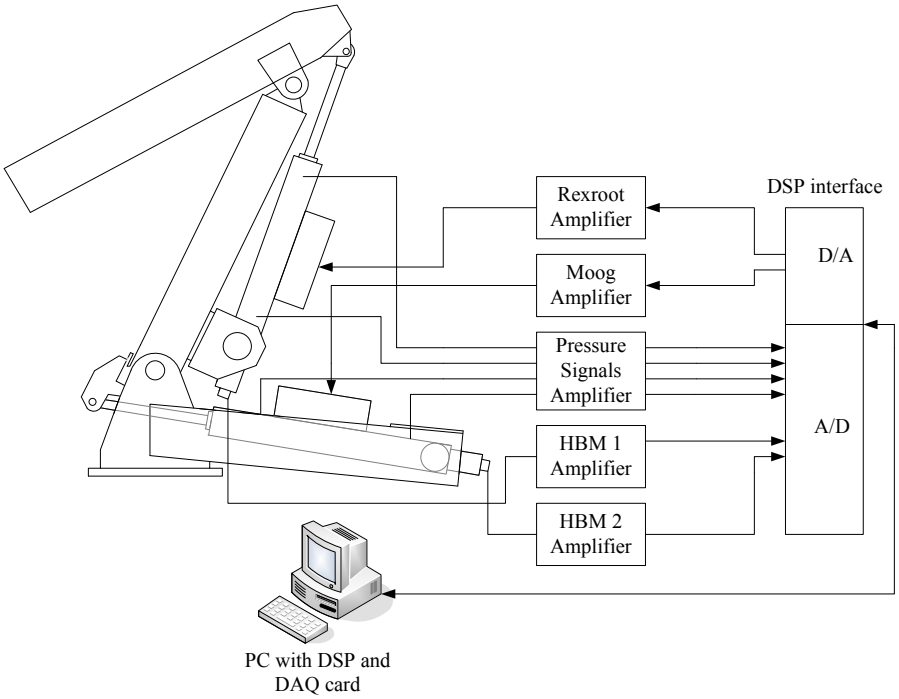

Figure P.1: Overview of lab setup

P.1 DSP System

The DSP (Digital signal processor) consists of three main parts, a DSP card, a DAQ card and a DSP interface. The DSP and DAQ cards are mounted in a PC via PCI facilitating relative quick data transfers of up to 132[MB/s]. Mounted on the DSP is also a processor, ram, and a BITSI interface connecting the DSP and DAQ card. The DAQ card facilitates the transport of data between the DSP card and the DSP interface where the various transducers and the servovalves are connected. The DSP interface is used for scaling signals, which is done by use of operational amplifiers, to and from the DAQ card which only supports signals in the range of $\pm 5[v]$.

P.2 Servo Valves and Safety Valves

The servo valves controlling the oil flow to and from the cylinders is mounted directly on cylinder 1 and 2. The Rexroot valve requires a control signal in the range of $\pm 10[v]$ whereas the Moog valve requires a signal in the range of $\pm 15[v]$ in order to insure the full operating range of the valves. Since the maximal signal output range of the DAQ card is $\pm 5[v]$ the signal for both the Rexroot and the Moog valve will have to be scaled in order to achieve the full operating range of the valves. The scaling is done by use of the operational amplifiers mounted on the DSP interface.

P.3 Pressure Transducers

The pressure transducers are mounted one on each side of each cylinder chamber allowing for data acquisition of pressure P_{1I}, P_{2I}, P_{1II} and P_{2II}. Each of the pressure transducers output a signal ranging from $0[v]-5[v]$, meaning that no scaling of the signals is necessary since the DAQ card as previously mentioned ranges from $\pm 5[v]$.

P.4 Position Transducers

The position transducers are mounted on the cylinders, and is used for measuring the position of the cylinder piston. The position transducers are coupled to a position transducer amplifier where the signal is amplified to a range from $0-10[v]$, meaning that the signal has to be scaled to $0-5[v]$ in order to fit the range of the DAQ card.

P.5 Code

The code is divided into two parts namely the DSP code and the PC code. The DSP code governs the behavior of the DSP whilst the PC code implements the graphical user interface hence forward designated GUI. The GUI allows the user of the system to communicate with the DSP allowing for fine tuning of some controller parameters, sampling of data and etc. The GUI is divided into several sections using tab sheets. The two main sheets are the ”controller type” and the ”trajectory” sheets. In the ”controller type” sheet (see figure P.2) it is possible to choose which controller to use with a given trajectory. In the ”trajectory” sheet (see figure P.3) a .txt file containing a trajectory can be read into system memory, and afterwards executed in order to run the desired trajectory. The remaining tab sheets makes it possible to see plots of position, pressure and valve voltage. When loading a trajectory and checking the ”sample data” function, data from the transducers will be sampled and displayed in the tabs containing the plotting functions. The data can also be saved to disc if desired, by pressing the ”save data” button in the main window. The code for the DSP can be found on the project CD.

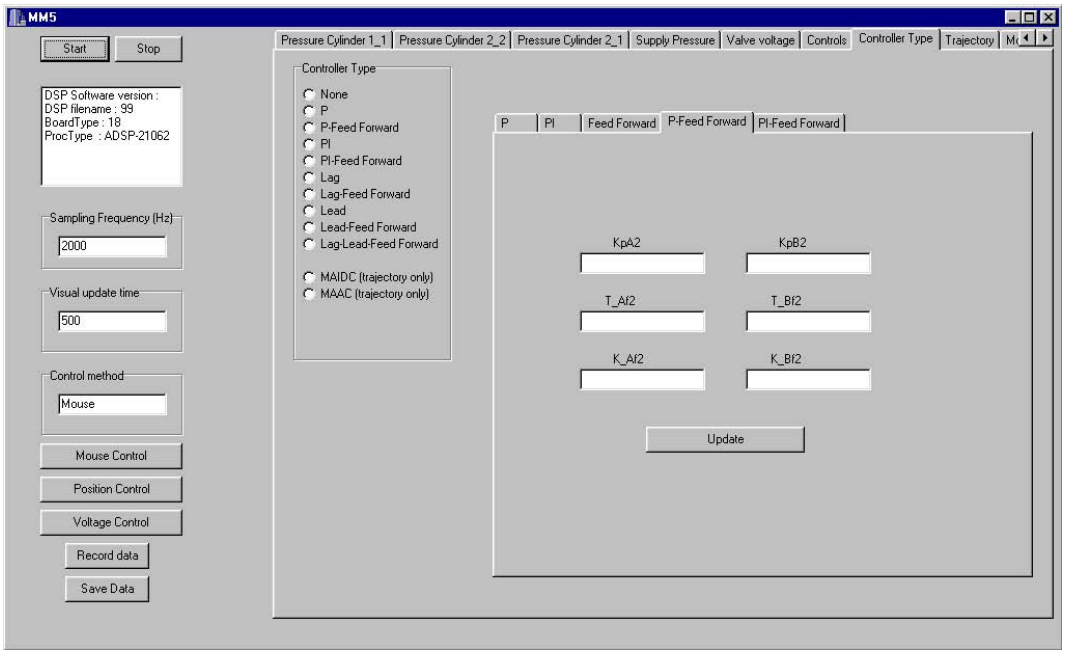

Figure P.2: GUI for choosing controller type.

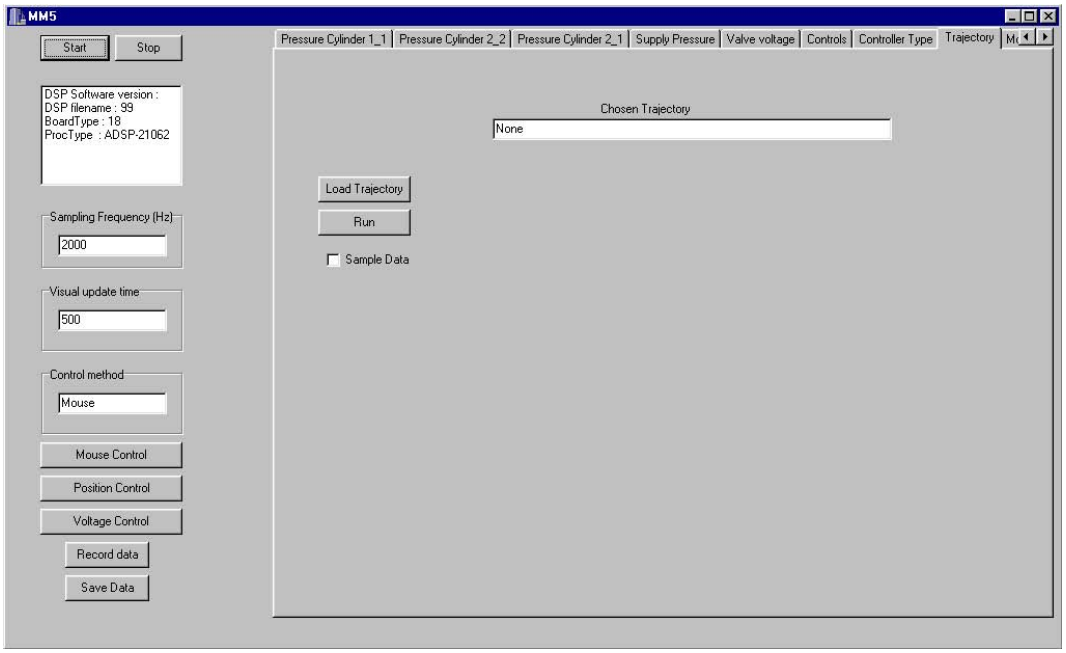

Figure P.3: GUI for loading and running trajectory.